UNIVERSITY OF SOUTHAMPTON

FACULTY OF ENGINEERING AND PHYSICAL SCIENCES

Institute of Sound and Vibration Research

Aerodynamic flow over cuboids and the noise generated

by

Yanan Wang

Thesis for the degree of Doctor of Philosophy

January 2020

UNIVERSITY OF SOUTHAMPTON

ABSTRACT

FACULTY OF ENGINEERING AND PHYSICAL SCIENCES
Institute of Sound and Vibration Research

Doctor of Philosophy

AERODYNAMIC FLOW OVER CUBOIDS AND THE NOISE GENERATED

by Yanan Wang

This thesis is motivated by the need to reduce train aerodynamic noise, especially the noise from pantographs and bogies which are comprised of bluff bodies including cuboids. The underlying physics of the flow over cuboids with different cross-sections and the emitted noise are studied. The effects of wall proximity and corner radii on the flow field and noise of a cube as well as the effect of the aspect ratio of cuboids are the main focus. The Delayed Detached Eddy Simulation method is adopted to investigate the flow features and obtain the noise source information. The far-field noise is then predicted using the Ffowcs Williams-Hawkings acoustic analogy. Benchmark comparisons on the flow over a wall-mounted cube and a sphere are conducted to validate the feasibility of the adopted methodology for describing the flow field; a separate simulation on a square cylinder is also implemented to gain confidence in predicting surface pressure fluctuations and the far-field noise. Good agreement has been achieved between results from the benchmark cases and those from the literature.

It is found that the wall proximity mainly affects the behaviour of the separated flow from the lower leading edge of the cube and also the flow separation along the ground. Large pressure fluctuations are observed close to the trailing edge and locations of the flow reattachment on the bottom of the cube. With the increase of the elevation height, the sound from the cube increases rapidly in the vertical direction and the maximum sound is observed when the cube is elevated by one quarter of the edge length above the ground. For rounded cubes, the flow separation is delayed with the increase of the corner radius; the shear layer moves towards the lateral surfaces and the recirculation length in the wake reduces. Flow features of the rounded cube vary with the Reynolds number, although no systematic dependence is observed. Large pressure fluctuations are found in the recirculating region on the lateral surface and near the trailing edge due to reduced recirculation length in the wake. Rounding the cube with a suitable radius can be an effective way to reduce the emitted noise. The minimum noise is found for a radius one third of the edge length. Cuboids with different aspect ratios are studied,

where the aspect ratio is defined as the ratio of the width in the spanwise direction to the length in the streamwise direction. The flow separated from the upper leading edge only reattaches to the top surface for aspect ratios smaller than 1 whereas the vortex shedding in the wake tends to be more evident as the aspect ratio is increased. The Reynolds number has negligible effect on the mean flow behaviours of the cuboid. Large pressure fluctuations happen with the flow reattachment and the formation of the secondary vortex near the trailing edge. The emitted noise from the cuboid is always higher in the cross-flow direction than that in the streamwise and spanwise directions. The maximum sound is found for the aspect ratio of 6.

Contents

List of Figures

List of Tables

Declaration of Authorship

I declare that the thesis entitled *Aerodynamic flow over cuboids and the noise generated* and the work presented in the thesis are both my own, and have been generated by me as the result of my own original research. I confirm that:

- this work was done wholly while in candidature for a research degree at this University;
- no part of this thesis has previously been submitted for a degree or any other qualification at this University or any other institution;
- where I have consulted the published work of others, this is always clearly attributed;
- where I have quoted from the work of others, the source is always given. With the exception of such quotations, this thesis is entirely my own work;
- I have acknowledged all main sources of help;
- where the thesis is based on work done by myself jointly with others, I have made clear exactly what was done by others and what I have contributed myself;
- parts of this work have been published as:
  - Wang, Y., Thompson, D., Hu, Z. (2019). Effect of wall proximity on the flow over a cube and the implications for the noise emitted. Physics of Fluids, 31(7), 077101.
  - Wang, Y., Thompson, D., Hu, Z. (2019). Effect of aspect ratios on flow and noise from cuboids. AIAA/CEAS Aeroacoustics Conference, Delft, Netherlands, May 20-24.
  - Wang, Y., Thompson, D., Hu, Z. (2018). Aerodynamic noise from trains: flow and aerodynamic noise generated by cuboids with different aspect ratios. The fourth International Conference on Railway Technology, Sitges, Barcelona, Sep. 3-7.
  - Wang, Y., Thompson, D., Hu, Z. (2018). Effect of rounded corners on the flow and noise from a cube. AIAA/CEAS Aeroacoustics Conference, Atlanta, Georgia, USA, Jun. 25-29.

– Wang, Y., Thompson, D., Hu, Z. (2017). Aerodynamic noise generated by pantograph knee joint. First International Conference on Rail Transportation, Chengdu, China, Jul. 10-12.

Signed:.....

Date:.....

Acknowledgements

First of all, I would like to express my sincere gratitude to my supervisors, Professor David Thompson and Dr. Zhiwei Hu. Thank them for their devoted guidance and supports all the way in my PhD study. They have casted great influence on me about how to be a researcher and how good mentors are. This four-year experence working with them is a life-long treasure, which will inspire me greatly in my future work.

I deeply appreciate the sponsorships from University of Southampton and the China Scholarship Council (CSC), which make possible this thesis come true. I also would like to thank Xiaowan Liu, who provided huge help at my beginning stage of the PhD study. Thank her for her kindness and patience, which mean a lot to me.

Thank colleagues in the Dynamics Group and friends I met in Southampton. Because of them, my time in Southampton becomes more enjoyable. Especially, I would like to thank Yingying Huang, Mengsi Wang and Ying Wang. We shared the same house in the first two years in Southampton and lived together like a family. Thank them made me feel be cared and supported. We had a lot of fun together to beat the loneliness.

Last but not the least, thank my family. Without their unconditional love and support, I could not be who I am. They will always be my motivation to become a better me.

Nomenclature

Roman symbols

A	Reference area (m^2)
c_0	Speed of sound (m/s)
C_d	Drag coefficient
C_l	Lift coefficient
C_s	Side-force coefficient
$\overline{C}_d$	Mean drag coefficient
$C_{d,\mathrm{rms}}$	Root mean square of drag coefficient
$C_{l,\mathrm{rms}}$	Root mean square of lift coefficient
$C_{s,\mathrm{rms}}$	Root mean square of side-force coefficient
C_f	Skin friction coefficient
C_p	Pressure coefficient
C_{pb}	Base pressure coefficient
$C_{p,\mathrm{min}}$	Minimum pressure coefficient
d	Wall distance (m)
$\tilde{d}$	Modified length scale in DES model (m)
D	Diameter of the sphere (m)
f	Frequency (Hz)
h	Elevation height (m)
H	Height of the cuboid (m)
$H(f)$	Heaviside function

L	Length of cube side (m)
L_p	Pressure fluctuation level (dB)
$L_{p,\text{int}}$	Integrated pressure fluctuation level (dB)
L_r	Recirculation length (m)
L_{rea}	Reattachment length (m)
L_{sec}	Length of the secondary vortex (m)
M	Mach number
p	Pressure (Pa)
$p^{'}$	Pressure fluctuation (Pa)
P_{ij}	Compressive stress tensor (N/m^2)
p_{ref}	Reference acoustic pressure ($=20\mu Pa$)
p_{rms}	Root mean square of the pressure fluctuation (Pa)
Q	Q criterion
Q_n	Normalised Q criterion
R	Corner radius (m)
Re	Reynolds number
S	Surface area (m^2)
S_{ij}	Mean strain rate tensor (1/s)
St	Strouhal number
t	Time (s)
T_{ij}	Lighthill stress tensor (N/m^2)
t^*	Normalised time scale
u_τ	Friction velocity (m/s)
U_n	Velocity normal component (m/s)
U_t	Velocity parallel component (m/s)
U_∞	Freestream velocity (m/s)
W	Width of the cuboid (m)

x, y, z	Cartesian coordinate system
y_1^+	Dimensionless first-cell spacing

Greek symbols

Δt	Physical time step (s)
Δx, Δy, Δz	Cell dimensions in x,y, and z directions (m)
Δ	Filter width (m)
$\delta(f)$	Dirac delta function
δ_{ij}	Kronecker delta
ρ	Density (kg/m^3)
$\rho^{'}$	Density perturbation (kg/m^3)
μ	Dynamic viscosity (N $\cdot$ s/m^2)
ν	Kinematic viscosity (m^2/s)
ν_t	Turbulent viscosity (m^2/s)
ν_{SGS}	Sub-Grid-Scale viscosity (m^2/s)
$\tilde{\nu}$	Modified turbulent eddy viscosity (m^2/s)
ϕ	Generic scalar quantity
λ	Wavelength (m)
∇	Gradient operator
τ_{ij}	Stress tensor (N/m^2)
τ_w	Wall shear stress (N/m^2)
Ω	Vorticity (1/s)

Abbreviations

2D	Two-dimensional
3D	Three-dimensional

ASP	Actively-controlled Single-arm Pantograph
CAA	Computational Aeroacoustics
CFD	Computational Fluid Dynamics
CFL	Courant-Friedrichs-Lewy
dB	Decibel
DDES	Delayed Detached Eddy Simulation
DES	Detached Eddy Simulation
DNS	Direct Numerical Simulation
FW-H	Ffowcs-Williams Hawkings
LBM	Lattice Boltzmann Method
LES	Large Eddy Simulation
MSD	Modelled Stress Depletion
OASPL	Overall Sound Pressure Level
PIMPLE	PISO-SIMPLE
PISO	Pressure-Implicit Split Operator
PIV	Particle Image Velocimetry
PSD	Power Spectra Density
RANS	Reynolds Averaged Navier-Stokes equation
RTRI	Railway Technical Research Institute (Japan)
S-A	Spalart-Allmaras turbulent model
SGS	Sub-Grid-Scale
SIMPLE	Semi-Implicit Method Pressure Linked Equations
SPL	Sound Pressure Level
TKE	Turbulence kinetic energy
TVD	Total Variation Diminishing
URANS	Unsteady Reynolds Averaged Navier-Stokes

Subscripts

$\parallel$	Parallel
0	Ambient freestream quantities
∞	Freestream quantities
i	Spatial or summation index

Superscripts

$-$	Mean value
$'$	Fluctuating component

Chapter 1

Introduction

1.1 Background and motivation

Higher speeds have always been the source of innovation for the development of trains, ever since the early nineteenth century. However, as train speeds increase, inevitably, so does the noise emission. Reducing railway noise is an especially important aspect for new high-speed projects. The sound power due to rolling noise is found to increase approximately in proportion to the third power of the train speed (Thompson, 2008), whereas the acoustic energy from aerodynamic noise increases more rapidly, at a rate between the 6th and 8th power of the flow speed (Curle, 1955; Lighthill, 1952). When the train speeds exceed about 300 km/h, flow-induced noise becomes dominant (Talotte, 2000). Clearly, the noise from high-speed trains cannot be reduced without a better understanding and control of the aerodynamic noise.

There are many sources of aerodynamic noise for high-speed trains, with pantographs and bogies identified as significant components (Mellet et al., 2006). Pantographs are mounted on the roof of the train contacting with the cable to collect power while the bogie is a modular subassembly of wheels and axles carrying the train. Especially the noise from pantographs, which is emitted from the top of the train, is difficult to shield by using conventional trackside noise barriers. Therefore, there is an urgent need to investigate the mechanisms of the noise generation from the pantograph as well as the train bogie. This could be beneficial for industry to tackle aerodynamic noise at an early stage of train design and minimize its negative impact on the environment. The noise from a pantograph or a bogie depends on the size and shape of its components, the flow conditions and the interaction between individual components.

Prediction models combining a better modelling of noise sources and advanced propagation methods are under development for pantograph and bogie noise. The component-based models applied to aerodynamic noise prediction for aircraft landing gears make

parametric study possible and are also promising for train pantograph and bogie noise predictions (Latorre Iglesias et al., 2017a). The pantograph and the train bogie can be simplified as a group of representative components and the overall noise from them can be approximated as the incoherent sum of the noise produced by all those components, assuming that interaction effects on noise can be neglected.

1.2 Research objectives

The aim of this thesis is to improve the understanding of the aerodynamic behaviour and noise generation around compact components such as those found in pantographs and bogies and to expand the database for the component-based model of the pantograph and bogie noise prediction. Particular aspects to be considered in this thesis include the dependence of the flow features and the far-field noise on the installation position, the geometry of the component and the incoming flow speed. A combination of Computational Fluid Dynamics (CFD) and Computational AeroAcoustic (CAA) methods is used to investigate the unsteady flow around these components and the resulting noise. The first step is to obtain an accurate description of the aerodynamic characteristics in the noise-generating near-field region by solving the governing equations of fluid motion using CFD approaches. Then the Ffowcs Williams-Hawkings (FW-H) equation is employed to predict sound propagation to the far-field region based on the information acquired from CFD.

1.3 The structure of thesis

The thesis is structured as follows: a review of the literature covering experimental and numerical investigations on noise generated by high speed trains, especially by pantographs and bogies is presented in Chapter 2. Fundamental studies on the flow field and noise induced by bluff bodies, such as cubes and cuboids, are also reviewed. In Chapter 3, the relevant computational methods employed in CFD and CAA techniques are described. The effect of wall proximity on the flow past an elevated cube and the emitted noise is studied numerically in Chapter 4. Before conducting simulations on the elevated cube, a benchmark case on the flow over a wall-mounted cube is implemented first to validate the adopted methodology and obtain guidelines for the numerical setup for the following simulations. Numerical investigations on the flow over cubes with rounded corners and the emitted noise are presented in Chapter 5. Five corner radii are taken into account from 0 to 40% of the cube length at five Reynolds numbers. Another benchmark case on the flow over a sphere is also presented in Chapter 5. Chapter 6 investigates the effect of the aspect ratio on the flow around cuboids and the generated

noise. Ten aspect ratios from 1/6 to 12 are considered at three flow speeds. Finally, the main conclusions and recommendations for future work are presented in Chapter 7.

1.4 Original contributions

- Although many investigations have been conducted on the wall-mounted cube, the flow over a cube elevated from the ground and also the emitted noise very little have been done. In this thesis, the flow characteristics of the elevated cube are investigated carefully and the sound emitted to the far field is predicted. Implications of the relationship between the flow and the far-field noise are obtained.

- For cubes, the flow always separates from the leading edge at Reynolds numbers greater than 3×10^5 (Castro and Robins, 1977). However, when the cube edges are rounded, the position of flow separation changes, as does the flow behaviour and the emitted noise. Flow features of the cube with a series of corner radii at different Reynolds numbers are analysed in this thesis. The effect of rounded corners on the far-field noise is also examined.

- The tonal noise from a square cylinder is generated due to the periodic vortex shedding in its wake (Lyn et al., 1995). As the length of the cylinder is reduced, the formation of the vortex shedding can be affected by varying the aspect ratio. Consequently, the sound emitted to the far field changes as well. The effect of the aspect ratio on the flow over cuboids and the far-field noise is studied in this thesis. Implications of the flow patterns on the far-field noise are determined.

Chapter 2

Literature review

This chapter introduces the main sources of railway noise, especially the aerodynamic noise from train pantographs and bogies. A review about feasible approaches to predict aerodynamic noise emitted from high-speed trains is then presented. In particular, a semi-empirical component-based model is described, which was originally proposed for aircraft landing gear noise but turns out to be promising in the application of pantograph and bogie noise prediction as well. Subsequently, studies on the flow over cubes and cuboids are reviewed, followed by the aerodynamic noise from bluff bodies.

2.1 Sources of train noise

High-speed trains are attracting more and more attention as a more sustainable means of transport than short-haul aircraft. The speeds of high-speed trains are increasing under the strong commercial drive, but consequently so does the noise produced. The noise emitted by modern electric high-speed trains mainly consists of rolling noise and aerodynamic noise (Thompson et al., 2015). For conventional trains running at speeds up to 250 km/h, the railway noise is primarily produced by the rolling noise due to the dynamic interaction between the wheels and rails (Thompson, 2008). However, the aerodynamic noise exceeds the rolling noise when the train speed is higher than about 300 km/h (Talotte, 2000). Figure 2.1 illustrates the corresponding trends of both rolling noise and aerodynamic noise with respect to train speeds. In Figure 2.1, aerodynamic noise exceeds rolling noise at about 370 km/h, which is slightly higher than the former reported transition speed. Nevertheless, it is clear that in order to control the maximum noise generated by high-speed trains, the role played by aerodynamic noise cannot be underestimated.

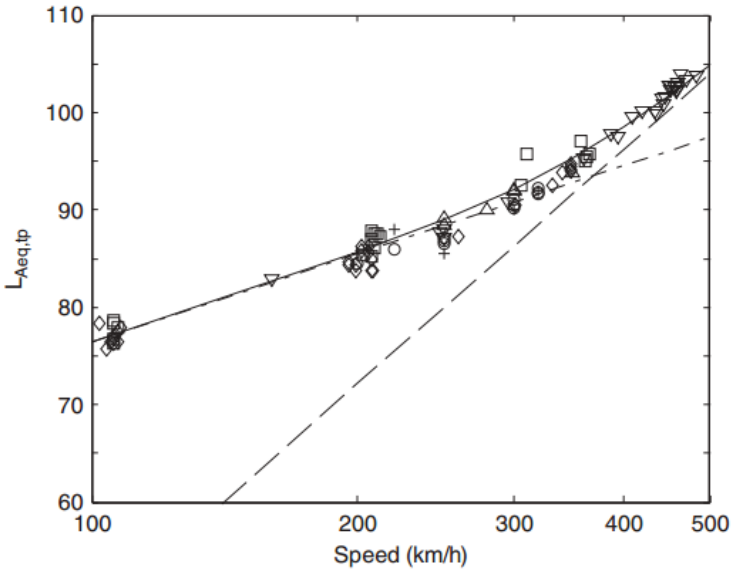

Figure 2.1: $L_{Aeq,tp}$ measured at 25m from TGV-A($\triangledown$,$\square$,$\diamond$), TGV-Duplex ($\circ$, $\triangle$) and Thalys ($+$). $(-.-.)$ Straight line with slope of 30 $\log_{10}V$ to represent rolling noise; $(- - -)$ straight line with slope of 80 $\log_{10}V$ to represent aerodynamic noise; $(-)$ total (Thompson, 2008).

The main aeroacoustic sources of high-speed trains are identified as follows (Talotte, 2000; Thompson et al., 2015):

- The pantograph
- The recess of the pantograph
- The bogies
- The inter-coach spacing
- The nose of the leading car
- The coach wall surfaces
- The rear power car
- The louvres and the cooling fans
- Protuberances, such as door handles and steps

The locations of the above mentioned aeroacoustic sources for a high-speed train are sketched in Figure 2.2.

In recent years, several prediction models for train noise have been developed (Gautier et al., 2000). According to both model complexity and potential use, three different categories among these models were identified by Talotte et al. (2003), including models describing physical mechanism of each individual source, sound propagation models and

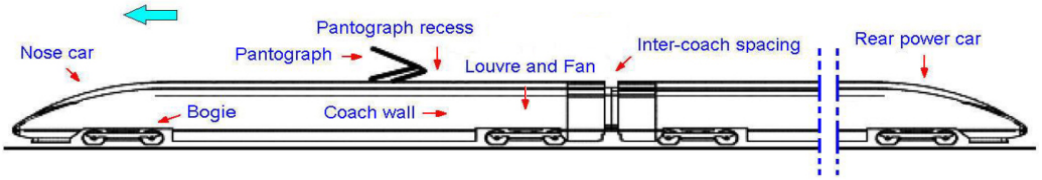

Figure 2.2: Locations of main aeroacoustic sources for a high-speed train (Zhu, 2015)

intermediate models. Considerable research was conducted on the modelling of rolling noise in the 1970s and 1980s and the most notable model for prediction of rolling noise is the TWINS model (Thompson et al., 1996). Although models for rolling noise are quite mature and have been verified by extensive field experiments, modelling aerodynamic noise from the train is a more recent subject for research and significant developments were envisaged (Talotte et al., 2003).

2.1.1 Pantograph noise

As shown in Figure 2.2, the pantograph is located on the roof of the train, therefore, the noise radiated from it cannot be shielded efficiently by conventional noise barriers, unless they are very tall. The time history of the A-weighted Sound Pressure Level (SPL) from Shinkansen S1 and S2 trains running at speeds of 235 km/h and 312 km/h on a viaduct with 2 m high noise barriers installed on both sides of the bridge is shown in Figure 2.3. The two most predominant peaks on each picture are generated by the pantographs.

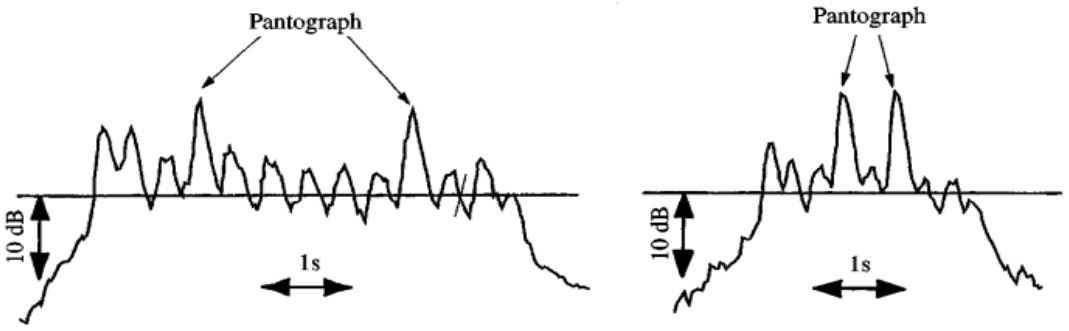

Figure 2.3: The time history of A-weighted SPL of Shinkansen S1 at speed of 235 km/h (left) and S2 at speed of 312 km/h (right) (Kitagawa and Nagakura, 2000)

Typically, pantographs consist of the contact trips, horns and horn bush all from the panhead, arms and a foot region, as illustrated in Figure 2.4. Currently, there are various different types of pantograph in operation. Two examples from Germany, DSA 350 SEK and a prototype Actively-controlled Single-arm Pantograph (ASP), are shown in Figure 2.5. Due to the important role pantographs are playing in the overall noise of

high-speed trains, considerable experimental and numerical investigations have been conducted on the pantograph noise. The mechanism of pantograph noise is characterised by periodic vortex shedding from struts with different diameters because of flow-component interaction and the noise mainly consists of Aeolian tones, which can be identified clearly by the narrow peaks in the noise spectra (Talotte, 2000). Fluctuating forces will be produced during the vortex shedding process, when vortices are shed from the surfaces of struts and interact with the surrounding flow; consequently, typical dipole sound is created. Although the pantographs in Figure 2.5 are mainly composed of slender struts, compact components resembling cuboids can also be found around the knee joint and the foot region. For high speed trains, the general speed ranges from 30 m/s to 70 m/s. The cross-section size of these cuboids is from 20 mm to 120 mm. Therefore, the corresponding Reynolds numbers range from 4×10^4 to 6×10^5.

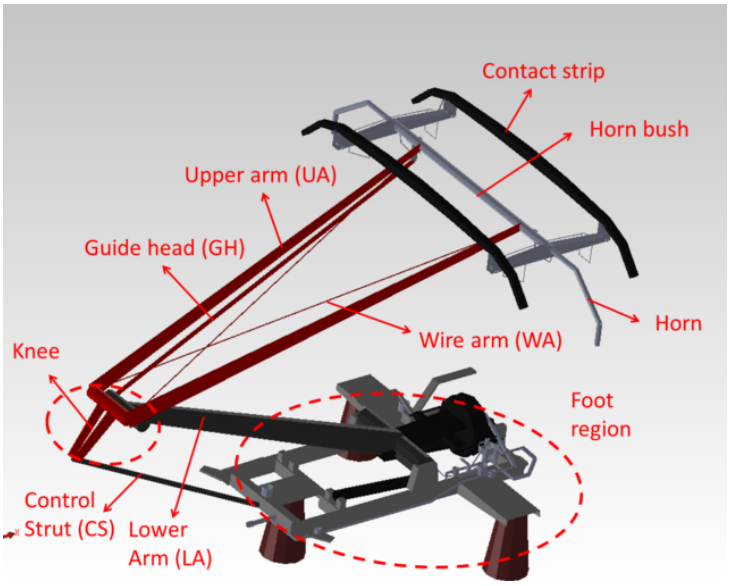

Figure 2.4: Components of the pantograph (Latorre Iglesias, 2015)

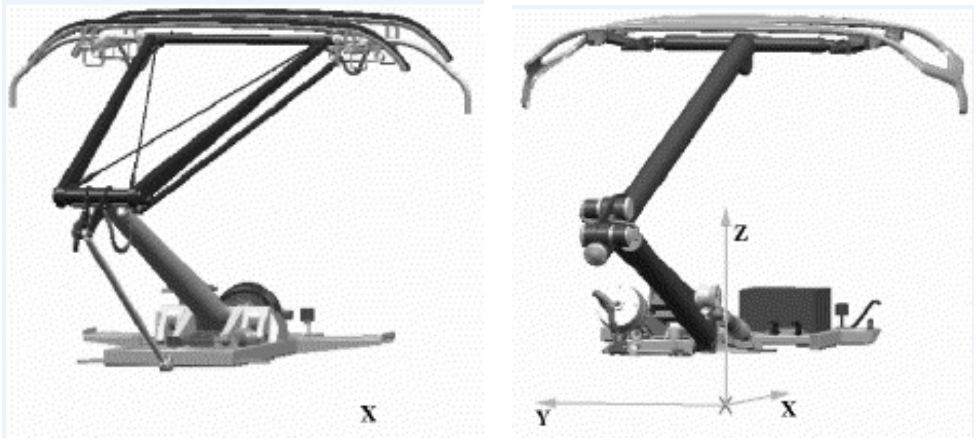

(a) DSA 350 SEK (b) ASP

Figure 2.5: DSA 350 SEK and prototype of ASP (Latorre Iglesias et al., 2015)

The main noise generating parts for the pantographs were identified by Grosche and Meier (2001) as the foot, the panhead and the knee joint. They used acoustic mirror techniques based on the noise measurement performed for a full scale DSA350 pantograph in a wind tunnel with a flow speed at 40 m/s. More elaborate measurements were carried out by Lölgen (1999) on full scale pantograph models in the wind tunnel of the Railway Technical Research Institute (RTRI). Lölgen (1999) pointed out that the noise from a DSA350SEK pantograph was characterised by Aeolian tones, as displayed in Figure 2.6. Components of the pantograph responsible for these peaks were identified as the control strut for the tonal noise at 300 Hz, the contact strips at 550 Hz, the horns at 900 Hz and the stroke limiting cage at 3500 Hz.

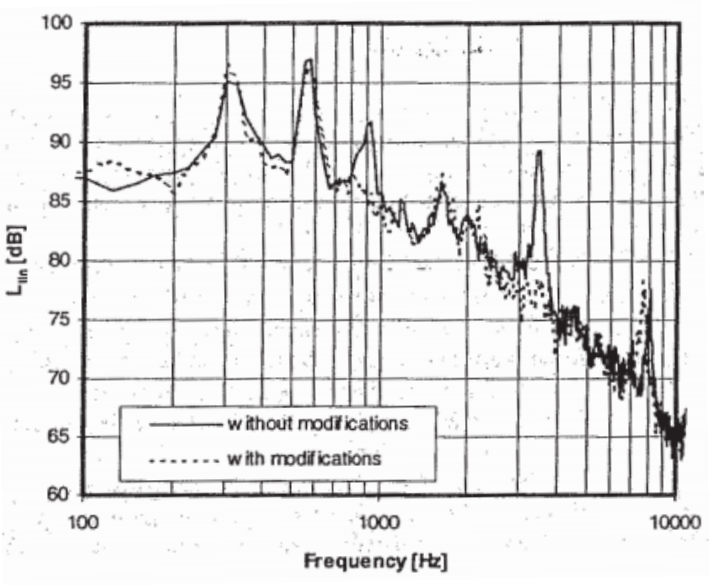

Figure 2.6: Noise spectra of a DSA350SEK pantograph with and without head motifications at 330 km/h (Lölgen, 1999)

A full scale pantograph installed inside the train roof cavity in both raised and lowered operating conditions was tested with turbulent inflow in a wind tunnel by Brick et al. (2011), as indicated in Figure 2.7. The 'spires' installed in the front of the train roof model in Figure 2.7 acted as a turbulence generator. They found that the noise level from the lowered pantograph was at least 8 dB lower than that from the raised one. In addition, the presence of the turbulence generator was beneficial for pantograph noise reduction, especially for the lowered condition. The relation between the overall noise generated by the pantograph and the train speed was found to follow a sixth power law. The same rule was found to be applicable to the cavity noise with turbulent incident flow, but a seventh power law was found instead in the absence of turbulence.

In recent years, endeavours have been made to use numerical techniques to investigate the flow behaviour and aerodynamic noise from pantographs. However, due to the complex geometry of pantographs and the limited computational capability of current

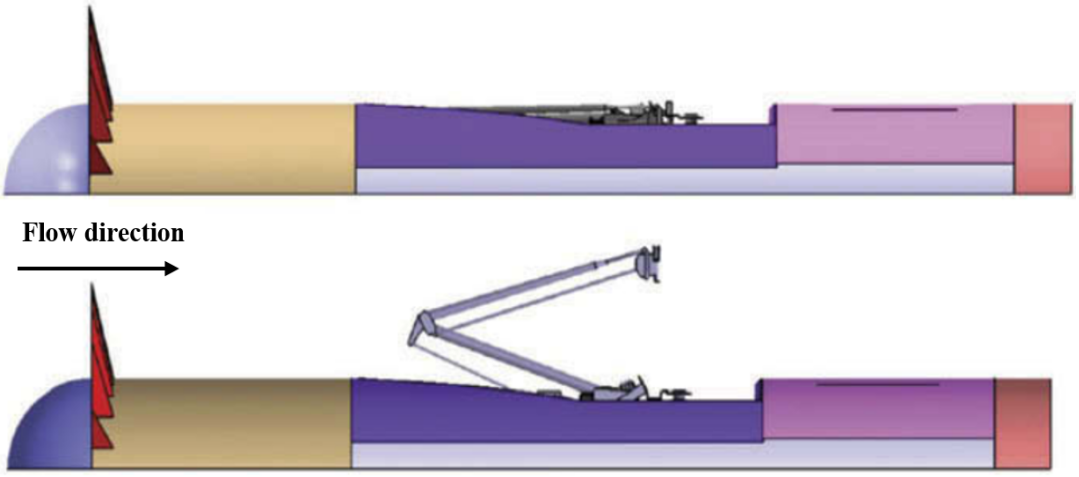

Figure 2.7: Arrangement of the experiments conducted by Brick et al. (2011)

computers, it is still not feasible to simulate the flow around a full 3D pantograph model directly to obtain credible details about the flow field sufficient for reliable aeroacoustic prediction.

The panhead is well known for its significant contribution to pantograph noise. Lee and Cho (2008) conducted numerical investigations on a simplified panhead at low speeds using incompressible unsteady 2D simulations combined with the FW-H acoustic analogy. They found that, not only low frequency noise, but also high frequency broadband noise was generated around the panhead region. Liu et al. (2014) simplified the pantograph as a combination of cylinders with appropriate sections. They started with investigations on flow around circular cylinders in cross-flow with different speeds and yaw angles employing the Delayed Detached Eddy Simulation (DDES) method. Subsequently, the far-field noise from each cylinder was predicted by using the FW-H equations. The results revealed detailed correlation between the generated noise and the yaw angle.

Ikeda and Mitsumoji (2008) evaluated dipole noise source contributions from the panhead and identified the source structure in the flow using a methodology proposed by Takaishi et al. (2004). In their work, Howe's vortex sound theory (Howe, 2003) was employed as an acoustic analogy. The net contribution of each noise source was inspected using the cross-correlation between the sound received in the far field and the source strength at each point around the object. The noise was estimated by the distribution of dipole noise source contributions. The methodology was extended by Takaishi et al. (2010) to make it possible to analyse the high frequency noise radiated from the region between the panhead and the support without requiring the assumption of acoustic compactness. They introduced the boundary element method to solve non-compact Green's functions; this is much more computationally efficient than the finite element method used in conventional CAA techniques.

2.1.2 Bogie noise

Usually, one or two pantographs are mounted on a train, while there are many more bogies. Significant noise is emitted from the bogie including both the aerodynamic and the rolling components. These two components are in close proximity and are difficult to be separated experimentally (Thompson et al., 2015). In particular, the noise from the leading bogie is more significant than that from other bogies due to the higher incoming flow speed. The geometry of the bogie is more complex than the pantograph. Figure 2.8 illustrates the bogie mock-up with a scale factor of 1/7 for acoustic measurements in an anechoic wind tunnel adopted by Latorre Iglesias et al. (2017b). As shown, cuboids are important components in the bogie. The bogie mock-up was mounted in the bogie cavity of a 1/7-scale train body. The far-field noise was measured by a microphone array consisting of 66 microphones in a spiral arrangement. Different bogie configurations and cavity shapes were considered and the flow speed ranged between 50 and 100 m/s. It was found that the sound spectrum from the bogie configuration was broadband and the sound directivity was nearly omnidirectional. The speed exponent of the Overall Sound Pressure Level (OASPL) from different bogie configurations was between 6.4 and 6.7. The noise level increased considerably when components of the bogie were not shielded by the bogie cavity exposing to the incoming flow.

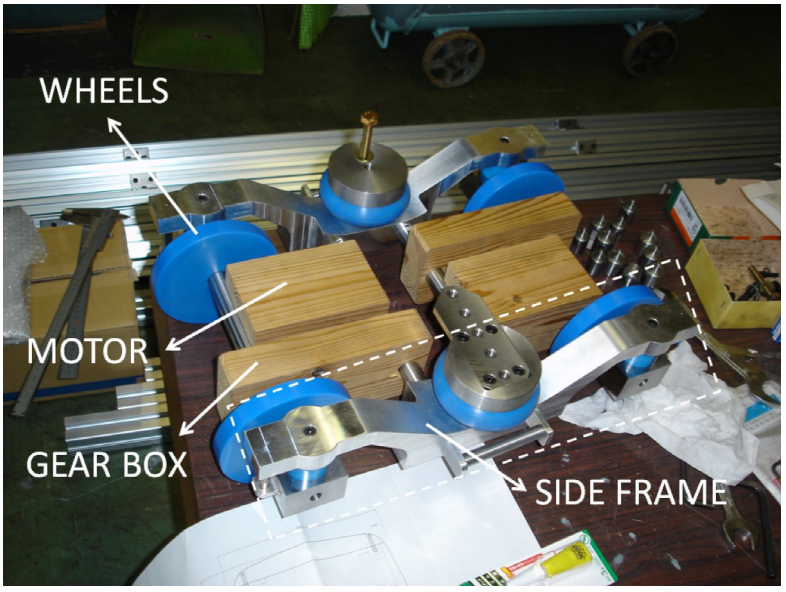

Figure 2.8: The bogie mock-up used in the measurements conducted by Latorre Iglesias et al. (2017b)

Uda et al. (2018) developed a method to estimate the aerodynamic noise from the train bogie quantitatively. Firstly, they conducted field measurements using hot-wire anemometers to obtain profiles of the flow velocity under the train floor along the sleeper direction. Then they adjusted the flow velocity in an anechoic wind tunnel to fit the measured data. The noise emitted from a 1/7-scale train bogie installed to a train model with the same scale was measured using a microphone array. Based on the measured

noise in the wind tunnel, a prediction model for the bogie noise was developed and validated by field tests. The noise emitted from the pantograph and the bogie of a Inter City Express (ICE) high-speed train at different Reynolds numbers was investigated in an anechoic wind tunnel by Lauterbach et al. (2012). The train was scaled with a factor of 1/25 and the Reynolds number was up to 3.7×10^6 based on the width of the scaled model. It was found that the noise radiated from the bogie cavity was dominant of that in the bogie area.

Zhu et al. (2016) adopted a hybrid method combining the CFD and CAA to numerically investigate the flow around a 1/10-scale simplified train bogie and the radiated noise. The flow behaviours were studied using the DDES method and the far-field noise was predicted using FW-H acoustic analogy. For validation purpose, the noise from a bogie model with the same scale was measured in an anechoic wind tunnel, so did that from tandem wheelsets. Good agreement was achieved in terms of the shape of the noise spectrum and the tonal peak. It was found that the flow over the train bogie was characterised by the coherent vortex shedding downstream the axles and intensive vortices with various scales from the wheel and the frame as illustrated in Figure 2.9. The tonal peak in the noise spectrum of the bogie corresponded to the vortex shedding frequency in the wake of the axles and a dipole-pattern sound directivity was found. In addition, the noise contribution from the wheelsets of the bogie was more significant than that from the frame. Subsequently, Effects of the moving ground (Zhu et al., 2017) and the fairing of the bogie cavity (Zhu et al., 2018) on the flow and acoustic fields for the train bogie were also studied.

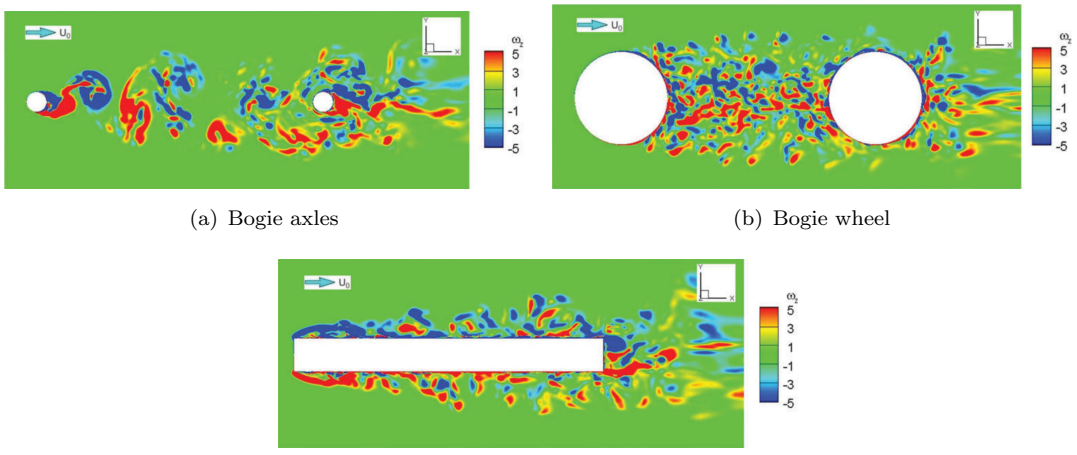

(a) Bogie axles

(b) Bogie wheel

(c) Bogie frame

Figure 2.9: Contours of the spanwise vorticity in the mid-span of bogie components (Zhu et al., 2016)

2.2 Prediction methods for aerodynamic noise

2.2.1 Numerical simulation methods

In recent years, significant developments of CFD techniques have made numerical investigation of aeroacoustics of high-speed trains possible. All the characteristics of aerodynamic noise, such as sound generation, propagation and emission, can be described by the compressible Navier-Stokes equations, which can be solved numerically through differential techniques in principle. Direct Numerical Simulation (DNS) can resolve all scales of turbulence from the smallest Kolmogorov length scale η to the largest integral scale L (Colonius and Lele, 2004). For application to railway noise, these scales range from the geometric length of the model in the order of metres to the dissipative turbulence scale the magnitude of which is several orders smaller (Thompson, 2008). The solution of DNS is accurate and it is sometimes termed a 'virtual wind tunnel'. To implement DNS, the spacing of the grid must be as small as η while the size of the computational domain has to be as large as L. The number of grid points N required for the mesh in one dimension can be estimated as:

$$N \sim \frac{L}{\eta} \sim Re^{\frac{3}{4}}$$

where Re is the Reynolds number based on L, which can be written as $Re = UL/\nu$ with U the flow velocity and ν the kinematic viscosity. For three-dimensional simulations, also taking into account the time step required to obtain stable and accurate solutions, the number of operations would be approximately proportional to:

$$N^4 \sim Re^3$$

Although the computing capability of current computers has grown considerably compared with that in the early 1980s, still only flow at moderate Reynolds numbers in simple geometries can be simulated with DNS. Assuming developments of computers are at the same pace as from the 1980s to nowadays, it would still be 60 to 80 years before a turbulent jet with a Reynolds number of 10^6 could be calculated using DNS (Wang et al., 2006b).

This implies that for engineering applications the main features of a turbulent flow need to be obtained without solving all the range of scales. Alternative methods are Reynolds Averaged Navier-Stokes equation (RANS) and Large Eddy Simulation (LES). RANS averages flow parameters such as pressure and velocity over a long time, and uses turbulence models to account for the effects of the resulting Reynolds stresses on mean flows. RANS seeks the time-averaged flow field and thus is not applicable to describe noise generation or radiation of unsteady acoustic fields. Unsteady RANS (URANS)

can capture slowly varying unsteady mean flow characteristics, but the limitation of this method is that the turbulence scales cannot be resolved.

In LES, spatial filters are introduced to separate the mean flow and large energetic eddies, which are resolved directly, from the small scale structures within the inertial and the dissipation range, which are modelled by a Sub-Grid-Scale (SGS) term (Smagorinsky, 1963). In this way, LES can be computationally much cheaper than DNS; however, it still puts demanding requirements on the size of the grids especially in the region near solid surfaces. Consequently, very small time steps are necessary, which means LES is also not practical for most industrial problems. The resolved scales for each CFD technique in a typical energy spectrum with respect to wavenumber are shown in Figure 2.10.

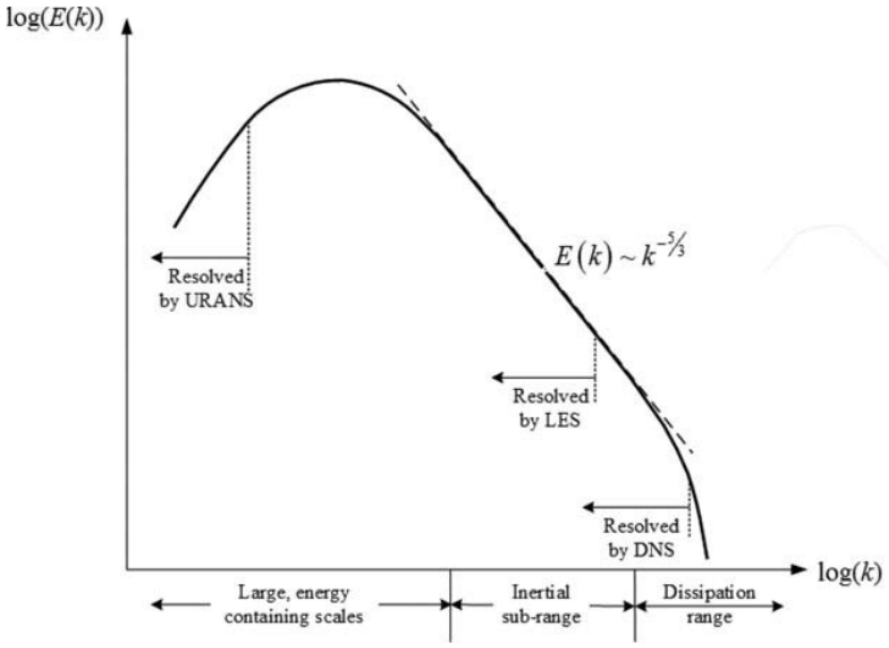

Figure 2.10: Resolved scales for each CFD technique (Thompson et al., 2015)

Hybrid techniques such as Detached Eddy Simulation (DES) and DDES are specifically designed to deal with wall-bounded flows at high Reynolds numbers, combining the merits of both LES and RANS in a single solution strategy (Wilcox et al., 1998). The hybrid models treat the entire boundary layer using RANS and resolve the rest of the flow field by employing LES. The computational resources demanded by DES are intermediate compared with those of RANS and LES and the accuracy of this approach is suitable for most practical problems with careful treatments on the corresponding flow regions of the two combining methods. DDES is a refinement of DES which prevents the switch from the RANS model to the LES model happening inside the wall boundary layers (Pope, 2001).

As discussed above, in principle the overall characteristics of the acoustic field, including sound generation and sound radiation, could be gained directly by employing the DNS technique. However, the limited computational capability of current computers motivates the developments of hybrid computational aeroacoustics (CAA) methods. The process to investigate the aeroacoustics is divided into two steps in the hybrid CAA methodology. In the first stage, the flow field is calculated through CFD approaches to provide an accurate description of the features of the sound source. The sound field is then computed in the subsequent step using an appropriate aeroacoustic theory. The most commonly used CAA methods include the Lighthill analogy, Curle's equation and Ffowcs Williams and Hawkings (FW-H) equation (Colonius and Lele, 2004). Figure 2.11 is a diagrammatic summary of the numerical approaches used for noise prediction.

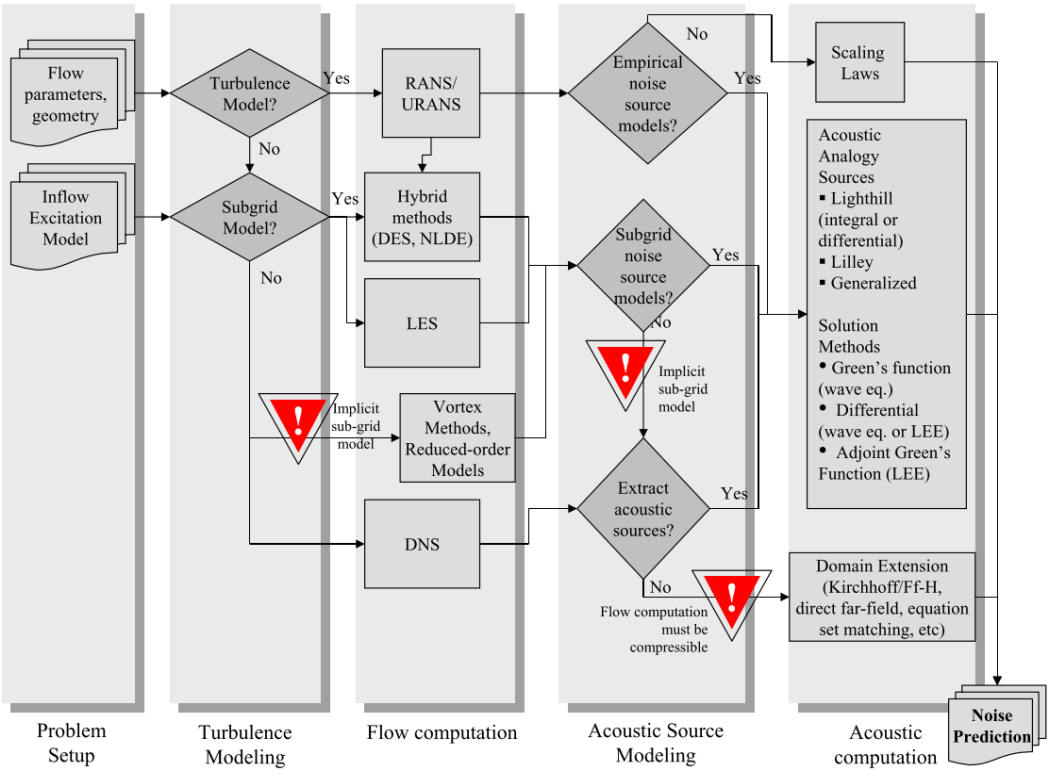

Figure 2.11: A hierarchy of noise prediction methods (Colonius and Lele, 2004)

2.2.2 Component-based model

Although CFD and CAA approaches are powerful tools to study the mechanisms and behaviour of aerodynamic and aeroacoustic subjects, the computational resources required are still very large for practical applications. Semi-empirical models can be used to predict the aerodynamic noise, which can cut down the computational costs significantly. However, to build semi-empirical models, experimental or numerical databases

are required. Parametric or component-based methods are commonly adopted for semi-empirical models (Thompson et al., 2015). The overall noise could be predicted as the incoherent sum of the noise from each component.

Such a semi-empirical model was developed by Smith and Chow (1998) for the application of aircraft landing gear noise prediction based on normalised spectra measured from different components. The model was validated by wind tunnel experiments with various full-scale landing gear configurations (Smith and Chow, 2002). A similar model was proposed by Guo (2005) to predict the noise from landing gears. Thompson et al. (2012) adapted Guo's model to predict aerodynamic noise generated by different parts of a train, including the pantograph, the nose and the bogies. They used the same empirical factors for landing gears due to the lack of a related components database. The results were promising but further improvements were required concerning the empirical parameters. Following this, Latorre Iglesias et al. (2015) proposed a more detailed noise prediction model for high-speed train pantographs, treating the pantograph as a combination of cylinders with appropriate cross-sections. The noise amplitude and spectrum of each strut in the pantograph was calibrated by using currently available experimental data for cylinders under various aerodynamic conditions. The predicted results matched well with noise measurements in a wind tunnel for full-scale pantographs. More details about these component-based models are presented in the following, especially on the pantograph.

Guo (2005) divided different components of the aircraft landing gear into three groups (large, medium and small), which are responsible for different parts of the noise spectra (low, medium and high frequencies). The OASPL generated by the landing gear was taken as the incoherent sum of noise emitted by each component. Thompson et al. (2012) adapted Guo's model to predict noise from a high-speed train pantograph. The far-field mean square sound pressure from the pantograph can be expressed as follows:

$$< p^2 >= \frac{(\rho_0 c_0^2)^2 M^6}{R^2(1 - M\ \cos\theta)^4} \sum_{components} \beta_{0i} S_i F_i(St) \tag{2.1}$$

where ρ_0 is the air density, c_0 is the sound speed, $M = U/c_0$ is the Mach number and U is the train speed. R denotes the distance between the noise source and the receiver. The term $(1 - M\cos\theta)^4$ introduces the convective amplification due to the relative motion between the noise sources and the observers, where θ is the angle between the flow direction and the direction of sound radiation from the source to the receiver. β_0, S and F are the amplitude factor, surface area and normalized spectrum, respectively of each component. The amplitude and shape of F_i are dependent on the Strouhal number St, where $St = fD/U$ and f is the frequency; D is the characteristic dimension of the geometry. i is the index for each component. Due to the lack of a suitable database for each pantograph component to fit the model, Thompson et al. (2012) used the same empirical parameters obtained by Guo. The predicted noise was compared

with experimental results of a full-scale pantograph measured in a wind tunnel. It turned out that the overall noise level was in a good agreement with that from the experiments; however, the spectral shape was quite different between the predicted and the experimental data. The shape of the measured noise spectrum was characterised by distinct peaks associated with specific noise sources, whereas, the noise spectrum predicted by Guo's model tended to be broad band, as shown in Figure 2.12.

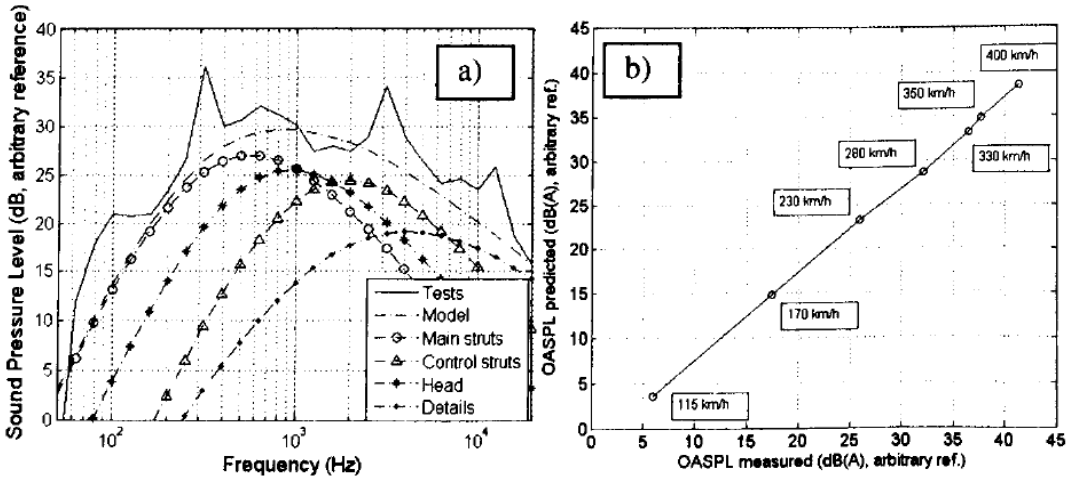

Figure 2.12: (a) Comparison of 1/3 noise spectrum between the prediction of adapted model and the measurement at speed of 330 km/h (b) Overall SPL from adapted model and tests for various flow speeds (Latorre Iglesias et al., 2015)

Following this, Latorre Iglesias et al. (2017a) extended this model to take into account obvious peaks appearing in the pantograph noise spectrum. The struts comprising the pantograph were identified as cylinders with different cross-sections, such as circular, square and elliptical. Once empirical constants were obtained for each strut using available databases, the overall noise from the pantograph could be predicted by this model. The mean square sound pressure in the far field for each strut was expressed as follows:

$$\overline{p(x)^2} = \frac{\rho_0^2 U^6 St^2 C_{l,\mathrm{rms}}^2 L l_c}{16 c_0^2 R^2 (1 - M\ \cos\theta)^4} \tag{2.2}$$

where St is the peak Strouhal number, l_c is the correlation length and $C_{l,\mathrm{rms}}$ is the fluctuating lift coefficient. In this way, rather than relying on a database of cylinder noise, which is quite scarce, empirical parameters could be obtained by using St, $C_{l,\mathrm{rms}}$ and l_c, which are found more widely in the literature. The values of empirical parameters were first obtained for two reference cases. A circular cylinder and a square one in a clean flow without turbulence were considered as the reference cases with the initial yaw angles and the angle of attack for the square cylinder both set to 0°. Subsequently, the influence of modifications regarding various factors relative to the reference cases were dealt with by means of correction coefficients. Commendable predictions were obtained compared with wind tunnel measurements. Details of the comparison at a speed of

330 km/h are presented in Figure 2.13. From Figure 2.13, it is clear that both the spectrum shape and the OASPL could be obtained with acceptable accuracy by the improved component-based model. The empirical constants in the extended prediction model were chosen taking into account the influence of various factors, such as the flow speed, the yaw angle, the cross-section shape, the aspect ratio and the incoming flow. The effect of each factor considered for one strut was assumed to be independent. Some factors such as flow interaction between different struts, tapered cross-section cylinders and surface roughness were not considered in the current model.

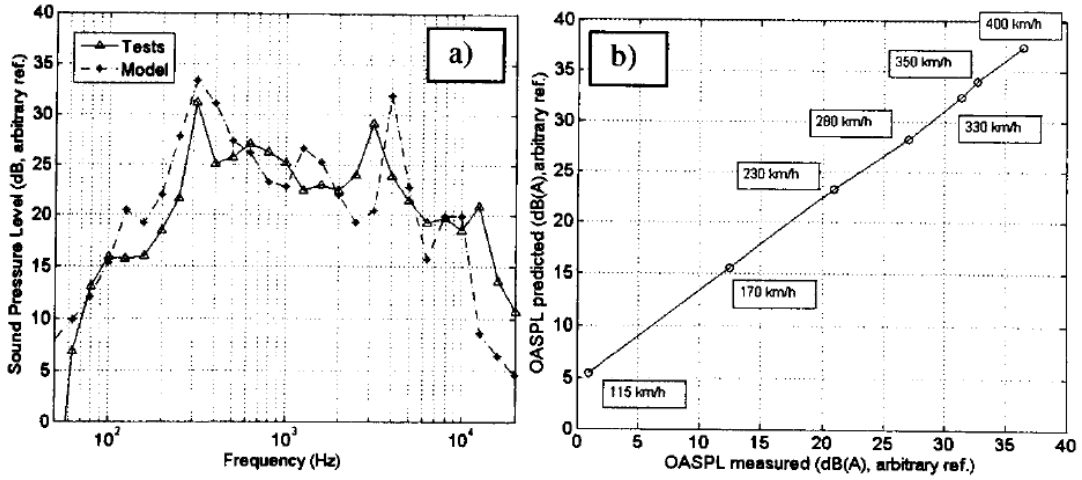

Figure 2.13: (a) Comparison of 1/3 noise spectrum between the prediction of extended model and the measurement at speed of 330 km/h (b) OASPL from extended model and tests for various flow speeds (Latorre Iglesias et al., 2015)

2.3 Flow past compact bluff bodies

From the above review sections, pantographs and bogies are major sources of train aerodynamic noise. According to the component-based method, the whole pantograph and bogie can be treated as a combination of bluff bodies with simple geometries and the overall noise is assumed to be the incoherent sum of the contribution from each component. In this thesis, compact components which closely resemble cubes or cuboids are the main objects to be investigated. Therefore, previous work on the flow over and noise from compact bluff bodies are reviewed in this and the following section.

2.3.1 Flow over a cube

Castro and Robins (1977) carried out experimental investigations to examine major features of the flow around a wall-mounted cube. This was placed in both a uniform flow and flow with upstream turbulence at a series of Reynolds numbers (Re) ranging

from 16,600 to 100,000 (based on the height of the cube and the freestream velocity). Here 'uniform' flow means uniform at the inlet of the wind tunnel test section while the turbulence intensity is very low except within the boundary layer. These measurements were used for assessing numerical calculations, as well as for explaining the flow features. Pressure coefficients on the cube surfaces, velocity profiles and the turbulence intensity in the wake of the cube were measured and compared under different flow conditions. The effect of the upstream turbulence on the wake flow was determined. In addition, they found that when Re exceeds about 30,000, the shear layer separates from the leading edges of the cube and the flow field has no further variations with increasing Re.

Martinuzzi and Tropea (1993) conducted experiments on the flow around surface-mounted prismatic objects covering a variety of width-to-height ratios in a fully-developed turbulent channel flow. Although the main purpose of their study was to investigate the influence of the aspect ratio on the three-dimensional flow around the prismatic objects, they also gave some insights into the flow pattern around a wall-mounted cube at a Reynolds number of 100,000. In their work, the separation line upstream of the cube and also the location of the horseshoe vortex were visualized using oil films while the flow patterns around the cube were studied by a laser sheet. Depardon et al. (2005) employed the Particle Image Velocimetry (PIV) technique combined with oil-flow visualization to analyse the flow topology around a wall-mounted cube, placed in turbulent boundary layers with $Re = 40,000$ and 160,000. To evaluate the effect of Reynolds number on the flow around a wall-mounted cube in a turbulent boundary layer, Lim et al. (2007) carried out a series of measurements in wind tunnels covering Reynolds numbers from 18,600 to 349,000 and even at a Reynolds number with a further increased order-of-magnitude measured in the field. It was found that although the mean flow features were not affected significantly by the variation of the Reynolds number, a dependence on Reynolds number was observed for the fluctuating statistics. Subsequently, measurements on a wall-mounted cube at $Re = 20,000$ were carried out by Lim et al. (2009) and the experimental results were compared with those from a specially tailored Large Eddy Simulation (LES). It was concluded that LES was a valid tool to investigate the flow over isolated bodies with a similar level of uncertainty to that obtained in the wind tunnel.

More recently, the flow around a cube at Reynolds numbers from 500 to 55,000 in a water tunnel was investigated by Khan et al. (2018) using PIV and dye visualization. Although advanced experimental techniques can be used to measure two- and even three-dimensional flow fields, it is still difficult to observe detailed flow structures, especially the unsteady flow features, which are responsible for noise generation. The wake flow behind a suspended cube at low Reynolds numbers in the range from $Re = 100$ to 400 was investigated experimentally by Klotz et al. (2014) in a horizontal water tunnel. The flow field was visualised by employing techniques of Laser Induced Fluorescence (LIF) and Particle Image Velocimetry (PIV). Non-axisymmetric flow in the wake of the

cube along with the hairpin vortex shedding phenomenon were observed for the studied Reynolds number regime. The experimental apparatus is illustrated in Figure 2.14. The side length of the cube in the experiment was 12 mm and a bent tube with a diameter of 1.7 mm, which is about 14% with respect to the size of the cube, was screwed to the front of the object as the support. To minimise the influence of the vertical part of the bent tube on the flow field, the tube was set to be 100 mm ($8L$) in the horizontal direction upstream of the cube.

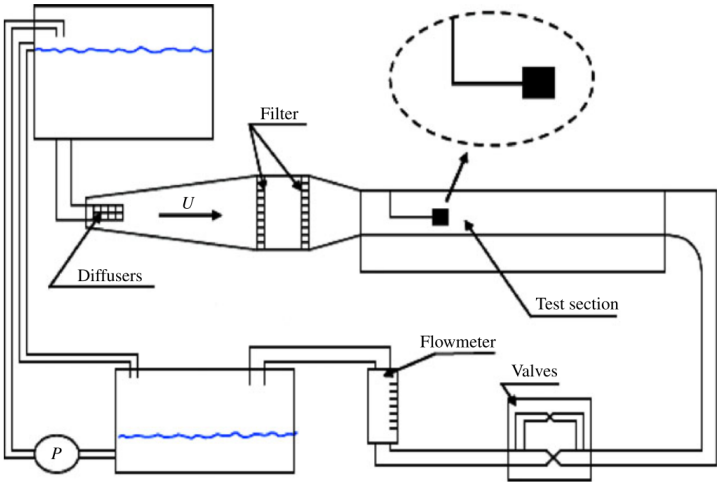

Figure 2.14: Schematic of the water channel and the experimental apparatus (Klotz et al., 2014)

With the rapid development in the capability of computers, numerical techniques become capable of treating more and more complex flows. Raul and Bernard (1991) proposed a vorticity transport closure scheme and used it to investigate the flow generated by a stationary cube. However, only time-averaged quantities were described in their work. Rodi et al. (1997) summarized the results from a workshop to assess the performance of LES in dealing with the flow past bluff bodies. One of the targeted test cases was a wall-mounted cube placed in a fully-developed channel flow at a Reynolds number of 40,000 and the results obtained numerically were compared with the measurements conducted by Martinuzzi and Tropea (1993). However, to save the computational effort, instead of solving the boundary layer directly, modelled wall-function boundary conditions were assigned near the cube surfaces in every numerical work submitted to the workshop. Satisfactory agreement was obtained for the velocity profiles between the simulations and the measurements. In addition, they concluded that significantly improved prediction of the velocity profiles can be obtained by adopting LES compared with Reynolds-averaged Navier-Stokes (RANS) models.

Saha (2004) performed Direct Numerical Simulations (DNS) for a cube in uniform flow at Reynolds numbers between 20 and 300. He explored transition of the flow at different Reynolds numbers topologically and also shed light on the mechanisms regarding the loss of planar symmetry in the wake of the cube at higher Reynolds numbers. Using

DNS, Yakhot et al. (2006b) investigated a cube placed in a fully developed channel flow at a Reynolds number of 5610. They described the flow patterns in detail and also discussed the unsteady interaction between the horseshoe vortex formed upstream of the cube and the arch-type flow structure observed in the wake. The spatial and temporal evolution of large-scale vortices around a wall-mounted cube were discussed further in a later publication (Yakhot et al., 2006a). More recently, Liakos and Malamataris (2014) also employed DNS to investigate the flow around a cube mounted in a channel under laminar flow conditions and studied Reynolds numbers from 1.33 to 2667. They found that a tornado shaped vortex was found near the side surface of the cube together with a three-dimensional horseshoe vortex. Moreover, the upper limit of the Reynolds number for which a steady laminar flow state occurs is roughly 2000.

2.3.2 Flow over a bluff body with rounded corners

Okamoto and Uemura (1991) measured the surface pressure of wall-mounted cubes with different rounded corners in a wind tunnel at a Reynolds number of 4.74×10^4. Based on the measured surface pressure distribution, drag coefficients were determined and analysed; vortices around the rounded cubes were visualised using the ink shedding method and velocity profiles in the near-wake were also presented. Direct numerical simulations (DNS) on the flow past a square cylinder with rounded or chamfered corners at a Reynolds number of 1×10^4 were conducted by Tamura et al. (1998). Measurements were performed for the same objects at the same conditions (Tamura and Miyagi, 1999). They pointed out that even a slight change of the corner shape could lead to significant variations in flow features; the pressure near the corner decreases significantly, leading to large reductions of the drag. Zhang and Samtaney (2016) also employed DNS to investigate the effect of corner radius on the flow past an isolated square cylinder at a Reynolds number of 1,000. Five different corner radii ranging from square to circular cross-sections were taken into account and the development of the separated and transitional flow was studied.

Hu et al. (2006) employed particle imaging velocimetry (PIV) and laser doppler anemometry (LDA) to investigate the near wake of square cylinders with different rounded corners. It was found that the vortex formation length in the base region was almost doubled as the ratio of the rounding radius to the cylinder width was increased from 0 to 0.5. The phase-averaged flow structures and the velocity profiles were also presented. Miran and Sohn (2015) conducted large eddy simulations (LES) to study the effect of rounded corners on the flow around a square cylinder at a Reynolds number of 500. They found that the drag is minimised when the rounded radius is 20% of the cross section width. They also reported PIV measurements in a water tunnel to investigate the effect of rounded corners on the near-wake flow of a square cylinder at a higher Reynolds number of 5,200 (Kumar et al., 2015) and detailed flow patterns in the wake

were described. Carassale et al. (2014) carried out measurements in a wind tunnel using a force balance and pressure taps to investigate the flow characteristics around square cylinders with rounded edges for Reynolds numbers between 1.7×10^4 and 2.3×10^5; three corner radii were considered. It was found that the separated flow reattached to the lateral surfaces further upstream as the corner radius was increased and this affected the Strouhal number.

2.3.3 Flow over finite length square cylinders

The flow around cuboids or finite length square cylinders differs considerably from that for infinite square cylinders. Considerable research has been reported on the flow over finite wall-mounted cylinders (Okajima, 1982; Wang et al., 2006a; Wang and Zhou, 2009). A detailed review about the flow structures in the wake of wall-mounted cylinders and the radiated noise was presented by Porteous et al. (2014). Different models were summarised describing the relationship between the shed vortices from the free end and the base of the cylinders. Measurements on the flow-induced noise from wall-mounted cylinders were also reviewed and compared. More recently, Yauwenas et al. (2019) experimentally and numerically investigated the aspect ratio effect on the flow structures of square finite wall-mounted cylinders. The wake velocity and surface pressure of the cylinders were measured in wind tunnels using hot-wire anemometers and pressure taps respectively. The aspect ratios studied experimentally ranged from 1.4 to 21.4 at Reynolds numbers of 1.4×10^4 and 1.1×10^4 based on the cylinder width. Complementary simulations were also performed using LES to obtain more flow features for four representative aspect ratios. A parametric diagram was proposed to categorise the transition of wake structures taking into account both the boundary layer thickness and the aspect ratio.

Zhang et al. (2017) performed direct numerical simulation (DNS) on a wall-mounted cylinder with an aspect ratio of 4. The Reynolds number ranged between 50 and 1000 based on the cylinder width. Three types of mean streamwise vortices around the cylinder were categorised in detail. The effect of the incoming boundary layer thickness on the shedding modes of a wall-mounted cylinder with an aspect ratio of 7 was investigated by Behera and Saha (2019) employing DNS. Six thicknesses of the turbulent boundary layer were considered at a Reynolds number of 250 based on the cylinder width. Both anti-symmetric and symmetric shedding patterns were observed in the wake of the cylinder. The symmetric shedding mode occurred more frequently with the increases of the boundary layer thickness. Cao et al. (2019) employed Immersed Boundary Method (IBM) to investigate surface flow patterns and pressure on wall-mounted cylinders with aspect ratios of 3 and 4. The studied Reynolds number calculated on the cylinder width was 5×10^4 and two angles of attack ($\alpha = 0°$ and $15°$) were considered. Near-wall flow topologies were described to clarify the three-dimensional effect of the flow over the

finite length square cylinders, including Critical points of wall streamlines, lines of the flow separation and reattachment. In addition, Beitel et al. (2019) measured the aerodynamic forces and the bending moment of circular wall-mounted cylinders in a wind tunnel. The aspect ratios ranged from 0.5 to 11 and the studied Reynolds number was 6.5×10^4 based on the diameter of the cross-section.

2.4 Aerodynamic noise from bluff bodies

For aerodynamic noise from bluff bodies, considerable experimental and numerical work has been carried out on the tonal noise induced by cylinders due to vortex shedding (Curle, 1955; Revell et al., 1978; Thomas et al., 2008; Latorre Iglesias et al., 2016; Liu et al., 2018; Ganta et al., 2019). In addition, Porteous et al. (2017) measured the noise and also the velocity profiles induced by finite wall-mounted square cylinders with different aspect ratios in an anechoic wind tunnel. The aspect ratio range considered in their work was from 0.29 to 22.9 and four regimes were identified based on the number of the observed shedding tones changing with the aspect ratio. The relationship between these acoustic tones and the vortex structures was also investigated.

Ji and Wang (2010) numerically studied the sound emitted from small steps with different heights placed in turbulent boundary-layer flow at low Mach numbers, combining LES, the Lighthill analogy and an analytical geometry-tailored Green's function. Hao et al. (2013) investigated the noise from small rounded steps adopting similar approaches. Acoustic measurements on the sound from forward and backward steps were conducted by Glegg et al. (2012). Unlike the noise generated by cylinders, the sound induced by small steps was found to be broadband and no distinct tonal peak could be observed. The sound level from these steps was closely linked with the flow reattachment on the step surfaces or on the ground.

Becker et al. (2005) measured the noise emitted from a forward-facing step with sharp corners in an aeroacoustic wind tunnel and numerical simulations were also performed under the similar flow conditions. In their numerical work, steps with three different corner radii were considered and the correlation between the near-field pressure fluctuation and the far-field noise was analysed to characterise the noise sources. Awasthi et al. (2018) carried out measurements on the pressure fluctuations of forward-facing steps with different corner radii immersed in a turbulent boundary layer, and also conducted measurements and predictions of the far-field noise from these steps (Awasthi et al., 2019). Four corner radii from 0 to 0.25 of the step height were considered at Reynolds numbers ranging from 3.5×10^4 to 1.04×10^5. The flow behaviour around these steps, the relationship between the pressure spectra and the separation bubble

formed downstream of the step and the effect of rounding on the noise level were reported. In addition, Awasthi (2015) also measured the sound from three-dimensional surface discontinuities represented by swept forward-facing steps with rounded corners.

Noise radiated from simple shapes, including a cube, a cube with round edges, a disc and a rectangular cuboid, was measured by Latorre Iglesias (2015) in an open-jet anechoic wind tunnel to assess the noise generated by train bogie components. These experiments only focused on noise radiation; details about the flow field regarding the physics of noise generation were not evaluated. A cube of width 150 mm was used for the noise tests and the experimental set-up is shown in Figure 2.15. Each object was held by a long cylinder attached to a baffle on one side and a stand on the other side. Porous foam was wrapped around the cylinder to suppress the vortex shedding from it. The distance between the object and the baffle was set to be 50 mm, to make sure the object was outside the boundary layer generated by the baffle. Uniform flows with speeds of 20, 25, 31.5, 40 and 50 m/s were provided by the contraction nozzle. Eight microphones were placed in the far field of the object to obtain the noise measurements. The experimental setup and specific positions of the microphones are indicated in Figure 2.16. As shown in Figure 2.16, the radius of the microphone array was 1.4 m, and the object is at the centre of it. The angle between adjacent microphones was 15°, while the whole array covered angles from −45° to 60°. The effect of background noise from both the baffle and the circular cylinder supporting the cube was assessed and shown above 100 Hz. OASPL and 1/3 octave noise spectra of the measured noise radiated from the object were presented by Latorre Iglesias (2015). These experimental results for the case of the cube are used for comparison with those of the numerical calculations conducted in the current work presented in Section 4.3.3.

Figure 2.15: Experimental set-up used for the noise tests of simple geometries including the cube (Latorre Iglesias, 2015)

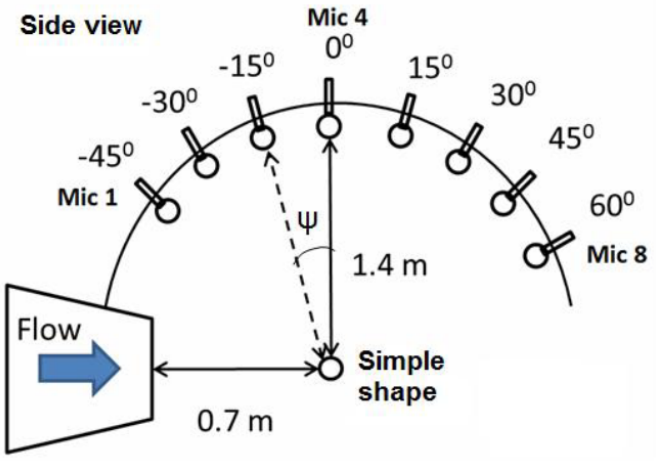

Figure 2.16: Sketch of the side view of the microphone array used for the measurements with the cube (Latorre Iglesias, 2015)

2.5 Summary

When train speeds exceed about 300 km/h, aerodynamic noise emitted from the train becomes dominant compared with the rolling noise. Bogies and pantographs are identified as significant aerodynamic noise sources for high-speed trains. Especially, pantographs are mounted on the roof of the train, conventional sound barriers with limited height cannot work efficiently in shielding the noise radiated from the pantograph. Research on noise mitigation of pantographs and bogies is necessary to achieve the aim of reducing the overall noise from high-speed trains.

Both experimental and numerical approaches have been adopted to investigate the flow field and radiated noise of pantographs and bogies. However, numerical work is more likely to allow better understanding of the mechanisms behind the generation of aerodynamic noise. Accounting for the computational capability of current computers, a combination of CFD and CAA methods is commonly used to predict noise in the far field instead of solving the governing equations directly. Even so, it is still impractical to simulate the flow around complex geometries. The semi-empirical component-based model proposed to predict noise from landing gears has been modified to estimate noise from pantographs and bogies. The pantograph and the bogie could be treated as a combination of simple shapes. The noise generated by the whole pantograph or bogie can be predicted by an incoherent sum of that from each component. Compact components in pantographs and bogies resembling cubes or cuboids are studied in this thesis. Previous work on the flow and acoustic fields of compact bluff bodies are also reviewed.

Chapter 3

Computational methodology

The numerical methods employed for the aerodynamic and aeroacoustic computations are presented in this chapter. Firstly, a CFD technique is employed to investigate the flow field around the object. Considering both accuracy and computational cost, a hybrid method DDES has been adopted using the open source software OpenFOAM. Subsequently, based on the aerodynamic calculation implemented in the first step, the noise radiated to the far field is predicted using the FW-H acoustic analogy. This step is carried out in the commercial code FLUENT. More details of the related methodologies used in the current work are introduced in the following sections.

3.1 Computational Fluid Dynamics

In recent years, CFD techniques have developed rapidly, which greatly facilitates numerical calculations in the field of aerodynamics and aeroacoustics. In CFD simulations, the Navier-Stokes equations are solved using numerical methods by discretising the flow region into grids.

3.1.1 Navier-Stokes equations

The Navier-Stokes equations are the governing equations for viscous flow, describing the spatial and temporal evolution of the fluid. For a Newtonian fluid, the unsteady compressible Navier-Stokes equations in conservative form can be written in tensor notation (using the summation convention) as (Pope, 2001):

$$\frac{\partial \rho}{\partial t} + \frac{\partial (\rho u_i)}{\partial x_i} = 0 \tag{3.1}$$

$$\frac{\partial (\rho u_i)}{\partial t} + \frac{\partial (\rho u_j u_i)}{\partial x_j} = f_i - \frac{\partial p}{\partial x_i} + \frac{\partial \tau_{ij}}{\partial x_j} \tag{3.2}$$

$$\frac{\partial}{\partial t}\left[\rho(e + \frac{1}{2}u_i u_i)\right] + \frac{\partial}{\partial x_j}\left[\rho u_j (h + \frac{1}{2}u_i u_i)\right] = -\frac{\partial q_j}{\partial x_j} + \frac{\partial (u_i \tau_{ij})}{\partial x_j} + f_i u_i \tag{3.3}$$

Equations (3.1), (3.2) and (3.3) from the Navier-Stokes equations and are the conservation laws for mass, momentum and energy, respectively. In the above equations, ρ is the density, p is the pressure, t is the time, u_i is the i-th component of velocity along the direction of x_i in space, f_i is the body force component, which is usually small and can be neglected for aerodynamic problems when only gravity is considered. e is the internal energy, $(e + \frac{1}{2}u_i u_i)$ is the total energy, $h = e + p/\rho$ is the specific enthalpy. q_j is the heat-flux vector, which can be defined as:

$$q_j = -\kappa \frac{\partial T}{\partial x_j} \tag{3.4}$$

where κ is thermal conductivity, and T is the temperature. τ_{ij} is the viscous stress tensor, which can be expressed as:

$$\tau_{ij} = 2\mu \left(s_{ij} - \frac{1}{3}\frac{\partial u_k}{\partial x_k}\delta_{ij} \right) \tag{3.5}$$

The viscosity μ is a property of the fluid, which can be measured in experiments and is considered to be a constant for subsonic flows. Finally the strain rate tensor s_{ij} is given as:

$$s_{ij} = \frac{1}{2}\left(\frac{\partial u_i}{\partial x_j} + \frac{\partial u_j}{\partial x_i} \right) \tag{3.6}$$

When the Mach number is low, conventionally less than about 0.3 (Kaushik et al., 1999), corresponding to a flow speed of about 100 m/s, the flow can be treated as incompressible. In this situation, which is the typical case for train noise, simulations can be simplified further. For incompressible flow, the flow density is assumed constant, (Pope, 2001), namely,

$$\frac{\mathrm{D}\rho}{\mathrm{D}t} = \frac{\partial \rho}{\partial t} + u_j \frac{\partial \rho}{\partial x_j} = 0 \tag{3.7}$$

In the absence of the body force, the Navier-Stokes equations for incompressible flow can be simplified as:

$$\frac{\partial u_j}{\partial x_j} = 0 \tag{3.8}$$

$$\rho\left[\frac{\partial u_i}{\partial t} + u_j\frac{\partial u_i}{\partial x_j}\right] = -\frac{\partial p}{\partial x_i} + \frac{\partial}{\partial x_j}(2\mu s_{ij}) \tag{3.9}$$

In incompressible flows, the thermodynamic field is decoupled from the hydrodynamic field, so the energy equation is not needed.

3.1.2 Turbulence models

Currently, the analytical solution of the Navier-Stokes equations cannot be obtained directly by mathematical tools. Numerical methods such as RANS, LES and DNS have been developed to address this problem as discussed in Section 2.2.1. In the present work, a hybrid RANS-LES model DDES is adopted in the open source CFD software OpenFOAM. Details of this approach are presented in the following sections.

3.1.2.1 Reynolds-averaged Navier-Stokes equations

For some industrial applications at high Reynolds numbers, only time-averaged flow features are necessary. The RANS method is established to model instantaneous perturbations of the flow characteristics (Wilcox et al., 1998), based on the Reynolds decompositions:

$$u_i = \bar{u}_i + u_i' \tag{3.10}$$

$$p = \bar{p} + p' \tag{3.11}$$

$$s_{ij} = \bar{s}_{ij} + s_{ij}' \tag{3.12}$$

where $\bar{u}_i$, $\bar{p}$ and $\bar{s}_{ij}$ represent mean variables, and u_i', p' and s_{ij}' are the perturbations. After substituting the Reynolds decompositions into Equation (3.8) and (3.9) and the time-averaging process, the Reynolds-averaged Navier-Stokes equations are obtained:

$$\frac{\partial \bar{u}_j}{\partial x_j} = 0 \tag{3.13}$$

$$\rho\frac{\partial \bar{u}_i}{\partial t} + \rho\frac{\partial}{\partial x_j}(\bar{u}_j\bar{u}_i) = -\frac{\partial \bar{p}}{\partial x_i} + \frac{\partial}{\partial x_j}(2\mu\bar{s}_{ij} - \rho\overline{u_j'u_i'}) \tag{3.14}$$

In Equation (3.14), $\tau_{ij}^t = -\rho\overline{u_j'u_i'}$ is named as the Reynolds-stress tensor introduced by the time-averaging process. τ_{ij}^t is a symmetric tensor with six components, representing the turbulent fluctuations on the mean flow. Therefore, a closure technique is required to address the ten unknowns in a system of four equations represented by Equation (3.13) and (3.14). Various models are developed for the turbulence closure problem, such as

one-equation S-A model (Spalart and Allmaras, 1992) and two-equation $k-\omega$ models (Wilcox, 2008). For all the RANS models, the governing equations are time-averaged, while the fluctuating features of the turbulence are modelled by the Reynolds-stress tensor. For flows with massive separation and numerous unsteadiness in the wake, the RANS model becomes limited to predict the flow features precisely.

3.1.2.2 Large Eddy Simulation

Based on Kolmogorov's first hypothesis, when the Reynolds number is high, small scale eddies in the turbulent flow can be treated as isotropic and their motions have a universal form (Kolmogorov, 1941). Conversely the large eddies containing most of the kinetic energy of the flow are much more anisotropic. Their behaviour will be affected by the geometry of the problem considered, the boundary conditions etc. (Versteeg and Malalasekera, 2007). One of the main obstacles in conducting simulations on turbulent flows is the broad range of length scales. For the RANS method, eddies of all length scales in the turbulent flow are modelled in an identical way, but in most practical cases, researchers are more interested in the information in large eddies, where most of the turbulent energy is contained. The LES method treats large eddies and small eddies in the turbulent flow separately, by solving the large eddies directly and using a Sub-Grid-Scale (SGS) model to address smaller ones, which behave much more uniformly.

Rather than using time-averaging, LES adopts a spatial filtering operation to separate the large and small eddies in space. Primarily, a filtering function will be selected with a certain cut-off width. All the eddies the size of which is larger than the cut-off width will be resolved without any modelling, whereas the turbulent eddies with a scale smaller than the cut-off width in the spatial filter will be screened out and instead be modelled. These filtered-out smaller eddies governed by the viscosity are responsible for energy dissipation in the turbulent flow. During the above processes, SGS stresses will be introduced between the lager eddies and the filtered-out smaller ones. Subsequently, a SGS model is developed to describe the effect of SGS stresses and an artificial eddy viscosity is used to guarantee that energy dissipation in the turbulent flow operates properly.

In LES, a spatial filter function is defined as:

$$\bar{\phi}(\mathbf{x},t) \equiv \int_{-\infty}^{\infty}\int_{-\infty}^{\infty}\int_{-\infty}^{\infty} G(\mathbf{x},\mathbf{x}',\mathbf{\Delta})\phi(\mathbf{x}',t)dx_1'dx_2'dx_3' \tag{3.15}$$

In this equation, $G(\mathbf{x},\mathbf{x}',\mathbf{\Delta})$ indicates the filter function applied in three-dimensional space rather than the time domain, where $\mathbf{x}$ represents each mesh point and $\mathbf{x}'$ is used to represent the region near $\mathbf{x}$. $\bar{\phi}(\mathbf{x},t)$ denotes the filtered parameter, while $\phi(\mathbf{x}',t)$ is

the original parameter. Δ is the cut-off width used to determine the retained larger eddies and the rejected smaller eddies.

The most commonly used filter functions in the LES method are the top-hat (box) filter, the Gaussian filter and the spectral cut-off filter (Versteeg and Malalasekera, 2007). In OpenFOAM, the implicit top-hat filter function is adopted as follows:

$$G(\mathbf{x}, \mathbf{x}^{'}, \mathbf{\Delta}) = \begin{cases} 1/\Delta^3 & |\mathbf{x} - \mathbf{x}^{'}| \leq \Delta/2 \\ 0 & |\mathbf{x} - \mathbf{x}^{'}| > \Delta/2 \end{cases}$$

In theory, the cut-off width could be chosen as any size, but it is meaningless to set the cut-off width smaller than the grid size in practical CFD projects, because details finer than the grids cannot be captured. For most cases, the cut-off width is taken to be of the same order as the grid size. In OpenFOAM, the *cubeRootVol* method was used to determine the cut-off width for the filter function:

$$\Delta = \sqrt[3]{\Delta x \Delta y \Delta z} \tag{3.16}$$

where Δx, Δy, Δz are the length, width and height of the grid cells, respectively. Δ is chosen as the cube root of this cell volume. The resolution of the grid cells is required to be similar in all three directions to compute the turbulent structures; in other words, grids in the computational domain ideally need to be cubic (Gramlich, 2012).

After the filtering operation, the unsteady Navier-Stokes equations become:

$$\frac{\partial \bar{u}_i}{\partial x_i} = 0 \tag{3.17}$$

$$\frac{\partial \bar{u}_i}{\partial t} + \frac{\partial \bar{u}_i \bar{u}_j}{\partial x_j} = -\frac{1}{\rho}\frac{\partial \bar{p}}{\partial x_j} - \frac{1}{\rho}\frac{\partial \tau_{ij}^R}{\partial x_j} + \nu \nabla^2 \bar{u}_i \tag{3.18}$$

where ν is the kinematic viscosity, which can be defined as:

$$\nu \equiv \frac{\mu}{\rho} \tag{3.19}$$

The variable τ_{ij}^R in the second term of Equation (3.18) denotes the SGS stress, which is required to be modelled. When the cut-off width is close to zero, the SGS stress will also tend to be infinitesimal, approaching the solution of DNS. Although only a small part of the turbulent energy is described by the SGS stresses compared with the Reynolds stresses in RANS, if the process of energy dissipation in small eddies cannot be modelled precisely, a boost of energy will occur and lead to instability of the computation. Similar to Reynolds stresses in RANS, SGS stresses can be resolved based on the Boussinesq hypothesis (Wilcox et al., 1998):

$$\tau_{ij}^R = -2\rho\nu_{SGS}\bar{s}_{ij} + \frac{1}{3}\tau_{kk}^R\delta_{ij} \tag{3.20}$$

In Equation (3.20), ν_{SGS} is the artificial viscosity. $\bar{S}_{ij}$ is the strain rate after the filtering operation:

$$\bar{s}_{ij} = \frac{1}{2}(\frac{\partial \bar{u}_i}{\partial x_j} + \frac{\partial \bar{u}_j}{\partial x_i}) \tag{3.21}$$

There are several SGS models applied in LES, such as the Smagorinsky-Lilly model (Smagorinsky, 1963), the dynamic model (Germano et al., 1991), and the approximate deconvolution model (Stolz et al., 2001). However, the most commonly used model to compute ν_{SGS} is the Smagorinsky-Lilly model. In this model, the viscosity determining the level of energy dissipation is presented as:

$$\nu_{SGS} = C_s \Delta^2 \left|\bar{S}\right| \tag{3.22}$$

In Equation (3.22), $\left|\bar{S}\right| = (2\bar{S}_{ij}\bar{S}_{ij})^{1/2}$ and C_s is the Smagorinsky coefficient. The value of the Smagorinsky coefficient is not fixed universally but should be chosen in the range from 0.09 to 0.15 (Lilly, 1966). In OpenFOAM, the value of the Smagorinsky coefficient is set to be 0.1, which is supposed to yield the most accurate results for a majority of flows (Churchfield et al., 2014). Despite the popularity of the Smagorinsky-Lilly model, in some cases this method generates too much dissipation near walls (Kleissl et al., 2006).

3.1.2.3 Hybrid RANS-LES methods

For complex geometries at high Reynolds numbers, the computational effort of LES is impractically high. A large number of grid cells are demanded, particularly in the near-wall boundary layer and a small time step is also required in LES to obtain a stable solution. The requirement of mesh resolution in the RANS model is much lower compared with LES. However, this method has limited capability in resolving large scale unsteady structures of the turbulent flow and is prone to underestimate the shear stress in flow separation regions. Thus, hybrid RANS-LES models have been proposed, aiming to supply remediation for the disadvantages of both RANS and LES. The principal idea of hybrid models is to realise LES simulations to some extent without unrealistically high computational cost, which is very likely to occur in full LES. To achieve this aim, a RANS model is employed near the wall, leading to a great reduction of mesh size. Figure 3.1 illustrates the different mesh resolution required by full RANS, full LES and a hybrid method based on a representative flat plate boundary layer. From Figure 3.1, it is clear that the lowest mesh refinement along the solid wall is required by the full RANS, followed by the hybrid method, and the mesh resolution for full LES is the highest. Since grids for LES simulations need to be close to cubic, highest mesh resolution is demanded in three dimensions, which means a significant number of grid cells are necessary for the full LES. The hybrid method treats the flow field in the boundary layer using a 'RANS-mode' and resolves large scale structures in the uniform

flow by means of LES. The restriction of a cubic mesh near the wall no longer applies for hybrid models, which make it possible for the hybrid method to combine the merits from both the full RANS and the full LES. Currently, the most popular hybrid approach is Detached Eddy Simulation (DES) proposed by Spalart and Allmaras (1992).

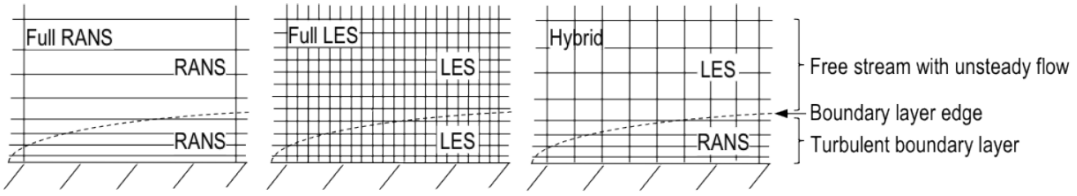

Figure 3.1: Comparison of mesh resolution required by full RANS (left), full LES (middle) and hybrid method (right) based on an representative flat plate boundary layer (Gramlich, 2012).

Detached Eddy Simulation

A one-equation RANS model is proposed by Spalart and Allmaras (1992) using a transport equation for the turbulent viscosity. The governing equations are modified to be:

$$\frac{\partial \tilde{\nu}}{\partial t} + u_j \frac{\partial \tilde{\nu}}{x_j} = c_{b_1} \tilde{S} \tilde{\nu} + \frac{1}{\sigma}[\frac{\partial}{\partial x_j}((\nu + \tilde{\nu})\frac{\partial \tilde{\nu}}{\partial x_j}) + c_{b_2}\frac{\partial \tilde{\nu}}{\partial x_i}\frac{\partial \tilde{\nu}}{\partial x_i}] - c_{w_1} f_w (\frac{\tilde{\nu}}{d})^2 \tag{3.23}$$

In Equation (3.23), ν is the molecular viscosity, $\tilde{\nu}$ is the modified turbulent viscosity, which can be expressed as:

$$\tilde{\nu} = \frac{\nu_t}{f_{\nu 1}(y^+)} \tag{3.24}$$

where, ν_t is the turbulent viscosity. $f_{\nu 1}$ is selected to ensure that the modified turbulent eddy viscosity ($\tilde{\nu}$) behaves uniformly in the whole boundary layer as $\tilde{\nu} \sim y$ (Spalart and Allmaras, 1992). $f_{\nu 1}$ can be expressed as:

$$f_{\nu 1} = \frac{\chi^3}{\chi^3 + c_{v1}^3} \tag{3.25}$$

with

$$\chi = \frac{\tilde{\nu}}{\nu} \tag{3.26}$$

where ν is the molecular viscosity. The remaining terms in Equation (3.23) are listed as follows:

$$\tilde{S} = \Omega + \frac{\tilde{\nu}}{k^2 d^2} f_{v2} \tag{3.27}$$

$$f_{v2} = 1 - \frac{\chi}{1 + \chi f_{v1}} \tag{3.28}$$

where $\Omega = \sqrt{2\omega_{ij}\omega_{ij}}$ denotes the vorticity magnitude and d is the distance from the wall. The function f_w is given by:

$$f_w = g\left[\frac{1+c_{w3}^6}{g^6+c_{w3}^6}\right]^{1/6} \tag{3.29}$$

where

$$g = r + c_{w2}(r^6 - r) \tag{3.30}$$

and

$$r = \min\left[\frac{\tilde{\nu}}{\tilde{S}k^2d^2}, 10\right] \tag{3.31}$$

Values of the coefficients in the above equations are $\sigma = 2/3, c_{b1} = 0.1355, c_{b2} = 0.622, c_{v1} = 7.1, k = 0.41, c_{w2} = 0.3, c_{w3} = 2$ and $c_{w1} = c_{b1}/k^2 + (1 + c_{b2})/\sigma = 3.239$ (Spalart and Allmaras, 1992). In addition, the modified turbulent viscosity conforms to $\tilde{\nu} = 0$ at the wall and $\tilde{\nu} = 3\nu_\infty \sim 5\nu_\infty$ in the far field, where ν_∞ is the kinematic viscosity defined in Equation (3.19).

The three terms on the right-hand side of Equation (3.23) are the production, the transportation and the destruction terms respectively. The physical wall distance d could be substituted by a length scale $C_{DES}\Delta$, where Δ is the size of the grid cells and $C_{DES} = 0.65$ is a constant (Shur et al., 1999). This modification makes it possible to include the mesh size in the Equation (3.23). In this way, the Spalart-Allmaras model for RANS transforms into a one-equation SGS model for LES and ν_t in Equation (3.24) becomes equivalent to the ν_{SGS}.

In order to achieve the transition from RANS to LES in the near-wall flow region, the wall distance d is replaced by $\tilde{d}$:

$$\tilde{d} = \min(d, C_{DES}\Delta) \tag{3.32}$$

The definition of $\tilde{d}$ can be understood easily, because the near-wall length scale should be kept smaller than the RANS grid length. In the proximity of the solid wall, where $d < C_{DES}\Delta$, the original RANS model is employed. When the distance from the wall satisfies $d > C_{DES}\Delta$, the adopted model switches to be LES. The transition process between RANS and LES, related with the wall distance is illustrated in Figure 3.2.

Delayed Detached Eddy Simulation

As described above, the DES method is devised to process the overall boundary layer by employing a RANS model, while the remaining region of the flow field is treated with LES. Despite the fact that DES is a promising approach to deal with separated flows

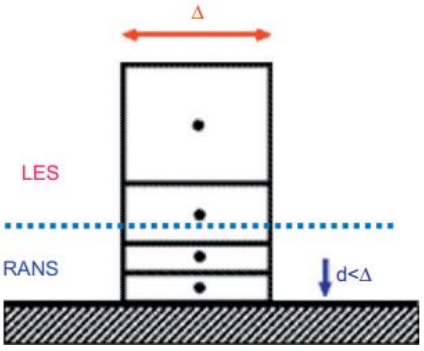

Figure 3.2: Illustration of the switch between RANS and LES in the traditional DES approach (Fröhlich and von Terzi, 2008).

at high Reynolds number, there are some undesirable imperfections inherent with this hybrid model.

Figure 3.3 shows example grids with three different resolutions in a boundary layer. Type I illustrates a typical DES model with a thin boundary layer. The size of the grid in the wall-parallel direction exceeds the boundary-layer thickness (δ). Thus, a 'RANS mode' is applied throughout the boundary layer, as intended in the design of DES. Type III is an extreme example for LES grids with grid spacing in all directions much smaller than the boundary-layer thickness. Under this circumstance, the model function works as an SGS model in the overwhelming majority of the boundary layer, and as a RANS-like wall model only very close to the wall. Although the case is not perfect, it has some virtues such as stability and simplicity. In addition, this model responds well to variations of Reynolds number and grid density. Unfortunately, the 'ambiguous' grid displayed in Type II activates the 'LES mode' in the upper two-thirds of the boundary layer. However, the grids are apparently not fine enough to resolve velocity fluctuations in the boundary layer. The turbulent eddy viscosity is reduced from RANS to LES. Consequently, the modelled Reynolds stress is also reduced without any sizeable resolved stress to restore the balance, leading to *Modelled Stress Depletion* (MSD) (Spalart et al., 1997). Serious cases of MSD may yield premature flow separation named *Grid Induced Separation*, as presented in the study of Menter and Kuntz (2004). Typically, MSD occurs during a mesh independence study when the grids are gradually refined. It may also appear when the thickness of a boundary layer grows (Spalart et al., 2006).

In order to ensure DES is reliable as designed and can be adaptive to variations of grid spacings as well as boundary-layer thickness, Delayed Detached Eddy Simulation (DDES) has been proposed to address the inherent deficiency described above. Spalart et al. (2006) added another function f_d to the dissipation length scale shown in Equation (3.32), so that DES can solve the whole boundary layer using RANS mode independently

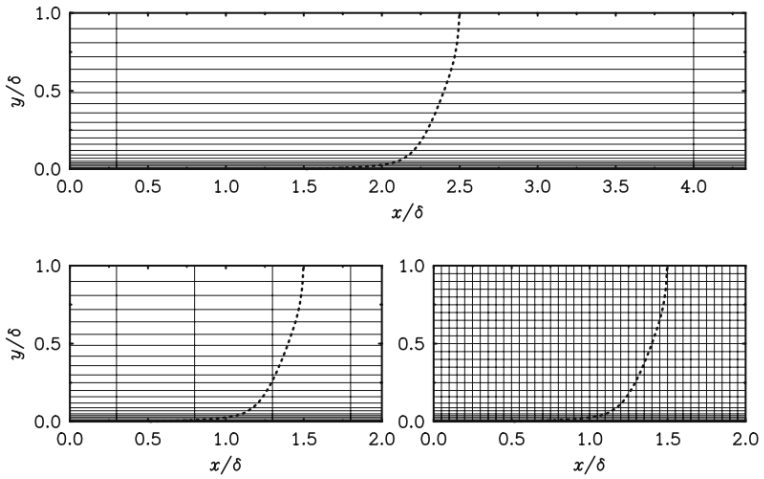

Figure 3.3: Example grids in a boundary layer. *Top* Type I, natural DES; *left* Type II, ambiguous spacing; *right* Type III, LES. - - - mean velocity. δ is the boundary-layer thickness. Assume $\Delta_z \approx \Delta_x \approx \Delta_\parallel$. (Spalart et al., 2006)

of the grid resolution. The modified length scale turns out to be:

$$\tilde{d} = d - f_d \max(0, d - C_{DES}\Delta) \tag{3.33}$$

with

$$f_d = 1 - \tanh([8r_d]^3) \tag{3.34}$$

$$r_d = \frac{\nu_t + \nu}{\sqrt{U_{i,j}U_{i,j}}k^2d^2} \tag{3.35}$$

In Equation (3.35), ν_t is the turbulent viscosity, ν is the molecular viscosity, $U_{i,j}$ is the gradient of velocity, k is the Karman constant, and d is the distance from the wall. $\tilde{\nu}$ in the S-A model can be written as $\tilde{\nu} = \nu_t + \nu$. f_d tends to 1 in LES mode and 0 elsewhere. In other words, when f_d tends to 0, a RANS mode is employed. On the other hand, while f_d is 1, the original DES mode is applied.

3.2 Computational aeroacoustics

The issue of how to predict the noise emitted from an unsteady flow field is of great practical interest. CAA is emerging as a numerical tool to address this problem. Combinations of traditional CFD and CAA with acoustic analogies are more effective for the industry. The basic idea of acoustic analogies is to present fluid mechanics equations as the wave equation with a distribution of equivalent sound sources from which the radiated noise to the far field can be determined. Lighthill's analogy was originally

devised for unbounded flows (Lighthill, 1952; Lighthill, 1954), which gave birth to the field of aeroacoustics. Extension of Lighthill's analogy was first made by Curle (1955) to account for the presence of fixed surfaces in the flow region and then by Ffowcs Williams and Hawkings (1969) for moving surfaces.

3.2.1 Lighthill's analogy

The starting point of Lighthill's analogy is the Navier-Stokes equations for a compressible viscous flow, which is stationary. The equations proposed by Lighthill are exact rearrangements of the mass and momentum conservation laws describing motion in an arbitrary continuous fluid (Equations (3.1) and (3.2)):

$$\frac{\partial \rho}{\partial t} + \frac{\partial \rho u_i}{\partial x_i} = 0 \tag{3.36}$$

$$\frac{\partial \rho u_i}{\partial t} + \frac{\partial}{\partial x_j}(\rho u_i u_j + p\delta_{ij} - \tau_{ij}) = 0 \tag{3.37}$$

where ρ is the density, u_i $(i = 1 \sim 3)$ is the component of the flow velocity in the x_i direction, p is the total pressure, δ_{ij} is the Kronecker delta function (δ_{ij}=1, for $i = j$; δ_{ij}=0, for $i \neq j$), τ_{ij} is the viscous stress tensor, which can be written as follows:

$$\tau_{ij} = \mu \left[\frac{\partial u_i}{\partial x_j} + \frac{\partial u_j}{\partial x_i} - \frac{2}{3} \left(\frac{\partial u_k}{\partial x_k} \right) \delta_{ij} \right] \tag{3.38}$$

in which μ is the dynamic viscosity.

After some algebraic manipulations, Lighthill's equation can be derived:

$$\frac{\partial^2 \rho'}{\partial t^2} - c_0^2 \nabla^2 \rho' = \frac{\partial^2 T_{ij}}{\partial x_i \partial x_j} \tag{3.39}$$

with c_0 is the sound speed and

$$T_{ij} = \rho u_i' u_j' + (p' - c_0^2 \rho')\delta_{ij} - \tau_{ij} \tag{3.40}$$

ρ' in Equation (3.40) is the density fluctuation and T_{ij} is called the Lighthill stress tensor, representing a distribution of 'quadrupole' sources:

- $\rho u_i' u_j'$ describes non-linear effects
- $p' - c_0^2 \rho'$ is associated with the non-isentropic effects
- τ_{ij} represents the effects of viscosity

The left-hand side of Equation (3.39) describes sound propagation with the standard wave operator and the terms on the right-hand side can be interpreted as equivalent

sources, which can generate exactly the same sound field through the wave equation as would the flow. If the source terms are known, the density fluctuation ρ' could be computed everywhere according to Equation (3.39). However, the density ρ is also a part of the acoustic sources. To address this issue, the fluid region can be divided into a small sound generation region and the surrounding acoustic far field. It is assumed that the source terms are only significant within the source region. Information regarding the source region could be obtained by means of measurements, modelling or numerical simulations. In the acoustic far field, all source terms are negligible and the only fluctuations are associated with acoustic waves, which are the only type of disturbances propagating far away from the flow. In the far field, the acoustic pressure perturbation satisfies $p' = c_0^2\rho'$. The Lighthill analogy turns the problem of sound prediction from a moving source into an equivalent classical acoustic problem, for a uniform flow at rest. The solution of the Lighthill equations can be obtained using the free space Green's function.

Consider a 3D acoustic field at the location $\mathbf{x}$ at time t generated by a single impulse source at spatial position $\mathbf{y}$ and time τ in free space. The point source can be described as $\delta(\mathbf{x}-\mathbf{y})\delta(t-\tau)$, and the acoustic field can be given by:

$$\frac{1}{c_0^2}\frac{\partial^2 G}{\partial t^2} - \nabla_{\mathbf{x}}^2 G = \delta(\mathbf{x}-\mathbf{y})\delta(t-\tau) \tag{3.41}$$

The solution of Equation (3.41) is the Green's function:

$$G(\mathbf{x}, t \mid \mathbf{y}, \tau) = \frac{1}{4\pi\left|\mathbf{x}-\mathbf{y}\right|}\delta(t-\tau-\frac{\left|\mathbf{x}-\mathbf{y}\right|}{c_0}) \tag{3.42}$$

where τ is the retarded time and can be calculated by:

$$\tau = t - \frac{\left|\mathbf{x}-\mathbf{y}\right|}{c_0} \tag{3.43}$$

The Green's function represents the impulse response due to a single point source. The solution of Lighthill's analogy can be seen as a sum of all the contributions made by every point $\mathbf{y}$ in the source region at every time τ. In this way, the solution of Equation (3.39) can be written as:

$$\rho'(\mathbf{x}, t) = \int\int \frac{\partial^2 T_{ij}(\mathbf{y}, \tau)}{\partial y_i \partial y_j} G(\mathbf{x}, t \mid \mathbf{y}, \tau)\mathrm{d}\mathbf{y}\mathrm{d}\tau \tag{3.44}$$

Substituting the Green's function from Equation (3.42) into Equation (3.44), the density fluctuation at the position of the far-field receiver ($\mathbf{x}$) can be described as:

$$\rho'(\mathbf{x}, t) = \frac{1}{4\pi c_0^2}\int_V \frac{\partial^2 T_{ij}(\mathbf{y}, \tau)}{\partial y_i \partial y_j}\frac{\mathrm{d}\mathbf{y}}{\left|\mathbf{x}-\mathbf{y}\right|} \tag{3.45}$$

In the geometric far field this can be approximated as:

$$\rho'(\mathbf{x},t) \simeq \frac{1}{4\pi c_0^2|\mathbf{x}|}\frac{\partial^2}{\partial x_i \partial x_j}\int_V T_{ij}\left(\mathbf{y}, t-\frac{|\mathbf{x}|}{c_0}+\frac{\mathbf{x}\cdot\mathbf{y}}{c_0|\mathbf{x}|}\right)\mathrm{d}\mathbf{y} \tag{3.46}$$

Using time derivatives instead, then:

$$\rho'(\mathbf{x},t) \simeq \frac{1}{4\pi c_0^2|\mathbf{x}|}\frac{x_i x_j}{|\mathbf{x}|^2}\frac{\partial^2}{\partial t^2}\int_V T_{ij}\left(\mathbf{y}, t-\frac{|\mathbf{x}|}{c_0}+\frac{\mathbf{x}\cdot\mathbf{y}}{c_0|\mathbf{x}|}\right)\mathrm{d}\mathbf{y} \tag{3.47}$$

The use of time derivatives is often preferred since it is more convenient to implement and can yield more accurate predictions compared with the integral on the volume. Mathematical derivations from Equation (3.46) to (3.47) was presented in detail by Goldstein (1976).

Dimensional analysis or *Scaling law* is an effective way to demonstrate the dependence of the sound amplitude and the total acoustic power on certain parameters. To achieve this goal, reference values for velocity, length and density are introduced as shown in Figure 3.4.

- u_s: magnitude of the velocity perturbation in the source region
- L: size of the source region
- ρ_s: density of the fluid in the source region
- U: flow velocity in the sound field
- λ: acoustic wavelength
- ρ_0: ambient density of the fluid in the sound field

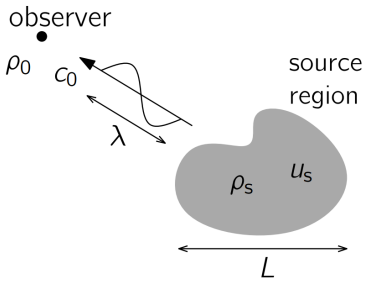

Figure 3.4: Scheme of reference values for dimensional analysis

It is assumed that the equivalent source in Lighthill's analogy can be treated as a compact source, for which the source region should be much smaller than the acoustic wavelength. The phase difference between signals emitted from different points in the source region can therefore be neglected. At low Mach number, the viscous shear stress τ_{ij} and the heat

conduction are negligible, and therefore the Lighthill stress tensor can be approximated as:

$$T_{ij} = \rho u_i' u_j' \tag{3.48}$$

For the non-linear source term, the following estimations can be made:

- Lighthill stress tensor: $T_{ij} = \rho u_i' u_j' \sim \rho_s u_s^2 \sim \rho_0 U^2$
- Time derivative: $\dfrac{\partial}{\partial t} \sim \dfrac{c_0}{\lambda} = \dfrac{U}{L}$
- Integral over the volume: $\int_V \mathrm{d}\mathbf{y} \sim L^3$

Note that $|\mathbf{x}| = x$ is an independent parameter. Based on the above estimations, the scaling law for the acoustic density in the far field described by Equation (3.47) can be expressed as:

$$|\rho'| \sim \rho_0 M^4 \frac{L}{x} \tag{3.49}$$

where M is the Mach number. Employing $I \sim c_0^3 |\rho'^2|/\rho_0$, the scaling law for the acoustic intensity I can be written as:

$$I \sim \rho_0 c_0^3 \left(\frac{L}{x}\right)^2 M^8 \tag{3.50}$$

which is the well-known 8^{th}-power law derived by Lighthill (Lighthill, 1954). From Equation (3.50), it is clear that the acoustic intensity of the quadrupole sources scales in proportion to the eighth power of the Mach number. Although only trends can be predicted by the scaling law, this method is efficient in identifying the factors inducing the noise generation.

3.2.2 Curle's analogy

Lighthill's analogy is obtained from the Navier-Stokes equations without taking into account the presence of solid boundaries in the flow. The interaction of solid bodies and the turbulent flow will yield fluctuating forces acting on the surface of the solid body, which can work as an additional acoustic source term compared with the case in an unbounded flow. Extension of Lighthill's theory was made by Curle (1955) to include the effect of solid boundaries on the noise generation. A dipole source due to the

fluctuating forces on the solid bodies was added to the solution of Lighthill's equation:

$$\rho^{'}(\mathbf{x},t) = \frac{1}{4\pi c_0^2}\frac{\partial^2}{\partial x_i x_j}\int_V \frac{T_{ij}(\mathbf{y}, t-|\mathbf{x}-\mathbf{y}|/c_0)}{|\mathbf{x}-\mathbf{y}|}\mathrm{d}V(\mathbf{y}) + \frac{1}{4\pi c_0^2}\frac{\partial}{\partial x_i}\int_S \frac{P_i(\mathbf{y}, t-|\mathbf{x}-\mathbf{y}|/c_0)}{|\mathbf{x}-\mathbf{y}|}\mathrm{d}S(\mathbf{y}) \tag{3.51}$$

where S is the surface of the solid boundary, $P_i = -n_j p_{ij}$, n_j is the unit normal vector of the solid boundary pointing towards the fluid. p_{ij} is the compressive stress tensor, which can be written as:

$$p_{ij} = p\delta_{ij} - \tau_{ij} \tag{3.52}$$

P_i is the force per unit area in the x_i direction acting on the fluid generated by the solid bodies in the flow. The corresponding sound field can be interpreted as a sum of the noise induced by a volume distribution of quadrupoles and a surface distribution of dipoles. Effects of sound reflection and diffraction at the solid walls are incorporated into the additional dipole field.

Similar to the dimensional analysis from Lighthill's analogy, the following estimations can made for the dipole sources:

- Fluctuating force: $P_i \sim \rho_0 U^2$
- Time derivative: $\dfrac{\partial}{\partial t} \sim \dfrac{c_0}{\lambda} = \dfrac{U}{L}$
- Integral over the surface: $\int_S \mathrm{d}\mathbf{y} \sim L^2$

Therefore, scaling laws for the second term on the right hand side of Equation (3.51), which describes the dipole source, can be derived as:

$$|\rho'| \sim \rho_0 M^3 \frac{L}{x} \tag{3.53}$$

$$I \sim \frac{c_0^3 |\rho'^2|}{\rho_0} = \rho_0 c_0^3 M^6 \frac{L^2}{x^2} \tag{3.54}$$

According to Equation (3.54), the acoustic intensity of a dipole source is proportional to the sixth power of the Mach number, which means if the Mach number is low, dipole sources due to flow interaction with solid surfaces can radiate sound more efficiently than quadrupole sources due to turbulence.

3.2.3 Ffowcs Williams-Hawkings analogy

Further generalization was applied to Curle's theory to take into account arbitrary motion of the solid boundaries by Ffowcs Williams and Hawkings (1969). A region of fluid

at rest ($\mathbf{u} = \mathbf{0}$, $\rho = \rho_0$, $p = p_0$, where ρ_0 and p_0 are the density and pressure in the ambient fluid respectively) was used to take the place of the solid body. Therefore, the original problem with a fluid region and solid boundaries was turned into an equivalent problem with fluid everywhere, as shown in Figure 3.5. In this way, the density in the overall region could be represented using a composite function as follows:

$$\tilde{\rho}(\mathbf{x}, t) = \rho_0 + [\rho(\mathbf{x}, t) - \rho_0]H(f) = \begin{cases} \rho(\mathbf{x}, t) & f > 0 \\ \rho_0 & f < 0 \end{cases} \tag{3.55}$$

where f is the indicator function. $f > 0$ is the flow region of interests; $f < 0$ denotes locations inside the solid body; $f = 0$ indicates the surface of the solid boundary. The divergence of f is the normal vector of the surface, namely, $\nabla f = \mathbf{n}$. The derivative of f with respect to time is the component of solid surface velocity normal to the boundary surface, namely, $\partial f/\partial t = -\mathbf{v} \cdot \mathbf{n} = -v_n$. $H(f)$ is the Heaviside function:

$$H(f) = \begin{cases} 1 & \text{for } f > 0 \\ 0 & \text{for } f < 0 \end{cases} \tag{3.56}$$

Similarly, the velocity component in the overall region is:

$$\tilde{u_i}(\mathbf{x}, t) = u_i(\mathbf{x}, t)H(f) = \begin{cases} u_i(\mathbf{x}, t) & f > 0 \\ 0 & f < 0 \end{cases} \tag{3.57}$$

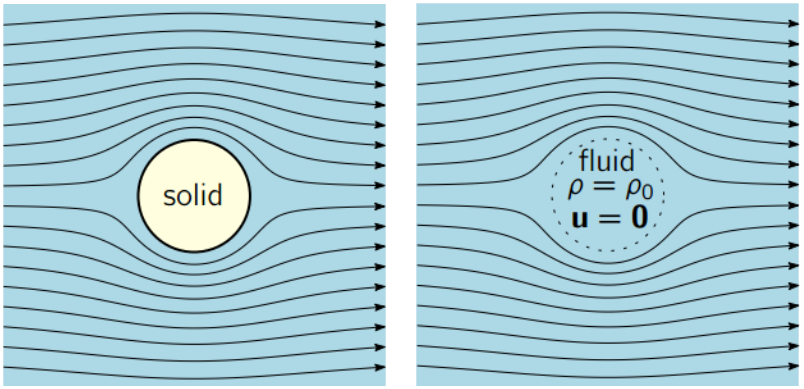

(a) Original problem (b) Equivalent problem

Figure 3.5: The Ffowcs Williams - Hawkings acoustic analogy

In fact, the FW-H analogy is also applicable to predict the sound radiated from a source region in the same way as the solid boundary. To achieve this, the control surface can be arbitrary, and is not confined to be a solid surface. For the impermeable surface of

the solid body, $\mathbf{u} \cdot \mathbf{n} = \mathbf{v} \cdot \mathbf{n}$, namely, $u_n = v_n$, where $\mathbf{u}$ is the velocity of the fluid and $\mathbf{v}$ is the velocity of the surface. However, if the control surface is permeable, these two velocities can be different, in other words, $\mathbf{u} \neq \mathbf{v}$.

Since the derivative of the Heaviside function is the delta function, the time derivative and gradient of Equation (3.55) can be written as:

$$\frac{\partial \tilde{\rho}}{\partial t} = H(f)\frac{\partial \rho}{\partial t} - (\rho - \rho_0)\delta(f)v_n \tag{3.58}$$

$$\nabla \tilde{\rho} = H(f)\nabla \rho + (\rho - \rho_0)\delta(f)\mathbf{n} \tag{3.59}$$

Because of the delta function, the second terms on the right hand side of Equation (3.58) and Equation (3.59), $(\rho - \rho_0)\delta(f)v_n$ and $(\rho - \rho_0)\delta(f)\mathbf{n}$, are only present on the control surface. Substituting the newly defined overall density $\tilde{\rho}$ into the conservation laws of mass and momentum given in Equation (3.36) and Equation (3.37), similar to the Lighthill's analogy, a wave equation with equivalent source terms can be derived:

$$\frac{\partial^2 \tilde{\rho}'}{\partial t^2} - c_0^2 \nabla^2 \tilde{\rho}' = \frac{\partial}{\partial x_i \partial x_j}[T_{ij}H(f)] - \frac{\partial}{\partial x_i}[F_i \delta(f)] + \frac{\partial}{\partial t}[Q\delta(f)] \tag{3.60}$$

where $Q = \rho u_n - (\rho - \rho_0)v_n$ is the monopole source term, describing the mass oscillation generated by motion of the solid object; $F_i = \rho u_i(u_n - v_n) + \rho n_i - \tau_{ij} n_j$ is the dipole source induced by forces applied on the fluid because of the solid surface; T_{ij} is the Lighthill stress tensor, the same term as in Lighthill's analogy, representing quadrupole sources in the flow region, generated by the fluid alone. Due to $\delta(f)$, the mass source and force source are present only on the control surface. The noise generated by dipole sources is often called 'loading noise', while that caused by monopoles is named 'thickness noise'. In addition, these equations are applicable both inside and outside the control surface. This is an extension of Lighthill's analogy that takes into account the effect of a moving surface. The left-hand side of Equation (3.60) is again a form of the wave equation, that describes the propagation of sound waves in a uniform quiescent flow.

The sound field generated by these equivalent sources in Equation (3.60), can be obtained by using the Green's function:

$$\begin{aligned} \rho'(\mathbf{x}, t) = & \frac{\partial^2}{\partial x_i \partial x_j} \int_V \frac{T_{ij}(\mathbf{y}, t - |\mathbf{x} - \mathbf{y}|/c_0)}{4\pi c_0^2 |\mathbf{x} - \mathbf{y}|} d\mathbf{y} \\ & - \frac{\partial}{\partial x_i} \int_S \frac{F_i(\mathbf{y}, t - |\mathbf{x} - \mathbf{y}|/c_0)}{4\pi c_0^2 |\mathbf{x} - \mathbf{y}|} d\mathbf{y} \\ & + \frac{\partial}{\partial t} \int_S \frac{Q(\mathbf{y}, t - |\mathbf{x} - \mathbf{y}|/c_0)}{4\pi c_0^2 |\mathbf{x} - \mathbf{y}|} d\mathbf{y} \end{aligned} \tag{3.61}$$

From Equation (3.61), it is clear that quadrupole sources are integrated over the control volume representing the whole flow region while both dipole sources and monopole

sources are integrated on the surface of the object.

For the 'thickness noise', the following estimations can be used to conduct dimensional analysis:

- Displaced mass: $Q \sim \rho_0 U$
- Time derivative: $\dfrac{\partial}{\partial t} \sim \dfrac{c_0}{\lambda} = \dfrac{U}{L}$
- Integral over the surface: $\int_S \mathrm{d}\mathbf{y} \sim L^2$

Hence, scaling laws for the acoustic density and intensity for 'thickness noise' are:

$$|\rho'| \sim \rho_0 M^2 \frac{L}{x} \tag{3.62}$$

$$I \sim \frac{c_0^3 |\rho'^2|}{\rho_0} = \rho_0 c_0^3 M^4 \frac{L^2}{x^2} \tag{3.63}$$

The acoustic intensity of monopole sources scales like M^4 compared with M^8 for the quadrupoles and M^6 for the dipoles. Therefore, when the Mach number is low, noise generated by monopole sources will tend to be more significant. For the case of high-speed trains, generally, the train could be treated as a rigid body without mass fluctuations on the surface; hence, the effect of monopoles is negligible. Moreover, as the Mach number is generally less than 0.3, the quadrupole sources can be neglected. Loading noise corresponding to the force applied by the train surface to the ambient air is dominant.

3.3 Summary

There are two major steps to be implemented in the current study. The first step is to calculate the flow field using the CFD technique. Conventional methods for CFD include RANS, LES and DNS. The computation cost for each approach in this sequence varies from the cheapest to the highest; conversely, the accuracy is successively increased. In this chapter, starting from the Navier-Stokes equations, the principles of LES were briefly introduced. In order to save computational effort further, a hybrid model DES has been proposed by Spalart and Allmaras (1992). However, there are some inherent shortcomings for DES to guarantee that the switch from 'RANS mode' to 'LES mode' occurs outside the boundary layer near solid walls in the flow. Aiming to resolve these drawbacks in DES, a modified model DDES was derived by Spalart et al. (2006), which is the method adopted in the current work. Acoustic analogies can be employed to predict the far-field noise based on the information obtained in the previous CFD work. Developments of aeroacoustics from Lighthill's analogy to the FW-H equations are also presented in this chapter. Since the train is moving in the air, the FW-H analogy for the solid boundaries is applicable for the current work and as the Mach number is generally

less than 0.3, only the noise source induced by the fluctuating pressure acting on the wall is considered.

Chapter 4

The effect of wall proximity

As reviewed in Section 2.2.2, the whole pantograph and bogie can be treated as a combination of bluff bodies such as cylinders or cuboids with different cross-sections. In order to gain insight into the emitted aerodynamic noise, studies on the flow characteristics are indispensable. Mach numbers smaller than 0.3 are considered in this project; therefore, the flow can be assumed to be incompressible (Turkel et al., 1993). The DDES approach is adopted in OpenFOAM 2.4.0 to investigate the flow past bluff bodies at Reynolds numbers in the range of engineering applications. Based on the fluctuating pressure on surfaces of the bluff body obtained from the CFD simulations, the noise emitted to the far field is then predicted using the FW-H acoustic analogy in the commercial software FLUENT. In this chapter, the installation effect of these bluff bodies with compact geometries is simplified as a cube with different wall proximities. As presented in Section 2.3, most of the experimental and numerical investigations on the cube flow considered a wall-mounted cube rather than a cube in free space and no previous work was reported on the flow around a cube with different wall proximities. For such experimental investigations a proper supporting system would be required to minimize the flow disturbance and avoid likely vibrations from supporting struts. However, the problem of the supporting system to study elevated objects is not a limitation in numerical simulations.

4.1 Flow over the wall-mounted cube

To evaluate the feasibility of the adopted methodologies and gain guidelines for the computational setup, a numerical investigation is carried out first replicating the measurements conducted by Castro and Robins (1977) on a wall-mounted cube placed in a uniform flow, employing DDES in OpenFOAM 2.4.0. The results are compared with the measurements of Castro and Robins (1977) and Depardon et al. (2005). The wall-mounted cube has a height of $L = 60$ mm while the free stream velocity is $U_\infty = 12.5$

m/s. The Mach number for this benchmark work is $M = U_\infty/c_0 = 0.037$. The corresponding Reynolds number $Re = U_\infty L/\nu = 5 \times 10^4$, where $\nu = 1.5 \times 10^{-5}$ m^2/s is the kinematic viscosity. This lies in the range ($Re \geq 3 \times 10^4$) where the flow over a cube is independent of Reynolds number (Castro and Robins, 1977).

4.1.1 Computational domain and boundary conditions

A balance between the blockage ratio and the required computing resources needs to be taken into account in determining the size of the computational domain. If the computational domain is not large enough, the flow field may not be fully developed due to the enforced boundary conditions. On the other hand, too large a computational domain will unnecessarily increase the resources required. The recommended limit for the blockage ratio, which is defined as the ratio of the section area of the tested object to the computational domain's frontal area, is 3% (Franke et al., 2004). An illustration of the computational domain is shown in Figure 4.1. Its overall size is $26L \times 7L \times 13L$. Therefore, the blockage ratio is about 1%. The origin of the coordinate system is located at the cube centre and the x-axis corresponds to the streamwise direction while the vertical (cross-flow) and lateral (spanwise) directions are represented by the y-axis and z-axis respectively.

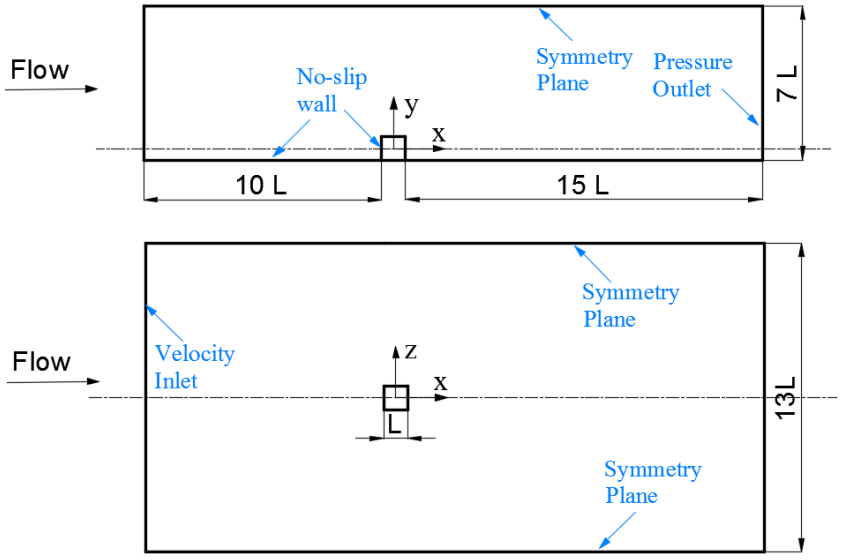

Figure 4.1: Sketch of the computational domain for the wall-mounted cube showing the boundary conditions

In solving the unsteady incompressible Navier-Stokes equations, appropriate boundary conditions need to be specified for a well-posed problem. As depicted in Figure 4.1, *Velocity Inlet* and *Pressure Outlet* boundary conditions are assigned for the inlet and outlet. *Symmetry Plane* is used for the top and side boundaries. *No slip wall* is applied to all solid surfaces, including the cube and the ground. All of these boundary conditions

describe physical information about the computational domain, and are built into the system by means of algebraic equations. Details of each boundary condition are given as follows:

- *Velocity Inlet*: The velocity field for the inlet is assigned as a fixed value in OpenFOAM. The velocity vector is prescribed as $\mathbf{u} = (12.5, 0, 0)$ m/s. Since only the gradient of the pressure exists in the related governing equations instead of the pressure itself, the pressure field for the inlet is set to have a zero gradient, which means the gradient of the pressure normal to the inlet is zero, $\partial p/\partial n = 0$.
- *Pressure Outlet*: Overall mass conservation in the computation region should be fulfilled when assigning the outlet boundary condition. Since a fixed velocity and pressure distribution are applied for the inlet, to meet this mass balance requirement, zero gauge pressure and zero gradient of the velocity field are prescribed for the outlet boundary.
- *Symmetry Plane*: No flow across the boundary and the gradients for all variables are zero. Thus, taking the velocity field as an example, $\mathbf{u} \cdot \mathbf{n} = 0$ and $\partial \mathbf{u}/\partial \mathbf{n} = 0$ can be used to describe the symmetry boundary.
- *No slip wall*: Zero velocity and zero gradient of pressure are applied to the wall.

4.1.2 Numerical schemes and solvers

The overall balance of numerical accuracy, stability and the computational cost should be considered when selecting the numerical schemes. The time step for CFD simulations needs to be small enough to make the simulation stable and to obtain credible features of the flow. For explicit time schemes, the Courant-Friedrichs-Lewy (CFL) condition is required for convergence. The basic idea of this CFL condition is to ensure the time step taken to calculate the flow physics in a discretised spatial cell is less than the time needed for the flow to travel to adjacent cells. The CFL number or Courant number can be defined as:

$$C = \frac{U\Delta t}{\Delta x} \leq C_{max} \tag{4.1}$$

where U is the flow speed, Δt is the time step to be determined and Δx is the smallest length of cells in the streamwise direction. The value of C_{max} varies with the numerical scheme adopted to solve the partial differential equations. Typically, $C_{max} = 1$ is chosen for an explicit scheme while a larger C_{max} may be used for implicit methods, which are less sensitive to numerical instability. Under the premise of convergence, a larger time step means less overall time consumption, which is obviously preferred in CFD simulations. In the current work, the unsteady terms ($\partial/\partial t$) are discretised using the *backward* method, which is an implicit scheme with second-order accuracy. The time

step can be determined according to the recommended CFL number range, $C_{max} \leq 2$ (Mockett et al., 2009).

The standard *Gaussian* finite volume integration is employed for the spatial discretisation in OpenFOAM, which is implemented by integrating values on cell faces. Therefore, an interpolation scheme is needed to obtain values on the cell surface from the cell centre. The *linear* scheme is used as the default numerical scheme for gradient (∇), divergence ($\nabla\cdot$) and Laplacian terms (∇^2), which represents the central differencing interpolation with second-order accuracy. In particular, the convection term in the transport equation (div(phi,U) in the OpenFOAM code) is calculated using the Total Variation Diminishing (TVD) interpolation approaches, such as the *Gauss limitedLinear* scheme or the *Linear-Upwind Stabilised Transport* (LUST) method designed for LES/DES in OpenFOAM. The TVD scheme is a combination of the *upwind* and *central* schemes intended to eliminate the inherent diffusion effect of the *upwind* method while maintaining stability (Sweby, 1984). The surface normal gradient terms (*snGradSchemes* in OpenFOAM code) are components of the gradient normal to the face connecting adjacent cells and are required in calculating the Laplacian term. The *corrected* scheme is applied to calculate the surface normal gradient with a correction of the non-orthogonality induced by skewed grids. The diffusion term in the momentum equations, namely, $\nabla \cdot (\nu \nabla U)$, is a Laplacian term. A surface normal gradient scheme for ∇U is required; therefore, the scheme *Gauss linear corrected* is used for the Laplacian term. A PIMPLE algorithm which is a combination of the Semi-Implicit Method for Pressure Linked Equations (SIMPLE) (Patankar and Spalding, 1983; Patankar, 2018) and the Pressure Implicit with Splitting of Operators (PISO) (Issa, 1986) algorithms is adopted in OpenFOAM to solve the pressure-velocity coupling term. More details of the PIMPLE algorithm can be found in the literature (Ferziger and Perić, 2002). In this thesis, two outer iterations (*nOuterCorrectors* in OpenFOAM) are used for the pressure-velocity coupling each time step while two inner loops (*nCorrectors* in OpenFOAM) are used for the pressure correction within each outer iteration.

4.1.3 Mesh generation and grid dependence investigation

To implement CFD simulations, the computational domain needs to be discretised into a finite number of cells with simple shapes, which can be considered as control volumes. Since the Spalart-Allmaras (S-A) model is adopted in the DDES used in the current work, which is able to obtain solutions in the viscous sublayer (Nguyen et al., 2007), special attention needs to be paid to the grid resolution in the near-wall boundary layer. y_1^+ is a non-dimensional parameter used to indicate the distance from the wall for a wall-bounded flow, given by:

$$y_1^+ = u_\tau y_1 / \nu \tag{4.2}$$

where ν is the kinematic viscosity of the flow, y_1 is the height of the first layer grids lying around the cube surface, u_τ is the skin-friction velocity, which can be defined as:

$$u_\tau = \sqrt{\frac{\tau_w}{\rho}} \tag{4.3}$$

with

$$\tau_w = \mu \frac{\partial u}{\partial y}|_{y=0} \tag{4.4}$$

being the wall shear stress. Normally, to implement the S-A model to resolve flows in the near-wall region, $y_1^+ \approx 1$ is required to guarantee the cells at the wall are fine enough, based on which the height of first layer grids (y_1) can be estimated.

A fully structured mesh is generated for the computational domain of the wall-mounted cube in which coarser cells are used further away from the cube with a stretching ratio about 1.09. Illustrations of the mesh are shown in Figure 4.2. Figure 4.2(a) shows the cells in the $z = 0$ plane, while Figure 4.2(b) displays the mesh topology close to the cube indicated by the red rectangle in Figure 4.2(a). Spherical cell blocks normal to the cube surfaces are built to avoid large skewness near the cube corners, based on which the mesh is then stretched out to the further from the cube. To eliminate the influence of numerical setup and to determine the most suitable resolution, balancing the accuracy and the computational cost, grid dependence investigations on meshes with different spatial resolutions are carried out and shown in Table 4.1 and 4.2. To speed up the grid dependence investigation, the maximum dimensionless first-cell spacing (y_1^+) for the cases given in Table 4.1 is set first to be 3 to estimate the promising mesh spacing. After that, the value of the designed maximum y_1^+ for cases given in Table 4.2 is reduced to 1.5, which is more desirable for the noise prediction. Since the height of first layer cells (y_1) is determined by the value of y_1^+, the mesh is refined in the streamwise (x) and the lateral (z) directions to obtain different spatial resolutions. The mesh size is set to be equal in the streamwise and lateral directions and is refined gradually with the smallest mesh spacing denoted as $\Delta_{x1,z1}$. The total number of cells is shown as N_{grid} in Table 4.1 and 4.2. To control the quantity of variables for comparison, a constant time resolution with a time step of 1×10^{-5} s is used for all the investigated grids in Table 4.1 and 4.2. The normalised scale of this time step is $t^* = U_\infty t/L = 0.002$ and the corresponding CFL numbers are less than 1.5. However, it is worth noting that the time step is supposed to be reduced for refined grids to capture the smaller scales in the flow. The time dependence on the simulation is not evaluated in this thesis. Special attention on the time resolution is indispensable for LES and DNS, for which the aspect ratio of the near-wall grids is very small.

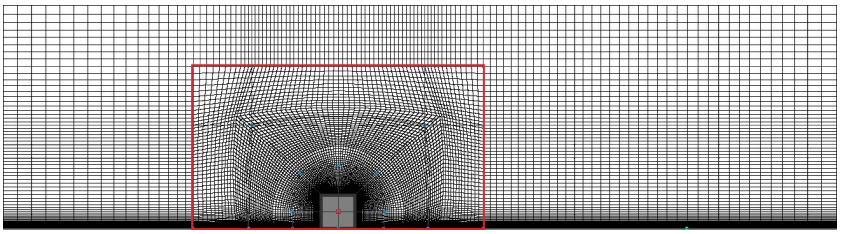

(a) Cells in the $z = 0$ plane

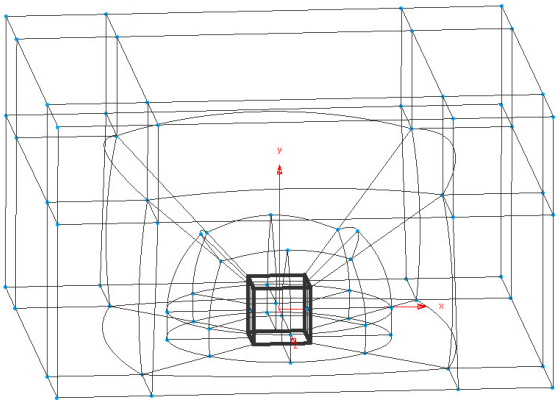

(b) Mesh topology

Figure 4.2: Illustrations of the mesh for the benchmark case

Case	N_{grid}	$\Delta_{x1,z1}$	$\overline{C}_d$	$\overline{C}_l$	$\overline{C}_s$	$C_{d,\text{rms}}$	$C_{l,\text{rms}}$	$C_{s,\text{rms}}$
1	330,528	$0.050L$	1.279	0.5178	0.0060	0.0527	0.0545	0.1440
2	867,024	$0.025L$	1.271	0.6043	-0.0036	0.0480	0.0608	0.1639
3	1,187,424	$0.020L$	1.217	0.6075	0.0003	0.0357	0.0550	0.1380
4	1,658,076	$0.013L$	1.212	0.6147	0.0008	0.0362	0.0581	0.1347

Table 4.1: Summary of grid dependence investigations for cases with $y_1^+ \leq 3$

Aerodynamic parameters (C_a), including the drag, lift and side-force coefficients (C_d, C_l and C_s, respectively) are defined as:

$$C_a = \frac{F_a}{0.5\rho U_\infty^2 A} \tag{4.5}$$

where F_a is the drag, lift or side force, i.e. the total force acting on the cube in the x, y or z directions, for C_d, C_l and C_s, respectively; ρ is the density of the fluid; U_∞ represents the free stream velocity and $A = L^2$ is the frontal area of the cube. Mean and root-mean-square (rms) values of these aerodynamic parameters are examined and compared in Table 4.1 and 4.2. The latter are strongly related to the emitted noise. As can be seen from Table 4.1, with progressive refinements of the mesh, only small variations of these aerodynamic parameters are observed between case 3 and case 4, which indicates convergence. Therefore, case 3 is chosen as the basis for the following

Case	N_{grid}	$\Delta_{x1,z1}$	$\overline{C}_d$	$\overline{C}_l$	$\overline{C}_s$	$C_{d,\text{rms}}$	$C_{l,\text{rms}}$	$C_{s,\text{rms}}$
5	1,341,740	$0.020L$	1.226	0.5979	-0.0008	0.0359	0.0505	0.1289
6	1,530,550	$0.016L$	1.220	0.6064	-0.0017	0.0341	0.0549	0.1291
7	1,799,092	$0.013L$	1.213	0.5877	0.0008	0.0357	0.0477	0.1128
8	4,466,480	$0.010L$	1.189	0.6278	0.0013	0.0345	0.0424	0.1034

Table 4.2: Summary of grid dependence investigations for cases with $y_1^+ \leq 1.5$

cases shown in Table 4.2 with a reduced maximum y_1^+ of 1.5.

The streamwise and the lateral directions have again been simultaneously refined based on the designed $y_1^+ \leq 1.5$ as listed in Table 4.2. According to these results, statistical convergence for both mean and rms values of the aerodynamic parameters has been achieved. Case 7, with a total of 1.8 million cells, is adopted as the benchmark case for the following comparisons with experimental results and numerical studies on the elevated cube. The maximum aspect ratio of the mesh around the cube is 158. The simulations in this thesis are carried out on the iridis 4 supercomputer at the University of Southampton. It takes about 60 hours wall time to run about 2 physical seconds ($t^* \approx 417$), when this benchmark case is calculated parallelly using 160 cores. Statistics is calculated up to about $t^* = 2000$ for this case. Figure 4.3 illustrates the performance of DDES at different positions in the central plane. Parameters of f_d, $\tilde{d}$, d are defined in Section 3.1.2.3 and U/U_∞ is the normalised streamwise velocity. The DDES is in the RANS mode when f_d=0 and changes to the LES mode implied by $f_d = 1$. As can be seen from Figure 4.3, the majority of the computational domain is resolved by the LES, while the RANS model is only employed very close to the wall. Some lines of f_d and the corresponding $\tilde{d}/d$ in Figure 4.3 are not smooth, which is caused by the post processing (see Equations (3.34) and (3.35)), considering the cell coordinates and flow parameters are interpolated to the investigated positions.

The distributions of y_1^+ along the cube surfaces and on the ground in the $x-y$ plane through the cube centre ($z = 0$) are illustrated in Figure 4.4. The maximum value of y_1^+ is less than 1.6 on the cube and 1.8 on the ground, while the y_1^+ values for the majority of the cells are below 1. The average value of y_1^+ in Figure 4.4(a) along the cube surfaces is 0.52 and that along the ground shown in Figure 4.4(b) is 0.53. Figure 4.5(a) depicts the profiles of the turbulence intensity ($\sqrt{\langle u^2 \rangle}/U_\infty$) and the mean streamwise velocity (U/U_∞) at a position one side-length upstream of the cube, i.e. at $x = -1.5L$, $z = 0$. This is plotted against the normalised height above the ground ($y/L + 0.5$) for the adopted case 7. The thickness of the layer with a turbulence intensity greater than 0.5% is about $0.1L$ (6 mm) in this numerical work, which is the same as that described in the measurements of Castro and Robins (1977). This is desirable as the current benchmark case is designed to replicate the measurement and the numerical setup is

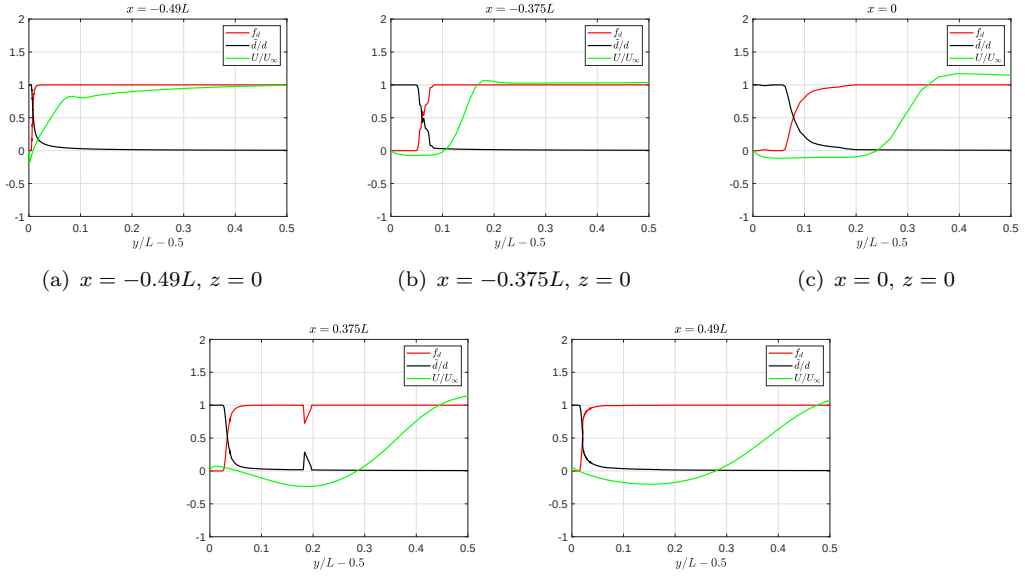

(a) $x = -0.49L$, $z = 0$ (b) $x = -0.375L$, $z = 0$ (c) $x = 0$, $z = 0$

(d) $x = 0.375L$, $z = 0$ (e) $x = 0.49L$, $z = 0$

Figure 4.3: Performance of the DDES model for the benchmark case

aimed to provide the same incoming boundary layer as the experiment. However, it is worth noting that the thickness of boundary layer is about $0.2L$ as indicated by the red line in Figure 4.5(a). Figure 4.5(b) shows the mean streamwise velocity upstream the cube along the centreline. It seems the position $6L$ upstream the cube is sufficient to assign the *Velocity Inlet* boundary condition for the simulation purpose only instead of the $10L$ shown in Figure 4.1. Since coarser cells are used further from the cube, the total number of cells only increases slightly due to the larger upstream computational domain.

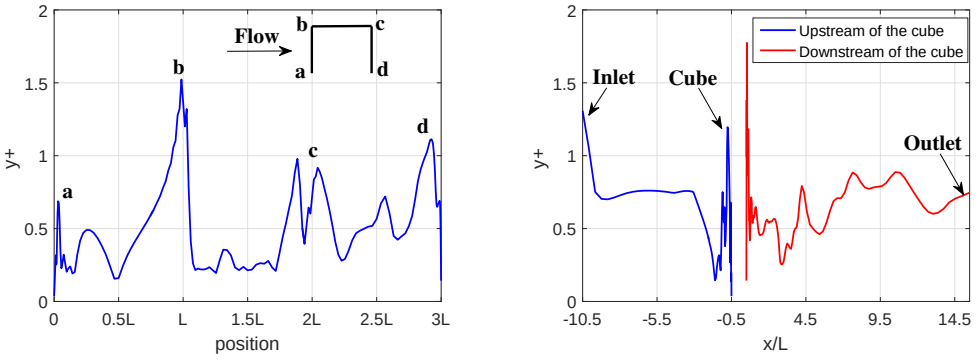

(a) y_1^+ around the cube (b) y_1^+ along the ground

Figure 4.4: The distribution of y_1^+ along solid walls at $z = 0$ for case 7

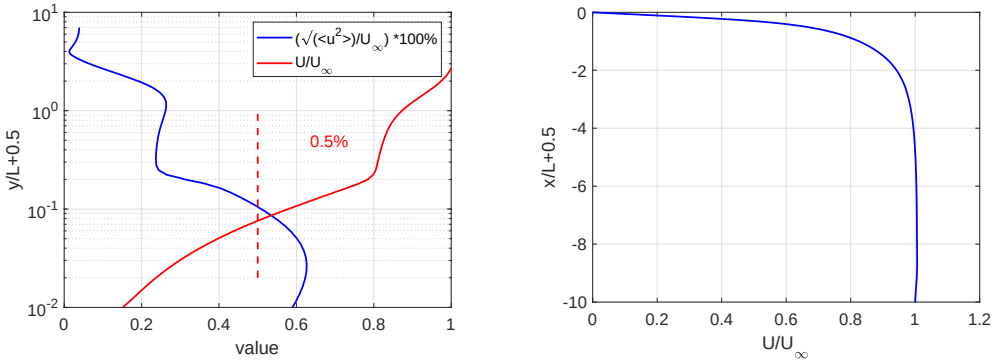

(a) The turbulence intensity and the streamwise velocity one side-length upstream of the cube

(b) The streamwise velocity along $y = 0$, $z = 0$

Figure 4.5: Velocity profiles of the benchmark case

4.1.4 Quantitative comparisons with the experimental measurements

The mean velocity profiles at different positions in the wake of the cube obtained from the simulation are compared with the experimental data from Castro and Robins (1977) in Figures 4.6 and 4.7; the red circles show the measurement locations and the blue dots represent grids in this simulation. The curves in Figure 4.6(a) at $x = 0$ start from $y/L = 0.5$, illustrating profiles of the mean streamwise velocity above the top surface through the cube centre. In Figures 4.6(b) and 4.6(c), they start from the ground at $y/L = -0.5$ for positions $0.5L$ ($x = L$) and $1.5L$ ($x = 2L$) downstream of the cube respectively. Figure 4.7 gives the wake velocity profiles at two different heights. Figures 4.6 and 4.7, show that good agreement is achieved between the current simulation and the measurement. The size of the reverse flow region above the cube is accurately predicted (Figure 4.6(a)). The shear layer, developed from flow separated at the cube leading edge, is also accurately predicted, with a slight over-estimation of the maximum velocity downstream of the cube shown in Figures 4.6(b) and 4.6(c). Similar over-estimations of the flow speed in the shear layer obtained from the simulation can also be found in Figure 4.7(a) and Figure 4.7(b) along the lateral direction. However, the size of the wake, implied by the width of the dip, is well captured.

The time-averaged pressure coefficient $C_p = (p - p_\infty)/(0.5\rho U_\infty^2)$, where $p_\infty = 0$ is the reference pressure, along the cube surfaces found in the current numerical work is compared with available measurements in Figure 4.8. In addition, the turbulence intensity, reflecting the fluctuating velocity of the flow, is shown in Figure 4.9. Although these results obtained from the simulation generally show good agreement with those from the measurements, some minor discrepancies can be seen in the wake of the cube, such as in Figures 4.9(b) and 4.9(c). It may be noted that the flow in the wake is more complex, and therefore is difficult to predict and especially to measure accurately, as any disturb to the flow would influence the measured data.

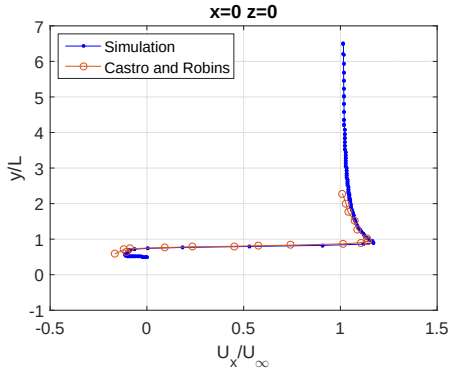

(a) $x = 0, z = 0$

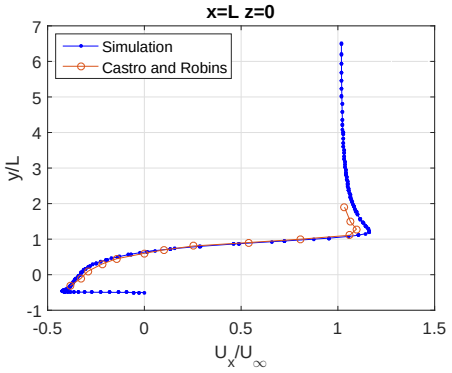

(b) $x = L, z = 0$

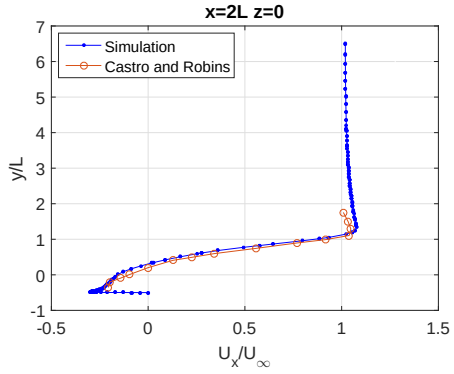

(c) $x = 2L, z = 0$

Figure 4.6: Comparison of the mean streamwise velocity at different positions in the $x - y$ plane between the simulation and the experimental results from Castro and Robins (1977)

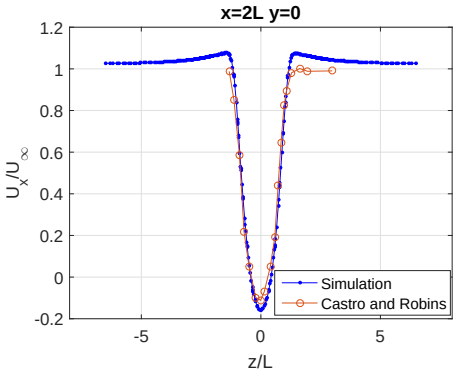

(a) $x = 2L, y = 0$

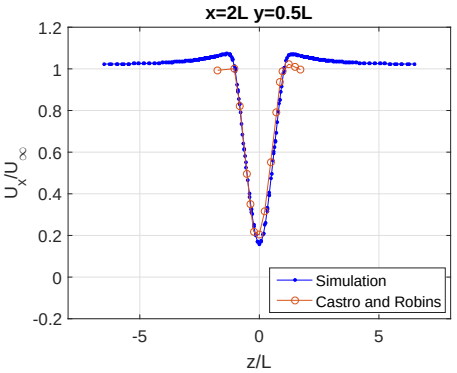

(b) $x = 2L, y = 0.5L$

Figure 4.7: Comparison of the mean streamwise velocity at different positions in the $y - z$ plane between the simulation and the experimental results from Castro and Robins (1977)

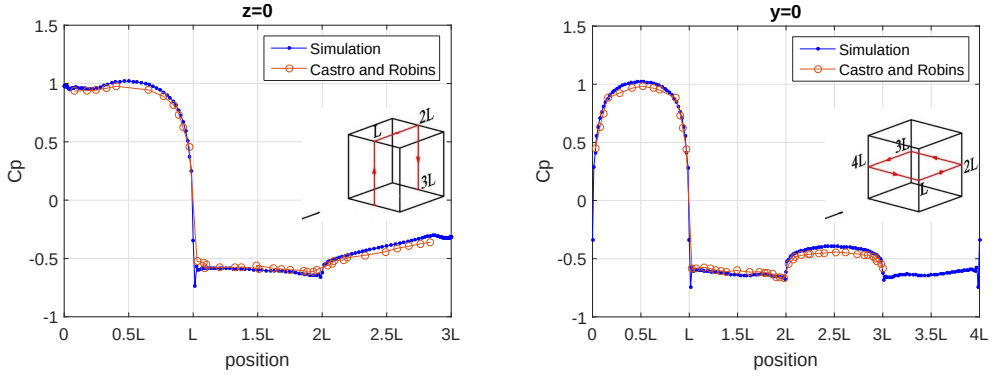

(a) In the $z = 0$ plane

(b) In the $y = 0$ plane

Figure 4.8: Comparison of the pressure coefficient (C_p) between current simulations and the experimental results from Castro and Robins (1977)

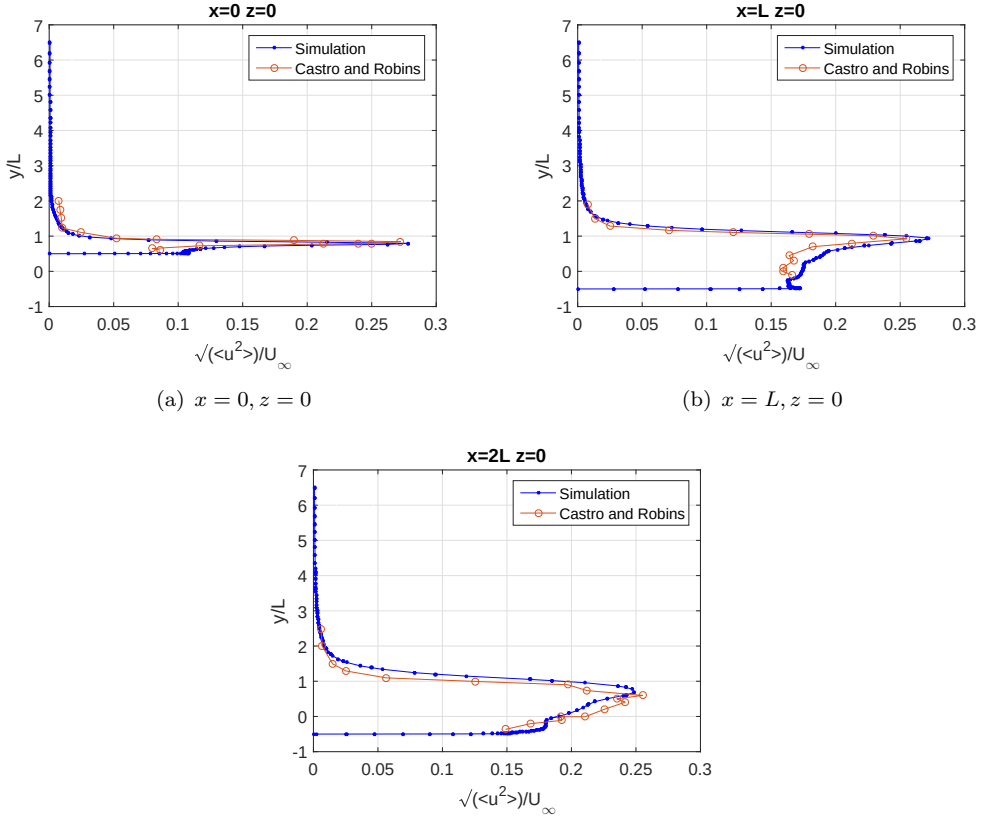

(a) $x = 0, z = 0$

(b) $x = L, z = 0$

(c) $x = 2L, z = 0$

Figure 4.9: Comparison of the turbulence intensity at different positions in the $x - y$ plane between the simulation and the experimental results from Castro and Robins (1977)

In summary, the current numerical results agree commendably with the experimental data reported by Castro and Robins (1977), which is a good indication of the feasibility of the adopted numerical methodology to predict the flow physics quantitatively.

4.1.5 Flow structures and near-wall flow pattern

Flow structures illustrated from a three-dimensional instantaneous flow around the cube are visualized in Figure 4.10, coloured by the time-averaged streamwise velocity. The vortices are embodied based on the second invariant of velocity gradient Q, which can be described as:

$$Q = \frac{1}{2}(\Omega_{ij}\Omega_{ij} - S_{ij}S_{ij}) \tag{4.6}$$

where Ω_{ij} is the rotation rate and S_{ij} is the strain rate:

$$\Omega_{ij} = \frac{1}{2}(\frac{\partial U_i}{\partial x_j} - \frac{\partial U_j}{\partial x_i}) \tag{4.7}$$

$$S_{ij} = \frac{1}{2}(\frac{\partial U_i}{\partial x_j} + \frac{\partial U_j}{\partial x_i}) \tag{4.8}$$

According to Equation (4.6), a positive value of Q implies the rotation strength is predominant over the strain strength, therefore indicating a vortical flow region. In Figure 4.10, $Q_n = 5$ is plotted, which is the normalized Q and is given by:

$$Q_n = \frac{Q}{(U_\infty/L)^2} \tag{4.9}$$

where L is the length of the cube side.

These results clearly show the horseshoe vortex from the upstream region running to the sides of the cube, as also reported by Castro and Robins (1977), and the transcritical bifurcation in the horseshoe vortex observed from the near-wall PIV measurements conducted by Depardon et al. (2005). In addition, the flow in the wake of the cube is highly three-dimensional and abundant vortices of different scales are formed in the wake without the evident periodic vortex shedding found in the wake of square cylinders (Norberg, 1993).

To give more insight into the flow topology, time-averaged streamlines are shown in Figure 4.11 for the $x - z$ plane at 0.5 mm ($y/L = 0.008$) above the ground. These are coloured by the mean pressure coefficient. The Node, Focus and Saddle points are also labelled in Figure 4.11, which are derived from the mathematical Critical Point Theory (Poincaré, 1882). Detailed definitions of these critical points can be found in the review presented by Délery (2001) and illustrations of critical points situated in the plane [p, q] are shown in Figure 4.12. The white lines in Figure 4.11 represent zero mean streamwise velocity, which can be used to determine the positions of flow

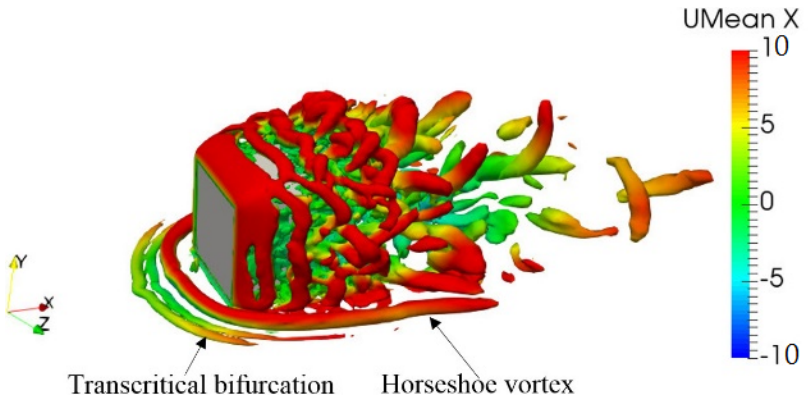

Figure 4.10: Isosurface of the instantaneous flow structure at $Q_n = 5$ coloured by the mean streamwise velocity

separation, reattachment and also the recirculation region in the wake. These results can be compared directly with the PIV measurement on the same plane and oil flow patterns on the ground obtained by Depardon et al. (2005) as shown in Figure 4.13. The measurement was performed for a wall-mounted cube of the same size ($L = 60$ mm) but at a smaller Reynolds number of 4×10^4. As Reynolds numbers in both the current simulation and the measurement performed by Depardon et al. (2005) are above the critical Reynolds number of 3×10^4, it is expected that the difference in Re should have negligible influence.

The saddle-node-saddle-node configuration in the flow upstream of the cube in Figure 4.11 provides hints concerning the transcritical bifurcation; this is also visible in the measured result of Depardon et al. (2005) shown in Figure 4.13, including both the oil-flow visualization and the PIV measurement. The position of the flow separation originating from the ground (marked as ①) in Figure 4.11 is about $0.84L$ ahead of the front surface of the cube, which is larger than that obtained from the near wall PIV ($0.69L$) at the same height in Figure 4.13. It is known that the location of flow separation along the ground is highly dependent on the boundary conditions, especially the thickness of the boundary layer, which was 12 mm in the PIV measurements (Depardon et al., 2005) but 6 mm in the current simulation and in the measurements performed by Castro and Robins (1977); this discrepancy in the separation position may therefore be due to the different boundary layer heights. A pair of counter-rotating vortices around the focus points (marked as ⑦ and ⑧) and a Saddle between them (marked as ⑥) can be observed in both Figure 4.11 and the measurements of Depardon et al. (2005) as displayed in Figure 4.13 at very similar locations in the wake of the cube. These are footprints of the arch vortex tubes.

A single Saddle was detected from the PIV measurements conducted by Depardon et al. (2005) near the reattachment zone in the wake as can be seen from Figure 4.13; in contrast, a Node and two Saddles (marked as ⑨, ⑩, and ⑪ respectively in Figure 4.11) can be observed from current simulation results, which are consistent with the flow

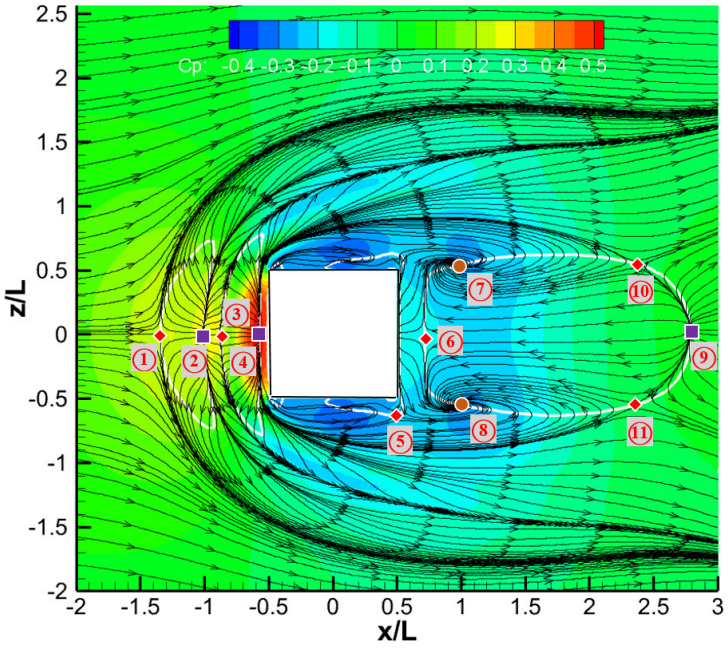

Figure 4.11: Time-averaged streamlines together with the contour of mean pressure coefficient in the $x - z$ plane 0.5 mm above the ground. (square: Node, circle: Focus, diamond: Saddle)

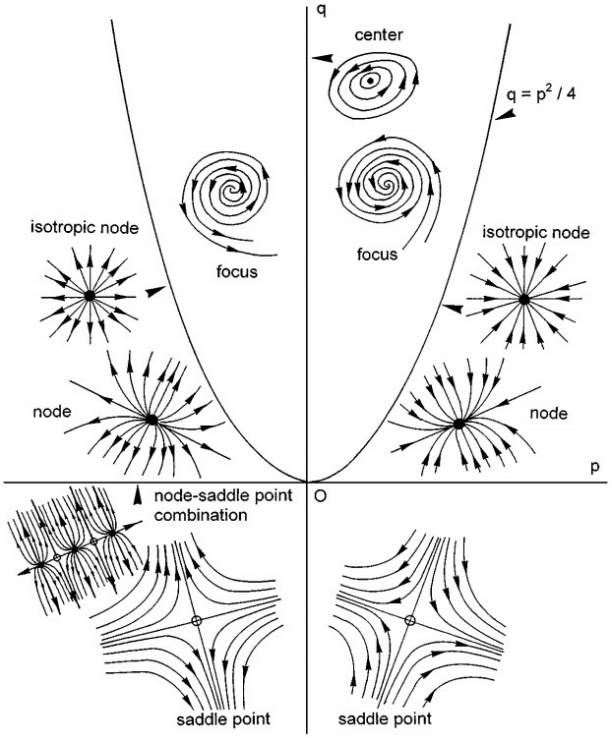

Figure 4.12: Elucidation of critical points for the flow topology (Délery, 2001)

structure derived from the oil-flow visualization on the floor in Figure 4.13. Moreover, the recirculation length, i.e. the distance from the rear surface of the cube to the reattachment point (marked as ⑨ in Figure 4.11), from the current study is about

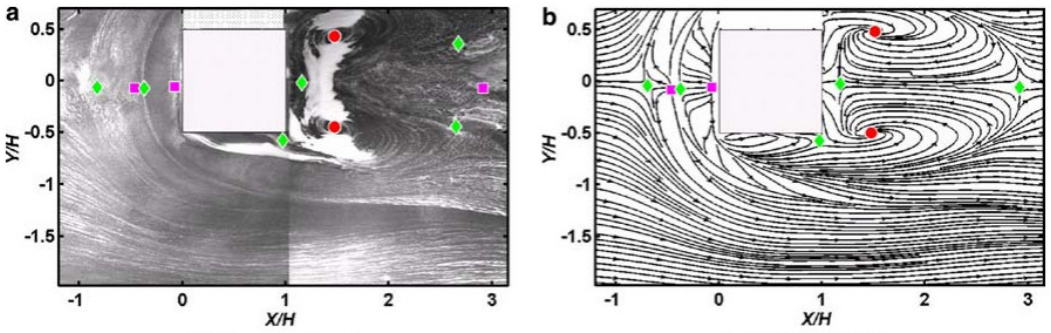

Figure 4.13: Flow topology from the oil flow visualization and the near-wall PIV planes 0.5 mm above the ground conducted by Depardon et al. (2005) (square: Node, circle: Focus, diamond: Saddle).

$2.28L$, which is larger than the corresponding length of $1.92L$ calculated from the PIV measurements at the same height. These discrepancies can again be attributed to the differences in the incoming flow boundary layer thickness. The flow in the wake of the cube reattaches to the ground earlier in the measurements than in the current numerical results and the variation of the near-wall flow topology with respect to the measurement height is speeded up. Despite the different incoming boundary layer conditions, key features of the flow patterns close to the ground have been obtained satisfactorily from the simulation and agree well in flow topology with the measurement conducted by Depardon et al. (2005), despite the differences in quantitative results.

Flow topologies, coloured by the mean streamwise velocity, on planes 0.5 mm ($0.008L$) away from the cube surfaces are illustrated in Figure 4.14. These can be compared with the available near-wall PIV measurements at the same positions by Depardon et al. (2005) as displayed in Figure 4.15. Great similarities in the flow topology and also the flow direction can be seen between Figure 4.14 and Figure 4.15 while the current simulation results agree better with the measurement at the higher Reynolds number $Re = 1.6 \times 10^5$. Similar to the measurements, the Saddle points near the upstream edge (marked as 'A' in Figure 4.14) can hardly be distinguished. A large Focus on the lateral side of the cube (marked as 'B') and Saddle points on the top and lateral surfaces (marked as 'C') can be found in both the numerical and experimental results.

To examine the flow patterns close to the cube in more detail, the time-averaged streamlines in planes $z = 0.0305$ m (i.e. 0.5 mm from the surface of the cube) and $y = 0.0305$ m along with contours of the mean streamwise velocity are shown in Figure 4.16. The red dashed rectangles represent the position of the cube. Due to the formation of the Focus 'B' and Saddle points 'C', reverse flow with negative mean streamwise velocities is dominant near the cube in the separated regions. As explained by Depardon et al. (2005) and Nakamura et al. (2001), the Focus 'B' is the lower part of the 'tornado' shaped vortex alongside the lateral cube surface, which was also reported by Martinuzzi and Tropea (1993). Meanwhile the upper end of this 'tornado' vortex degenerates on

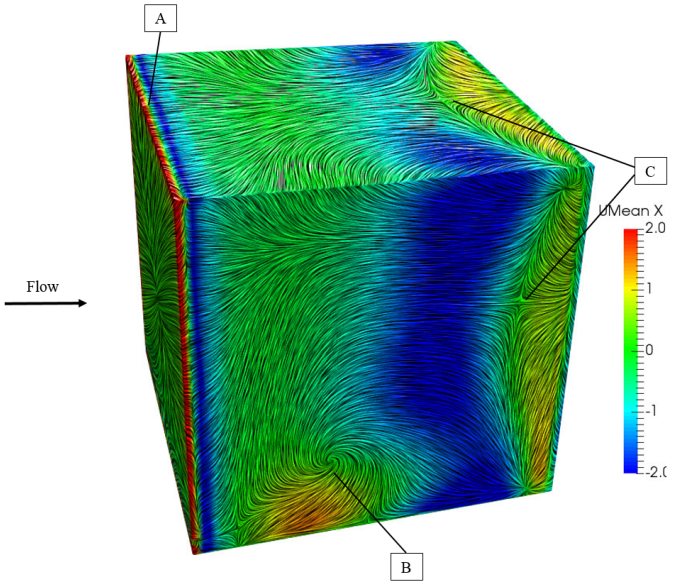

Figure 4.14: Flow topology obtained numerically in planes 0.5 mm above the cube coloured by the mean streamwise velocity.

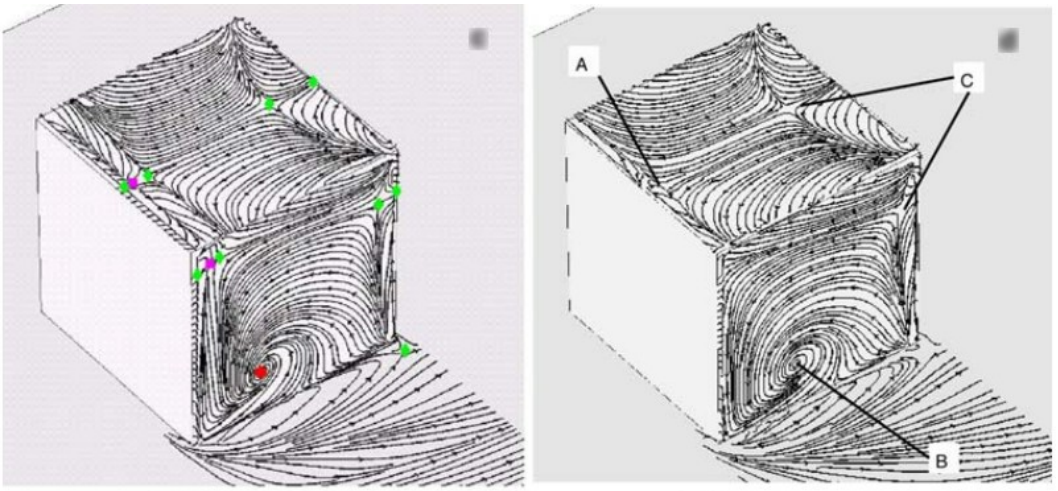

Figure 4.15: Flow topology from near-wall PIV planes 0.5 mm away from the cube conducted by Depardon et al. (2005) (square: Node, circle: Focus, diamond: Saddle).

the upper edge of the cube in flow configurations with high test sections relative to the cube size (namely, a larger ratio of H_c/L, where H_c is the height of the channel and L is the cube size). The Saddle points 'C' identified in Figures 4.14 and 4.16 are formed due to the secondary vortices near the trailing edges, because the fully separated flow from the leading edges does not reattach to the lateral surfaces, which is consistent with the descriptions of the flow around the cube reported by Rodi et al. (1997), and Hunt et al. (1978).

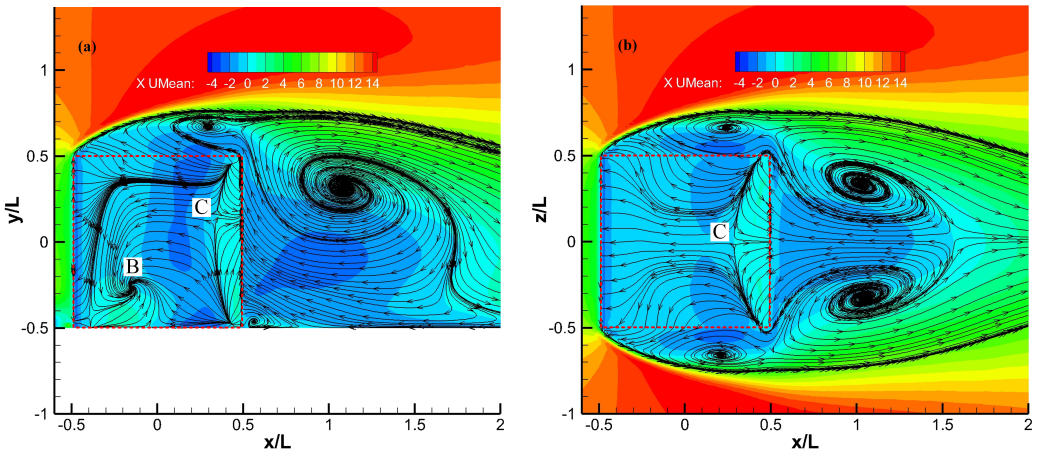

(a) $z = 0.0305$ m (b) $y = 0.0305$ m

Figure 4.16: Time-averaged streamlines together with contours of the mean streamwise velocity in planes offset by 0.5 mm from the cube

In summary, commendable agreement between the numerical simulations and measurements on a wall-mounted cube has been achieved both quantitatively and topologically, covering the pressure distribution along the cube surfaces, time-averaged velocity profiles, together with the turbulence intensity in the wake of the cube. This verifies the feasibility of the adopted DDES approach to predict the flow physics including the region near the wall.

4.2 The effect of wall proximity effect on the cube flow

To investigate the effect of wall proximity on the flow over the cube and also on the emitted noise, the wall-mounted cube from Section 4.1 is elevated to a series of heights above the ground. It is worth noting that the Reynolds number studied in this chapter is relatively low, considering the typical numbers for compact components in train pantographs as mentioned in Section 2.1.1. However, once the value of Re exceeds 3×10^4, the Reynolds number effect on the flow over a cube is supposed to be limited. The elevation height between the cube bottom surface and the ground is varied from $h = L/12$ to L; a cube in free space is also considered as a limiting case. For comparison purposes, features of the flow past the wall-mounted cube ($h = 0$) obtained from the benchmark case are also presented in this section.

4.2.1 Computational setup

The simulation setup of numerical investigations on the elevated cube is similar to the wall-mounted case, apart from adding a region between the cube and the ground varying according to the elevation height, as illustrated in Figure 4.17. The incoming flow

velocity for all cases is kept at 12.5 m/s, corresponding to a Reynolds number of 5×10^4. A fully structured mesh is generated in each case based on the criteria derived from the benchmark case (case 7 in Table 4.2). Similar to Figure 4.2 for the benchmark case, details of the mesh for the $h = L/2$ are illustrated in Figure 4.18 as examples. The grids in the gap between the cube and the ground are carefully generated to ensure that the maximum $y_1^+ < 2$ is achieved for both the cube surface and the ground and the average y_1^+ is well below 1. Distributions of y_1^+ in the $z = 0$ plane along solid walls for the case with $h = L/2$ are illustrated in Figure 4.19. The maximum y_1^+ on the cube surface is about 1.60 and the average is about 0.59. On the ground, the maximum y_1^+ is about 1.45 and the average is about 0.64. For the cube in free space the imposed boundary condition for the bottom of the computational domain is *Symmetry Plane* with $h = 6L$, whereas for all the other cases the *No slip wall* is used. Boundary conditions for all other computational domain surfaces are the same as for the wall-mounted case. A time step of 1×10^{-5} s is again used for all cases and the corresponding maximum CFL number is less than 1.5, implying an adequate temporal resolution.

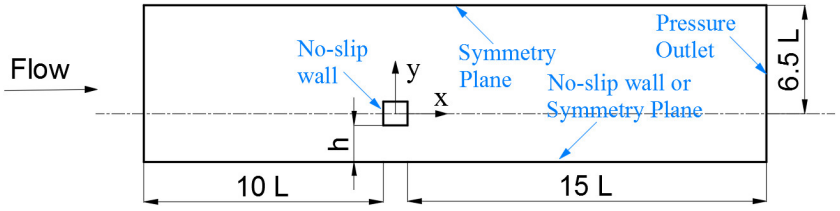

Figure 4.17: Sketch and boundary conditions of the computational domain for the elevated cube

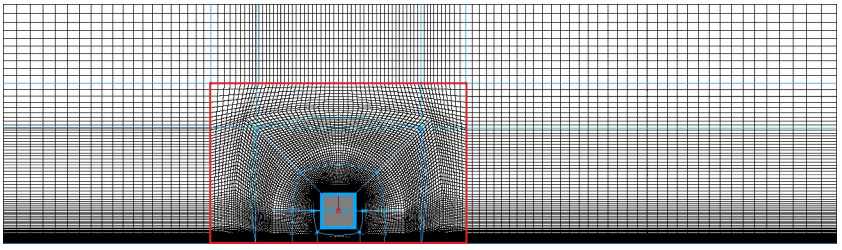

(a) Cells in the $z = 0$ plane

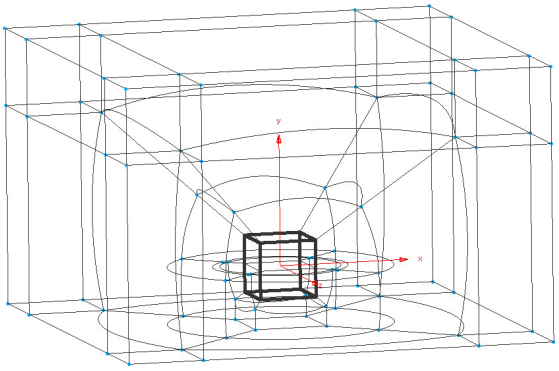

(b) Mesh topology

Figure 4.18: Illustrations of the mesh for the $h = L/2$

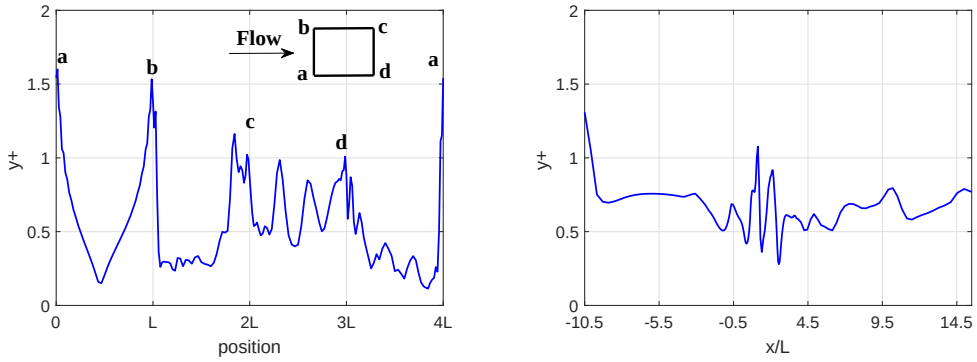

(a) y_1^+ around the cube

(b) y_1^+ along the ground

Figure 4.19: The distribution of y_1^+ along solid walls in the $z = 0$ plane for $h = L/2$

4.2.2 Aerodynamic coefficients

Time histories of the drag, lift and side-force coefficients (C_d, C_l and C_s) are illustrated in Figure 4.20 for selected elevation heights from a normalized time $t^* = tU_\infty/L = 450$ to $t^* = 650$. Compared with the wall-mounted cube ($h = 0$), the mean lift coefficient (red lines) drops quickly once the cube is elevated, while the fluctuation of the side-force coefficient (the green line) is suppressed. The changes in drag are small. The mean and rms values of these aerodynamic coefficients, calculated from $t^* = 450$ to $t^* = 1500$ for each elevation height, are summarised in Table 4.3.

h	N_{grid}	$\overline{C}_d$	$\overline{C}_l$	$\overline{C}_s$	$C_{d,\text{rms}}$	$C_{l,\text{rms}}$	$C_{s,\text{rms}}$
0	1,799,092	1.213	0.5877	0.0008	0.0357	0.0477	0.1128
$L/12$	1,979,016	1.205	-0.1107	0.0014	0.0301	0.0508	0.0994
$L/6$	1,929,036	1.139	-0.0806	-0.0007	0.0364	0.0593	0.0774
$L/5$	1,984,002	1.130	-0.0742	-0.0013	0.0345	0.0567	0.0716
$L/4$	2,038,968	1.159	-0.0565	0.0035	0.0335	0.0649	0.0762
$L/3$	2,087,486	1.139	-0.0483	0.0018	0.0330	0.0698	0.0751
$L/2$	2,229,714	1.147	-0.0320	0.0018	0.0372	0.0811	0.0828
$3L/4$	2,374,956	1.161	-0.0179	0.0012	0.0347	0.0890	0.0779
L	2,407,232	1.156	-0.0106	0.0011	0.0327	0.0842	0.0843
∞	1,702,660	1.134	0.0001	0	0.0288	0.0713	0.0712

Table 4.3: The effect of ground proximity on the cube at $Re = 5 \times 10^4$

To visualize the trends of C_d, C_l and C_s with the elevation height h, the mean values from Table 4.3 are plotted in Figure 4.21(a) and the rms values in Figure 4.21(b).

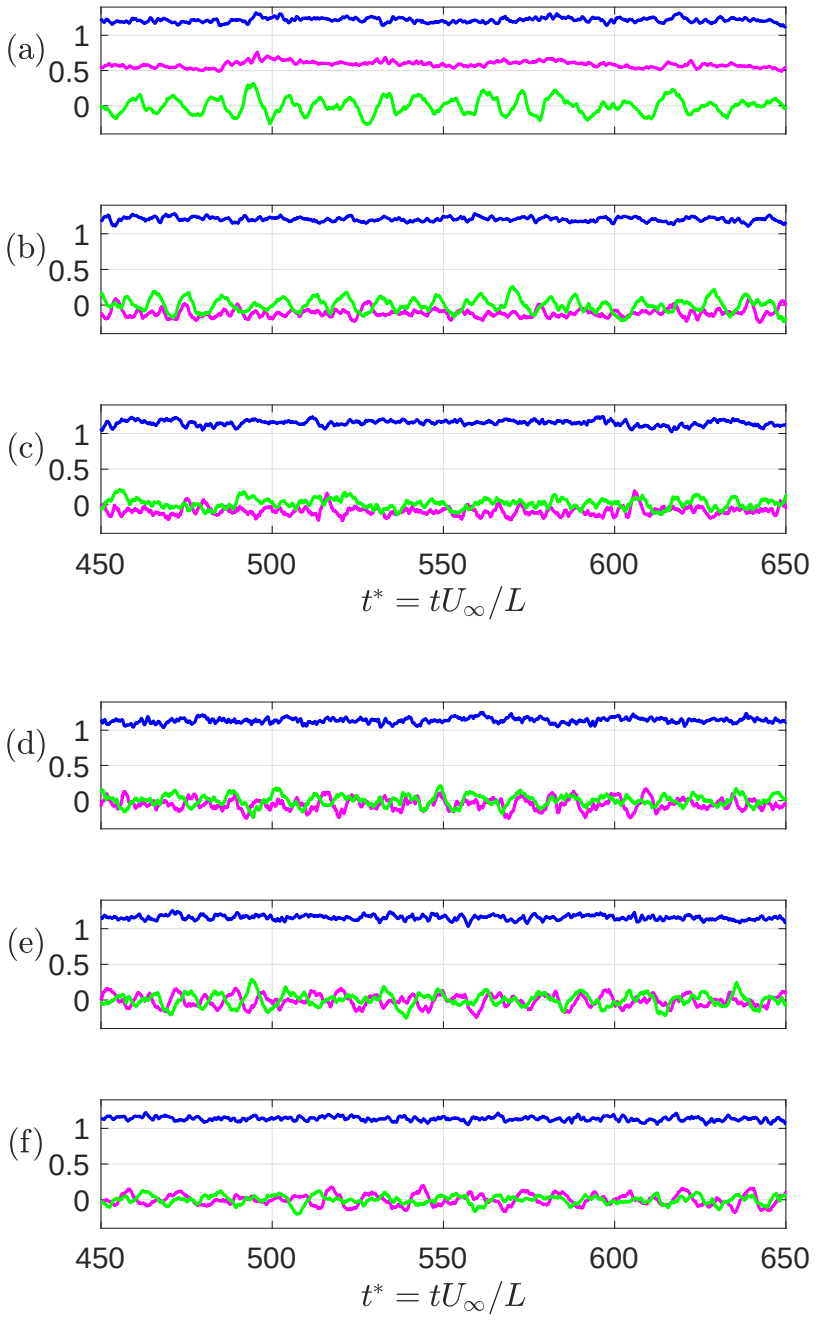

Figure 4.20: Time histories of C_d (blue), C_l (red) and C_s (green) for different elevation heights (h) plotted against normalized time $t^\star$. From (a) to (f), $h = 0$, $L/12$, $L/6$, $L/3$, L, ∞, respectively

Dashed lines are used to link statistics from $h = 0$ to $L/12$, since values in between are not investigated in this thesis. The mean lift coefficient drops significantly from $\overline{C}_l = 0.59$ at $h = 0$ to $\overline{C}_l = -0.11$ for $h = L/12$; with further increases of h, the lift coefficient recovers gradually and approaches zero in free space (at infinite h). The effect of wall proximity on the mean drag coefficient $\overline{C}_d$ is quite limited with values remaining around 1.2. The mean side force coefficient $\overline{C}_s$ retains a value of zero throughout due

to symmetry. For comparison, a measured value of $\overline{C}_d$ of 1.17 was found for a cube supported by a T-strut at a Reynolds number of 1.7×10^5 by Nakaguchi (1978). Raul and Bernard (1991) also found a value of 1.17 for the drag coefficient for a cube in free space at $Re = 1.4 \times 10^4$ based on numerical simulations. Anderson (1977) reported $\overline{C}_d = 1.09$ for the cube flow at a Reynolds number of 3×10^5. The predicted value of $\overline{C}_d$ for a cube at a Reynolds number near 5×10^4 was found to be about 1.4 using explicit equations developed by Haider and Levenspiel (1989).

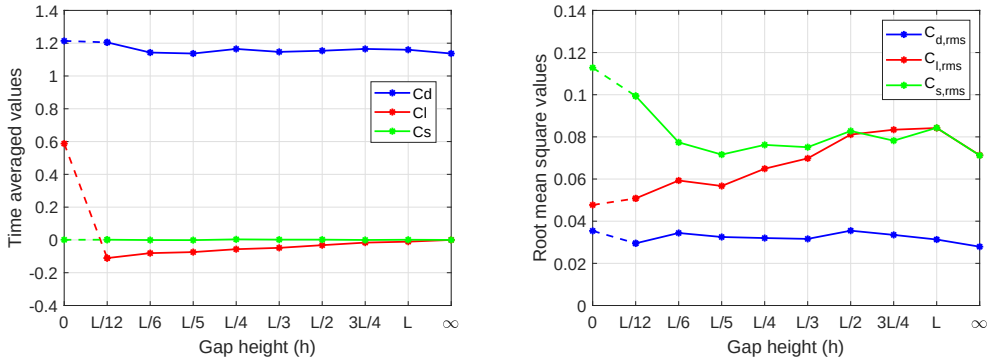

(a) (b)

Figure 4.21: Mean (a) and rms (b) values of C_d, C_l, C_s for different elevation heights (h)

The rms values of these aerodynamic coefficients reflect oscillations of the overall force acting on cube surfaces, which are instructive in evaluating the dipole sources for far-field noise prediction. As shown in Figure 4.21(b), the fluctuation of C_d is always the smallest and is less affected by the variation of h than that for C_l and C_s. The rms value of C_l increases from $h = 0$ to $h = L$, and then drops slightly from $h = L$ to $h = \infty$. The rms value of C_s reduces first when the wall-mounted cube is lifted to $h = L/5$; for larger values of h it remains around 0.075. In addition, when the cube is close to the ground ($h \leq L/3$), $C_{s,\mathrm{rms}}$ is greater than $C_{l,\mathrm{rms}}$ due to flow structures near the ground along the cube side surfaces, which will be analysed in more detail in Section 4.2.4. For the elevation heights larger than $L/2$, the rms values of the lift and side-force coefficients are very close to each other, indicating that the limiting effect of the ground is diminishing. All these variations of the aerodynamic coefficients are closely linked with the flow behaviour, which will be discussed in Section 4.2.3 and 4.2.4.

The Power Spectral Densities (PSD) of the drag, lift and side-force coefficients for $h = 0$, $L/12$, $L/6$, $L/3$, L and ∞ are presented in Figure 4.22 to illustrate the trend with respect to the variation of elevation height. These PSDs are obtained using Welch's method with a 50% overlapping Hanning window. The frequency resolution is about 3 Hz ($St = fL/U_\infty = 0.0144$). Since the spectra drop rapidly at frequencies higher than $St = 1$, Figure 4.22 only shows the range up to $St = 10$. The shapes of the spectra for C_d, shown in Figure 4.22(a), are all similar and there are no evident peaks. In contrast,

broadband peaks centred about $St = 0.1$ can be seen in the spectra of C_l (Figure 4.22(b)) and C_s (Figure 4.22(c)), which reflect a weak periodic vortex shedding.

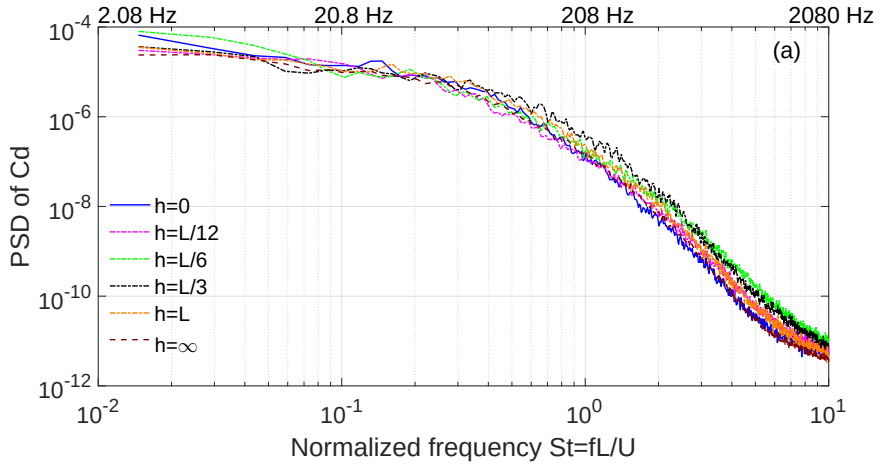

(a)

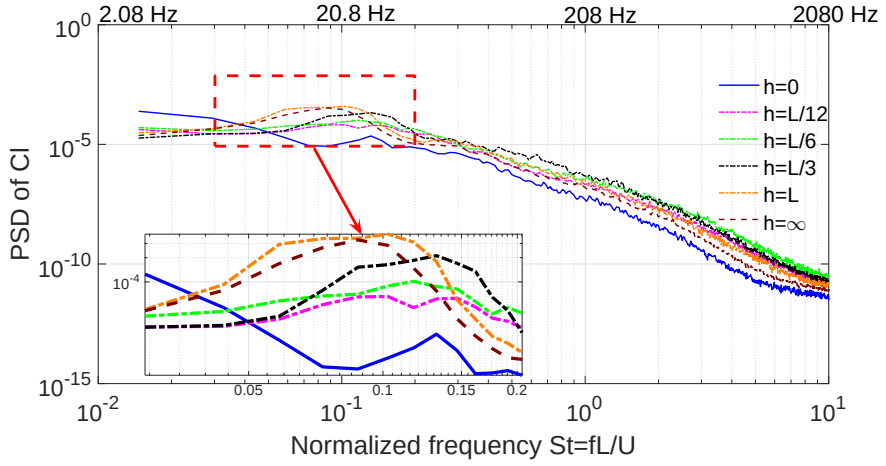

(b)

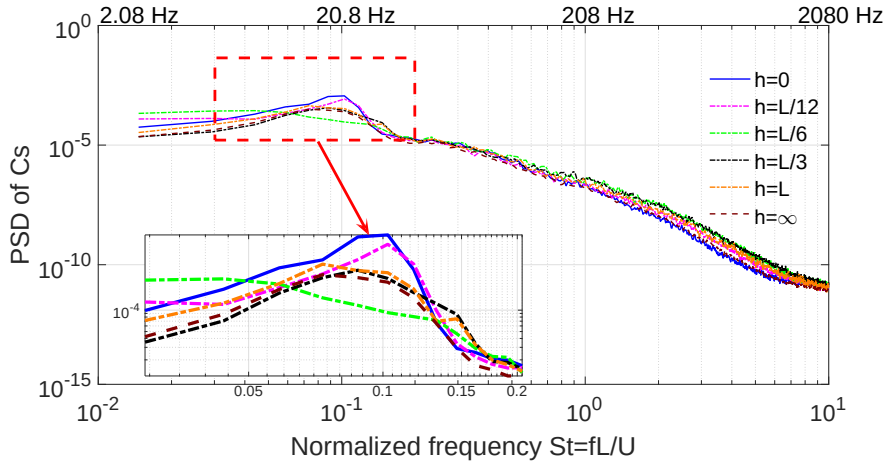

(c)

Figure 4.22: PSDs of (a) C_d, (b) C_l and (c) C_s for different elevation heights

Compared with the narrow high amplitude peak centred near $St = 0.13$ for a square cylinder (Norberg, 1993), the intensity of the periodic vortex shedding induced by the cube is much weaker due to the more three-dimensional flow interactions. As shown in Figure 4.22(b), the periodic flow behaviour in the lift direction keeps evolving with the increase of the elevation height. The central frequency of these broadband peaks for the lift coefficient reduces slightly with the increase of the elevation height h, while their amplitude increases gradually as the cube is elevated from 0 to L but drops slightly for the free space case ($h = \infty$). The most evident peak in the spectra of C_s displayed in Figure 4.22(c) is found in the wall-mounted case. However, this broad peak is suppressed as the cube is lifted to $h = L/6$ due to the flow evolution beneath the cube. With the further increase of h, the broad peak for the side-force coefficient appears again. In addition, the broadband peak in the side-force coefficient appears at a similar frequency for different values of h.

In summary, the effect of wall proximity on the drag coefficient of the cube is less significant than that on the lift and side-force coefficients. Once the wall-mounted cube is elevated from the ground, the mean lift coefficient drops to a negative value and with the increase of the gap size (h), it grows gradually back to zero. In general, the rms drag coefficient is the smallest and does not vary much with the elevation height. The rms values of the side force coefficient $C_{s,\mathrm{rms}}$ drop with increased gap sizes whereas $C_{l,\mathrm{rms}}$ increases. The rms values of the lift and side-force coefficients become similar when the elevation height exceeds $L/2$. The spectra of these aerodynamic coefficients tend to be broadband, although broad peaks centred about $St = 0.1$ can be seen for C_l and C_s. With the increase of the elevation heights, the broadband peak in the cross-flow direction evolves gradually. However, the peak in the spanwise direction is suppressed at $h = L/6$.

4.2.3 Flow topology around the cube

To analyse the effect of the elevation height on the flow pattern, mean streamlines in the $z = 0$ plane are shown in Figure 4.23 for representative elevation heights. These are plotted together with contours of the mean pressure coefficient. The white thick solid lines represent locations where the streamwise velocity is zero. The flow patterns at elevation heights of $L/5$ and $L/4$ are similar to that for the case at $h = L/6$, therefore are not shown here. In addition, main features of the flow around the cube are similar for elevation heights $L/3$, $L/2$ and $3L/4$.

As can be seen from Figure 4.23(a), the flow separates at the leading edge of the wall-mounted cube and no flow reattachment can be observed on the top surface. Instead, the flow reattaches directly to the ground at the position marked as 'RP' in the wake of the cube and a small secondary vortex is formed near the trailing edge of the top surface. Vortices upstream of the cube, marked 'A' and 'B' in Figure 4.23(a), are footprints of the

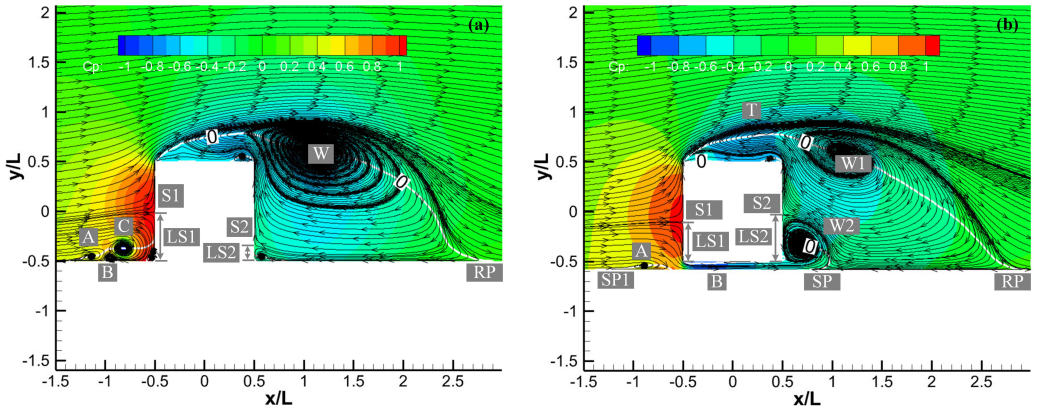

(a) $h = 0$

(b) $h = L/12$

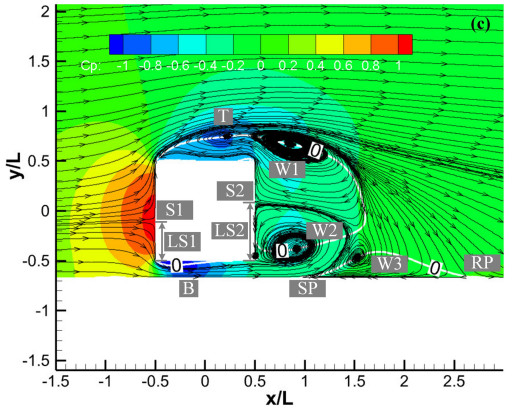

(c) $h = L/6$

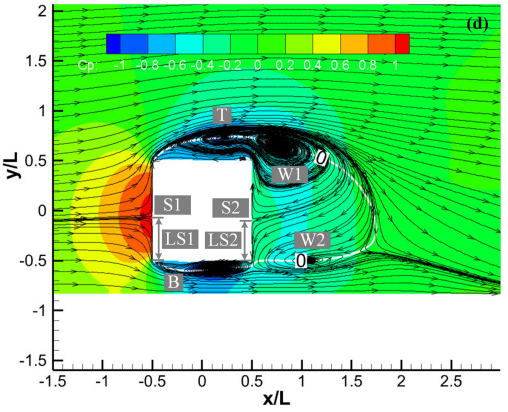

(d) $h = L/3$

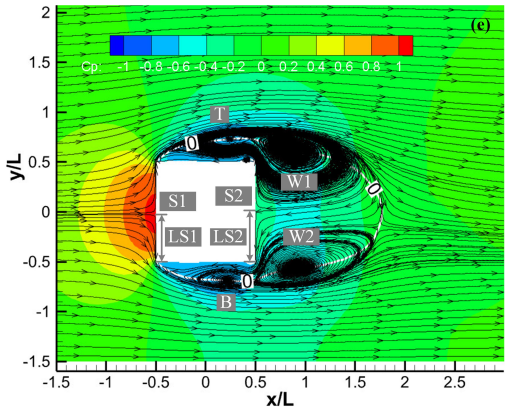

(e) $h = L$

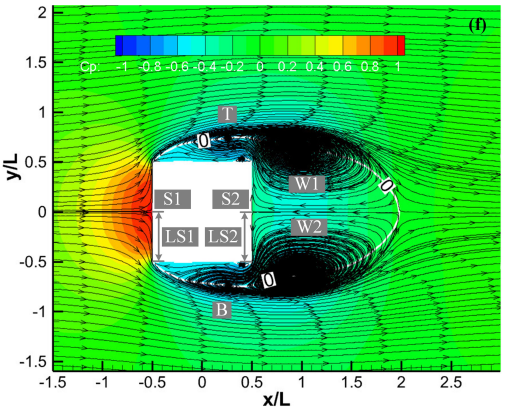

(f) $h = \infty$

Figure 4.23: Time-averaged pressure distribution contour together with mean streamlines in the $z = 0$ plane for $h = 0$, $L/12$, $L/6$, $L/3$, L, and in free space ($h = \infty$)

transcritical bifurcation discussed in Section 4.1.5, while the larger vortex marked 'C' is the horseshoe vortex. The flow spreads from the stagnation point marked 'S1' on the front surface and the distance from 'S1' to the ground ('LS1') is about $0.49L$. However, the stagnation point on the rear surface marked 'S2', is much closer to the ground with a distance of $LS2 = 0.15L$. One large vortex marked 'W', rotating clockwise, can be seen

in the recirculation region downstream of the cube in Figure 4.23(a), with a small vortex at the corner between the cube rear surface and the ground, rotating anti-clockwise.

As the cube is elevated, the flow topology changes with the elevation height, as shown in Figure 4.23(b) to Figure 4.23(f). The flow separation and the trace of the horseshoe vortex upstream of the wall-mounted cube can only be observed for the elevation height of $L/12$; these are indicated by 'SP1' and the vortex 'A' in Figure 4.23(b). With further increase of the elevated height, the flow remains attached to the ground upstream of the cube and the horseshoe vortex in front of the cube disappears. For all cases, the flow separates at the leading edge of the top surface; the separated flow forms a shear layer and recirculation regions. The recirculation regions formed above the cube, marked 'T' in Figure 4.23, are similar for different elevated heights and the flow does not reattach to the top surface. In contrast, the vortex beneath the cube marked 'B' in Figure 4.23 keeps evolving with the increase of h; especially for the cube in free space, the vortex 'B' becomes symmetric with respect to the vortex 'T'. Apart from the cube in free space, the flow structures downstream of the cube are all asymmetric, with the upper vortex dominant due to the constrained evolution of the vortex 'B' between the cube and the ground.

Flow separation on the ground downstream of the cube can be observed for $h = L/12$ to $L/4$ at the positions labelled 'SP' in Figure 4.23; with the increase of the elevation height, 'SP' moves further downstream. At the elevation height of $h = L/12$ in Figure 4.23(b), the separated flow along the ground reattaches to the rear surface of the cube. The flow through the gap between the bottom of the cube and the ground breaks the large eddy 'W' formed in the wake of the wall-mounted cube shown in Figure 4.23(a), causing an additional vortex marked 'W2' to be formed. In contrast, $h = L/6$, $L/5$ and $L/4$, the flow separated from the ground reattaches further downstream and three vortices are formed in the wake of the cube as illustrated in Figure 4.23(c), labelled as 'W1', 'W2' and 'W3', respectively. With the further increase of the elevation height, as shown in Figure 4.23(d) to Figure 4.23(f), flow separations and reattachments no longer occur on the ground. Two vortices marked 'W1' and 'W2' are formed in the wake of the cube for the elevation heights $h \geq L/3$.

To identify the flow behaviour in the gap between the cube and the ground more clearly, Figure 4.24 displays a close-up view of the region beneath the cube for the elevation heights of $L/12$, $L/6$, $L/5$ and $L/4$. As can be seen, the flow separating from the lower leading edge of the cube reattaches on the bottom surface for the first three cases. Particularly, for the elevation height of $h = L/5$, the flow reattaches at a location very close to the trailing edge of the bottom surface. For the elevation heights larger than $L/5$, the flow separated from the lower leading edge no longer reattaches to the bottom of the cube.

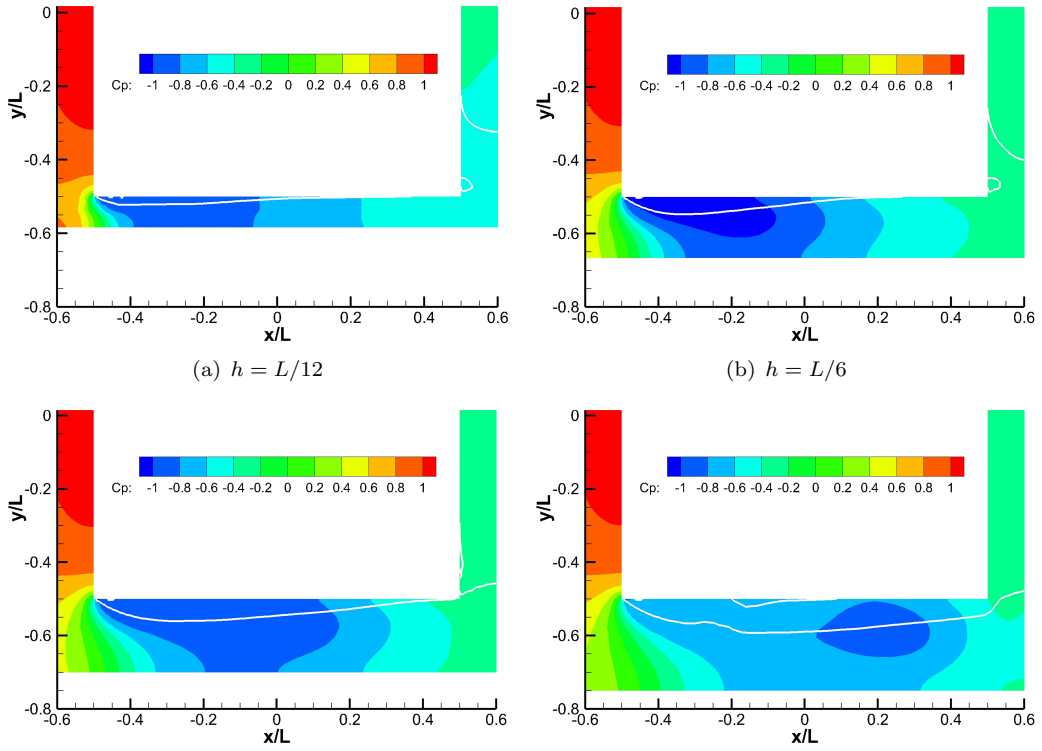

(a) $h = L/12$ (b) $h = L/6$

(c) $h = L/5$ (d) $h = L/4$

Figure 4.24: A close-up view of pressure distribution in the region beneath the cube in the $z = 0$ plane for $h = L/12$, $L/6$, $L/5$ and $L/4$

In summary, when the wall-mounted cube is gradually lifted from the ground, three features of the flow near the cube are mainly affected. The first is the separation position of the flow along the ground, which is related with the formation of the horseshoe vortex. As the cube is lifted, the position of flow separation on the ground moves downstream with the increase of the elevation height and vanishes for $L \geq L/3$. The second feature is the behaviour of the flow separated from the upper leading edge of the cube. It reattaches to the ground for $h = 0$ and $L/12$, but joins the flow coming through the gap when the cube is further elevated. The last feature is the flow separated from the cube lower leading edge in the gap, which reattaches to its bottom surface for elevation heights not greater than $L/5$, while there is no reattachment for larger values of h.

Mean stagnation points on both the front and rear surfaces are important indicators to characterize the flow pattern and also affect the distribution of surface pressure. The variation of stagnation points with respect to the elevation heights are shown in Figure 4.25. This shows $LS1/L$ and $LS2/L$, the relative heights from the bottom of the cube. The stagnation point on the front surface drops once the wall-mounted cube is lifted because of the intense negative pressure between the bottom surface of the cube and the ground. With the further increase of h, the front stagnation point gradually moves upward to $0.5L$, as observed for the cube in free space; this occurs due to the relief of the negative pressure region in the gap with the increased height. The stagnation

point on the rear surface moves up significantly when the cube is lifted from the ground to $h = L/6$, because the flow through the gap between the cube bottom and the ground facilitates the evolution of the second vortex 'W2' in the wake of the cube. However, the position of the rear stagnation point drops to around $0.5L$ when the cube is lifted from $h = L/6$ to $L/5$, and the separated flow in the gap reattaches close to the trailing edge of the bottom surface. After that, it recovers a little from $h = L/5$ to $L/4$ with the disappearance of the flow reattachment on the bottom surface. The flow topology for the case with $h = L/4$ is similar to that for $h = L/6$ as shown in Figure 4.23(c). As the elevation height increases from $L/4$ to $L/3$ the flow behind the cube no longer separates along the floor. With the disappearance of the vortex 'W3', the vortex 'W2' moves further downstream and closer to the ground. Consequently, the location of the stagnation point on the rear surface drops significantly from $h = L/4$ to $h = L/3$ in Figure 4.25. For larger values of h, it increases gradually and finally arrives at the middle of the rear surface for the cube in free space.

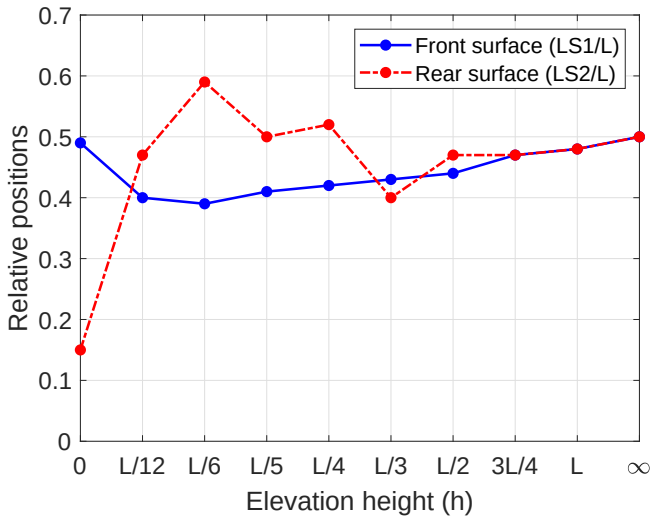

Figure 4.25: Variation of the front and rear stagnation position of the cube with the elevation height

4.2.4 Near-wall flow patterns

To depict a more comprehensive picture of the flow, Figure 4.26 illustrates mean streamlines in the $x - z$ plane close to the ground (at 0.5 mm, $0.008L$, above the ground) for representative elevation heights; these are coloured by the mean pressure coefficient. As the elevation height is reduced, the influence of the cube on the near-ground flow pattern becomes more evident. The streamlines are deflected showing more complex flow patterns. The footprint of the horseshoe vortex can only be seen in Figure 4.26(a) for an elevation height of $L/12$. The flow separation along the ground downstream of the cube can be detected for cases with elevation heights between $h = L/12$ and $h = L/4$ as

shown in Figure 4.26(b) for a representative case at $h = L/6$. The white line representing locations of zero streamwise velocity in Figure 4.26 indicates the separation location. These are consistent with flow features identified in the previous section (Section 4.2.3). In addition, at this position 0.5 mm above the ground, two foci in the wake of the cube can be seen in Figure 4.26(a) for $h = L/12$ indicating the arch vortex tube shown for the wall-mounted cube in Figure 4.11.

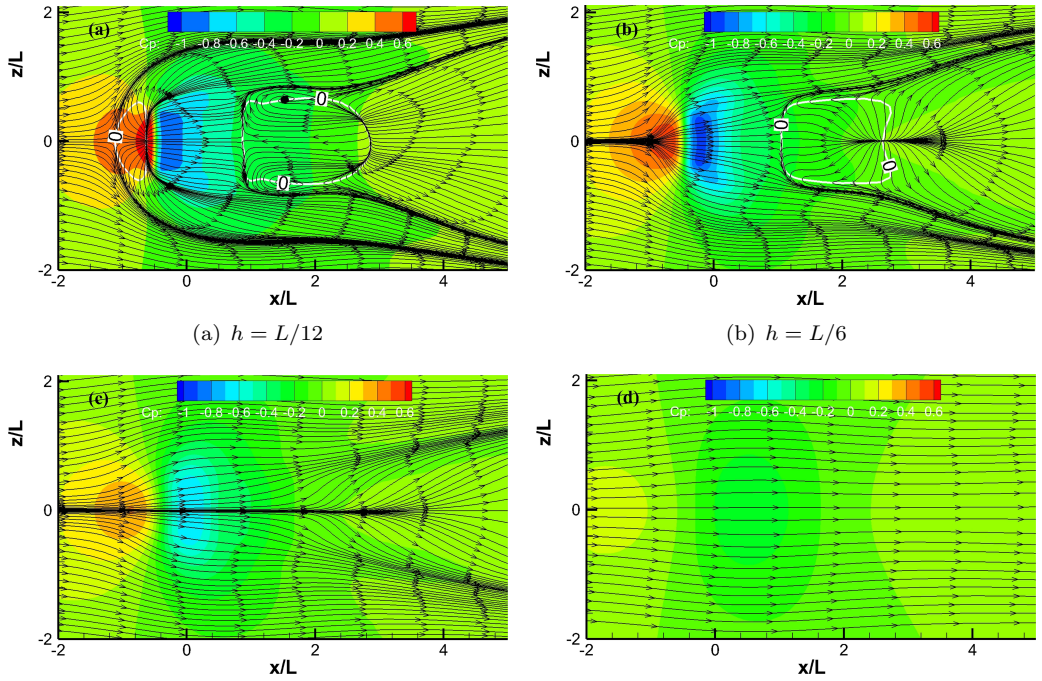

(a) $h = L/12$ (b) $h = L/6$

(c) $h = L/3$ (d) $h = L$

Figure 4.26: Time-averaged pressure distribution contour together with mean streamlines in the $x - z$ plane 0.5 mm above the ground for different elevation heights (h)

Similarly, to illustrate the effect of wall proximity on the flow structures close to the bottom of the cube, Figure 4.27 displays time-averaged streamlines in the $x - z$ plane (at 0.5 mm, $0.008L$, below the bottom of the cube) together with contours of the mean pressure coefficient for representative cases. The white lines in Figure 4.27 represent zero streamwise velocity while the red dashed lines indicate the position of the cube. The footprint of the flow reattachment on the bottom surface of the cube can be clearly seen in Figure 4.27(a) and Figure 4.27(b). This is implied by the region surrounded by the white line inside the red dashed square. Moreover, the increasing size of the affected region beneath the cube reflects the evolution of the vortex formed on the cube bottom surface (labelled as 'B' in Figure 4.23) with the increase of the gap between the cube and the ground. The Saddle points marked 'SW', together with the white lines in the cube wake shown in Figure 4.27(a) and Figure 4.27(b), are footprints of the vortex 'W1' in Figure 4.23(b) and the vortex 'W3' in Figure 4.23(c).

With the increase of the elevation height from $h = L/6$ to $L/2$ (some cases are not shown in Figure 4.27), the position of the Node 'N1' moves downstream gradually. For further increased elevation heights, the nodes on the cube bottom observed in Figure 4.27(b) and Figure 4.27(c) vanish while a Saddle (marked 'S2') appears in the wake as seen in Figure 4.27(d) and Figure 4.27(e). The Saddle 'S1' near the trailing edge of the cube bottom in Figure 4.27(d) and Figure 4.27(e) is formed due to the secondary vortex. The position of the Saddle 'S1' moves upstream with the increase of the elevation height, implying the evolution of the secondary vortex. Two foci (marked 'F1' and 'F2' respectively) emerge in Figure 4.27(d) and Figure 4.27(e), representing vortices in the wake on this plane. It is also worth noting that the flow separated from the leading edge no longer reattaches to the lateral surfaces of the cube for the elevation heights of $h = L$ and ∞ with two lateral vortices formed centred at foci 'F3' and 'F4'.

4.2.5 Mean pressure coefficients along the cube surfaces

Variations of the flow around the cube for different wall proximities as described above can also be reflected in the pressure on the cube surfaces. Distributions of the mean pressure coefficient C_p along the cube surfaces are shown in Figure 4.28 in the $z = 0$, $y = 0$ and $x = 0$ planes through the cube centre for representative elevation heights (h). Positive gauge pressure is only observed on the front surface, while the pressure on all other surfaces is negative due to the flow separation from the leading edges. This explains why the wall-mounted cube has a positive lift. The most significant differences in the pressure distributions for different elevation heights lie on the bottom surface, i.e. between $3L$ and $4L$ as illustrated in both Figure 4.28(a) and Figure 4.28(c).

The dip of the pressure at $4L$ in Figure 4.28(a) is due to the flow separation from the leading edge of the bottom surface. The position of the minimum pressure between $3L$ and $4L$ in Figure 4.28(a) reflects the location where the separation bubble 'B' beneath the cube, shown in Figure 4.23, evolves to its largest size under the cube bottom. In addition, it may be noted that the pressure distributions near $3L$ in Figure 4.28(a) for the elevation heights of $L/12$ and $L/6$ are much smoother than for larger elevation heights. The intense change of pressure near the trailing edge of the cube bottom (at $3L$ in Figure 4.28(a)) for elevation heights greater than $L/5$ can be explained by the disappearance of the flow reattachment on the cube bottom, as described in Section 4.2.3. This allows the flow in the wake of the cube to recirculate to the gap between the cube bottom and the floor, as indicated by the directions of the streamlines in Figure 4.23.

The pressure on the front (between 0 and L) and rear surfaces (between $2L$ and $3L$) in Figure 4.28(a) and Figure 4.28(b) tends to be less sensitive to the variation of h. In general, the shape between $3L$ and $4L$ in Figure 4.28(c) along the cube bottom is more curved when the cube is closer to the ground, implying stronger influence of the

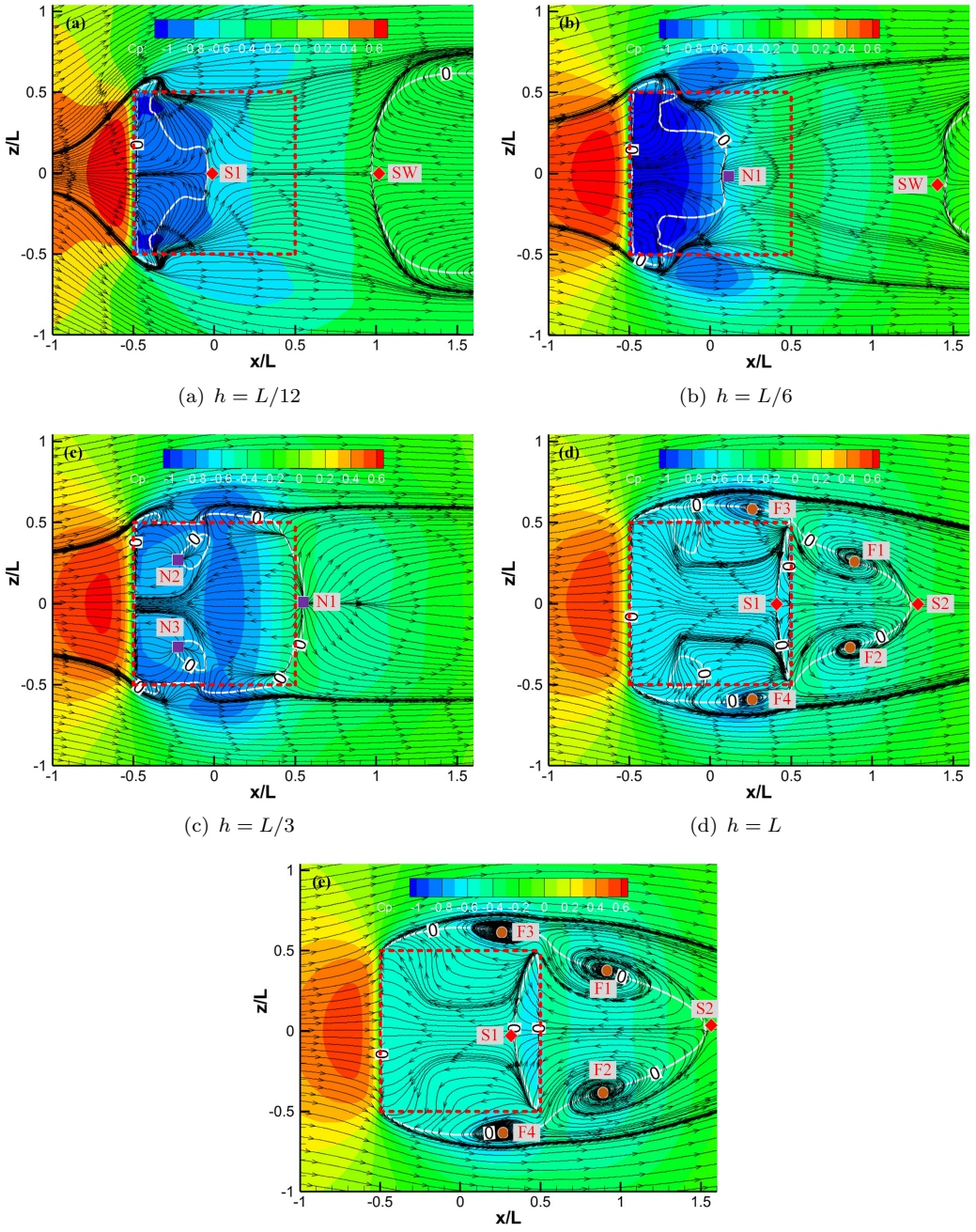

(a) $h = L/12$ (b) $h = L/6$

(c) $h = L/3$ (d) $h = L$

(e) $h = \infty$

Figure 4.27: Time-averaged pressure contours together with mean streamlines in the $x - z$ plane 0.5 mm below the bottom of the cube for different elevation heights (h) (square: Node, circle: Focus, diamond: Saddle)

wall proximity on the flow. However, the greatest variation of the surface pressure in Figure 4.28(c) is observed in the case $h = L/6$. This reveals the strongest interference between the flows separated from the leading edge of the cube bottom and lateral surfaces, which explains the suppressed broadband peak in Figure 4.22(c).

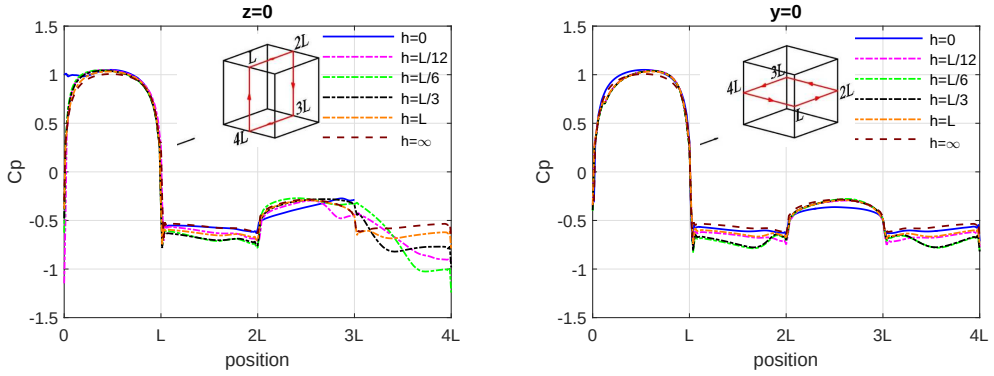

(a) In the $z = 0$ plane

(b) In the $y = 0$ plane

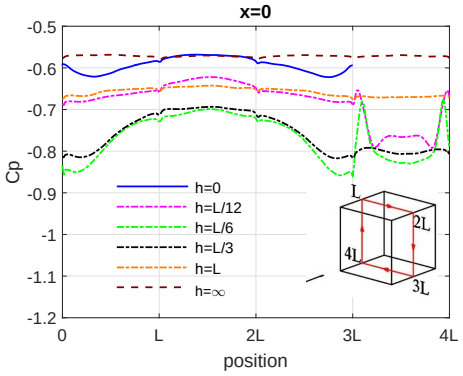

(c) In the $x = 0$ plane

Figure 4.28: The distribution of the pressure coefficient (C_p) for different elevation heights (h)

4.2.6 Turbulence kinetic energy around the cube

The turbulence kinetic energy (TKE) is defined as:

$$k = \frac{1}{2}\left(\overline{(u')^2} + \overline{(v')^2} + \overline{(w')^2}\right) \tag{4.10}$$

where u', v' and w' are the velocity fluctuations in the streamwise, cross-flow and spanwise directions respectively and the overbar indicates a time average. Contours of TKE in the $z = 0$ plane for each elevation height are displayed in Figure 4.29. As in previous figures, the white lines labelled with zero denote positions of zero mean streamwise velocity. The distribution of TKE reflects unsteady features of the flow, which are closely related to the fluctuating pressure on the cube surfaces, and in turn is instructive for the noise prediction. High TKE implies strong turbulent flow and consequently large surface pressure fluctuations. However, it is worth noting, the results displayed in Figure 4.29 are the combination of the predicted TKE in the RANS region and the resolved part of TKE using the LES mode. The part of the SGS TKE filtered out in the LES is not evaluated in this thesis.

As can be seen from Figure 4.29, high values of TKE can always be observed due to the shear layer formed by the flow separated from the leading edge of the top surface. For the purpose of reference, contours of the mean streamwise velocity (U/U_∞) are also shown in Figure 4.30. Although the mean streamwise velocity in the gap between the cube and the ground is very large for the elevation height of $L/12$, the limited space restricts unsteady flow developing, leading to low TKE in the gap as shown in Figure 4.29(b). With the increase of the elevation height, the TKE of the flow separated from the lower leading edge becomes more and more intense, while the maximum TKE on the top of the cube is only slightly affected. The TKE for all cases with wall proximity is higher than the free space case.

4.2.7 Pressure fluctuations on the cube surfaces

The wall pressure fluctuations, reflecting the strength of dipole sources, are important in predicting the far-field noise. However, no measurements on the pressure fluctuations of a cube are available in the literature. To strengthen confidence in the acquisition of wall pressure fluctuations from the adopted numerical methodology, another simulation on a square cylinder is conducted and the fluctuating pressure obtained numerically is compared with experimental results from Pocha (1971) and Vickery (1966). The width and height of the square cylinder are the same as the side length of the cube (L) in this work, while the length in the spanwise direction is $L_z = 6L$. Apart from the periodic boundary condition applied in the spanwise direction, the assigned boundary conditions for the square cylinder are the same with those for the cube in free space. The grid resolution along the cross-section of the square cylinder is the same as that for the cube cases, while the mesh in the spanwise direction is evenly distributed with a resolution of $0.067L$. The fluctuating pressure coefficient is defined as $C_p' = p_{\text{rms}}/(0.5\rho U_\infty^2)$, where p_{rms} is the root-mean-square value of the pressure fluctuation. Figure 4.31 shows the distribution of C_p' in the $z = 0$ plane on the cylinder surfaces calculated using DDES in this work, compared with the measurements reported by Pocha (1971) and Vickery (1966). Reasonable agreements of the wall pressure fluctuation between the numerical and experimental work have been achieved as can be seen in Figure 4.31. However, some discrepancies are observed near the rear corner of the cylinder, where it is more difficult to measure the fluctuating pressure.

Contours of the root-mean-square pressure fluctuations on the cube surfaces are shown in Figure 4.32. The pressure fluctuations are expressed in dB as:

$$L_p = 10\log\left(\frac{p_{\text{rms}}}{p_{\text{ref}}}\right)^2, \text{ where } p_{\text{ref}} = 2\times10^{-5}\,\text{Pa} \tag{4.11}$$

To display the distribution of pressure fluctuations on each cube surface, the cube is stretched out and an illustration of the stretched out view is displayed in Figure 4.32(a).

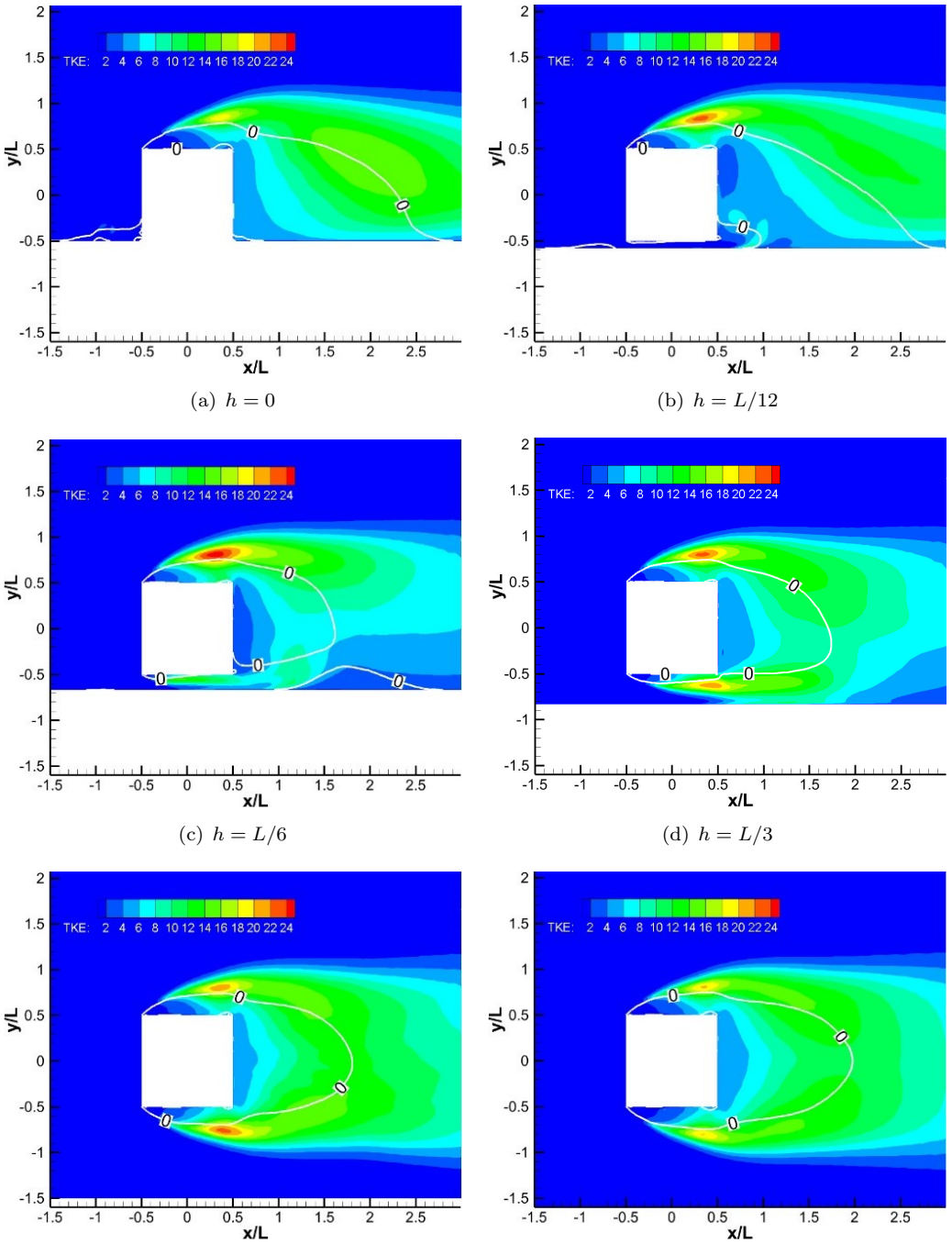

(a) $h = 0$ (b) $h = L/12$

(c) $h = L/6$ (d) $h = L/3$

(e) $h = L$ (f) $h = \infty$

Figure 4.29: Contours of the turbulence kinetic energy (TKE) for different elevation heights (h)

Since the rms pressures on the left and right cube surfaces are the same, only the right surface is displayed.

As shown in Figure 4.32, pressure fluctuations on the frontal surface caused by the impinging flow are always the lowest. In contrast, the highest fluctuations always occur near the top and side trailing edges, because the separated flow wraps around the cube

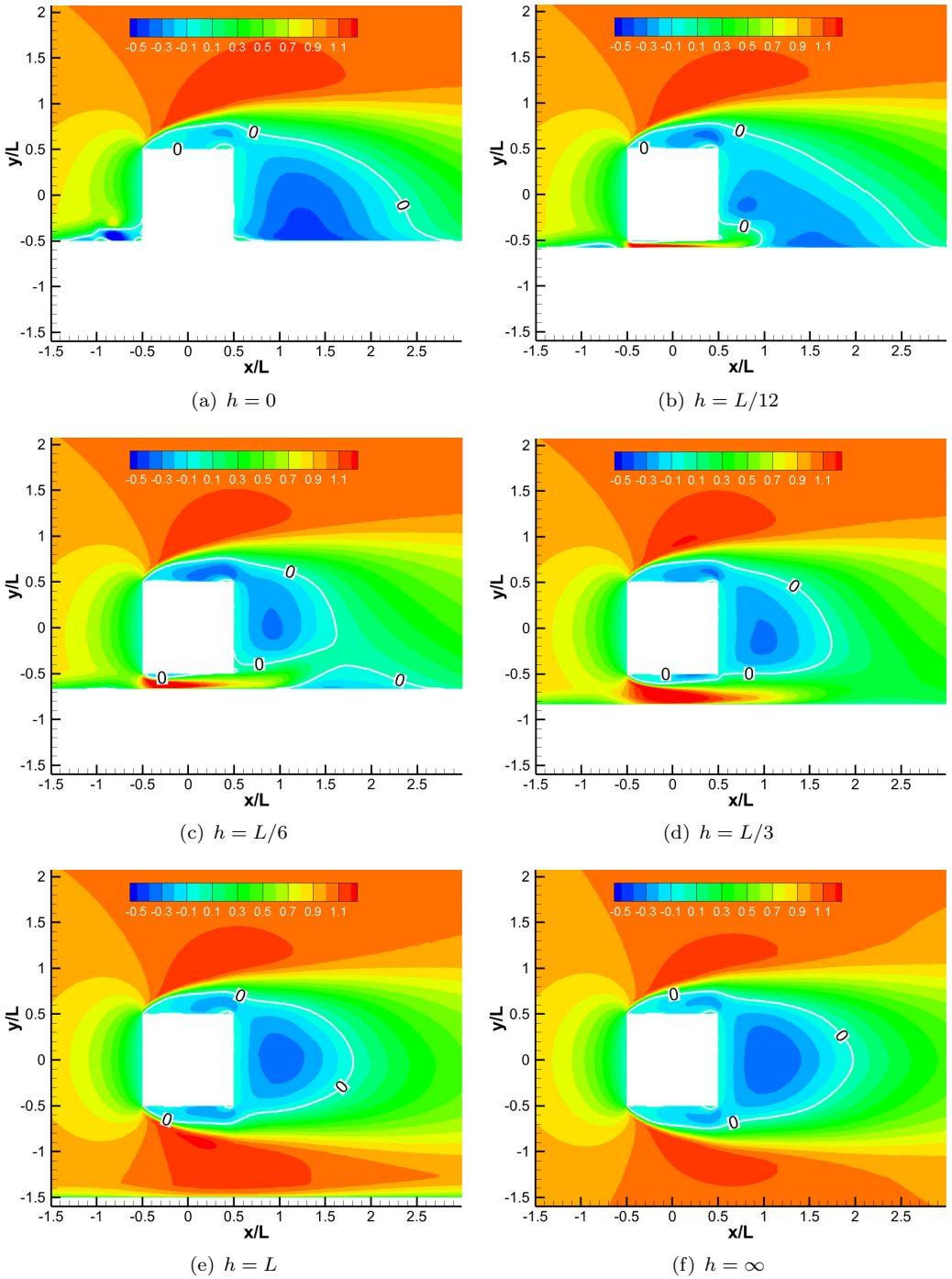

(a) $h = 0$ (b) $h = L/12$

(c) $h = L/6$ (d) $h = L/3$

(e) $h = L$ (f) $h = \infty$

Figure 4.30: Contours of the streamwise velocity (U/U_∞) for different elevation heights (h)

trailing edges to form the vortex in the wake ('W1' and 'W2' in Figure 4.23). In addition, the rms values of the fluctuation pressure induced by flow separations near the leading edges are about 15 dB lower than the maximum, which appears at the trailing edge.

The distribution of pressure fluctuations on the bottom surface is most sensitive to wall proximity. In the case of $h = L/12$, the cube is very close to the ground and there is

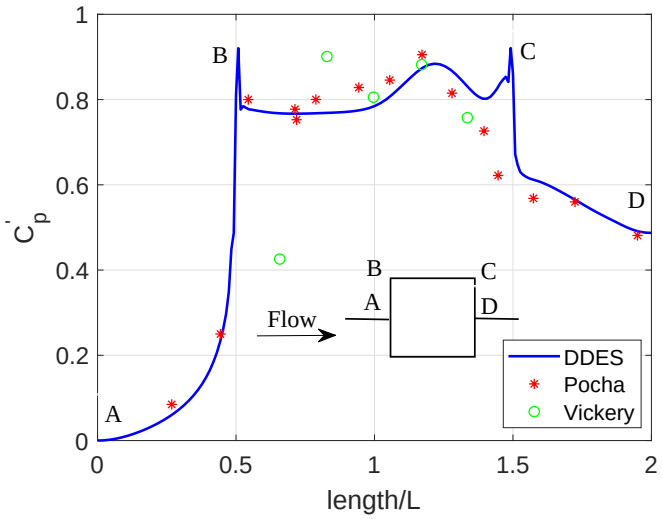

Figure 4.31: Comparison of the pressure fluctuation (C_p') on the square cylinder between the simulation and the experimental results from Pocha (1971) and Vickery (1966)

limited flow separation from the lower leading edge. However, the separated flow near the side surfaces moves beneath the cube due to the negative pressure there, leading to the high pressure fluctuations near the lower side edges seen in Figure 4.32(c). With the increase of the elevation height, the separated flow from the lower leading edge reattaches to the cube bottom in the cases $h = L/6$ and $L/5$ causing high pressure fluctuations on the cube bottom surface as illustrated in Figure 4.32(d). For $h \geq L/4$, instead of reattaching to the bottom of the cube, the flow separated from the lower leading edge wraps around the trailing edges to the wake. With the increase of the elevation height, the high pressure fluctuation region moves downstream towards the lower trailing edge as the vortex 'B' in Figure 4.23 grows. Due to the growing size of vortex 'B', the magnitude of L_p on the cube bottom reduces slightly. In summary, the wrapping behaviour of the flow near the cube trailing edges, including the flow reattachment, has the greatest effect on the pressure fluctuations on the cube surfaces. The magnitude of the pressure fluctuations is related to the vortex size.

The pressure fluctuations on the ground decay rapidly with the increase of the gap height as illustrated in Figure 4.33. For the wall-mounted case, highest pressure fluctuations on the ground is caused by the arch vortex in the wake of the cube. The horseshoe vortex upstream of the cube introduces moderate pressure fluctuations on the ground, as shown in Figure 4.33(a). When the cube is lifted, the pressure fluctuations on the ground are mainly due to flow separation on cube bottom surface. Further increasing h, p_{rms} reduces rapidly.

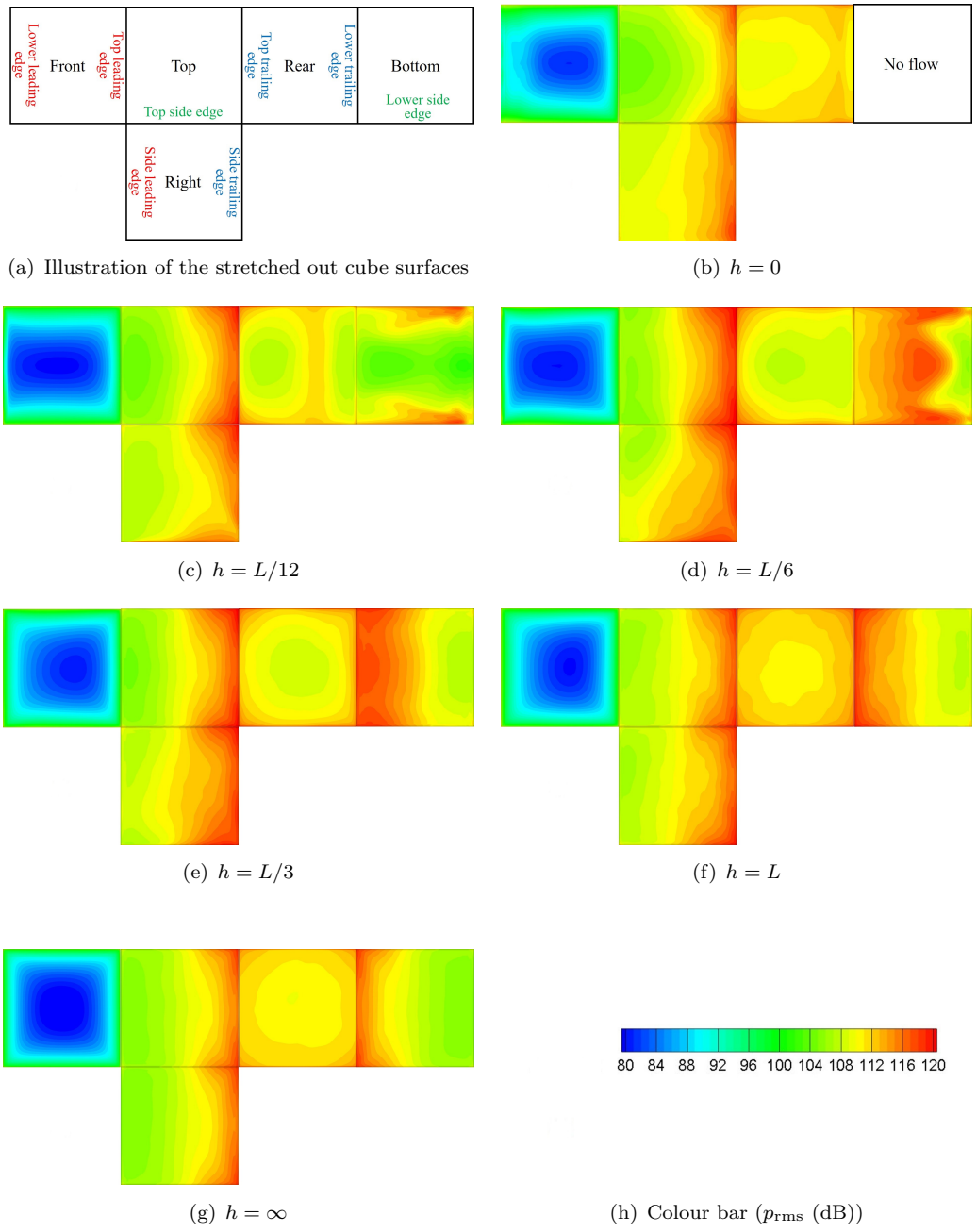

(a) Illustration of the stretched out cube surfaces

(b) $h = 0$

(c) $h = L/12$

(d) $h = L/6$

(e) $h = L/3$

(f) $h = L$

(g) $h = \infty$

(h) Colour bar (p_{rms} (dB))

Figure 4.32: Contours of the pressure fluctuations on the cube surfaces

4.3 The effect of wall proximity on the radiated noise

At low Mach numbers, quadrupole sources induced by the turbulent flow are much less significant than dipole sources due to the fluctuating pressure on solid surfaces (Curle, 1955). Since the Mach number studied in the current work is about 0.037, which is very low, only dipole sources are taken into account.

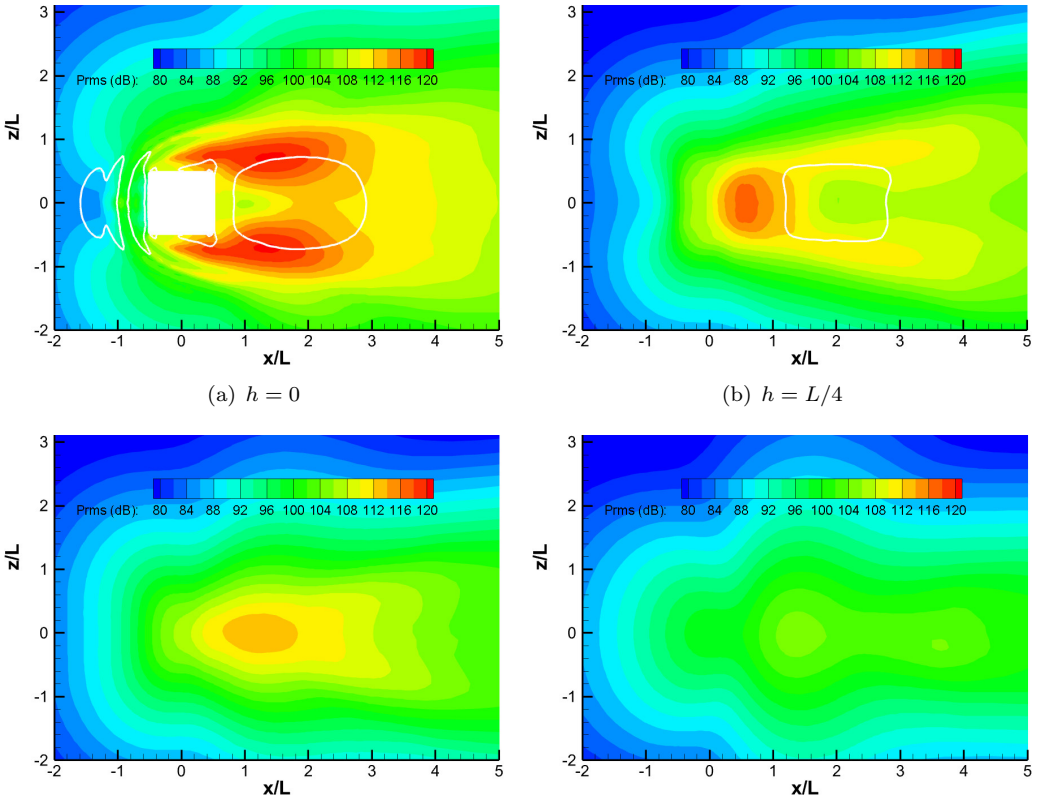

(a) $h = 0$ (b) $h = L/4$

(c) $h = L/2$ (d) $h = L$

Figure 4.33: Contours of the pressure fluctuations on the ground

4.3.1 Noise from a square cylinder

Due to the scarcity of the available acoustic measurements on cubes in the literature, the emitted noise from the square cylinder described in Section 4.2.7 is firstly predicted and compared with measured data of Liu et al. (2018) to evaluate the feasibility of the adopted method in noise prediction. The fluctuating pressure on the cylinder surfaces is obtained from the CFD simulation and the noise propagating to the far field from the cylinder is then predicted using the FW-H analogy. For the purpose of comparison, the noise predicted from the square cylinder in this work is corrected for differences in the flow speed, section area and receiver distance to be equivalent to those in the measurements (Liu et al., 2018). According to Curle (1955), the mean square acoustic pressure ($\overline{p(x)^2}$) generated by sources of fluctuating pressure on solid boundaries is proportional to the section area of the object (L^2), the sixth power of the flow speed (U_∞^6) and $1/r^2$, where r is the distance from the receiver to the noise source, as shown in follows:

$$\overline{p(x)^2} = \frac{\rho_0^2 U_\infty^6 St^2 C_{l,\mathrm{rms}}^2 L^2}{16 c_0^2 r^2} \tag{4.12}$$

In Equation (4.12), the rms values of the lift coefficient ($C_{l,\mathrm{rms}}$) is used to predict the far-field noise, which is applicable for compact sources only.

The PSDs of the emitted noise obtained from both the numerical and the experimental work are presented in Figure 4.34(a), at a receiver 1.18 m away from the square cylinder in the cross-flow direction (y-axis) at a flow speed of 20 m/s. The overall sound pressure level (OASPL) for the square cylinder is calculated by integrating the PSDs over the range of Strouhal numbers from 0.07 to 2. The ΔOASPL denotes the difference of the OASPL at different receivers relative to that in the cross-flow direction, namely, $\theta = 90°$, where θ is the radiation angle. The sound directivity for the square cylinder is shown in Figure 4.34(b) and is compared with the measured data (Liu et al., 2018). The symbols in Figure 4.34(b) represent receivers at different locations. As can be seen, the predicted noise agrees quite well with the measurements. Especially, for the OASPL, most of the discrepancies are within 1 dB.

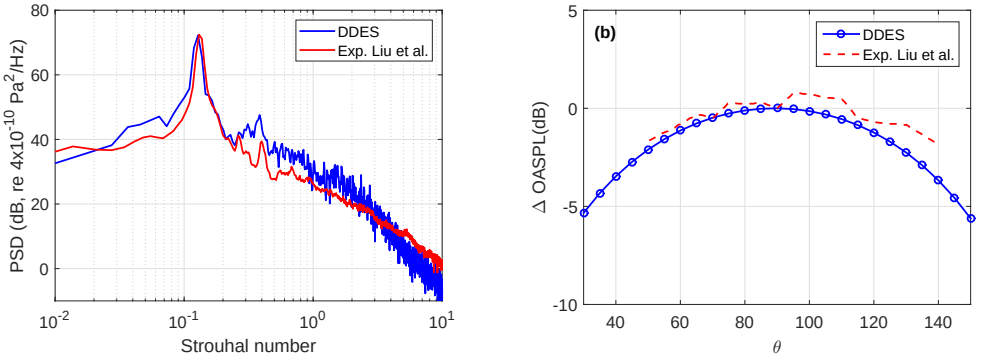

Figure 4.34: Comparison of the predicted noise from a square cylinder between the simulation and the experimental results from Liu et al. (2018), (a) noise spectra in the cross-flow direction and (b) OASPL as a function of radiation angles

4.3.2 Noise from the elevated cube

As shown in Figure 4.32, high pressure fluctuations on the cube are mainly concentrated near the trailing edges. It is assumed that the whole cube is acoustically compact, which leads to more efficient far-field noise prediction. Although the ground is a legitimate part of the boundary, in the present study only the noise induced by pressure fluctuations on the cube surfaces is considered. The cube surfaces are therefore chosen as the FW-H surface. In addition, to evaluate the noise reflected from the ground, the cube is mirrored with respect to the floor as an extra analogous source (Fahy and Thompson, 2016). The use of the free-field half-space Green's function automatically satisfies the Sommerfeld radiation condition.

The noise spectra at receivers 10 m ($167L$) away from the cube centre along the x, y, and z axes, as illustrated in Figure 4.35, for representative elevation heights are shown as examples in Figure 4.36. Broadband peaks can be recognized at around 20 Hz ($St = fL/U_\infty = 0.1$) in the results for the lateral (z-axis) and vertical (y-axis) directions in Figures 4.36(b) and 4.36(c) respectively. However, no evident peak can be seen in Figure 4.36(a) which shows the noise for a receiver in the streamwise (x) direction. These features observed from the noise spectra are consistent with the spectra of C_d, C_l and C_s shown in Figure 4.22. The frequency of the broadband peak in the noise spectra tends to be insensitive to the variation of the wall proximity. However, it can be noted that when $h = L/6$, the broadband peak in the lateral (z) direction is suppressed, similar to the spectrum of C_s. With further increase of the elevation height, the broadband peak observed at the receiver (0, 0, 10) appears again. In all cases the spectra fall at high frequencies, above approximately $St = 1 \sim 2$.

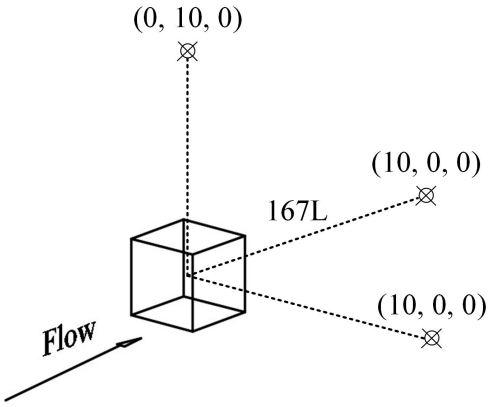

Figure 4.35: An illustration of the receiver locations

The OASPL is obtained by integrating the PSD over the frequency range up to a Strouhal number of 10 (2000 Hz) for the above described receivers at each elevation height; the results are shown in Figure 4.37. For an acoustic point source near a rigid wall at low frequencies, if the distance between the original source and the image source is small compared with the acoustic wavelength, the combined source region can be treated as compact (Fahy and Thompson, 2016). The sound pressure at the receiver position is approximately doubled due to the presence of the wall, leading to an increase of sound pressure level by 6 dB. The effect on the predicted noise of including the ground reflection for each elevation height has been evaluated and found to be very close to 6 dB in all three directions, with a maximum difference of less than 0.1 dB. Therefore, the compact assumption in this work is valid up to 2000 Hz. In Figure 4.37, the open symbols linked with dashed lines for the free space case denote the predicted noise increased by 6 dB to mimic the noise reflected from the ground in the other cases for the purpose of comparison.

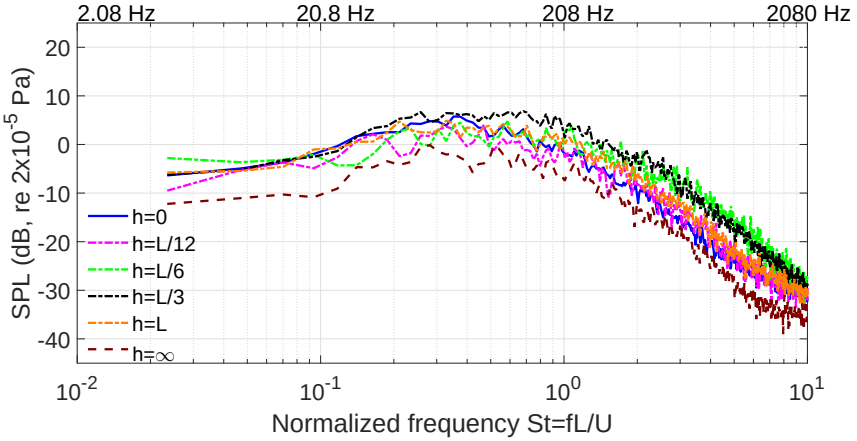

(a) Streamwise direction (10, 0, 0)

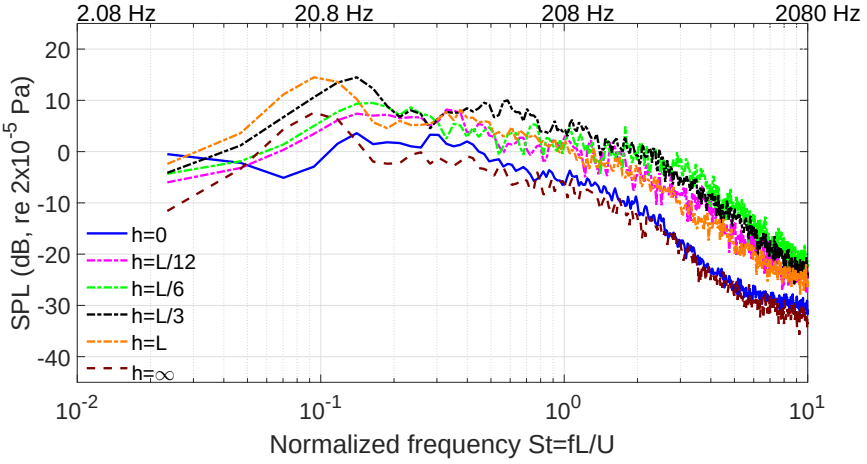

(b) Vertical direction (0, 10, 0)

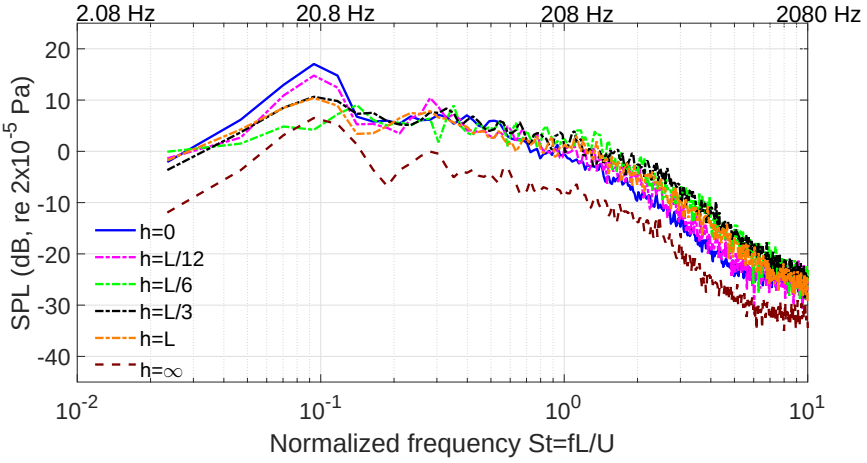

(c) Lateral direction (0, 0, 10)

Figure 4.36: The predicted noise spectra for different elevation heights (frequency resolution: $\Delta f = 1.22$ Hz)

As shown in Figure 4.37, in general, the sound pressure level (SPL) in the streamwise direction (x-axis) is smaller than that in the vertical (y-axis) and the lateral (z-axis)

directions for elevated cases ($h > 0$). The highest sound level in the vertical direction occurs for $h = L/4$, and the noise level in the streamwise direction also reaches its maximum value for this case. The noise in the vertical direction for $h = 0$ is lower than all the other cases. However, the radiated noise in the lateral direction is the largest for the wall-mounted cube. The sound variation in the streamwise and the lateral directions for different elevation heights is smaller than 5 dB, while that in the vertical direction observed at the receiver (0, 10, 0) is about 10 dB.

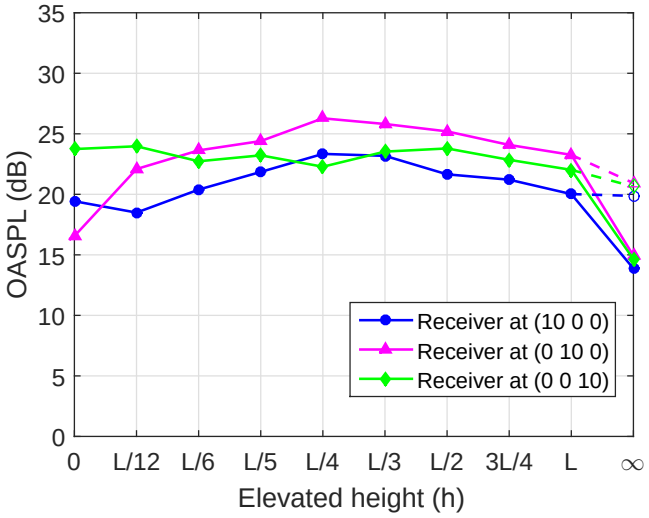

Figure 4.37: The predicted OASPL for different elevation heights (h)

To evaluate the contribution of the noise from the broadband peak in the vertical and the lateral directions, the solid lines in Figure 4.38 again denote the overall sound up to a Strouhal number of 10 (2000 Hz) while the dashed lines show the sound from the broadband peak integrated over the frequency range from $St = 0.05$ (10 Hz) to $St = 0.2$ (42 Hz). In each case, the noise from the cube in free space is again compensated by 6 dB to allow direct comparison with the other cases. As can be seen from Figure 4.38, the broadband peak makes a significant contribution to the far-field noise, although for most cases it is more than 3 dB lower than the overall level.

Comparing the overall sound and the noise caused by the broadband peak at the vertical receiver (0, 10, 0), for the elevation heights from $L/12$ to $L/4$, the dashed line is about 8.5 dB lower than the solid one. As described in Section 4.2.3, when the cube is lifted from $h = L/4$ to $L/3$, the flow separation along the ground disappears. Further increasing h, with the development of the vortex 'B' in the gap between the cube bottom and the ground shown in Figure 4.23, the noise at frequencies higher than $St = 0.2$ starts to drop. In the lateral direction, the periodic flow behaviour is suppressed when the cube is lifted from $h = L/12$ to $L/6$, and consequently, the OASPL observed at (0, 0, 10) drops.

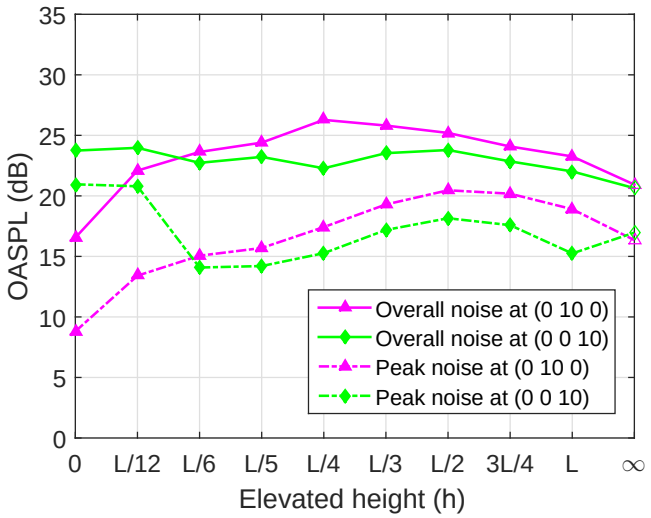

Figure 4.38: The overall noise and the noise from the broadband peak for different elevation heights (h)

Figure 4.39 shows the sound directivities in the $x-z$ plane ($y=0$) and the $x-y$ plane ($z=0$) for the cube with different wall proximities. The sound directivity is obtained from the predicted OASPLs at different receives, 10 m (167 L) away from the cube centre. There are 37 receivers set in the $z=0$ plane from 0° to 180° with an increase space of 5° for the elevation heights from $h=0$ to L, while 72 receivers are distributed evenly from 0° to 360° for all the studied elevation heights in the $y=0$ plane. To compare results with the cube with finite elevation heights (h), the noise emitted from the cube in free space shown in Figure 4.39 is increased by 6 dB at each receiver to mimic the noise reflection from the ground.

As can be seen from Figure 4.39(a), in the $y=0$ plane, the sound directivity of the cube with $h=L/3$ is almost omni-directional, while a more dipole-like directivity is found from the case with $h=L/12$. Despite the varying shapes of the sound directivity with the change of elevation heights in Figure 4.39(a), highest noise is always observed in the spanwise direction, namely at the receiver (0, 0, 10), while the lowest noise is in the streamwise direction at (10, 0, 0). In addition, the sound directivity in the $x-z$ plane shown in Figure 4.39(a) tends to be symmetric with respect to the axes. However, in the $x-y$ plane shown in Figure 4.39(b), the highest noise is not always observed from the vertical direction at the receiver (0, 10, 0) and slightly asymmetric sound directivities are found in cases with $h=0$ and $h=L/3$.

4.3.3 Validation of the predicted noise

Relevant measurements on cubes that can be used for the validation purposes are scarce. Latorre Iglesias (2015) conducted aeroacoustic measurements in an anechoic wind tunnel to study the sound emitted from a cube elevated by $L/3$ from a stiff panel. The cube was

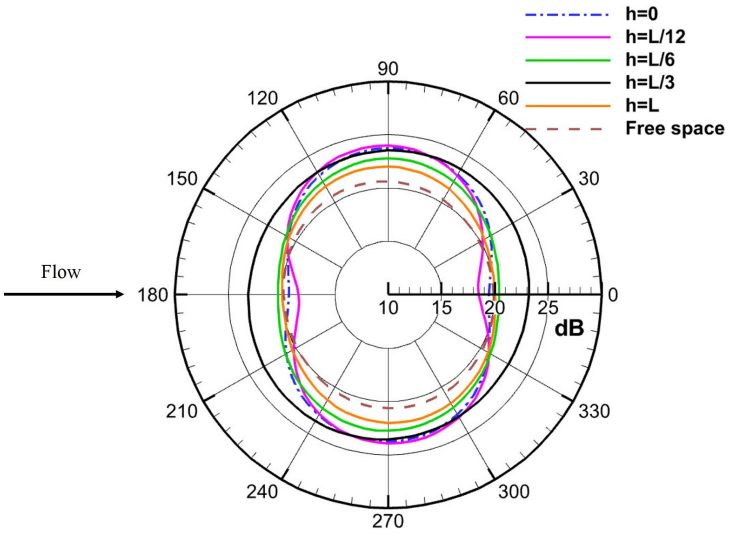

(a) $x-z$ plane ($y=0$)

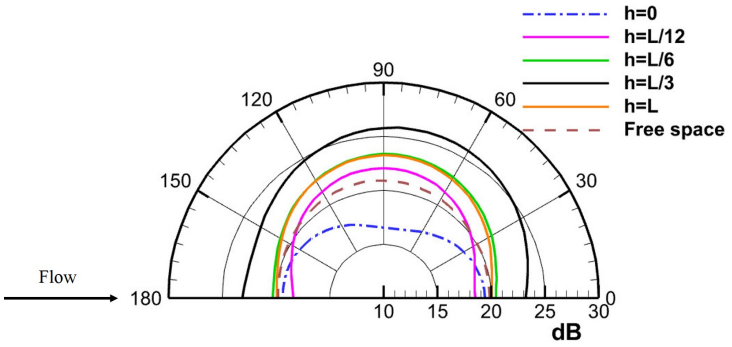

(b) $x-y$ plane ($z=0$)

Figure 4.39: Sound directivity for different elevation heights (h)

held by a long strut passing through it normal to the stiff panel supported by this panel and a stand outside the flow region (see Figure 2.15). However, the noise at frequencies lower than 100 Hz was contaminated due to the background noise of the wind tunnel. In addition, although acoustic treatments were implemented using open cell foam to suppress the noise generated by the supporting strut, the effect of this strut on the flow field around the cube and then on the corresponding emitted noise is hard to evaluate.

The far-field noise predicted in this work is compared with the measurement carried out by Latorre Iglesias (2015) in Figure 4.40. The noise predicted from the cube with an elevation height of $L/3$ in this work is corrected based on Equation (4.12) to have the same section area, receiver distance and flow speed with those reported for the measurements (Latorre Iglesias, 2015). Good agreement is obtained in the range of the Strouhal numbers from about 0.6 to 3, while the noise at lower values of St, which is of more interest for this case is not available in the measurement due to the background noise. However, considerable discrepancies between the numerical and the experimental results are found at higher Strouhal numbers. Since the noise spectra drop quickly in

both the simulation and the experiment when $St \geq 3$, these discrepancies at higher Strouhal numbers are not critical in predicting the OASPL.

As described above, due to the scarcity of the relevant acoustic measurements in the literature, the noise predictions on the elevated cube have not been fully validated and only some implications of the wall proximity effect on the emitted noise from a cube are presented. The main difficulties in implementing experimental studies on the broadband noise from a cube with different wall proximities lie in the background noise of the wind tunnel and also the influence of the supporting system.

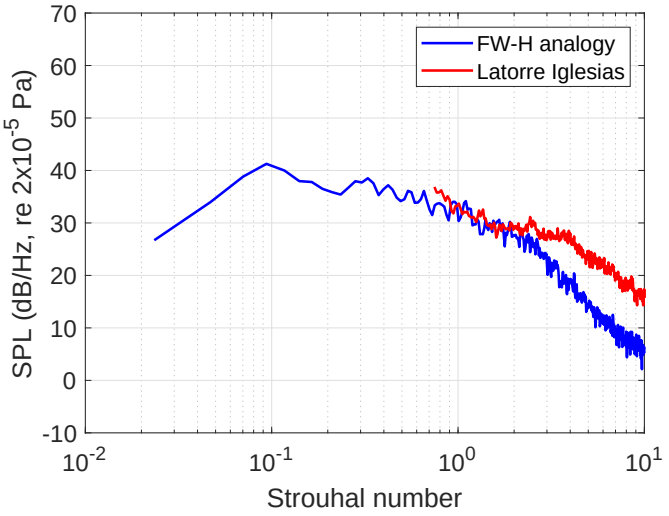

Figure 4.40: Comparison of the noise emitted from the cube with an elevation hight of $L/3$ between the result predicted in this work and the measurement conducted by Latorre Iglesias (2015)

4.4 Summary

In this chapter, numerical simulations have been presented for a wall-mounted cube in uniform flow as a first step to investigate the most suitable spatial resolution of the mesh and also to validate the feasibility of the adopted numerical methodology by comparing the results with existing measurements. Subsequently, the influence of wall proximities between $h = L/12$ and L, and in free space on the flow around the cube is examined in detail at a Reynolds number of 5×10^4. The sound field generated by the elevated cube is also examined and some implications are presented. The DDES approach is adopted in OpenFOAM and used to reveal flow features around the cube and to obtain the fluctuating pressure acting on the cube surfaces. The far-field noise is then predicted using the FW-H equations based on the sampled surface pressure.

When the cube is placed on the ground, a horseshoe vortex is formed in front of the cube and an arch-type vortex tube can be observed in the wake. However, the formation

of the horseshoe vortex and the arch tube is weakened when the cube is lifted slightly from the ground. The flow separated from the top leading edge reattaches to the ground when the cube is wall-mounted or lifted to $L/12$ above the ground. For elevation heights from $h = L/6$ to $L/4$, the flow along the ground separates in the wake of the cube while the flow separation on the ground disappears for larger values of h. Flow reattachments on the bottom surface of the cube can be observed in cases with $h = L/12$, $L/6$ and $L/5$. In particular, at $h = L/5$, the flow reattaches to the trailing edge of the bottom surface. The mean lift coefficient drops significantly when the wall-mounted cube is lifted to $h = L/12$. The rms values of the drag coefficient $C_{d,\mathrm{rms}}$ are always lower than $C_{l,\mathrm{rms}}$ and $C_{s,\mathrm{rms}}$. For $h \leq L/3$, fluctuations of the side-force coefficient are larger than those for the lift coefficient. With further increases of the elevation height, $C_{l,\mathrm{rms}}$ becomes close to $C_{s,\mathrm{rms}}$. In addition, high pressure fluctuations are found near the cube trailing edge and locations where the flow reattaches on the bottom of the cube.

For the noise radiated from the cube with different wall proximities, no evident peaks can be observed from the noise spectra in the streamwise direction while a broadband peak centred near $St = 0.1$ is found in both the vertical and the lateral directions, contributing significantly to the far-field noise. The broadband peak in the lateral direction is suppressed when the cube is elevated to a height of $h = L/6$, but it reappears for larger elevation heights. When the cube is close to the ground ($h \leq L/12$), the noise in the lateral direction is greater than that in the vertical and streamwise directions. With the increase of the elevation height, the noise in the vertical direction increases quickly and reaches a maximum when the cube is elevated to $h = L/4$. An increase of 10 dB is observed for this direction compared the wall-mounted case; the sound then reduces slightly for further increases in the elevation heights. The noise in the streamwise direction is generally lower than that in the other directions.

Chapter 5

The effect of corner rounding

In practice, cubic and cuboid objects in engineering structures have rounded corners. In order to investigate the effect of corner rounding on the flow and resulting noise, the calculation scheme used in the previous chapter is extended to the case of rounded cubes. The flow past a rounded cube at different Reynolds numbers is investigated in this chapter employing DDES in OpenFOAM and the far-field noise is also predicted using the FW-H acoustic analogy in FLUENT.

5.1 Computational setup

A rounded cube with dimensions $L = 75$ mm is considered, which is rounded at all edges with a radius R. Five different corner radii are taken into account: $R/L = 0$, 1/12, 1/6, 1/3 and 2/5. The rounded cube is considered to be in free space. The computational domain in the $z = 0$ plane, together with the assigned boundary conditions, are illustrated in Figure 5.1. Those in the $y = 0$ plane are identical due to symmetry of the computational domain. The origin of the coordinate system is located in the cube centre and the $x-$, $y-$, $z-$ axes represent the streamwise, cross-flow (vertical) and spanwise (lateral) directions respectively. The free-stream velocities of the incident flow considered are $U_\infty = 10$, 15, 20, 30 and 40 m/s. The corresponding Reynolds numbers are $Re = 50,000$, $75,000$, $100,000$, $150,000$ and $200,000$, respectively. However, limited by the computational resources, the investigated Reynolds numbers are still lower than the highest Re cared for the train pantographs and bogies. The overall size of the computational domain is $26L \times 13L \times 13L$ giving a maximum blockage ratio 0.6%. $Velocity\,Inlet$ and $Pressure\,Outlet$ boundaries are adopted in the simulation, as shown in Figure 5.1. The cube surface is assigned as a $No-slip\,wall$ and $Symmetry\,Plane$ is applied to the other boundaries.

Fully-structured meshes are generated for all the simulations in this chapter and details of the mesh for the $R/L = 2/5$ is shown in Figure 5.2. Figure 5.2(a) illustrates the cells in

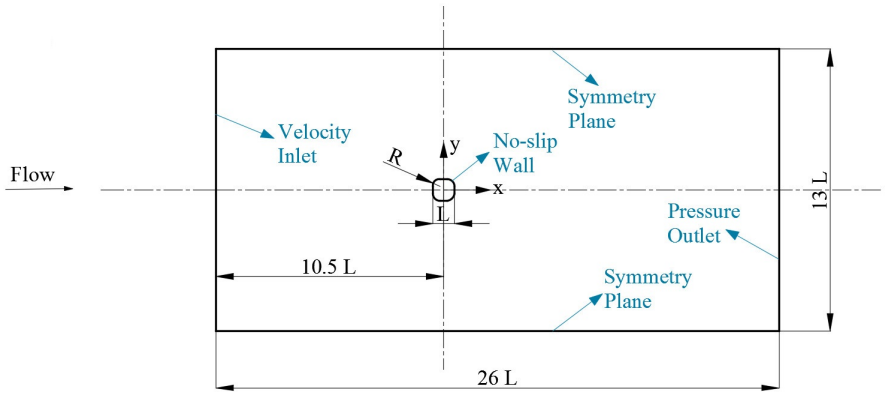

Figure 5.1: Sketch of the computational domain in the $z = 0$ plane

the $z = 0$ plane. The mesh topology surrounded by the red rectangle in Figure 5.2(a) is shown in Figure 5.2(b). The innermost blocks are spherical normal to the cube surfaces to optimise the grid skewness near cube corners. The grid resolution in this chapter is determined based on the grid dependence study of the wall-mounted cube described in Section 4.1. The maximum dimensionless wall distance of the first layer (y_1^+) is targeted at 1.5, with an average value well below 1. The minimum aspect ratio of the first-layer grids is located at the rounded corners, with $\Delta x/\Delta y = \Delta z/\Delta y \approx 30$ (Δx, Δy and Δz are the grid dimensions) while the maximum aspect ratio is about 120 in the middle of the cube edges. To capture the flow separation well, grids on the rounded corners are distributed evenly with the smallest aspect ratio. Therefore, the total number of grid cells (N_{gird}) increases for enlarged corner radii and Reynolds numbers. The N_{gird} for the cube at $Re = 50,000$ is 796,000, increasing to 22.9 million for the case with $R/L = 2/5$ at $Re = 200,000$, as the overall grid size grows with the increase of the corner radius and the Reynolds number. About 5 physical seconds ($t^* \approx 667$) can be obtained during a wall time of 60 hours using 160 cores for the cube with sharp corners at $Re = 50,000$, while less than 0.05 s ($t^* \approx 27$) is calculated for the cube with $R/L = 2/5$ at $Re = 200,000$ under the same condition. In this chapter, the aerodynamic coefficients are calculated in the period from $t^* = 400$ to 2000 for $Re = 50,000$, 75,000 and 100,000, while t^* is up to about 1800 for $Re = 150,000$ and 1500 for the highest Re. The time step used for all these simulations is 1×10^{-5} s with corresponding maximum Courant-Friedrichs-Lewy (CFL) numbers lower than 2. The numerical scheme adopted in this chapter is the same as that described in Section 4.1.2. Figure 5.3 shows parameters of the DDES model at different positions in the $z = 0$ plane for the $R/L = 1/12$ at $Re = 50,000$ as examples. As can be seen, the RANS mode is used within $0.1L$ to the cube surface. Since the cell size (Δ) is larger at a lower Reynolds number, the region using the RANS mode decreases for an increased Re according to Equation (3.33).

To further validate the above described mesh resolution in addition to the benchmark case in Section 4.1, grid dependence studies are implemented for the $R/L = 1/12$ at $Re = 200,000$. The original mesh for this case is coarsened and refined respectively by

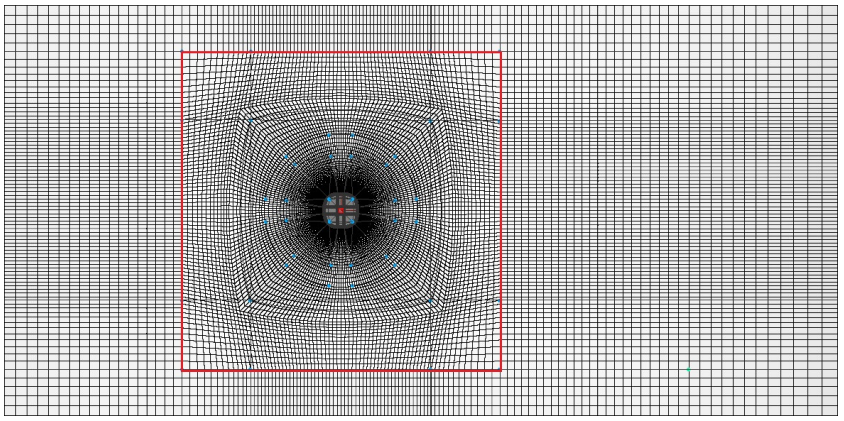

(a) Cells in the $z = 0$ plane

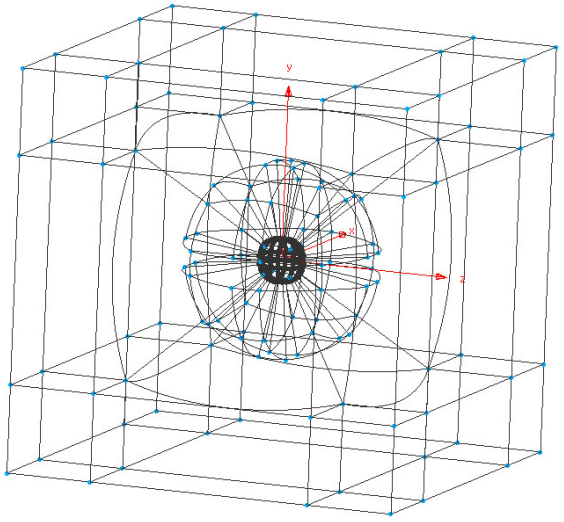

(b) Mesh topology

Figure 5.2: Illustrations of the mesh for the $R/L = 2/5$

a ratio of $\sqrt{2}$ to obtain the new meshes for trial. Details of the grid investigations are shown in Table 5.1, where N_{grid} denotes the total number of cells. The frontal area of this case is chosen as the reference area to calculate the aerodynamic coefficients. The mean lift and side-force coefficients are close to zero due to the symmetry. As can be seen from Table 5.1, statistics only changes slightly with the further refined mesh, which implies the original grid resolution is sufficient.

R/L	mesh	N_{grid}	$\overline{C_d}$	$C_{\text{d},rms}$	$C_{\text{l},rms}$	$C_{\text{s},rms}$
1/12	coarse	6.39×10^6	0.4022	0.0153	0.0225	0.0236
1/12	original	1.06×10^7	0.3945	0.0129	0.0197	0.0202
1/12	refined	2.60×10^7	0.4071	0.0116	0.0209	0.0211

Table 5.1: Grid dependence investigations on the $R/L = 1/12$ at $Re = 200,000$

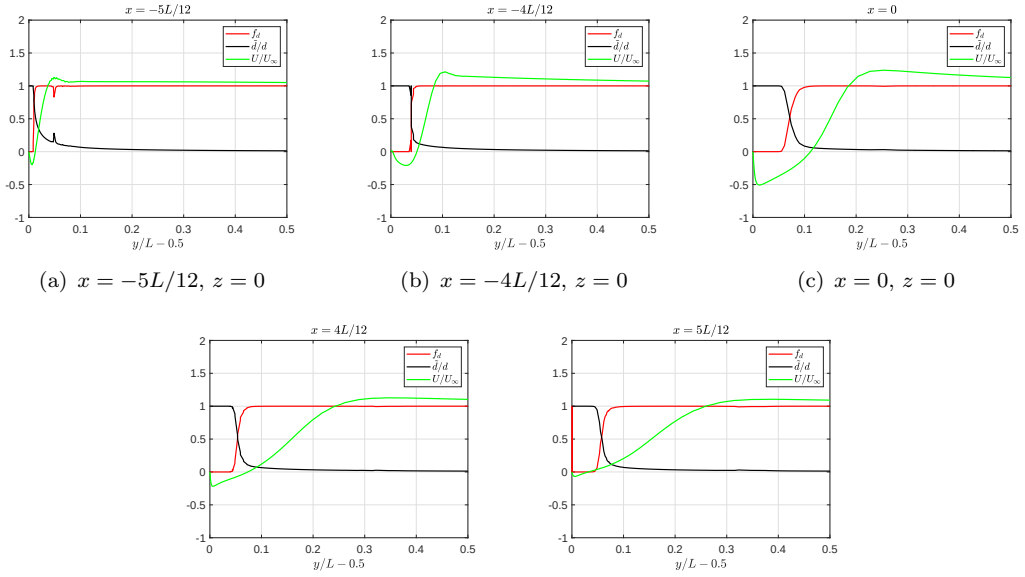

(a) $x = -5L/12$, $z = 0$ (b) $x = -4L/12$, $z = 0$ (c) $x = 0$, $z = 0$

(d) $x = -4L/12$, $z = 0$ (e) $x = 5L/12$, $z = 0$

Figure 5.3: Performance of the DDES model for $R/L = 1/12$ at $Re = 50,000$

5.2 Benchmark case of sphere in uniform flow

For the cube with sharp corners, the flow always separates from the leading edges when the Reynolds number is greater than about 30,000 (Martinuzzi and Tropea, 1993; Rodi et al., 1997; Yakhot et al., 2006b). However, once the sharp corners are rounded, the location of the flow separation varies. In particular, when the radius of the rounded corner is $R/L = 0.5$, the cube becomes a sphere with a diameter $D = L$. To increase confidence in the adopted numerical methodology, especially in predicting flow separation locations accurately, another benchmark case on the flow around a sphere at a Reynolds number of 50,000 is carried out and compared with results from the literature. A similar mesh and computational domain are used as described in Section 5.1. Figure 5.4 illustrates the distribution of y_1^+ on the sphere surface in the $z = 0$ plane; the position is denoted by the angle ϕ, which is measured clockwise from the front stagnation point. As shown in Figure 5.4, the maximum value of y_1^+ is smaller than 1.5; the mean value of y_1^+ is 0.73.

According to the literature (Sakamoto and Haniu, 1990; Taneda, 1978; Achenbach, 1974, 1968), the flow around a sphere changes slightly in the Reynolds number range from $Re = 10^4$ to 3×10^5. This is in the subcritical region where the boundary layer separates from the sphere surface as laminar before transition happens. Results obtained employing DDES from the current study are compared with the measurements of Achenbach (1972) at a Reynolds number of 1.62×10^5, which is in the same regime. Figure 5.5(a) shows the comparison of the surface pressure coefficient $C_p = (P - P_\infty)/(0.5\rho U_\infty^2)$, where P is the mean pressure on the sphere surface and $P_\infty = 0$ is the reference pressure. Figure 5.5(b)

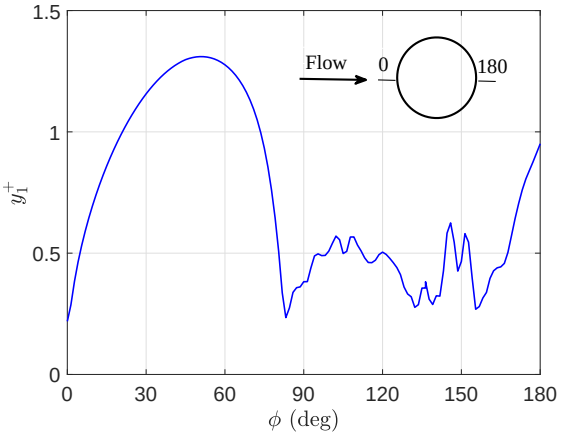

Figure 5.4: The distribution of y_1^+ along the sphere surface in the $z = 0$ plane

shows the skin friction coefficient normalised by the Reynolds number $\tau_w/(\rho U_\infty^2)Re^{1/2}$, where τ_w is the wall shear stress.

A commendable agreement of the pressure distribution has been achieved between the simulation and the measurement as shown in Figure 5.5(a), while the agreement for the skin friction in Figure 5.5(b) is also reasonable. Despite the slight over-prediction of the skin friction coefficient at positions $\phi < 60°$, the location of the flow separation, where the skin friction first becomes zero, is captured accurately ($\phi \approx 82°$). The probable reason for the discrepancy is the limited capability of turbulent models for transitional flow, considering the fact that the boundary layer separation from the sphere surface is laminar in the subcritical flow region (Achenbach, 1972).

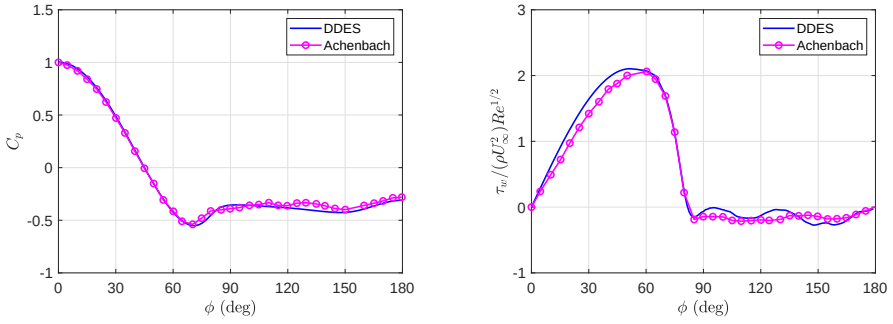

(a) Pressure distribution

(b) Skin friction distribution

Figure 5.5: Distributions of pressure and skin friction along the sphere surface in the $z = 0$ plane compared with the measurements from Achenbach (1972)

Figure 5.6 compares the current velocity profiles at $x/D = 0.3$ with the measurements conducted by Bakić et al. (2006) at a Reynolds number of 51,500 and the LES of Schmidt (2002) at Re=50,000. In Figure 5.6, $\overline{U}$ and $\overline{V}$ denote mean streamwise and cross-flow velocities respectively, while the subscript rms indicates the root mean square values. The mean and rms streamwise velocities (Figure 5.6(a) and Figure 5.6(c)) agree well with

both the measurement and the LES. Predictions of the mean and rms cross-flow velocities (Figure 5.6(b) and Figure 5.6(d)) correctly capture the shape of the profiles from the literature despite slight differences in the magnitude, indicating good predictions of the separate shear layer. In addition, mean and rms values of the streamwise velocity in the wake of the sphere at $x/D = 0.5$, 1 and 2 obtained from this work are also compared with results from the literature (Bakić et al., 2006; Schmidt, 2002) in Figure 5.7. Note that in both the measurements conducted by Bakić et al. (2006) and LES simulations implemented by Schmidt (2002), a string with a diameter of $d = 0.12D$ was used to support the sphere in its wake. Considering this difference in the setup, the results from the current DDES can be considered sufficiently close to the published results.

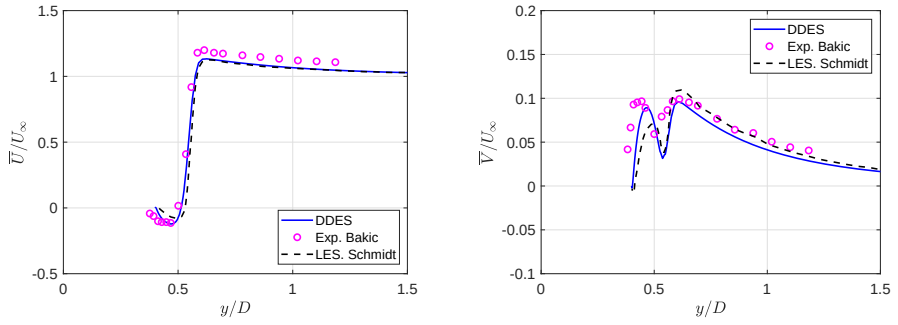

(a) Mean streamwise velocity

(b) Mean cross-flow velocty

(c) rms values of streamwise velocity

(d) rms values of cross-flow velocity

Figure 5.6: Velocity profiles at x/D=0.3 compared with Bakić et al. (2006) and Schmidt (2002)

The flow parameters of the sphere in cross-flow obtained from the current work are presented in Table 5.2 and compared with available experimental and numerical results. In Table 5.2, $\overline{C}_d$ is the mean drag coefficient, L_r is the length of the recirculation region in the wake and $St = fD/U_\infty$ is the Strouhal number associated with the vortex shedding, where f is the peak frequency. L_r is measured in the $z = 0$ plane from the rear base point of the sphere at $(0.5D, 0, 0)$ to the location where the streamwise velocity recovers to zero from negative values. Good agreement in terms of these statistics is achieved between this work and the literature.

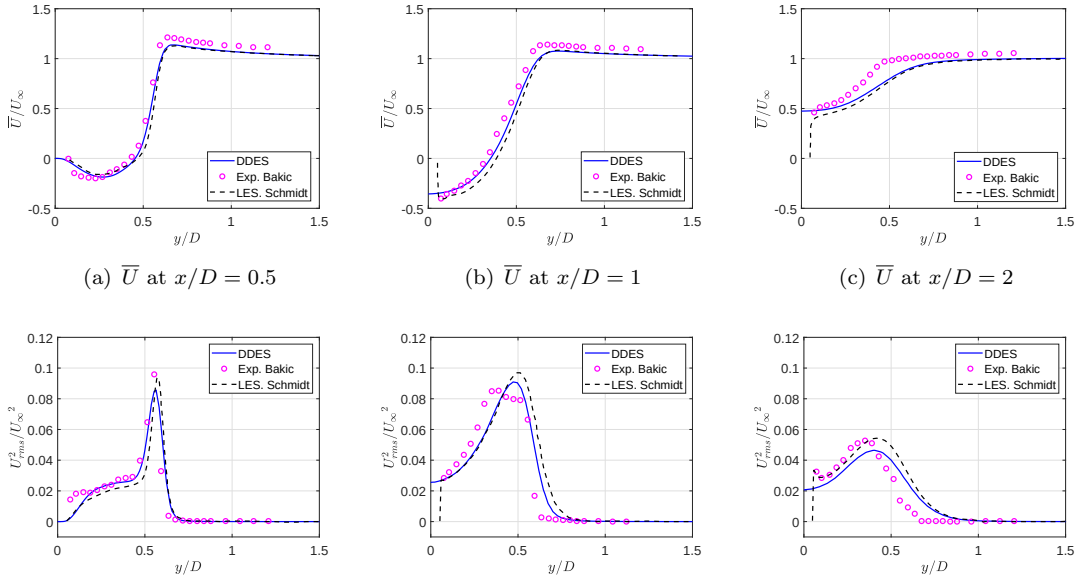

(a) $\overline{U}$ at $x/D = 0.5$ (b) $\overline{U}$ at $x/D = 1$ (c) $\overline{U}$ at $x/D = 2$

(d) U_{rms} at $x/D = 0.5$ (e) U_{rms} at $x/D = 1$ (f) U_{rms} at $x/D = 2$

Figure 5.7: Velocity profiles at x/D=0.5, 1 and 2 compared with Bakić et al. (2006) and Schmidt (2002)

	Method	Re	$\overline{C}_d$	L_r/D	St
Present	DDES	5×10^4	0.476	0.89	0.192
Achenbach (1972)	Exp.	5.06×10^4	0.480		
Wieselsberger (1921)	Exp.	5.02×10^4	0.478		
Schlichting and Gersten (2016)	Exp.	1×10^4	0.4		0.195
Tomboulides (1993)	LES	2×10^4		0.85	0.19
Constantinescu and Squires (2004)	DES	1×10^5	0.414		
Rodríguez et al. (2013)	DDES	2×10^4	0.411		0.198
Robertson et al. (2015)	DDES	1×10^4	0.402		0.195

Table 5.2: Statistical parameters of the flow around a sphere

As described above, distributions of the skin friction and pressure coefficients around the sphere surface, the velocity profiles at different positions and also some key parameters describing the flow obtained from the current simulation show good agreement with data reported in the literature, which provides validation of the current DDES approach.

5.3 Flow around cubes with rounded corners

5.3.1 Aerodynamic coefficients

For the rounded cubes, the frontal area, as the reference area for the aerodynamic coefficients, varies with the corner radius between L^2 for the cube and $\pi L^2/4$ for the sphere. In general, each simulation was run for over 40 flow-through times ($26L/U_\infty$ in current work) to ensure that the flow develops to a statistical steady state. This was checked by monitoring and comparing the aerodynamic coefficients averaged over every two flow-through times. The aerodynamic coefficients are collected once the variation of the values averaged in each time segment is within 10 %. Figure 5.8 summarises the drag coefficients obtained for the cube with different corner radii and at different Reynolds numbers. The total mean drag coefficients are shown in Figure 5.8(a), while contributions of the viscous force to it are illustrated in Figure 5.8(b). The dashed line in Figure 5.8 represents the average value over different Reynolds numbers. The calculated mean lift and side-force coefficients (not shown) are very close to zero, confirming convergence of the statistics for symmetrical objects. For comparison purposes, the mean drag coefficient of the sphere obtained from the benchmark case is also shown, namely $R/L = 1/2$. This has been obtained only at $Re = 50,000$, but the drag coefficient $\overline{C}_d$ for a sphere tends to be constant in the studied range of Reynolds numbers (Achenbach, 1972).

As can be seen from Figure 5.8(a), the values of $\overline{C}_d$ for each value of R/L at different Reynolds numbers collapse well to the trend denoted by the dashed line and the absolute differences from the average value at the studied Reynolds numbers are within 15%. The mean drag coefficient does not change monotonically with the increase of the corner radius. The lowest mean drag coefficient is observed at $R/L = 1/3$ for all the Reynolds numbers considered, while the highest value is found from the cube ($R/L = 0$). A similar trend of $\overline{C}_d$ was observed from square cylinders with different corner radii reported by Miran and Sohn (2015), for which the minimum $\overline{C}_d$ was found near $R/L = 0.2$. Bearman et al. (1984) measured the drag coefficients of cylinders with rounded corners in an oscillatory flow and reported the lowest $\overline{C}_d$ at $R/L = 0.265$. Here the mean drag coefficient drops significantly when the cube corners are rounded even with a small radius $R/L = 1/12$. With the increase of the radius from $L/12$ to $L/3$, the variation in the mean drag coefficient is much smaller. For radii greater than $L/3$, the drag coefficient increases slightly, although its value is still much smaller than that for the cube. The mean drag coefficient of the rounded cube with $R/L = 1/12$ is most affected by the Reynolds number. The contribution of the viscous force to the total drag is always smaller than 6% as shown in Figure 5.8(b). Especially, for the cube with $R/L = 0$, this contribution is almost zero. For most of the cases, the greatest contribution of the viscous force is found for the $R/L = 1/3$ at different Reynolds numbers.

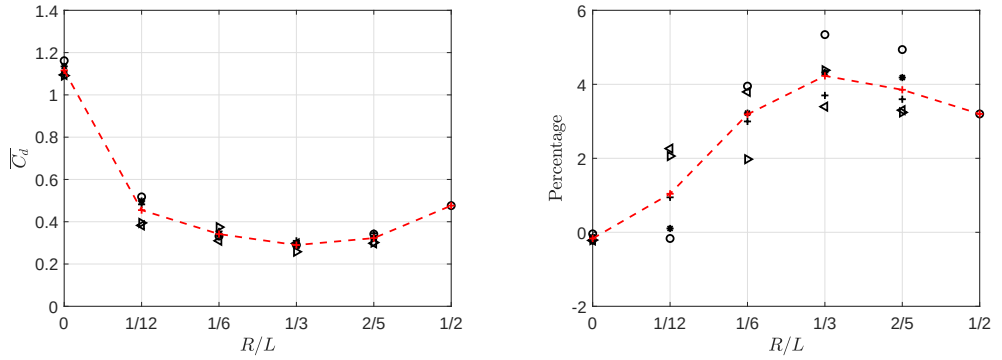

(a) The mean drag coefficient ($\overline{C}_d$) (b) Contribution of the viscous force to the total drag

Figure 5.8: Trends of the drag coefficient varying with the corner radius (R). $\circ$: $Re = 50,000$; $*$: $Re = 75,000$; $+$: $Re = 100,000$; $\triangleleft$: $Re = 150,000$; $\triangleright$: $Re = 200,000$; $-+-$: Average value

The dependence on the corner radius of the root mean square values of both the drag and lift coefficients, denoted as $C_{d,\text{rms}}$ and $C_{l,\text{rms}}$, is plotted in Figure 5.9 using the same scales; the average values over different Reynolds numbers are shown by the dashed line. The rms values of the side-force coefficient are not displayed as they are virtually the same as those for $C_{l,\text{rms}}$ due to symmetry. As shown in Figure 5.9, values of $C_{l,\text{rms}}$ are higher than those for $C_{d,\text{rms}}$ in all the investigated cases. In addition, the dependence of $C_{l,\text{rms}}$ on the radius R in Figure 5.9(b) is much more significant than that observed for $C_{d,\text{rms}}$ in Figure 5.9(a). Similar to $\overline{C}_d$, the rms values of the drag and lift coefficients do not change monotonically with the corner radius. In general, the lowest value of $C_{d,\text{rms}}$ is observed for $R/L = 1/3$, while the minimum value for $C_{l,\text{rms}}$ is found in the case with $R/L = 1/12$. The values of both $C_{d,\text{rms}}$ and $C_{l,\text{rms}}$ increase significantly from $R/L = 1/3$ to 2/5 at each investigated Re and then drop for the sphere.

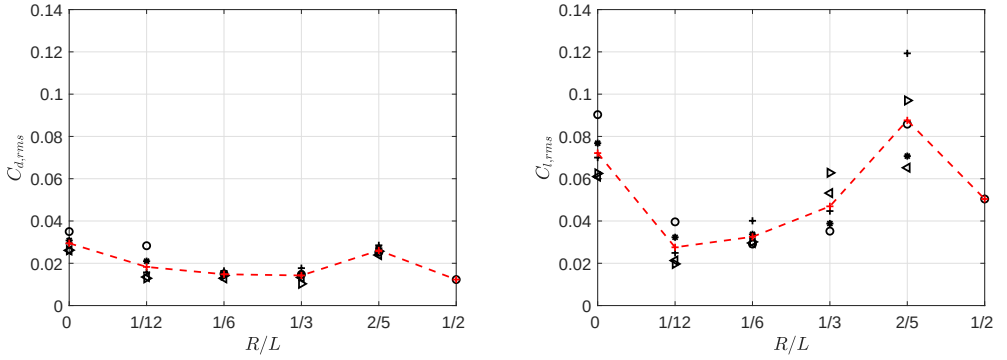

(a) $C_{d,\text{rms}}$ varying with the corner radius (b) $C_{l,\text{rms}}$ varying with the corner radius

Figure 5.9: The trend of the root mean square values of the drag and lift coefficients varying with the corner radius (R). $\circ$: $Re = 50,000$; $*$: $Re = 75,000$; $+$: $Re = 100,000$; $\triangleleft$: $Re = 150,000$; $\triangleright$: $Re = 200,000$; $-+-$: Average value

As can be seen in Figure 5.9, the rms values of aerodynamic coefficients are also affected to some extent by the Reynolds number. The rms values of the drag coefficient are most sensitive to the Reynolds number at $R/L = 1/12$. The rms values of the lift coefficient are even more strongly dependent on the Reynolds number. The value of $C_{l,\mathrm{rms}}$ changes the most with Reynolds numbers for the case with $R/L = 2/5$. Also for the cube with $R = 0$, the rms values of the force coefficients are more sensitive to the change of Reynolds numbers than the mean drag coefficient in Figure 5.8(a), which was also observed by Lim et al. (2007). However, although the rms values of these aerodynamic coefficients are dependent on the Reynolds number, there is no systematic dependence.

The rms values shown in Figure 5.9 are also the square root of the area below the power spectral density (PSD) curves of the aerodynamic coefficients (Smith, 2007). The power spectral densities of the drag and lift coefficients at $Re = 50,000$ for cubes with different corner radii are shown in Figure 5.10 as examples. These are calculated from the time histories of the force coefficients using Welch's method. A Hanning window is applied with 50% overlapping segments. The frequency resolution in Figure 5.10 is 1.5 Hz ($St = 0.011$) for the cubes with $0 \leq R/L \leq 2/5$, and 1.2 Hz ($St = 0.009$) for the sphere with $R/L = 1/2$. As can be seen from Figure 5.10(a), no evident peaks are found in the spectra of C_d for Strouhal numbers smaller than 1; for Strouhal numbers above 1, the amplitudes of the drag coefficient spectra in Figure 5.10(a) reduce rapidly. For the PSDs of the lift coefficient given in Figure 5.10(b), the spectra drop quickly at Strouhal numbers above 0.3. In addition, a broadband peak centred near $St = 0.1$ can be seen in the spectrum for the cube ($R/L = 0$), and a narrower peak centred about $St = 0.16$ is clearly seen for the rounded cube with $R/L = 2/5$. However, no evident peaks are identified for the other cases in Figure 5.10(b). These peaks are related with periodic vortex shedding in the wake and are the main reasons for the higher values of $C_{l,\mathrm{rms}}$ observed for the cube ($R/L = 0$) and the case with $R/L = 2/5$ in Figure 5.9(b).

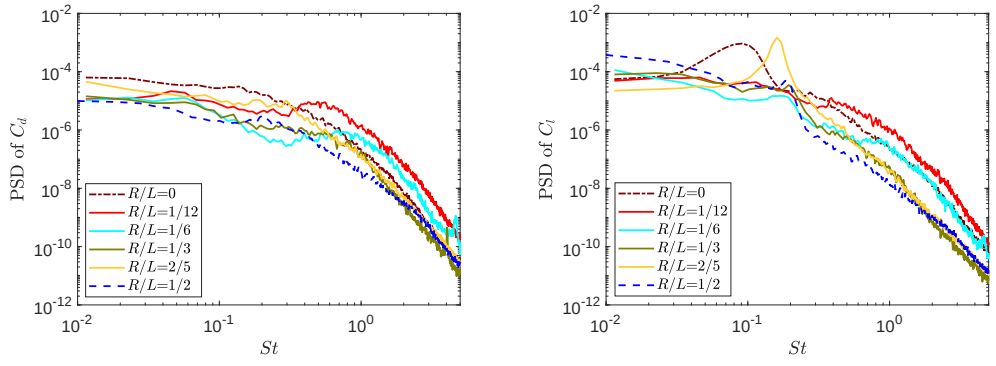

(a) PSDs of the drag coefficeint

(b) PSDs of the lift coefficeint

Figure 5.10: PSDs of the aerodynamic coefficients for different corner radii at $Re = 50,000$

To illustrate the Reynolds number dependence of the results shown in Figure 5.9, PSDs of C_d for $R/L = 1/12$ at different Reynolds numbers are shown in Figure 5.11(a), while the spectra of the lift coefficient for $R/L = 2/5$ are displayed in Figure 5.11(b). In Figure 5.11(a), no apparent peaks can be detected and the frequency range most affected by the Reynolds number is $St \leq 1$, which is also true for cases with other corner radii (not shown). Major changes of the spectra in Figure 5.11(b) for $R/L = 1/12$ mainly occur between $St = 0.05$ and 0.2, and the spectra drop rapidly when the Strouhal number exceeds 0.2. Distinct peaks centred between $St = 0.06$ and 0.16 with different amplitudes are observed at different Reynolds numbers, which explain the fluctuations of $C_{l,\mathrm{rms}}$ for $R/L = 2/5$ in Figure 5.9(b). However, the distinct peaks seen in Figure 5.11(b) only appear for the case with $R/L = 2/5$ and are not observed for other cases studied here.

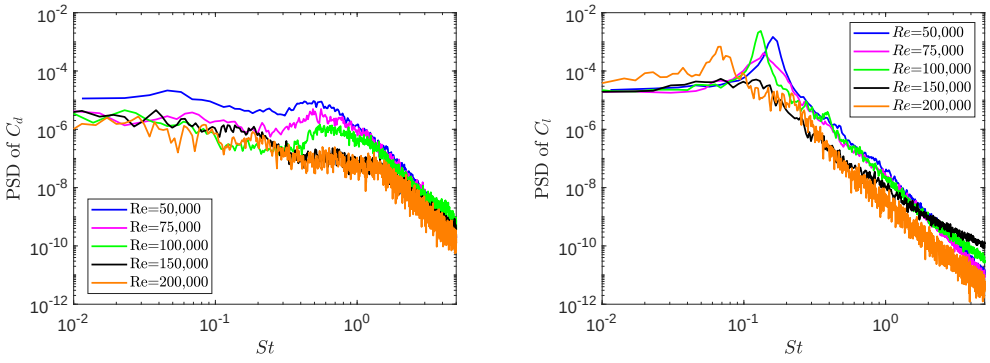

(a) PSDs of C_d for $R/L = 1/12$

(b) PSDs of C_l for $R/L = 2/5$

Figure 5.11: PSDs of the aerodynamic coefficients at different Reynolds numbers

In summary, these force coefficients are affected by both the corner radius and the Reynolds number, and their rms values are much more sensitive than the mean drag coefficient. In addition, the value of $C_{l,\mathrm{rms}}$ is higher than $C_{d,\mathrm{rms}}$ for all cases considered. The mean drag coefficient and the rms values of the aerodynamic coefficients do not change monotonically with the increase of the corner radius. The value of $\overline{C}_d$ drops significantly once the sharp corners of the cube are rounded and the lowest value is observed for $R/L = 1/3$. Larger values of $C_{d,\mathrm{rms}}$ and $C_{l,\mathrm{rms}}$ are observed for $R/L = 0$ and 2/5. These large fluctuations observed in $C_{l,\mathrm{rms}}$, especially for the case with $R/L = 2/5$, are closely related to periodic shedding in the wake, which will be discussed in Section 5.3.2.1. However, no systematic dependence of these force coefficients on the Reynolds number is found.

5.3.2 Flow patterns around cubes with rounded corners

5.3.2.1 Visualization of flow structures

Comparisons of the normalised instantaneous spanwise vorticity (ω_z) for cubes with different corner radii at the Reynolds number of 50,000 are shown in Figure 5.12. This spanwise vorticity is given by $\omega_z = (\partial V/\partial x - \partial U/\partial y)/(U_\infty/L)$, where V and U are the cross-flow ($y-$axis) and the streamwise ($x-$axis) velocities respectively. As can be seen from Figure 5.12, the flow patterns change noticeably with the variation of the corner radius. The flow separates from the leading edge for the cube with sharp corners ($R/L = 0$). With the increase of the corner radius, the separation position moves gradually downstream. As R/L is increased from 0 to 2/5, the separated shear layer moves closer to the side surfaces and the wake formed behind becomes narrower. However, the shear layer becomes more deflected for the sphere. In addition, as indicated by the spectra of the lift coefficient shown in Figure 5.11(b), the phenomenon of vortex shedding is most evident in the wake of the rounded cube with $R/L = 2/5$ shown in Figure 5.12(e).

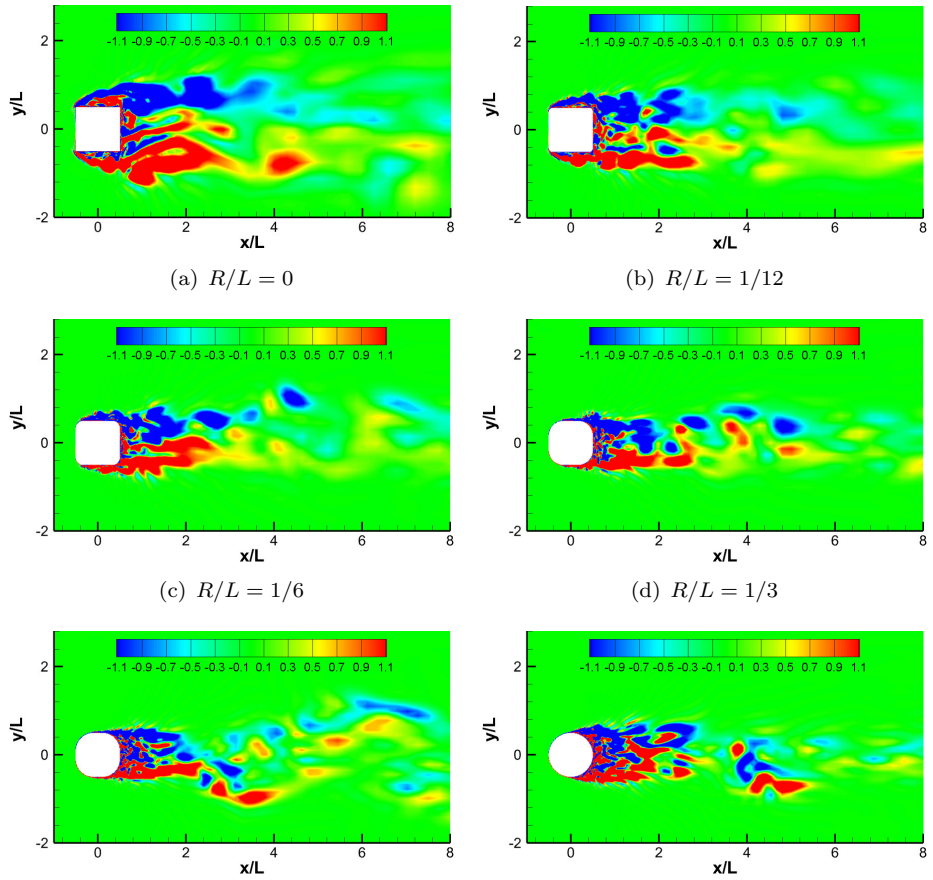

(a) $R/L = 0$ (b) $R/L = 1/12$

(c) $R/L = 1/6$ (d) $R/L = 1/3$

(e) $R/L = 2/5$ (f) $R/L = 1/2$

Figure 5.12: Contours of the instantaneous spanwise vorticity (ω_z) for cubes with different corner radii at $Re = 50,000$

Time-averaged streamlines in the $z = 0$ plane, together with the contours of the pressure coefficient (C_p), are shown in Figure 5.13 for different corner radii at $Re = 50,000$. Due to the symmetry of the geometry, only the upper part of the rounded cubes is shown in Figure 5.13; moreover, flow features in the $y = 0$ plane are the same. As the flow features observed near all four side surfaces are the same, these four surfaces are referred to as lateral surfaces in the following descriptions. The thick white line in Figure 5.13 denotes locations of zero streamwise velocity, which helps to visualise positions of flow separation, reattachment and also the recirculation length in the wake. As can be seen, mean flow features around the rounded cube change significantly with the corner radius. With the increase of the corner radius from $R/L = 0$ to 2/5, the location of the flow separation moves downstream and the recirculation region of the separated flow above the lateral surfaces reduces. In addition, the size of the recirculation region formed in the wake is also sensitive to the corner radius. The secondary vortices formed near the trailing edges of the cube, highlighted in the rectangle in Figure 5.13(a), disappear with the introduction of the corner radius. Similar flow features described above are also observed at other Reynolds numbers (not shown), apart from an increase in the recirculation region above the lateral surface for $R/L = 1/6$ at $Re = 200,000$. Parameters reflecting mean flow characteristics, such as the separation angle and the recirculation length, will be discussed quantitatively in the Sections 5.3.2.2 and 5.3.2.3 below.

From Figure 5.13(a) for the cube, the separated flow convects downstream and forms vortices in the wake without reattaching to the cube surfaces. Similar flow behaviour can also be observed for $R/L = 1/12$ (Figure 5.13(b)) and for the sphere (Figure 5.13(f)). Unlike the flow around the cube, the separated flow from rounded cubes with $R/L = 1/6$, 1/3 and 2/5 shown in Figure 5.13(c)-5.13(e) reattaches to the lateral surfaces before the trailing corner and then separates again from the trailing corners. Therefore, two mean flow patterns can be identified, as shown schematically in Figure 5.14. The dashed line in Figure 5.14 represents the developed bubble from the separated flow. θ is the separation angle measured between the upstream direction and the line linking the corner centre and the separation point. L_s and H shown in Figure 5.14(b) are the length and height of the bubble formed on the lateral surfaces. A reduction in L_s always occurs together with a reduction in H. In summary, the flow around the cube and sphere at all the investigated Reynolds numbers, along with the case with $R/L = 1/12$ at $Re = 50,000$ belong to pattern 1, while the flow induced by all the other rounded cases studied here follows pattern 2. In general, the transformation of the flow from pattern 1 to pattern 2 is facilitated by increasing the corner radius. For the second flow pattern, L_s and H tend to reduce as R is increased, although it is difficult to quantify this effect.

Figure 5.15 shows the mean streamlines and the pressure contours around the rounded cube with $R/L = 1/12$ at different Reynolds numbers; the case of $Re = 50,000$ was shown in Figure 5.13(b). Similar to increasing the corner radius, when the Reynolds number is increased, vortices formed due to the separated flow move closer to the lateral

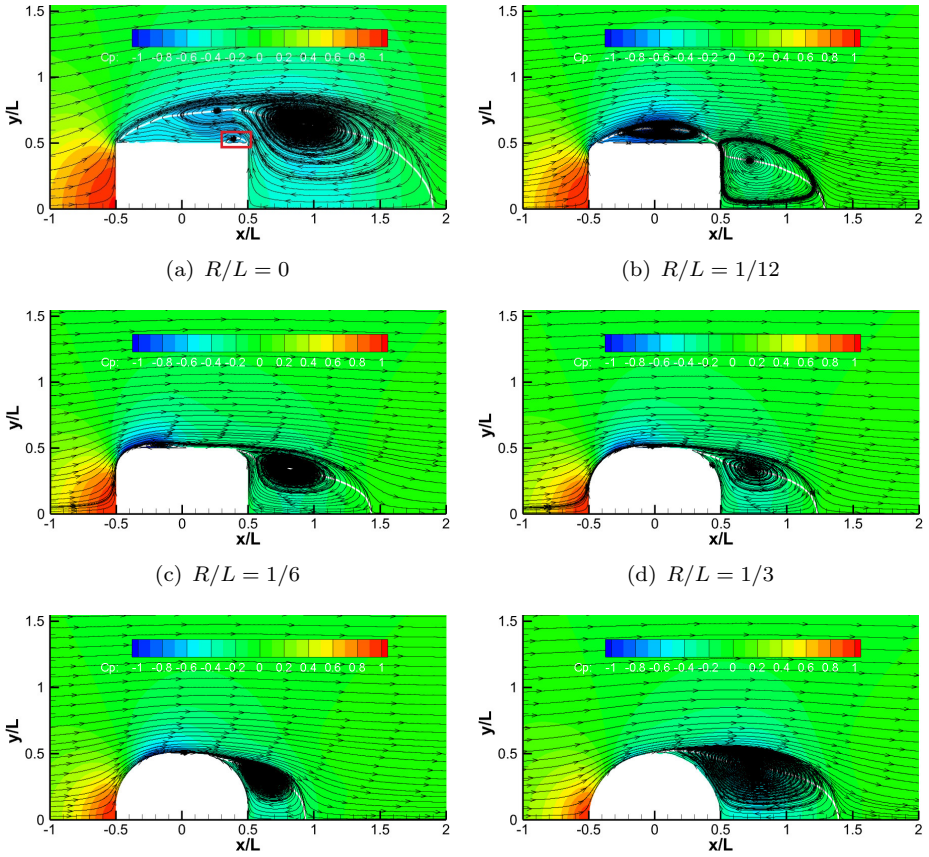

(a) $R/L = 0$ (b) $R/L = 1/12$

(c) $R/L = 1/6$ (d) $R/L = 1/3$

(e) $R/L = 2/5$ (f) $R/L = 1/2$

Figure 5.13: Mean streamlines and pressure contours in the $z = 0$ plane for cubes with different corner radii at $Re = 50,000$

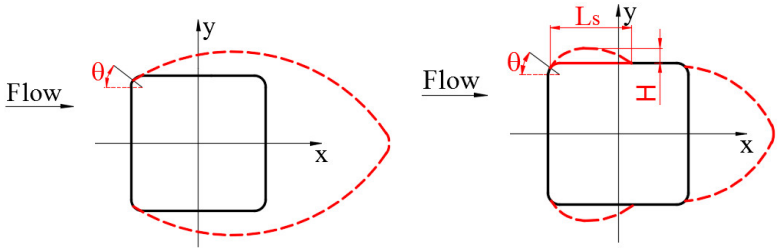

(a) Pattern 1 (b) Pattern 2

Figure 5.14: Flow patterns around cubes with rounded corners

surfaces with a reduction in L_s and H (defined in Figure 5.14). However, similar trends are not found for larger radii. For $R/L = 1/6$, the size of the recirculation region above the lateral surfaces fluctuates with the Reynolds number, while for $R/L = 1/3$ and $2/5$, the separated flow is very close to the lateral surfaces and the varying trend of L_s and H with the Reynolds number can hardly be characterised. In addition, as illustrated in Figure 5.15, the size of the recirculation regions in the wake for the different cases is also dependent on the Reynolds number; more details are presented in Section 5.3.2.3.

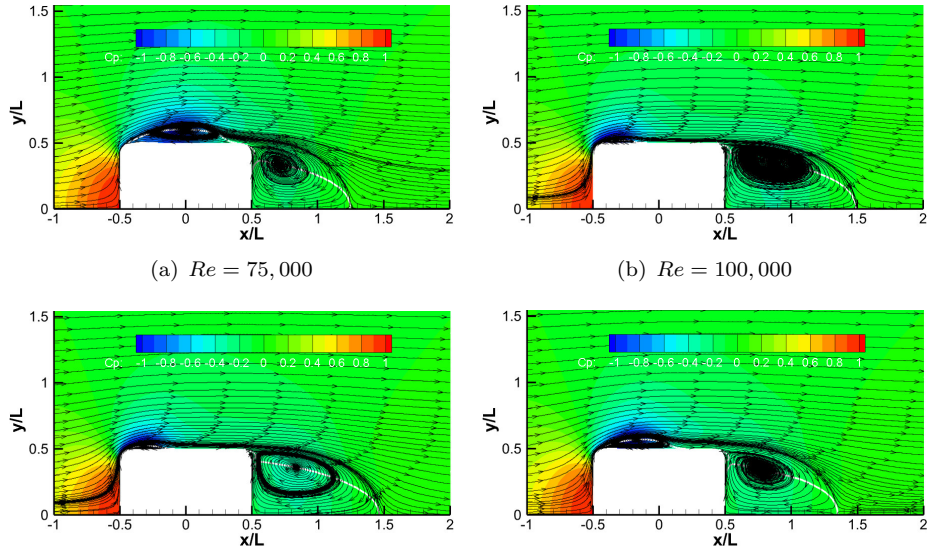

(a) $Re = 75,000$ (b) $Re = 100,000$

(c) $Re = 150,000$ (d) $Re = 200,000$

Figure 5.15: Mean streamlines and pressure contours in the $z = 0$ plane for the rounded cube with $R/L = 1/12$ at different Reynolds numbers

5.3.2.2 Locations of flow separation

As discussed above, the flow separation point changes considerably with the variation of the corner radius. Similar to the determination of the separation angle in the benchmark case on the sphere, described in Section 5.2, the values of θ for the rounded cubes are determined from the distribution of the skin friction coefficient (C_f). Summaries of the separation angles in the $z = 0$ plane for all the investigated cases are presented in Figure 5.16, showing the trend of the separation angle corresponding to the change of the corner radius. Since for the cube the incoming flow always separates from the leading edge, the separation angle for this case ($R/L = 0$) is indeterminate, but for convenience is assigned the value to be 45°. As shown in Figure 5.16, as the corner radius increases from $R/L = 1/12$ to $2/5$, the separation location moves downstream as indicated by the increased values of θ. The largest separation angle is about 85° for the case with $R/L = 2/5$, which is slightly higher than that for the sphere (82°), although the separation position for $R/L = 2/5$ is further upstream than that for the sphere. In addition, the separation angles shown in Figure 5.16 are all smaller than 90°, which means the incoming flow separates before it reaches the end of the leading corner. According to Figure 5.16, the variation of θ with the Reynolds number for each radius is not monotonic. These separation angles are more sensitive to the Reynolds number for $R/L = 1/12$ and $1/6$ than for larger corner radii. However, the arc lengths involved are smaller for small values of R. The flow separation is closely related with the distribution of the surface pressure, which will be discussed in the Section 5.3.3 together with illustrations of the separation line on the cube surfaces.

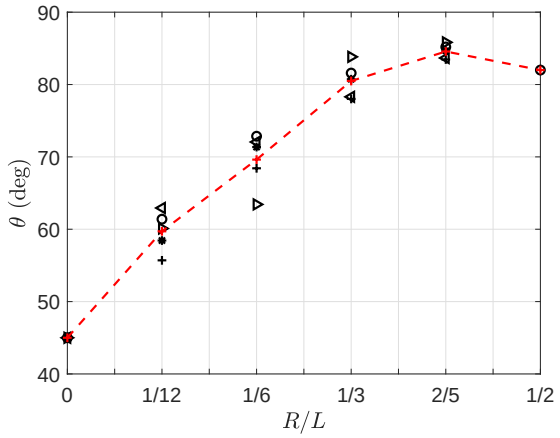

Figure 5.16: The trend of the separation angle (θ) varying with the corner radius (R). $\circ$: $Re = 50,000$; $*$: $Re = 75,000$; $+$: $Re = 100,000$; $\triangleleft$: $Re = 150,000$; $\triangleright$: $Re = 200,000$; $-+-$: Average value

5.3.2.3 Recirculation length in the wake

The recirculation length (L_r) in the wake is measured from the rear surface to the location on the centreline ($y = 0, z = 0$) where the mean streamwise velocity recovers from negative values to zero. As can seen from Figure 5.13 and Figure 5.15, the recirculation length changes considerably with the variation of both R/L and Re. The velocity profiles in the wake of the cube along the centreline can be used to determine the values of L_r. Summaries of the recirculation length in the wake, including the average trend of L_r as it changes with the corner radius, are displayed in Figure 5.17. The recirculation length reduces significantly once the cube corners are rounded with a radius of $R/L = 1/12$. With the further increase of R/L from 1/12 to 2/5, the value of L_r drops at a slower rate but it increases again for the sphere. The recirculation length in the wake is roughly inversely proportional to the base pressure coefficient (C_{pb}) (Bearman, 1965), which is derived from the pressure directly at the back of the object and is discussed in the following Section 5.3.3. In addition, the formation of the circulation bubble in the wake of the cubes is strongly dependent on the Reynolds number, but no systematic dependence could be found for the studied cases. The recirculation length for $R/L = 2/5$ fluctuates the most.

5.3.3 Pressure distributions along the cube surfaces

The position of the flow separation is closely related to the pressure gradient along the cube surfaces since the flow separates when the adverse pressure gradient in the boundary layer is sufficient. The surface pressure distributions in the $z = 0$ plane are displayed in Figure 5.18(a) for different corner radii at the Reynolds number of 50,000. Figure 5.18(b) shows the pressure distribution for $R/L = 1/12$ at different Reynolds

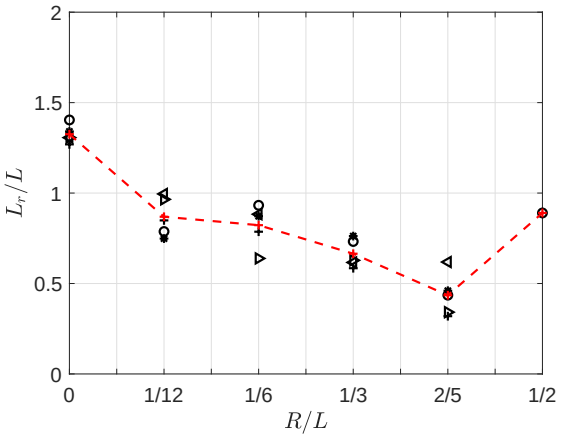

Figure 5.17: The trend of the recirculation length (L_r) varying with the corner radius (R). ∘: $Re = 50,000$; ∗: $Re = 75,000$; +: $Re = 100,000$; ◁: $Re = 150,000$; ▷: $Re = 200,000$; $-+-$: Average value

numbers. The pressure distributions in Figure 5.18(a) and Figure 5.18(b) start from the frontal stagnation point and the abscissa is the distance around the surface normalised by one quarter of the perimeter.

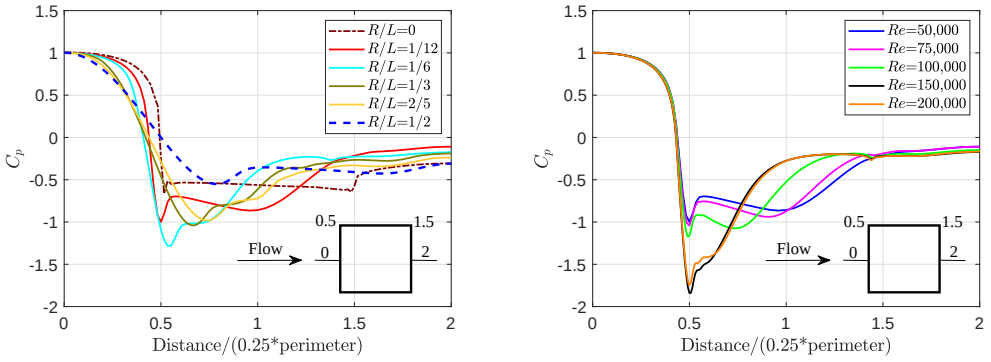

(a) $Re = 50,000$ (b) $R/L = 1/12$

Figure 5.18: Distributions of the mean pressure coefficient (C_p) along cube surfaces in the $z = 0$ plane.

As can be seen from Figure 5.18(a), the value of the minimum pressure coefficient ($C_{p,\min}$) changes significantly for different corner radii. The variation of $C_{p,\min}$ for all the investigated cases is summarised in Figure 5.19(a). The values of $C_{p,\min}$ for cubes with rounded corners are smaller than that for the cube and the sphere. In addition, $C_{p,\min}$ becomes less sensitive to Reynolds number with the increase of the corner radius. The trends of $C_{p,\min}$ at different Reynolds numbers in Figure 5.19(a) are strongly linked to that for the separation angle shown in Figure 5.16. Large variations of $C_{p,\min}$ imply differences in pressure recovery and adverse pressure gradients, which lead to considerable changes of the flow separation.

With the increase of the corner radius, the position of the minimum pressure coefficient ($C_{p,\min}$) gradually moves downstream as seen in Figure 5.18(a), giving a large region of favourable pressure gradient, which helps in delaying flow separation. This is consistent with the trend of the separation angle shown in Figure 5.16, apart from the slight drop in the separation angle for the sphere. As illustrated in Figure 5.18(b), the position of $C_{p,\min}$ is almost independent of the Reynolds number for the case of $R/L = 1/12$. The variations of the position of $C_{p,\min}$ are also very small for the other rounded cubes at different Reynolds numbers, as plotted in Figure 5.19(b) against the corner radius. The steepest increase can be found between $R/L = 1/6$ and $1/3$.

The base pressure coefficients (C_{pb}), are summarised in Figure 5.19(c). C_{pb} increases when the cube is rounded with $R/L = 1/12$, but drops as the corner radius is further increased. In addition, C_{pb} for the cubes with smaller rounded radius tends to be more affected by changes in the Reynolds number. However, the variation of $C_{p,\min}$ with the Reynolds number for each rounded cube observed in Figure 5.19(a) has the opposite trend to the corresponding change of the mean drag coefficient shown in Figure 5.8(a). This suggests the value of $C_{p,\min}$ is more responsible for the change in $\overline{C}_d$ than the base pressure coefficient in the cases studied here, since $C_{p,\min}$ affects the pressure distribution near the leading corner on the front surface.

As shown in Figure 5.18(b), the value of $C_{p,\min}$ for the cube with $R/L = 1/12$ drops significantly when Re is increased from $100,000$ to $150,000$ along with a more rapid recovery of the negative pressure. This large reduction in $C_{p,\min}$ leads to the corresponding large increase of the separation angle shown in Figure 5.16. Consequently, the flow patterns close to the cube surfaces change considerably with Re. To identify the reasons, Figure 5.20 compares the pressure contours on the lateral surface of the cube with $R/L = 1/12$ for $Re = 100,000$ and $150,000$ and also the mean streamlines obtained from the first layer of the mesh on the lateral surface. Critical points (Node and Saddle) characterising the flow topology are also labelled in Figure 5.20. The dotted white rectangle denotes the flat part of the surface and the white solid line shows locations of zero streamwise velocity. As can be seen, with the increase of the Reynolds number from $100,000$ to $150,000$, the separation line moves downstream to reach the flat part (the dotted rectangle). A Node labelled 'N3' can be seen at $Re = 100,000$ in Figure 5.20(a) and two vortices are formed beside it near the leading edge of the dotted rectangle, namely, at the end of the leading corner. However, the Node 'N3' disappears at the higher Reynolds number shown in Figure 5.20(b), together with these two vortices beside it. Nodes 'N1' and 'N2' formed near the side corners move upstream as does the Saddle 'S1'. In summary, the pressure distribution on the cube surfaces is Reynolds number dependent, which affects positions of the flow separation. The flow topology close to the cube changes correspondingly.

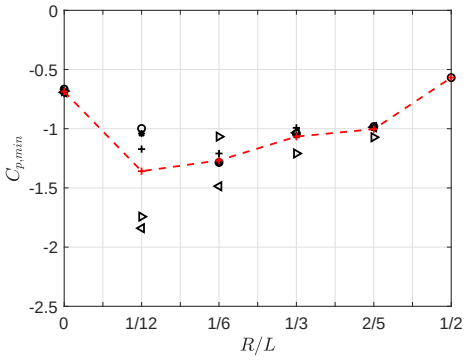

(a) Minimum pressure coefficient ($C_{p,\min}$)

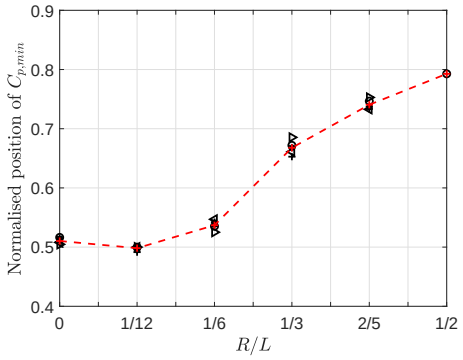

(b) Normalised position of $C_{p,\min}$

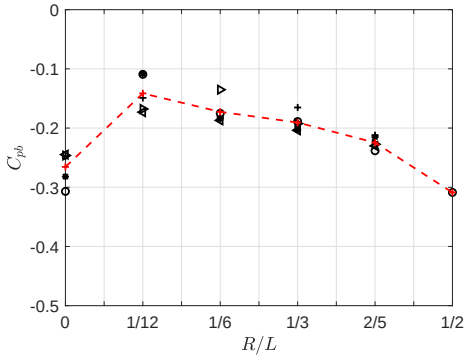

(c) Base pressure coefficient

Figure 5.19: Main features of the pressure distribution along cube surfaces in the $z = 0$ plane. $\circ$: $Re = 50,000$; $*$: $Re = 75,000$; $+$: $Re = 100,000$; $\triangleleft$: $Re = 150,000$; $\triangleright$: $Re = 200,000$; $-+-$: Average value

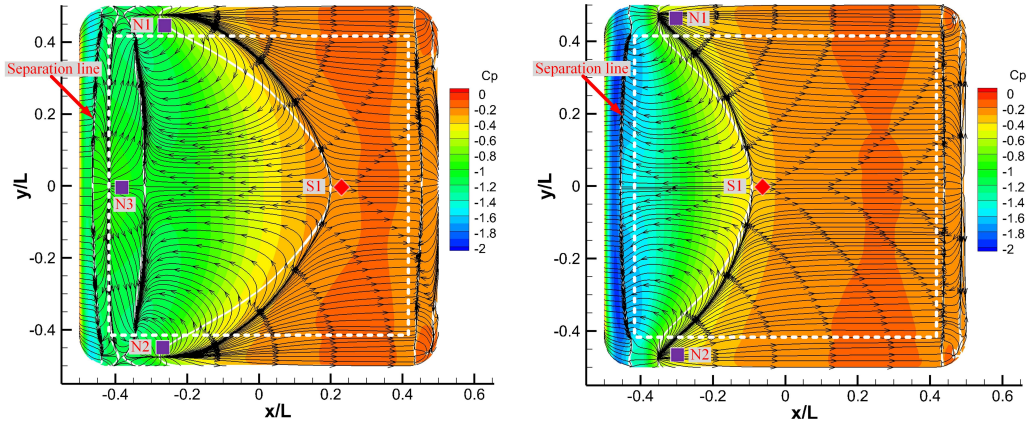

(a) $Re = 100,000$ (b) $Re = 150,000$

Figure 5.20: Mean streamlines and pressure contours close to the lateral surface of the cube with $R/L = 1/12$ at different Reynolds numbers (square: node; diamond: saddle)

5.3.4 Pressure fluctuations on the cube surfaces

Contours of the rms pressure fluctuations (p_{rms}) on the lateral surfaces are shown in Figure 5.21 for $Re = 50,000$, together with the flow patterns represented by the time-averaged streamlines obtained from the first layer mesh beside the lateral surface. In Figure 5.21, the rms values of the surface pressure are given in dB (see Equation (4.11))

Due to the symmetry of the objects, only the flat parts of the frontal and the rear surfaces cannot be observed from Figure 5.21. However, the pressure fluctuations on the flat part of the frontal area caused by the flow impingement are about 35 dB lower than the highest fluctuation observed on the lateral surfaces, while those on the flat part of the rear surface are about 15 dB lower. Therefore, these parts have little influence on the radiated noise.

As can be seen from Figure 5.21, the distribution of the pressure fluctuations changes significantly with the increase of the corner radius. For the cube in Figure 5.21(a), the strongest pressure fluctuation occurs close to the trailing edge where the secondary vortex forms (see Figure 5.13(a)), represented by Saddle 'S1' and Nodes 'N1' and 'N2'. For the case with $R/L = 1/12$ in Figure 5.21(b), the separated flow partially reattaches to the lateral surface with Nodes 'N4' and 'N5' appearing. The largest values of p_{rms} are found around the white lines close to Nodes 'N1' and 'N2', implying locations of flow reattachment. For larger corner radii, $R/L = 1/6$ to $2/5$, as shown in Figure 5.21(c) - 5.21(e), the separated flow completely reattaches to the lateral surface with a recirculation bubble being generated and high pressure fluctuations being observed inside the recirculation region. The highest fluctuating pressure in the recirculation bubble close to the lateral surface is observed for $R/L = 1/6$ in Figure 5.21(c). The size of the recirculation bubble reduces with the further increase of the corner radius as shown previously in Figure 5.13(c) - 5.13(e), and so does the pressure fluctuation inside it. In addition, due to the shortened recirculation length formed in the wake of the rounded cube with larger corner radius, as shown in Figure 5.17, the pressure fluctuations close to the rear corner increase.

To show the effect of Reynolds number, Figure 5.22 displays flow patterns and contours of the pressure fluctuation on the lateral surface for $R/L = 1/6$. Due to the similar position of the separation line, flow patterns observed in Figure 5.21(c) and Figure 5.22(a)-5.22(c) are similar. This is despite the different size of the recirculation region indicated by the white solid line, inside which high pressure fluctuations are observed. However, the separation line moves upstream considerably from $Re = 150,000$ to $Re = 200,000$, which is consistent with the drop in the corresponding separation angle seen in Figure 5.16. Consequently, a Node 'N3' and two additional vortices appear close to the leading edge of the flat surface in Figure 5.22(d) and the level of pressure fluctuations near this location reduces significantly. In addition, variations of the pressure fluctuation close to the rear rounded corners can also be observed in Figure 5.22, which are caused by the

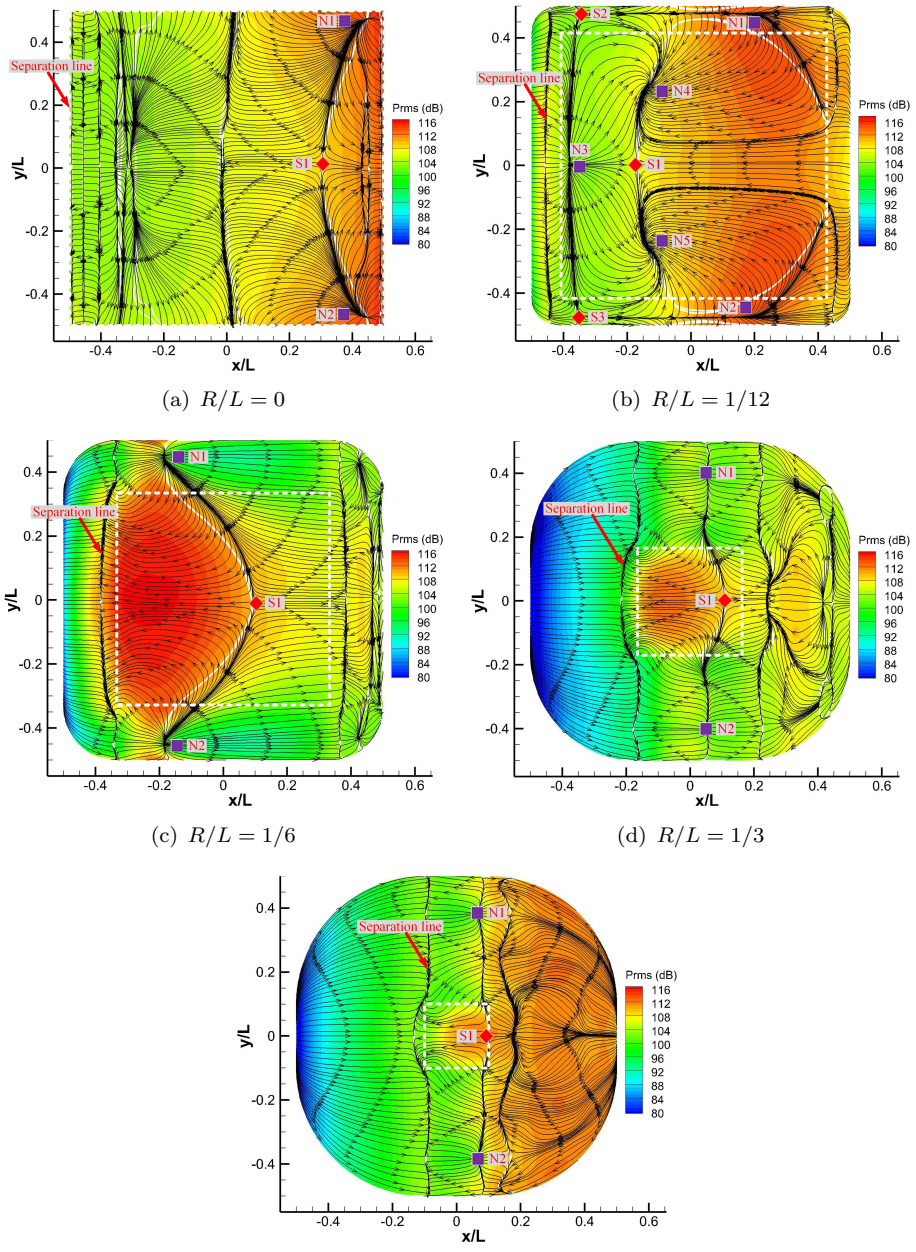

(a) $R/L = 0$ (b) $R/L = 1/12$

(c) $R/L = 1/6$ (d) $R/L = 1/3$

(e) $R/L = 2/5$

Figure 5.21: Mean streamlines and contours of pressure fluctuations on the lateral surface of cube and rounded cubes at $Re = 50,000$. (square: node; diamond: saddle)

different sizes of the recirculation region formed in the wake, as shown in Figure 5.17. As described above, the distribution of the pressure fluctuation is strongly related to the flow structures close to the cube surfaces, which are dependent on both the corner radius and the Reynolds number. In summary, high pressure fluctuations are associated with the formation of the secondary vortex for the flow pattern 1 shown in Figure 5.14(a) while the recirculation bubble, the flow reattachment on the lateral surfaces and also the shortened recirculation length in the wake are responsible for high values of p_{rms} for

the flow pattern 2 in Figure 5.14(b).

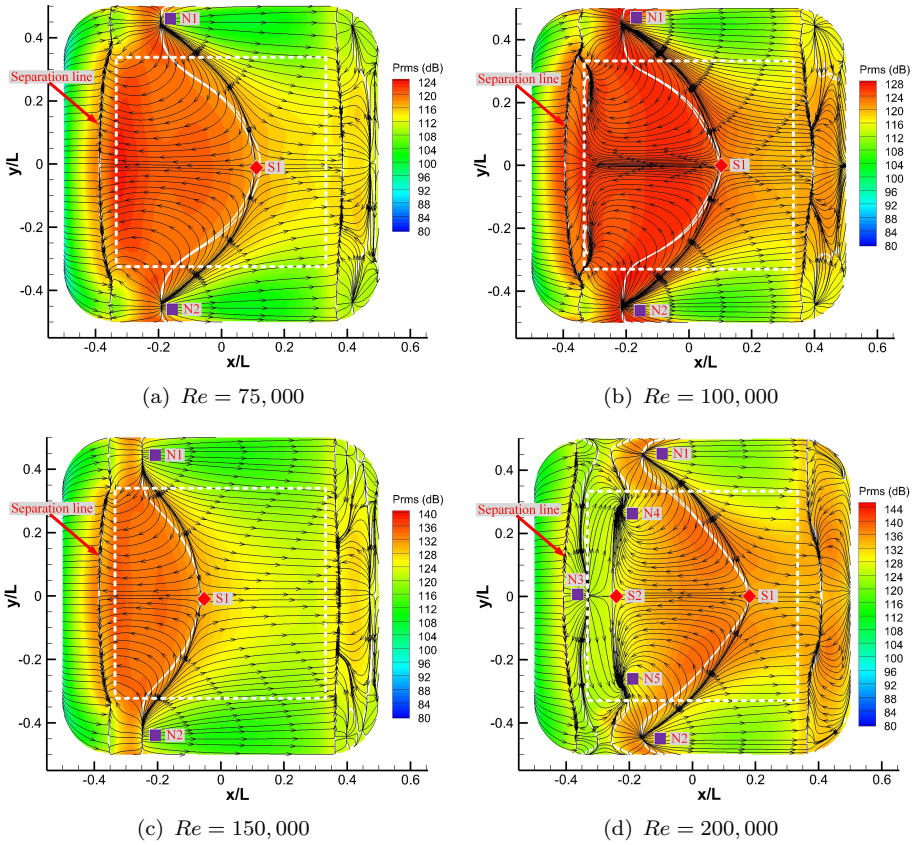

(a) $Re = 75,000$ (b) $Re = 100,000$

(c) $Re = 150,000$ (d) $Re = 200,000$

Figure 5.22: Mean streamlines and contours of pressure fluctuations on the lateral surface of the rounded cube with $R/L = 1/6$ at different Reynolds numbers. (square: node; diamond: saddle)

Although the rms value of the surface pressure cannot be equated with the noise source, this statistical parameter gives an indication of the strength of the dipole source. To illustrate the overall level of the pressure fluctuations covering different p_{rms} distributions, the value of p_{rms}^2 from each cell on the cube surface is integrated to give:

$$L_{p,\text{int}} = 10\log_{10}\left(\frac{\int_S p_{\text{rms}}^2 dS}{p_{\text{ref}}^2}\right) \tag{5.1}$$

where $p_{\text{ref}} = 2 \times 10^{-5}$ Pa and S is the overall surface of the cube. Figure 5.23 shows values of $L_{p,\text{int}}$ obtained from all the cases studied. For each Reynolds number the highest value of $L_{p,\text{int}}$ is observed for $R/L = 1/12$, while the lowest value is found at $R/L = 1/3$. The overall trend of $L_{p,\text{int}}$ with the corner radius is similar for lower Reynolds numbers from $Re = 50,000$ to $100,000$. However, $L_{p,\text{int}}$ changes more rapidly with R/L at $Re = 150,000$ and $200,000$.

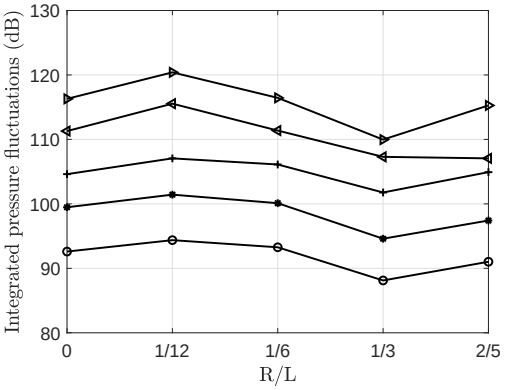

Figure 5.23: The trend of the integrated pressure fluctuations ($L_{p,\text{int}}$) varying with the corner radius (R). —o—: $Re = 50,000$; —*—: $Re = 75,000$; —+—: $Re = 100,000$; —◀—: $Re = 150,000$; —▶—: $Re = 200,000$

5.4 Noise from cubes with rounded corners

Having studied the flow behaviours in detail, in this section the radiated noise is predicted. Since the largest Mach number studied in this chapter is less than 0.12, only dipole sources are considered in the noise prediction. The fluctuating pressure on the cube surfaces is obtained from the CFD simulations, and the far-field noise is predicted using the FW-H acoustic analogy in the commercial software FLUENT. Since the surface integration is adopted in the FW-H acoustic analogy in FLUENT (ANSYS, 2011), the distribution of the fluctuating pressure on the cube surfaces due to the acoustic non-compactnesss is taken into account. However, the noise scattering phenomenon is not considered in this work, because use is made of the free-space Green's function embedded in FLUENT, rather than the geometry-tailored Green's function.

The far-field noise is obtained at 10 m ($133L$) from the centre of the cube at different receivers. Figure 5.24 shows the 1/3 octave band spectra of the predicted noise at (10, 0, 0) in the streamwise direction and (0, 10, 0) in the cross-flow direction for cubes with rounded corners at $Re = 200,000$. The sound pressure level (SPL) in the frequency domain changes considerably as the corner radius is varied and is also affected by the position of the receivers. Compared with the noise spectrum of the cube $R/L = 0$, the sound for $R/L = 1/12$ and 1/6 drops by up to about 10 dB for frequencies lower than $St = 0.6$ and the highest noise level is observed close to $St = 1$. However, for the cubes with larger corner radii ($R/L = 1/3$ and 2/5), the highest sound level occurs at frequencies lower than $St = 0.6$ and the noise at Strouhal numbers greater than 1 decreases rapidly with increasing frequency. In general, the noise levels at Strouhal numbers less than 0.6 observed at (0, 10, 0) are higher than those at (10, 0, 0), while the opposite trend occurs for $St \geq 1$.

The SPL at $St = 10$ is around 20 dB or more lower than the maximum level of the spectrum in each case. This is also the case for the other Reynolds numbers studied.

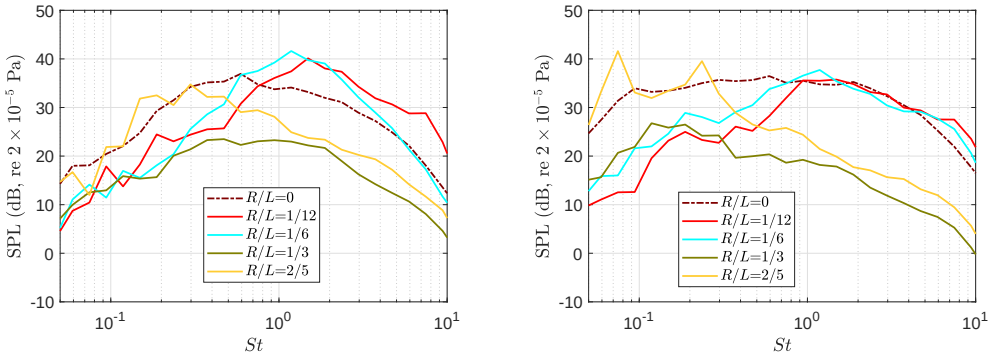

(a) Receiver (10, 0, 0) (b) Receiver (0, 10, 0)

Figure 5.24: 1/3 octave band sound pressure spectra for rounded cubes at $Re = 200,000$

Consequently, the OASPL can be calculated by integrating the noise PSD up to a Strouhal number of 10. The OASPLs at receivers (10, 0, 0) and (0, 10, 0) are shown in Figure 5.25 with respect to the corner radius at different Reynolds numbers. The solid lines in Figure 5.25 represent the far-field noise at (10, 0, 0) in the streamwise direction, while the dotted lines are for the receiver at (0, 10, 0) in the cross-flow direction. In general, the overall trends of the OASPL are consistent with those of the integrated pressure fluctuations shown in Figure 5.23. Although the lowest noise level is always observed for $R/L = 1/3$ in Figure 5.25, similar to the results for $L_{p,\mathrm{int}}$, the highest sound level is not always found for $R/L = 1/12$. The OASPLs at (10, 0, 0) and (0, 10, 0) are similar to each other for cubes with corner radii ranging from $R/L = 0$ to 1/3, while larger differences between the noise levels are observed for $R/L = 2/5$.

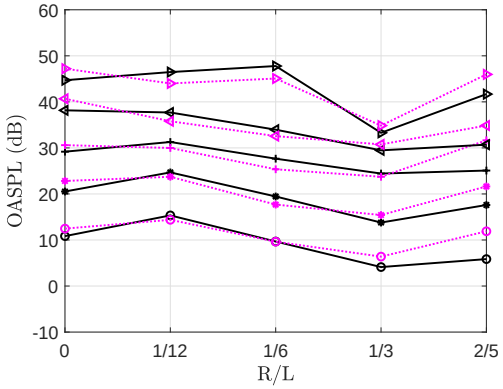

Figure 5.25: The predicted OASPL. ——: receiver (10, 0, 0); .....: receiver (0, 10, 0); ○: $Re = 50,000$; ∗: $Re = 75,000$; +: $Re = 100,000$; ◁: $Re = 150,000$; ▷: $Re = 200,000$

Figure 5.26 shows the speed dependence of the OASPL at (10, 0, 0) and (0, 10, 0) for different corner radii. As can be seen, the far-field noise grows at a rate close to $60\log U_\infty$, especially the sound from the cube. Based on the sixth power law of the flow

speed observed in Figure 5.26, the OASPLs at (10, 0, 0) and (0, 10, 0) at different flow speeds are corrected to 40 m/s ($Re = 200,000$) and compared in Figure 5.27. As the corner radius is increased from $R/L = 1/12$ to $1/3$, the noise emitted to the far field decreases rapidly at both receivers. However, the sound level increases when the corner radius is further increased to $R/L = 2/5$. Although the sound pressure levels are corrected to correspond to the same flow speed, differences of up to 10 dB are found between the OASPL calculated at $U_\infty = 40$ m/s ($Re = 200,000$) and that corrected from other flow speeds. In summary, the sound emitted from rounded cubes with different corner radii approximately follows the sixth power law of the flow speed. When the corner radius is in the range from $R/L = 1/12$ to $1/3$, increasing the corner radius is an effective way to mitigate the far-field noise. However, with the further increase of the corner radius, the emitted noise may increase again.

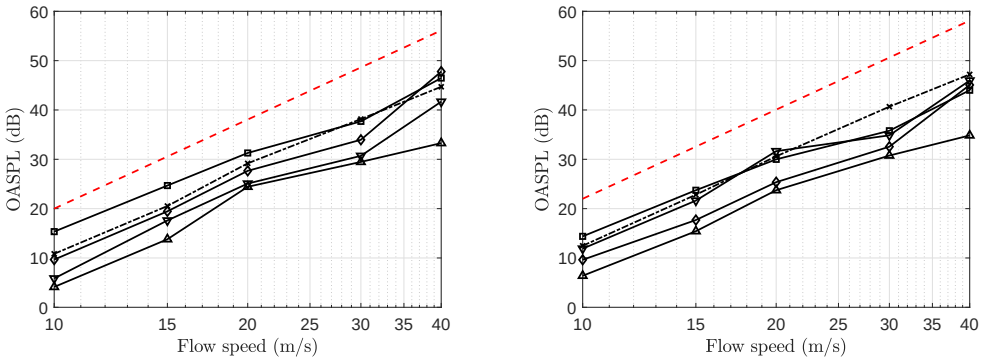

(a) Receiver (10, 0, 0) (b) Receiver (0, 10, 0)

Figure 5.26: Speed dependence of the OASPL. -·-·-: $R/L = 0$; —■—: $R/L = 1/12$; —◇—: $R/L = 1/6$; —△—: $R/L = 1/3$; —▽—: $R/L = 2/5$; - - -: $60\log U_\infty$

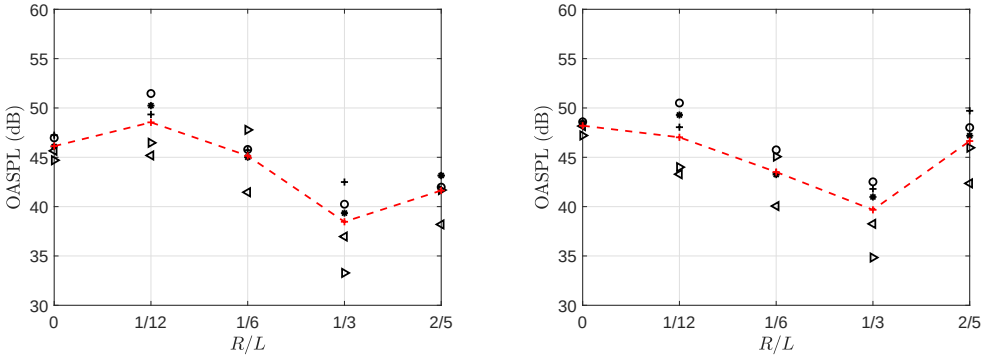

(a) Receiver (10, 0, 0) (b) Receiver (0, 10, 0)

Figure 5.27: OASPL at the streamwise and the cross-flow receivers corrected to be at $Re = 200,000$. ○: $Re = 50,000$; ∗: $Re = 75,000$; +: $Re = 100,000$; ◁: $Re = 150,000$; ▷: $Re = 200,000$; − + − : Average value

The sound directivities in the $z = 0$ plane for rounded cubes with different corner radii are shown in Figure 5.28. These are obtained from the predicted OASPLs at 72 different

receivers distributed on a circle 10 m away from the cube centre with a spacing of 5°. These OASPLs at different flow speeds are corrected to correspond to 40 m/s based on the sixth power law of the flow speed. The directivity for $R/L \leq 1/3$ tends to be omni-directional. However, the sound directivity for $R/L = 2/5$ closer to that of a typical dipole with greater sound level observed in the cross-flow direction.

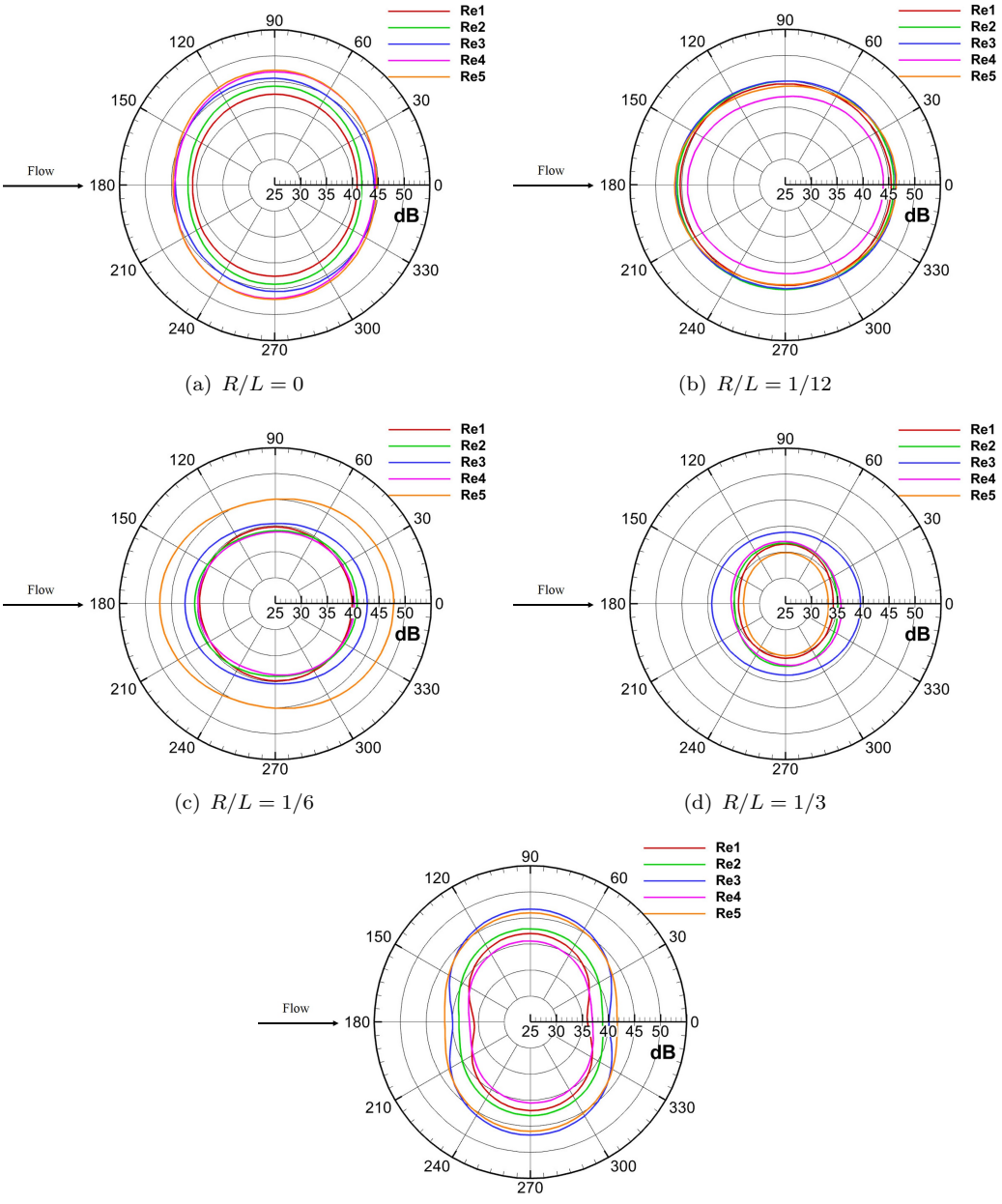

(a) $R/L = 0$ (b) $R/L = 1/12$

(c) $R/L = 1/6$ (d) $R/L = 1/3$

(e) $R/L = 2/5$

Figure 5.28: Sound directivity in the $z = 0$ plane normalised to $Re = 200,000$ ($Re1 = 50,000$, $Re2 = 75,000$, $Re3 = 100,000$, $Re4 = 150,000$, $Re5 = 200,000$)

5.5 Summary

The flow past cubes with rounded corners is investigated numerically in this chapter. The noise emitted to the far field is also examined. A benchmark case on the flow past a sphere is first compared with available results in the literature to validate the adopted numerical methodology. Subsequently, simulations on cubes with rounded corners ranging from $R/L = 0$ to $2/5$ at Reynolds numbers from 50,000 to 200,000 are presented. The DDES approach is adopted to investigate the flow characteristics. Based on the fluctuating pressure sampled from the CFD, the far-field noise is then predicted using the FW-H acoustic analogy.

The mean drag coefficient drops significantly when the cube is rounded with $R/L = 1/12$. However, its value does not change monotonically with the increase of the corner radius and the lowest value is observed for $R/L = 1/3$. The variation of the minimum pressure coefficient ($C_{p,\mathrm{min}}$) is found to be more responsible for the change of the mean drag coefficient than that of the base pressure coefficient is. The rms values of the drag and the lift coefficients are more dependent on R/L and Re than the mean values and $C_{l,\mathrm{rms}}$ is always higher than $C_{d,\mathrm{rms}}$. Periodic vortex shedding is more evident in the wake of the rounded cube with $R/L = 2/5$, leading to large values of $C_{l,\mathrm{rms}}$ and significant fluctuations. Flow patterns around the cubes change significantly with the variation of both the corner radius and the Reynolds number. In general, the separation point at the leading corner moves downstream with the increase of the radius, while the separated bubble moves closer to the lateral surfaces and the recirculation length formed in the wake reduces. The distribution of pressure fluctuations is strongly related with the near-wall flow patterns. A decreased size of the recirculation region in the wake and the flow reattachment on the lateral surface can cause large pressure fluctuations.

The emitted noise generally increases with the sixth power of the flow speed. The introduction of the rounded corners changes the shape of the noise spectrum. The emitted noise is reduced significantly with the increase of the corner radius from $R/L = 1/12$ to $1/3$, but the sound level goes up again for a further increase in corner radius to $R/L = 2/5$. This implies that corner rounding may be an effective way to mitigate the noise emitted from a cube, although care is needed in determining the corner radius.

Chapter 6

The effect of aspect ratios of a cuboid

Bluff bodies closely resembling cuboids with different aspect ratios are also important components in the train bogies and pantographs. The flow around cuboids or finite length square cylinders differs considerably from that for infinite square cylinders and hence so does the emitted noise. In this chapter, the effect of the aspect ratios on the flow past cuboids in free space and also on the far-field noise is investigated numerically. As in the previous chapters, DDES is adopted in OpenFOAM to study the flow characteristics and the FW-H acoustic analogy in FLUENT is used for the noise predictions.

6.1 Computational setup

The length, height and width of the cuboid are represented by L, H and W respectively. The height of the cuboid (H) in the cross-flow direction along the $y-$ axis is used as the characteristic length, which is kept constant as 75 mm for all cases. The aspect ratio is defined as the width of the cuboid in the spanwise direction over its length in the streamwise direction, namely, W/L. A series of aspect ratios are taken into account ranging from 1/6 to 12 (1/6, 1/3, 1/2, $1/\sqrt{2}$, 1, $\sqrt{2}$, 2, 3, 6, 12) and Figure 6.1 illustrates geometries of the cuboids with different aspect ratios. The origin of the coordinate locates at the center of cuboids, while L, H and W are along the $x-$, $y-$ and $z-$ axes respectively. For cases with $W/L < 1$, the cuboid width W in the $z-$ direction is kept the same as the height (H), 75 mm, and the cuboid length L in the $x-$ direction is increased accordingly as shown in Figure 6.1(a). In contrast, when $W/L > 1$, the length L is kept constant as 75 mm and the width W is varied to obtain different aspect ratios as illustrated in Figure 6.1(c). In Particular, when $W/L = 1$ shown in Figure 6.1(b), the cuboid becomes a cube.

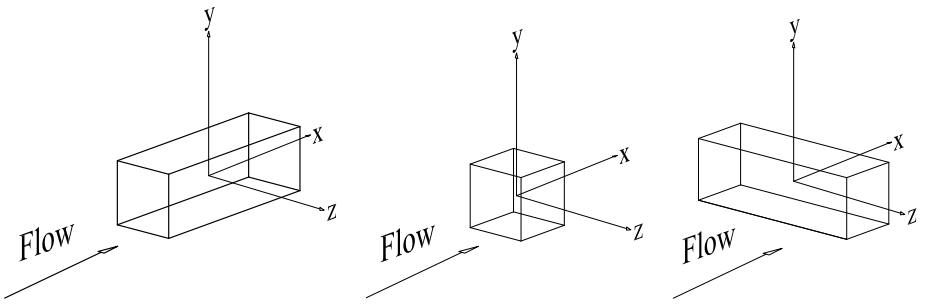

(a) $W/L < 1$ (b) $W/L = 1$ (cube) (c) $W/L > 1$

Figure 6.1: Illustrations of cuboids with different aspect ratios

A sketch of the computational domain together with the assigned boundary conditions is shown in Figure 6.2. Three incoming flow velocities are considered, $U_\infty = 10$ m/s, 20 m/s and 40 m/s. The corresponding Reynolds numbers are $Re = U_\infty H/\nu = 50,000$, $100,000$ and $200,000$ respectively, even though they are smaller than the highest Re cared about for high speed trains. Since the incoming flow speed is low, the flow is assumed to be incompressible. In addition, as depicted in Figure 6.2, $Velocity\,Inlet$, $Pressure\,Outlet$, $Symmetry\,Plane$ and $No-slip\,wall$ are assigned as the boundary conditions for the numerical simulations.

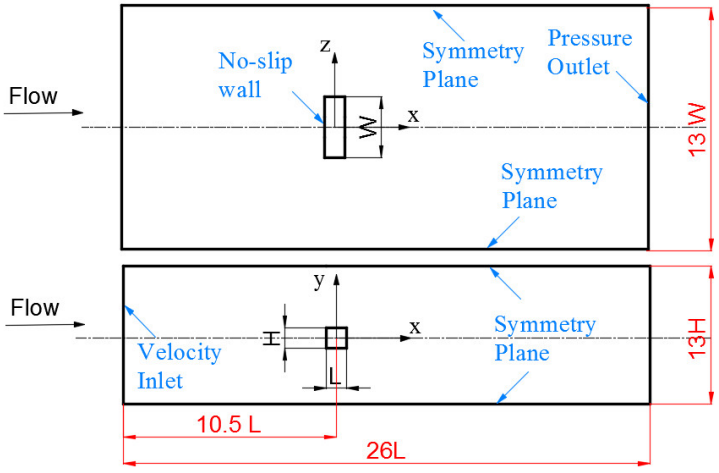

Figure 6.2: Sketch and boundary conditions of the computational domain

Fully-structured meshes are generated based on the spatial resolution obtained from the benchmark case on the wall-mounted cube presented in Section 4.1. Figure 6.3 illustrates the mesh for the $W/L = 12$ as examples. The grid blocks surrounded by the red rectangle in Figure 6.3(a) are displayed in Figure 6.3(b). Details of the grid resolution are presented in Table 6.1. The non-dimensional first cell height at the wall (y_1^+) is targeted to be 1.5, based on which the height of the first layer grid (Δ_{y1}) normal to the wall can be calculated. The finest grids are used at the cuboid surfaces and these are progressively increased using a stretch ratio of 1.09 further from them. The minimum grid spacing along sides of the cuboid ($\Delta_{\min(x1,z1)}$) is at the sharp corners,

while the maximum spacing ($\Delta_{\max(x1,z1)}$) is at the middle of sides. The resolution is increased gradually from the corner to the middle. For $W/L \neq 1$, the value of L or W is increased accordingly. Therefore, although the minimum resolution along each side is the same, the maximum value increases in proportion to the side length. Consequently, for different aspect ratios, a range of values for the $\Delta_{\max(x1,z1)}$ in the middle of the sides is used as shown in Table 6.1.

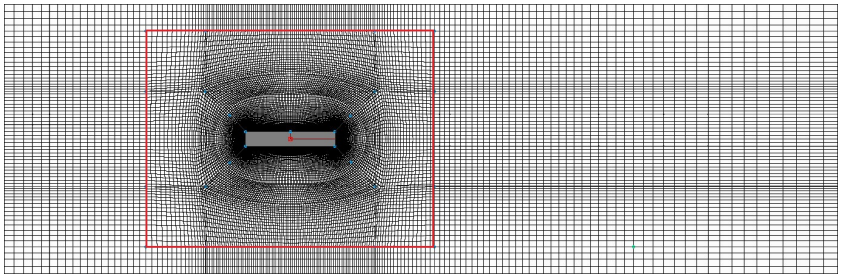

(a) Cells in the $z = 0$ plane

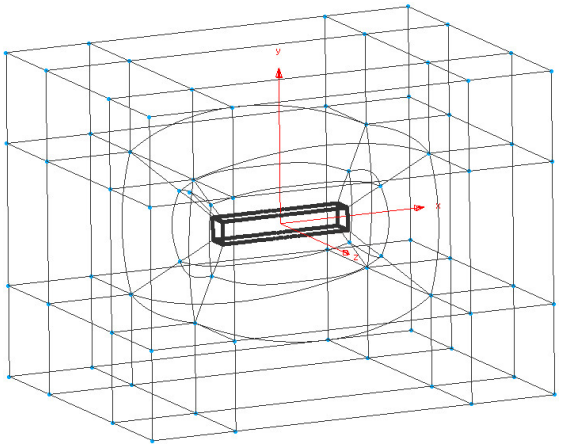

(b) Mesh topology

Figure 6.3: Illustrations of the mesh for the $W/L = 12$

U_∞ (m/s)	targeted y_1^+	Δ_{y1}/H	$\Delta_{\min(x1,z1)}/H$	$\Delta_{\max(x1,z1)}/H$
10	1.5	5.67×10^{-4}	2.67×10^{-2}	4.67 - 13.3 $\times 10^{-2}$
20	1.5	3.00×10^{-4}	1.84×10^{-2}	3.20 - 11.3 $\times 10^{-2}$
40	1.5	1.57×10^{-4}	0.97×10^{-2}	1.67 - 8.00 $\times 10^{-2}$

Table 6.1: Details of the grid resolution

To gain confidence in the above described mesh resolution in addition to the benchmark case on the wall mounted cube in Section 4.1, grid dependence investigations are conducted on the bounding cases with $W/L = 1/6$ and 12 at $Re = 50,000$. The grid resolution for these two bounding cases is either coarsened and refined respectively by a ratio of $\sqrt{2}$ to obtain the new mesh. The total number of cells (N_{grid}) for the coarse, original and finer meshes can be found in Table 6.2. The frontal area, namely $A = W \times H$, is

adopted as the reference area to calculate the drag, lift and side-force coefficients (C_d, C_l, C_s respectively) of the cuboids with different aspect ratios. Consequently for $W/L \leq 1$, $A = L^2$; whereas for $W/L > 1$, A increases in proportion to the aspect ratio. The mean drag coefficient ($\overline{C_d}$) and root-mean-square (rms) values of these aerodynamic coefficients for the meshes with different resolutions are shown in Table 6.2. These statistics are sampled from a normalised time $t^* = tU_\infty/H = 400$ to 1800. Due to the symmetry of the geometry, the mean lift and side-force coefficients are zero. As shown in Table 6.2, although some differences are seen between the coarse mesh and the original one, with further increase of the grid resolution, these aerodynamic coefficients only change slightly, which means the original mesh resolution in Table 6.1 is sufficient.

W/L	mesh	N_{grid}	$\overline{C_d}$	$C_{\text{d},rms}$	$C_{\text{l},rms}$	$C_{\text{s},rms}$
1/6	coarse	1.18×10^6	1.007	0.0171	0.0523	0.0508
1/6	original	1.71×10^6	0.980	0.0138	0.0434	0.0435
1/6	refined	3.16×10^6	0.971	0.0116	0.0392	0.0395
12	coarse	1.29×10^6	1.452	0.0897	0.0815	0.0123
12	original	1.79×10^6	1.509	0.0551	0.0865	0.0119
12	refined	3.90×10^6	1.525	0.0538	0.0857	0.0117

Table 6.2: Grid dependence investigations on the bounding cases at $Re = 50,000$

For aspect ratios greater than 1, the overall grid size grows with the increase of the aspect ratio and the Reynolds number, while it decreases for larger W/L when the aspect ratio is smaller than unity. The overall grid sizes are similar for cases with reciprocal values of W/L at the same Reynolds number. The total number of grid cells for the cuboid with $W/L = \sqrt{2}$ at $Re = 50,000$ is 780,000 increasing to 7.8 million for the case with $W/L = 12$ at $Re = 200,000$. During 60 hours wall time, about 5 physical seconds ($t^* = t * U_\infty/H \approx 667$) are calculated using 160 cores for the cuboid with $W/L = \sqrt{2}$ at $Re = 50,000$, while about 0.4 seconds only ($t^* \approx 213$) for the $W/L = 12$ at $Re = 200,000$. Generally, statistics in this chapter is calculated up to about $t^* = 2000$ at different Reynolds numbers. It is ensured that the maximum value of the non-dimensional first cell height at the wall (y_1^+) is less than 2, while most of the values are smaller than 1 with an average of about 0.7. Distributions of y_1^+ around the cuboid with $W/L = 12$ at $Re = 200,000$ are shown in Figure 6.5 as examples. The time step for simulations in this chapter is again 1×10^{-5} s, with corresponding CFL numbers smaller than 2. The numerical schemes adopted in this chapter are also the same as those described in previous chapters. For comparison, the results for the cube at flow speeds of 10 m/s, 20 m/s and 40 m/s obtained from Chapter 5 are also presented in the following sections of this chapter. Figure 6.4 illustrates the performance of the DDES model in the $z = 0$ plane for the $W/L = 12$ at $Re = 100,000$ as examples, from which

the RANS mode is used up to about $0.2L$ from the cuboid surface. Unsmooth lines in Figure 6.4 is caused by the post processing in calculating f_d (see Equation (3.34)).

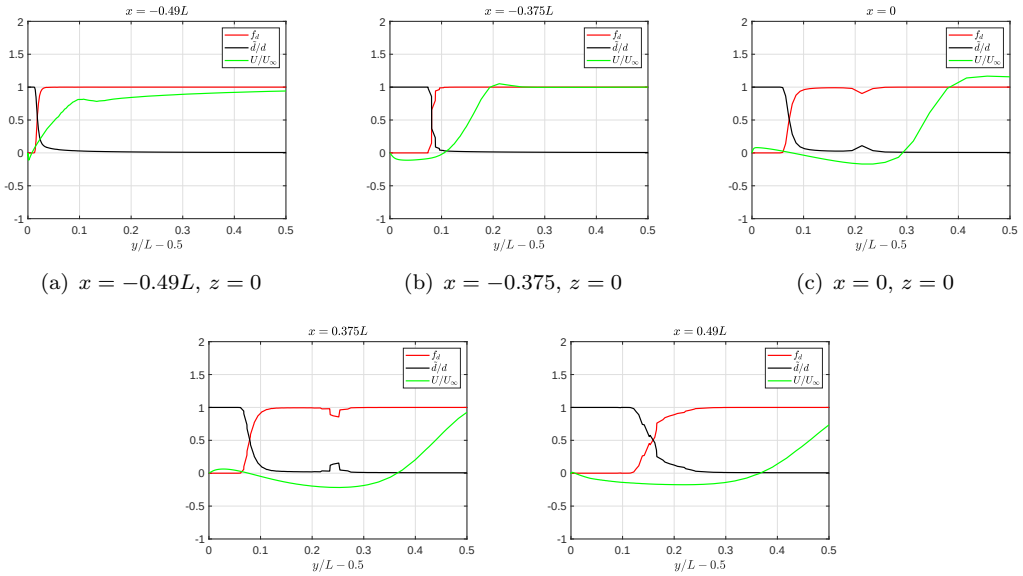

(a) $x = -0.49L$, $z = 0$ (b) $x = -0.375$, $z = 0$ (c) $x = 0$, $z = 0$

(d) $x = 0.375L$, $z = 0$ (e) $x = 0.49L$, $z = 0$

Figure 6.4: Performance of the DDES model for $W/L = 12$ at $Re = 100,000$

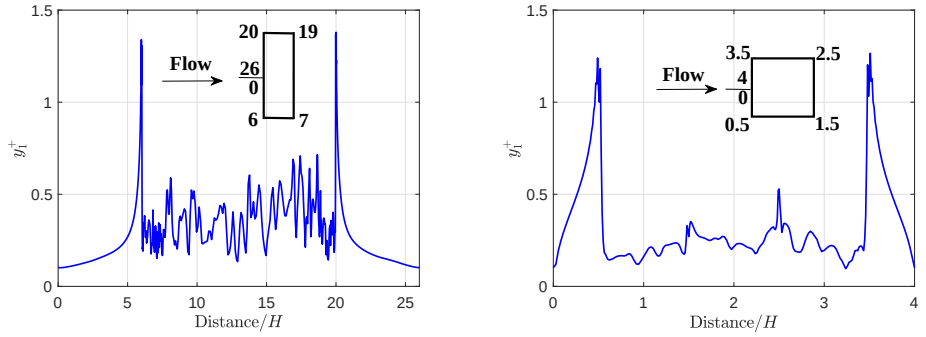

(a) $y = 0$ plane (b) $z = 0$ plane

Figure 6.5: The distribution of y_1^+ along the cuboid with $W/L = 12$ at $Re = 200,000$

6.2 The effect of the aspect ratio on the flow

6.2.1 Aerodynamic coefficients

The frontal area, namely $A = W \times H$, is adopted as the reference area to calculate the drag, lift and side-force coefficients of the cuboids with different aspect ratios. Consequently for $W/L \leq 1$, $A = L^2$; whereas for $W/L > 1$, A increases in proportion to the aspect ratio. Figure 6.6 shows time histories of C_d, C_l and C_s at $Re = 100,000$

from a normalised time $t^* = tU_\infty/H = 820$ to 900 for representative cuboids with $W/L = 1/6$, $1/\sqrt{2}$, 1, $\sqrt{2}$, 6, and 12 respectively. Main features of these times histories at $Re = 50,000$ and 200,000 are similar to those observed in Figure 6.6. As can be seen, the mean lift and side-force coefficients are very close to zero due to symmetry of the objects, while the mean drag coefficient ($\overline{C}_d$) is close to 1. In addition, once the aspect ratio exceeds 1, the drag coefficient grows for larger W/L, even though the reference area A also increases. With the increase of the aspect ratio, fluctuations of the lift coefficient change more significantly than the drag and side-force coefficients. Higher frequency fluctuations of C_l are seen for cuboids with $W/L < 1$, while the highest amplitude of C_l is observed in the case with $W/L = 6$.

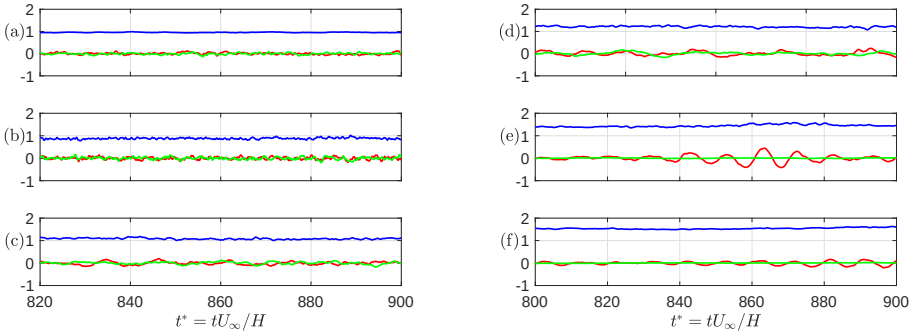

Figure 6.6: Time histories of C_d (blue), C_l (red) and C_s (green) at $Re = 100,000$ for aspect ratios (W/L) plotted against normalized time $t^\star$. From (a) to (f), $W/L = 1/6$, $1/\sqrt{2}$, 1, $\sqrt{2}$, 6, and 12, respectively

The $\overline{C}_d$ and root-mean square (rms) values of these aerodynamic coefficients for cuboids with all the studied aspect ratios calculated from time histories sampled from $t^* = 500$ to 2400 at different Reynolds numbers are presented in Figure 6.7. Also shown are the measured results of a square cylinder ($W/L = \infty$) at $Re = 100,000$ from experiments conducted by Vickery (1966). Aerodynamic coefficients of square cylinders tend to be consistent in the literature, therefore only the results obtained by Vickery (1966) are shown as examples. The trends of these aerodynamic coefficients with respect to the aspect ratio are similar at different Reynolds numbers. The mean drag coefficient is more independent of Reynolds number compared with the rms values of C_d, C_l and C_s, while the rms values tend to drop slightly at a higher Re.

For cuboids with $W/L < 1$, $\overline{C}_d$ reduces with the increase of W/L, and the mean drag coefficient of the cuboid with $W/L = 1/\sqrt{2}$ is the lowest of those shown in Figure 6.7(a). The value of $\overline{C}_d$ increases considerably from $W/L = 1/\sqrt{2}$ to 1 and it grows for further increase of W/L. The rms values of the drag and lift coefficients shown in Figure 6.7(b) and Figure 6.7(c) increase from $W/L = 1/6$ to 6 and tend towards the value for a square cylinder. However, the results for $W/L = 12$ drop below this trend line. According to Fox and West (1993), the 'infinite' condition of the cylinder can be achieved for

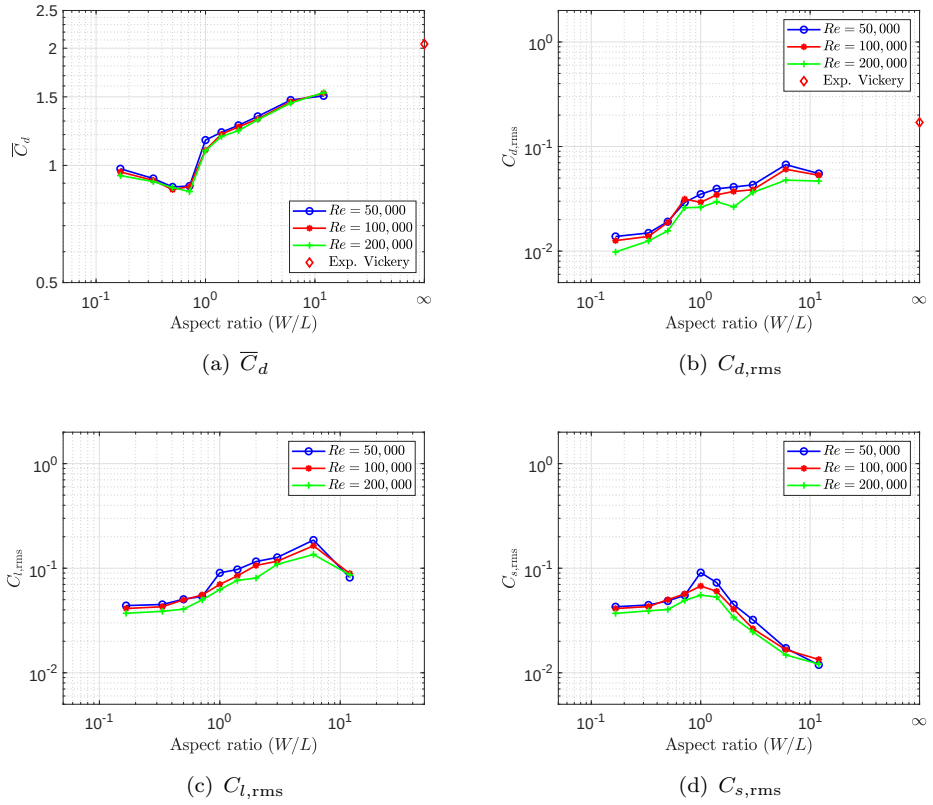

(a) $\overline{C}_d$ (b) $C_{d,\mathrm{rms}}$

(c) $C_{l,\mathrm{rms}}$ (d) $C_{s,\mathrm{rms}}$

Figure 6.7: The trend of aerodynamic coefficients changing with the aspect ratio at three Reynolds numbers and the measured results of the square cylinder at $Re = 100,000$ (Vickery, 1966)

aspect ratios greater than 30. The results for $C_{s,\mathrm{rms}}$ in Figure 6.7(d) show that, with the increase of W/L, it grows first to a maximum for the cube with $W/L = 1$. For $W/L > 1$, $C_{s,\mathrm{rms}}$ reduces roughly in proportion to W/L, since rms values of the side force remain roughly constant while the normalising area increase. Values of $C_{s,\mathrm{rms}}$ for infinite cylinders are not found in literature.

The PSDs of these aerodynamic coefficients are presented in Figure 6.8 for cuboids with representative aspect ratios at $Re = 100,000$ as examples. The spectra at the other Reynolds numbers show similar trends. As before, the PSDs are obtained using Welch's method. A Hanning window is applied with 50% overlapping and the frequency resolution is about 1.22 Hz ($St \approx 0.005$). The shapes of the PSDs for cuboids with $W/L < 1$ are similar to each other and only the bounding cases with $W/L = 1/6$ and $1/\sqrt{2}$ are displayed as examples in Figure 6.8. Force spectra of the cuboids with $W/L = \sqrt{2}$, 6 and 12 are also shown, while those for $W/L = 2$ and 3 lie between them and have similar features.

No evident peaks can be observed in spectra of C_d, C_l and C_s for $W/L < 1$. The PSDs of C_d for cuboids with $W/L < 1$ increase gradually at Strouhal numbers greater than 0.08 as the aspect ratio is increased, while the spectra of the lift and side-force coefficients are

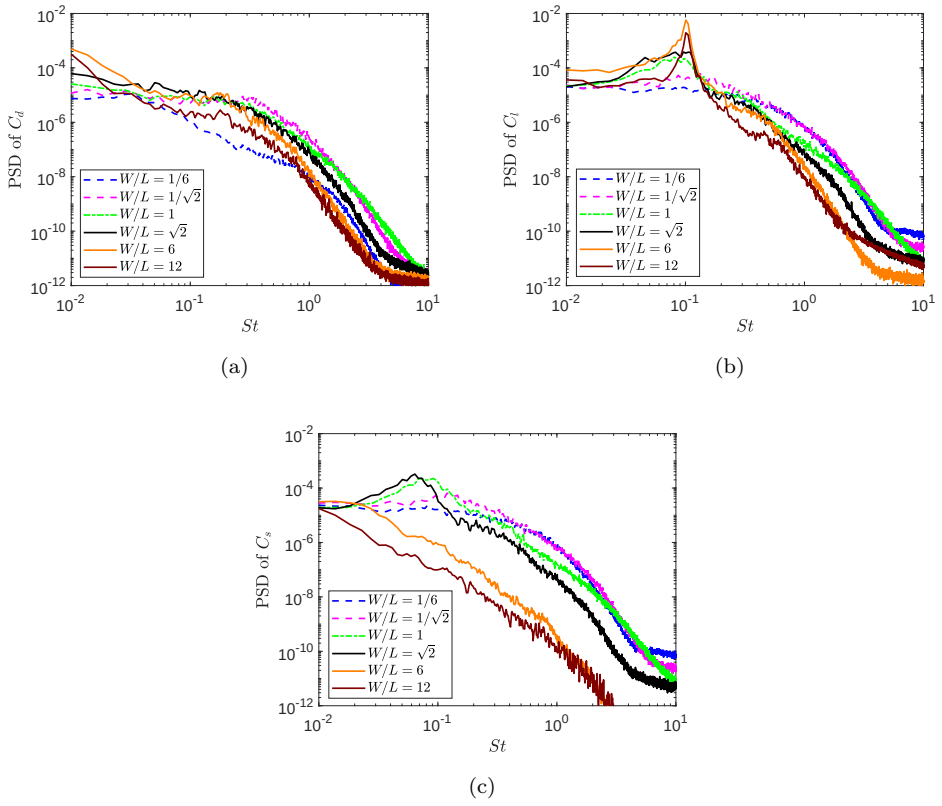

Figure 6.8: PSDs of (a) C_d, (b) C_l, (c) C_s at $Re = 100,000$ for different aspect ratios (W/L)

almost unchanged for cases with $W/L < 1$. Although the PSDs of the drag coefficient are also broadband for cases with $W/L \geq 1$ in Figure 6.8(a), distinct peaks centred close to $St = 0.1$ can be seen in the spectra of C_l in Figure 6.8(b), while the Strouhal number of a square cylinder is close to 0.13 (Lee, 1975). These become narrower as the values of W/L are increased. In Figure 6.8(c), broadband peaks occur in the PSDs of C_s for cuboids with $W/L = 1$ and $\sqrt{2}$. However, with the further increase of the aspect ratio, the broadband peaks disappear and the amplitudes of the spectra drop rapidly due to the effect of the normalising area. Features of these aerodynamic coefficients described above are closely related with the flow patterns, which will be analysed in detail in Section 6.2.2.

6.2.2 Flow patterns around the cuboid

6.2.2.1 Instantaneous flow structures

To illustrate flow behaviours around these cuboids, Figure 6.9 shows the normalised instantaneous spanwise vorticity (ω_z) in the central plane for representative aspect ratios at $Re = 100,000$. It can be seen that the flow always separates from the leading

edges of the cuboids, which also happens at $Re = 50,000$ and $200,000$. Therefore, the flow patterns around these cuboids are almost the same at different Reynolds numbers and only those at $Re = 100,000$ are presented in the following sections as examples. However, as can be seen in Figure 6.9, the flow structures around these cuboids change significantly with the aspect ratio. For cuboids with $W/L < 1$, the separated flow breaks into intensive and irregular vortices around the cuboid; these vortices are convected downstream and dissipated rapidly without forming strong periodic vortex shedding in the wake. In contrast, when the aspect ratio exceeds unity, the separated flow becomes more and more coherent with the increase of W/L and the vortices convected to the wake of the cuboid start to shed alternately, which explains the distinct peaks in C_l observed for cuboids with $W/L > 1$ in Figure 6.8(b).

6.2.2.2 Time-averaged flow patterns in the $z = 0$ plane

To characterise the time-averaged flow patterns surrounding these cuboids, mean streamlines in the $z = 0$ plane are shown in Figure 6.10 for cuboids with representative aspect ratios at $Re = 100,000$. Contours of the time-averaged pressure coefficient (C_p) are also shown. Figure 6.11 presents close-up views of the flow patterns near the top surface of the cuboid. Since symmetric mean flow patterns are observed, indicating convergence of the numerical calculations, only the parts above $y/H = 0$ are displayed in these figures. The white thick line denotes locations of zero streamwise velocity, which is used to show flow separation, reattachment and the recirculation length in the wake. As can be seen from Figure 6.10, the incoming flow always separates at the leading edge of the cuboid. However, the recirculation length in the wake of these cuboids changes significantly with the variation of W/L, implied by the position of the white thick lines intersecting with $y/H = 0$.

As shown in Figure 6.10(a) and Figure 6.10(b), the flow separated from leading edges of the cuboids with $W/L < 1$ reattaches to the top surface and remains attached until reaching the trailing edges. In particular, the position of the flow reattachment moves towards the trailing edge of the cuboid as the aspect ratio is increased from $W/L = 1/6$ to $1/\sqrt{2}$. This can be seen from the close-up view of the flow pattern near the cuboid with $W/L = 1/\sqrt{2}$ in Figure 6.11(a). However, for cuboids with $W/L \geq 1$ shown in Figure 6.10(c) - 6.10(f), instead of reattaching to the top surface of the cuboid, the separated flow is convected downstream to the wake and forms a large recirculation region behind the cuboid. As highlighted by the red dotted rectangles in Figure 6.11(b) - 6.11(e), secondary vortices can be seen close to the trailing edges of these cuboids, the size of which changes considerably for different aspect ratios.

In summary, the flow always separates from leading edges of these cuboids with different aspect ratios. For cuboids with aspect ratios smaller than 1, the separated flow reattaches to the lateral surfaces and the location of the flow reattachment moves to

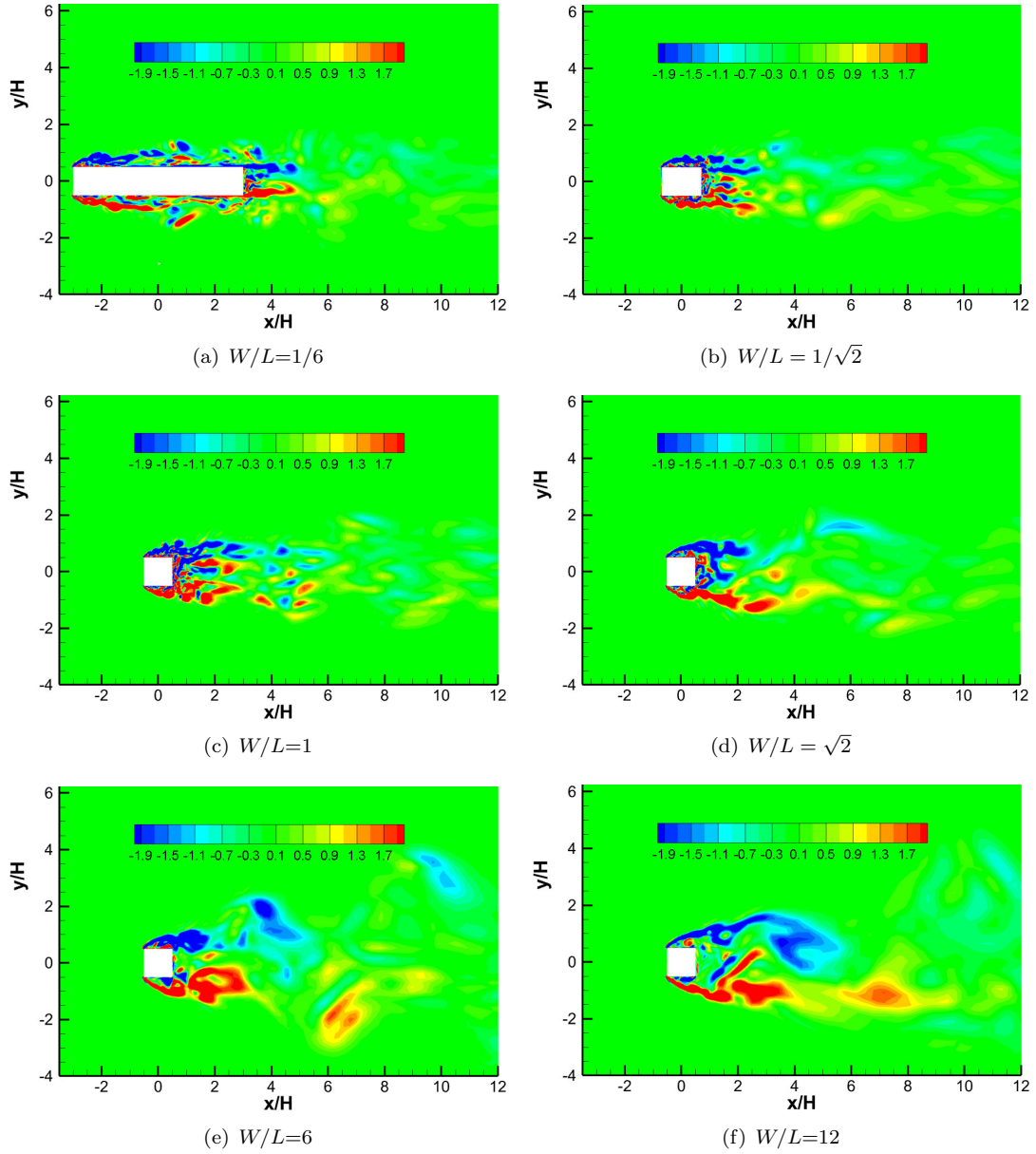

(a) W/L=1/6 (b) $W/L = 1/\sqrt{2}$

(c) W/L=1 (d) $W/L = \sqrt{2}$

(e) W/L=6 (f) W/L=12

Figure 6.9: Contours of the instantaneous spanwise vorticity (ω_z) in the central plane for cuboids with different aspect ratios at a Reynolds number of 100,000

the trailing edge at $W/L = 1/\sqrt{2}$. However, no flow reattachment can be observed on the top and bottom surfaces of cuboids with $W/L \geq 1$; the separated flow is convected downstream to the wake with a secondary vortex formed near the trailing edge of the cuboid. The size of the secondary vortex for cuboids with aspect ratios greater than 1 and the recirculation length in the wake of all the presented cases in Figure 6.10 are significantly affected by the variation of the aspect ratio, more details of which will be discussed quantitatively in the following part of this section.

The recirculation length L_r is measured from the rear surface of the cuboid to the location where the negative streamwise velocity recovers to zero. Therefore, the velocity

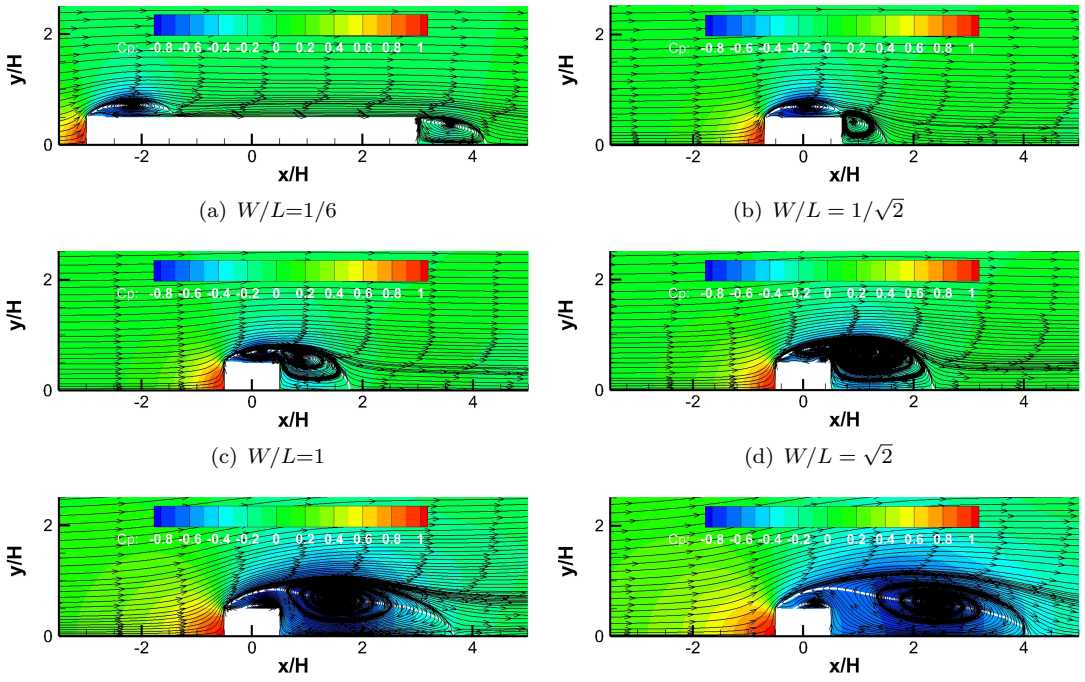

(a) W/L=1/6 (b) $W/L = 1/\sqrt{2}$

(c) W/L=1 (d) $W/L = \sqrt{2}$

(e) W/L=6 (f) W/L=12

Figure 6.10: Time-averaged pressure distribution contour together with mean streamlines in the $z = 0$ plane for cuboids with different aspect ratios at a Reynolds number of 100,000

profiles along the centreline ($y = 0$, $z = 0$) in the wake of the cuboid can be used to determine the values of L_r. Figure 6.12(a) shows the mean streamwise velocity profiles along the centreline in the wake for representative cuboids at $Re = 100,000$ as examples, which are almost the same as those at $Re = 50,000$ and $200,000$. The recirculation length of cuboids with different aspect ratios is implied by the distance between the start point of these profiles to the intersection point with $U/U_\infty = 0$.

A summary of the recirculation lengths of all the studied cuboids is presented in Figure 6.12(b). Results of the L_r for a square cylinder are also shown at $Re = 21,400$ measured by Lyn et al. (1995), at $Re = 8.2 \times 10^4$ obtained using DDES by Liu (2017) and LES at $Re = 2.2 \times 10^4$ from Sohankar et al. (2000). As shown in Figure 6.12(b), the trend of L_r corresponding to the aspect ratios is independent of the Reynolds number. The lowest value of L_r is found in the case with $W/L = 1/\sqrt{2}$. The recirculation length drops first from $W/L = 1/6$ to $1/\sqrt{2}$, then increases quickly with the further increase of W/L from $1/\sqrt{2}$ to 12. However, the value of L_r for the cuboid with $W/L = 12$ is much higher than results for a square cylinder ($W/L = \infty$). The recirculation length in the wake of the cuboid is expected to approach the value of a square cylinder for further increased aspect ratios ($W/L > 30$ (Fox and West, 1993)).

Figure 6.13 summarises the length of the separation bubble on the lateral surface in the $z = 0$ plane. For $W/L < 1$, in Figure 6.13(a), this is the distance between the leading

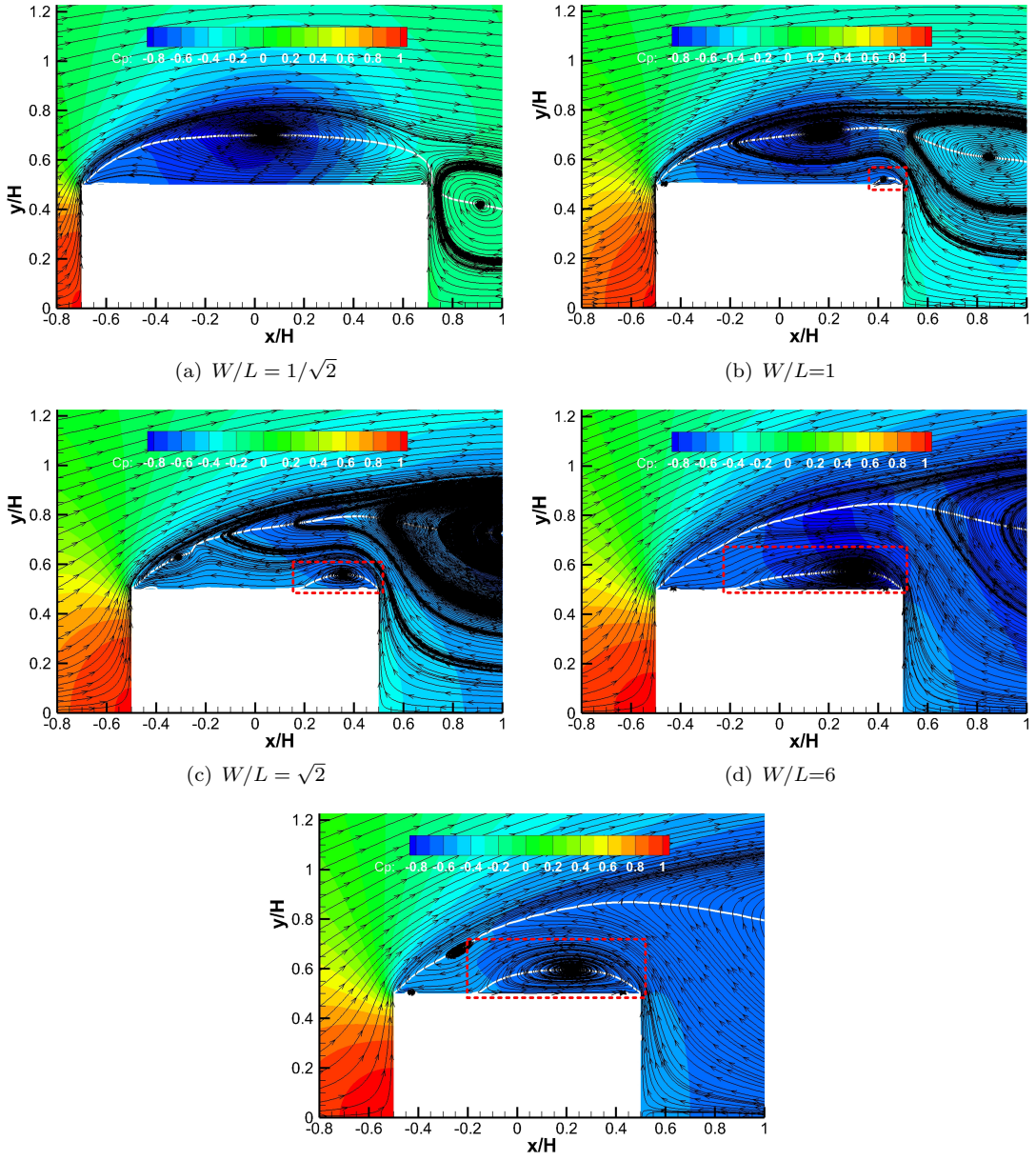

(a) $W/L = 1/\sqrt{2}$ (b) W/L=1

(c) $W/L = \sqrt{2}$ (d) W/L=6

(e) W/L=12

Figure 6.11: A close-up view of the flow pattern in the $z = 0$ plane near the cuboids with $W/L = 1$, $\sqrt{2}$, 6 and 12, coloured by the pressure coefficient at a Reynolds number of 100,000

edge and the location where the separated flow reattaches to the top surface (L_{rea}). For $W/L \geq 1$, in Figure 6.13(b), it is the length of the secondary vortex, measured from the trailing edge to its end on the top surface (L_{sec}). The position of the zero skin friction coefficient ($C_f = 0$) along the cuboid is used to determine values in Figure 6.13, combined with the white lines shown in Figure 6.10 and Figure 6.11.

As shown in Figure 6.13, the trend of the reattachment length with respect to the aspect ratio is consistent at different Reynolds numbers. However, the values are clearly dependent on Re. For cuboids with $W/L < 1$ in Figure 6.13(a), L_{rea} reduces with the

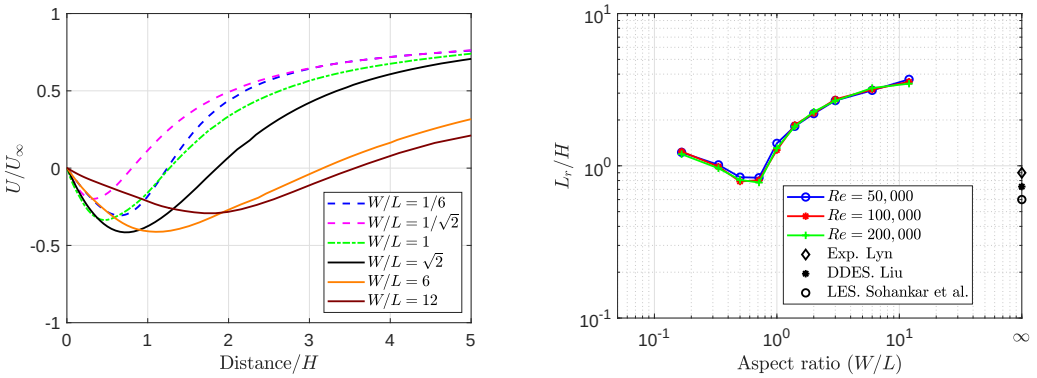

(a) Velocity profiles along $y = 0$, $z = 0$ (b) Recirculation length in the wake

Figure 6.12: (a) Velocity profiles along the centre line ($y = 0$, $z = 0$) and (b) the recirculation length (L_r) in the wake of the cuboids together with results for the square cylinder in literature

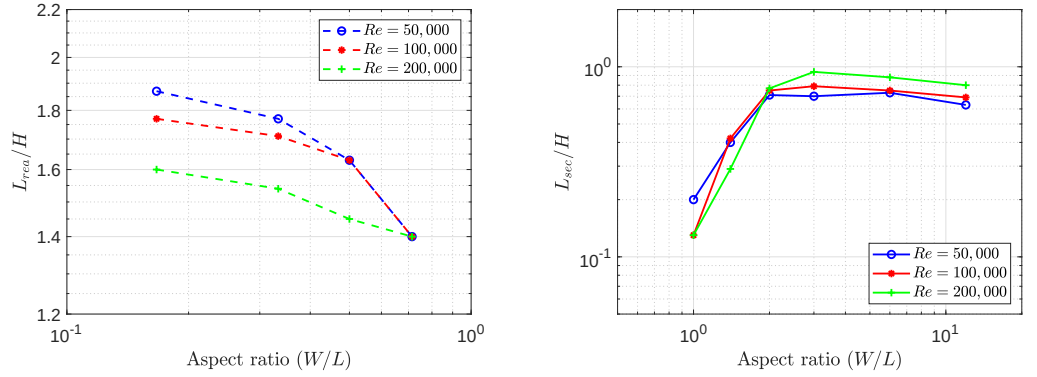

(a) $W/L < 1$ (b) $W/L \geq 1$

Figure 6.13: Lengths of the flow reattachment in the $z = 0$ plane on the lateral surface of cuboids with different aspect ratios (W/L)

increase of both the aspect ratio and the Reynolds number, although L_{rea} corresponds to the trailing edge for the cuboid with $W/L = 1/\sqrt{2}$, at which it is independent of Re. In Figure 6.13(b) for cuboids with $W/L \geq 1$, L_{sec} grows rapidly from $W/L = 1$ to 2, while values for larger aspect ratios are greater than $0.7H$ and only change slightly. It is noteworthy that although the L_{sec} does not change much for cuboids with $W/L \geq 2$, the height of the secondary vortex expands gradually with the increase of the aspect ratio as illustrated in Figure 6.11(d) and Figure 6.11(e).

6.2.2.3 Time-averaged flow patterns in the $y = 0$ plane

Flow patterns in the $y = 0$ plane are the same as those in the $z = 0$ plane for cuboids with $W/L \leq 1$ due to the symmetry of the geometries. However, once the aspect ratio exceeds 1, the flow structures in the $y = 0$ plane start to differ from those in the $z = 0$

plane discussed above. Figure 6.14 presents mean streamlines around cuboids with $W/L = \sqrt{2}$, 6 and 12 in the $y = 0$ plane together with contours of the mean pressure coefficient, while Figure 6.15 shows close-up views of the flow patterns near the lateral surfaces of these cuboids. White lines in Figure 6.14 and Figure 6.15 indicate locations with zero streamwise velocity, as supplementary visualization of the flow.

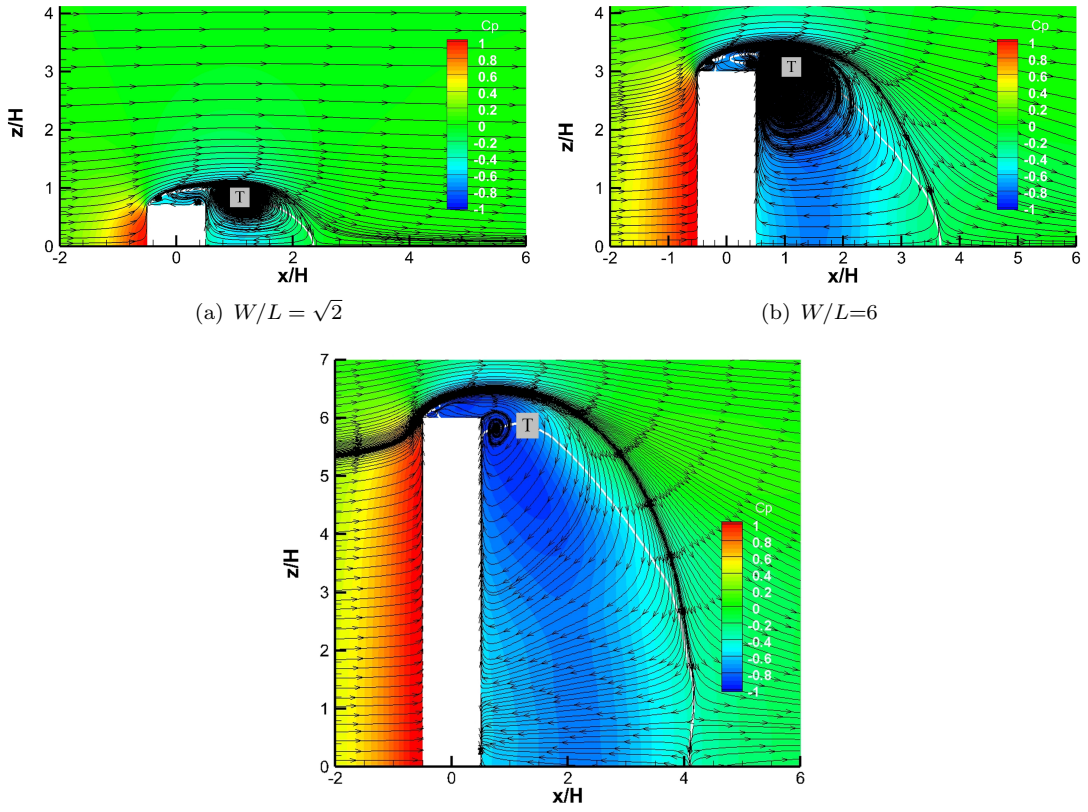

(a) $W/L = \sqrt{2}$

(b) W/L=6

(c) W/L=12

Figure 6.14: Time-averaged pressure distribution contour together with mean streamlines in the $y = 0$ plane for cuboids with $W/L > 1$ at a Reynolds number of 100,000

As shown in Figure 6.14, the separated flow moves downstream to the wake of cuboids and forms a recirculation bubble labelled as 'T'. With the increase of the aspect ratio from $W/L = \sqrt{2}$ to 12, the size of the vortex 'T' first increases and then decreases, with its position moving towards the trailing edge. Similar to the secondary vortex observed in the $z = 0$ plane in Figure 6.11(b) - 6.11(e), a secondary vortex formed due to the reverse flow from the wake can also be seen in the $y = 0$ plane close to the trailing edges of cuboids with W/L from $\sqrt{2}$ to 3. An example of $W/L = \sqrt{2}$ is shown in Figure 6.15(a) and the secondary vortex is highlighted by the red dotted rectangle. However, the secondary vortex in the $y = 0$ plane moves off the lateral surface as the aspect ratio is increased from 3 to 6 and a small vortex labelled as 'A' is formed in Figure 6.15(b). For further increased aspect ratio of 12, the secondary vortex disappears as shown in

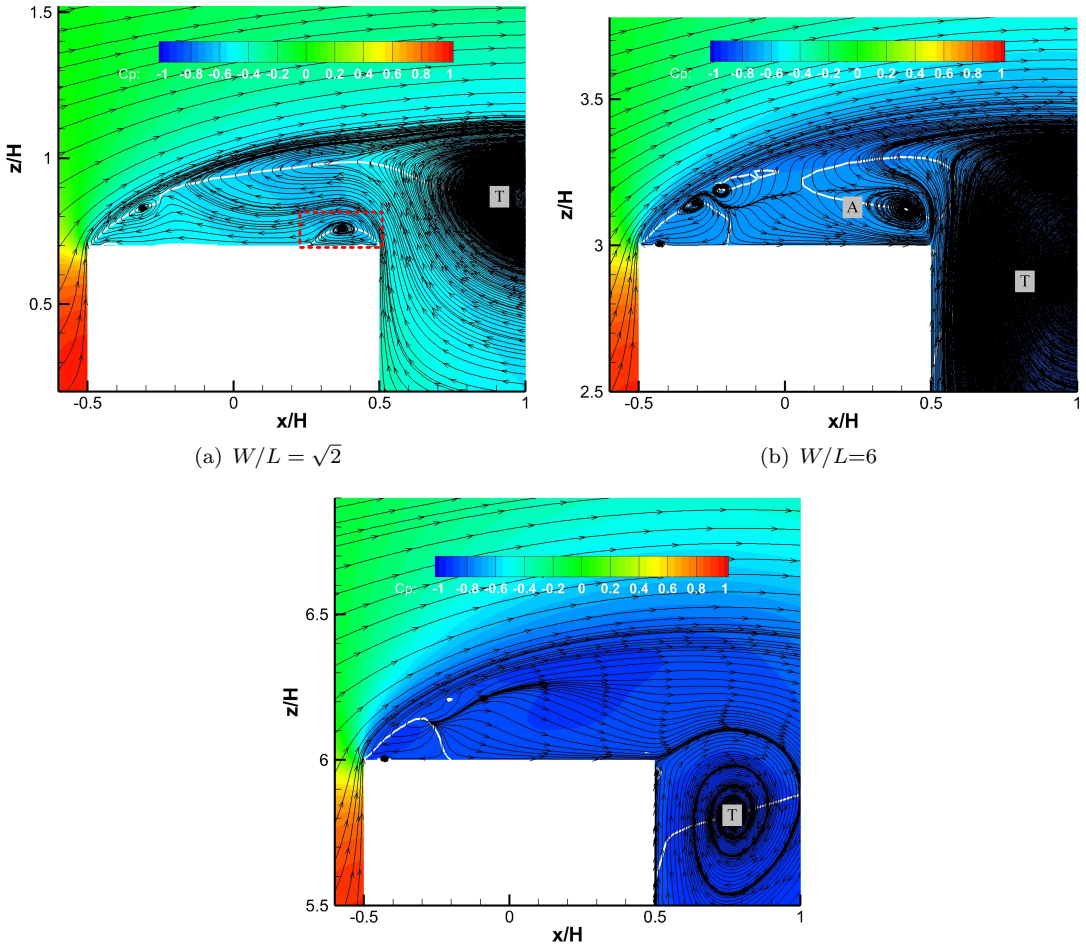

(a) $W/L = \sqrt{2}$

(b) W/L=6

(c) W/L=12

Figure 6.15: Close-up views of the flow pattern in the $y = 0$ plane near the cuboids with $W/L = \sqrt{2}$, 6 and 12, coloured by the pressure coefficient at a Reynolds number of 100,000

Figure 6.15(c), which implies the reverse flow from the wake becomes too weak to reach the lateral surface due to the enlarged distance along the spanwise direction.

6.2.3 Mean pressure coefficients along the cuboid surfaces

The distribution of the surface pressure is closely related to the flow patterns described above. Figure 6.16 presents the pressure coefficient (C_p) around surfaces of the cuboids at $Re = 100,000$. These results are similar at $Re = 50,000$ and 200,000. The pressure distributions in Figure 6.16 start from the stagnation point on the frontal surface. The distance along each surface is normalised by the corresponding length of the cross-section as illustrated in Figure 6.16(a). Figure 6.16(b) displays the pressure distribution in the $z = 0$ plane for $W/L \leq 1$, which is the same with that in the $y = 0$ plane. As shown in Figure 6.16(b), pressure distributions on the frontal surface from 0 to 0.5 for $W/L \leq 1$ are almost the same in each case while the pressure distributions on the rear surface from

1.5 to 2 are similar for each case with $W/L < 1$ but are higher than for the cube. A pressure plateau is found on the top surface of the cuboid with $W/L = 1/6$, indicated by the blue dashed line from 0.5 to 1.5. The pressure increases quickly from a negative value and is almost level for the remaining part of the top surface. The negative pressure on the top surface is caused by the separated flow from the leading edge and the pressure recovers quickly because of the flow reattachment, downstream of which the pressure slightly changes. With the increase of the aspect ratio from 1/6 to $1/\sqrt{2}$, the size of the level pressure on the top surface diminishes relative to the length L; particularly for $W/L = 1/\sqrt{2}$, it disappears because the separated flow reattaches to the trailing edge as shown in Figure 6.11(a). For $W/L = 1$, the separated flow no longer reattaches to the top surface and the pressure is distributed more evenly on it as denoted by the green dashed line.

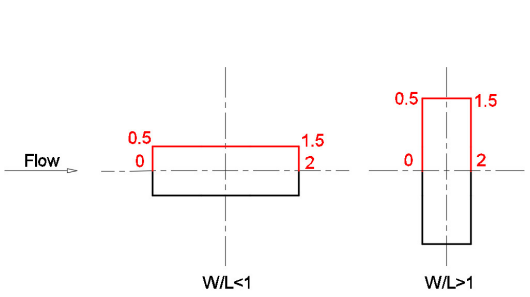

(a) Illustration of the normalised position

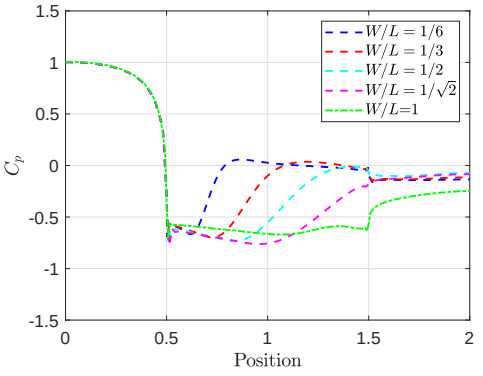

(b) $W/L \leq 1$ in the $z = 0$ plane

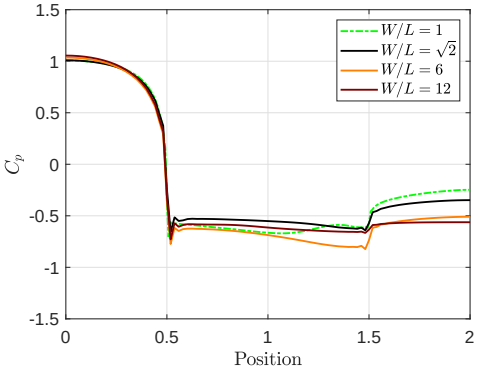

(c) In the $z = 0$ plane

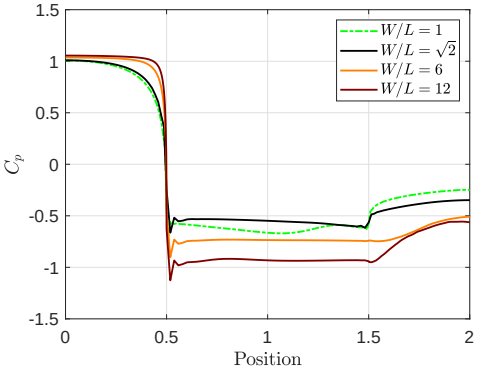

(d) In the $y = 0$ plane

Figure 6.16: Distributions of the mean pressure coefficient (C_p) for the cuboids at $Re = 100,000$

Figure 6.16(c) illustrates pressure distributions in the $z = 0$ plane for cuboids with representative aspect ratios ($W/L \geq 1$). Again, the pressure on the frontal surface is almost the same in each case, whereas, the pressure on the top and rear surfaces is more sensitive to the aspect ratio. The pressure distribution on the top surface for $W/L \geq 1$

is much flatter than that for $W/L < 1$ due to the disappearance of the flow reattachment and it changes only slightly for different aspect ratios. In addition, for $W/L \geq 1$, the pressure on the rear surface tends to drop gradually with the increase of the aspect ratio. Distributions of C_p in the $y = 0$ plane for representative aspect ratios are shown in Figure 6.16(d). For $W/L > 1$, the pressure on the lateral surface drops considerably as the aspect ratio is increased due to the development of edge vortex shown in Figure 6.15. In addition, it is interesting to note that for cases with a secondary vortex formed on the cuboid surface close to the trailing edge ($W/L \geq 1$ in the $z = 0$ plane and $1 \leq W/L \leq 3$ in the $y = 0$ plane), a steep increase of the pressure can be seen at the position 1.5.

A summary of the base pressure coefficient (C_{pb}) for all the cuboids is presented in Figure 6.17, together with the measured C_{pb} of a square cylinder at $Re = 100,000$ (Vickery, 1966). It turns out that the effect of Reynolds number on C_{pb} is negligible. The values of C_{pb} increase gradually as the aspect ratio is increased from 1/6 to $1/\sqrt{2}$, but drops significantly from $1/\sqrt{2}$ to 1. For larger values of W/L, the base pressure coefficient keeps dropping. In addition, the trend of C_{pb} with respect to the aspect ratio is the opposite to that of the mean drag coefficient (Figure 6.7(a)).

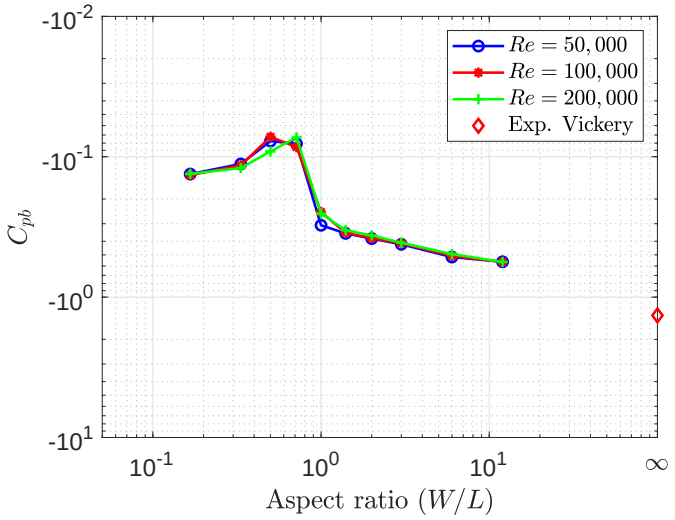

Figure 6.17: The base pressure coefficient (C_{pb}) for cuboids with different aspect ratios and the measured result of the square cylinder at $Re = 100,000$ (Vickery, 1966)

6.2.4 Turbulence kinetic energy around the cuboid

To illustrate the unsteadiness of the flow, Figure 6.18 shows the turbulence kinetic energy close to the cuboid in the $z = 0$ plane at $Re = 100,000$. For $W/L \leq 1$, the highest value of TKE appears in the shear layer above the top surface, and with the increase of the aspect ratio, this value gradually increases as shown in Figure 6.18(a) - 6.18(c). However, for further increased aspect ratios in Figure 6.18(d) - 6.18(f) ($W/L > 1$), the turbulence

kinetic energy in the wake becomes more dominant due to the evolution of the vortex shedding.

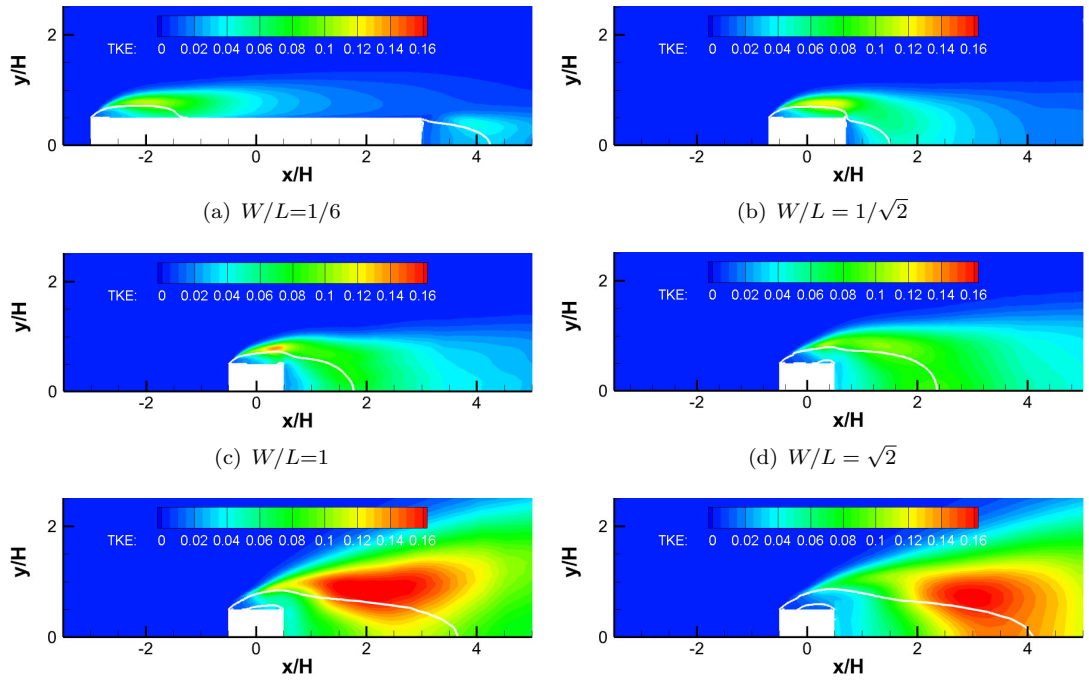

(a) W/L=1/6 (b) $W/L = 1/\sqrt{2}$

(c) W/L=1 (d) $W/L = \sqrt{2}$

(e) W/L=6 (f) W/L=12

Figure 6.18: Contours of TKE in the $z = 0$ plane for cuboids with different aspect ratios at a Reynolds number of 100,000

6.2.5 Pressure fluctuations on the cuboid surfaces

Figure 6.19 displays contours of the pressure fluctuations (L_p) on the cuboid surfaces at $Re = 100,000$, where the rms values of the pressure fluctuation are expressed in decibel (see Equation (4.11)). With the increase of the aspect ratio, the pressure fluctuations on the rear surface increase accordingly. For $W/L < 1$, large pressure fluctuations occur within the flow recirculation region on the top and the lateral surfaces as illustrated in Figure 6.19(a) and Figure 6.19(b). For $W/L = 1$ in Figure 6.19(c), regions with high pressure fluctuations on the top and lateral surfaces decrease with the disappearance of the flow reattachment and the highest p_{rms} is observed close to the trailing edges. The distribution of the pressure fluctuations on the top and lateral surfaces from $W/L = \sqrt{2}$ to 3 is similar to that of the cube. However, the overall level of the pressure fluctuations on the cuboid surfaces for $W/L = 6$ and 12 is much higher than that for lower aspect ratios, as can be observed in Figure 6.19(e) and Figure 6.19(f), while the highest p_{rms} is again found near the trailing edge.

The near-wall flow patterns obtained from the first layer grids on the top surface of cuboids with representative aspect ratios are shown in Figure 6.20. These are coloured

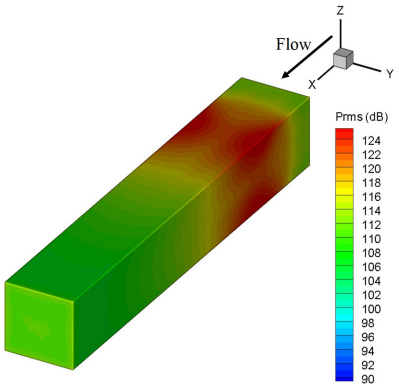

(a) W/L=1/6

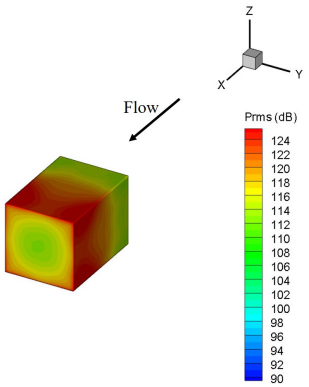

(b) $W/L = 1/\sqrt{2}$

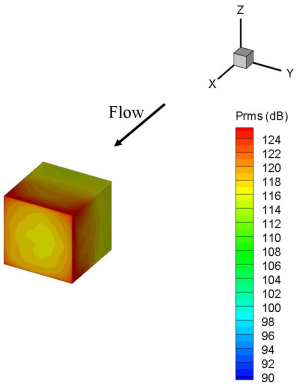

(c) W/L=1

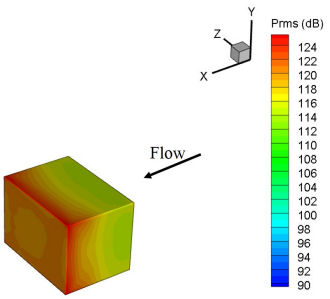

(d) $W/L = \sqrt{2}$

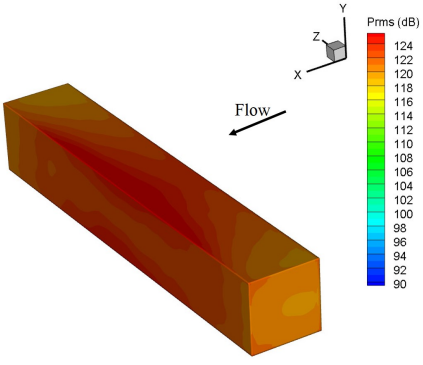

(e) W/L=6

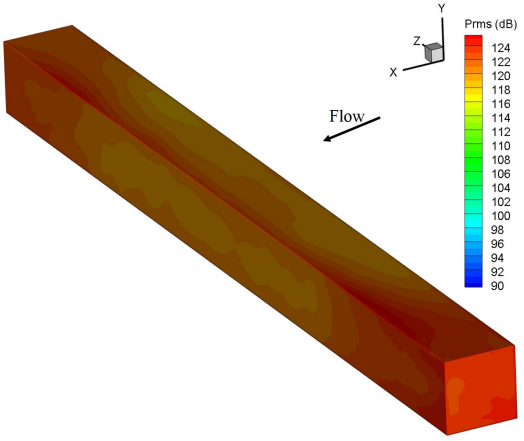

(f) W/L=12

Figure 6.19: Contours of the pressure fluctuation (p_{rms}) for cuboids with different aspect ratios at a Reynolds number of 100,000

by the pressure fluctuations on the top surface. The white lines represent locations of

zero streamwise velocity. As can be seen from Figure 6.20(a) and Figure 6.20(b), the highest pressure fluctuations for $W/L < 1$ happen at the Nodes labelled as 'N1' and 'N2' on the reattachment line. These Nodes move closer to the trailing edge with the increase of the aspect ratio. Since the near-wall flow patterns and distributions of the pressure fluctuations for $W/L = 1$, $\sqrt{2}$, 2 and 3 are similar, only those for $W/L = \sqrt{2}$ are shown in Figure 6.20(c). The highest pressure fluctuations are found near Nodes 'N3' and 'N4' close to the rear corners, formed due to the secondary vortex in Figure 6.11(c). Figure 6.20(d) shows the flow patterns for $W/L = 6$, which are similar to those for $W/L = 12$, despite more flat streamlines near the rear corner. A Node 'N5' is formed close to the centreline of the top surface ($z/H = 0$) and the pressure fluctuations in the centre are highest.

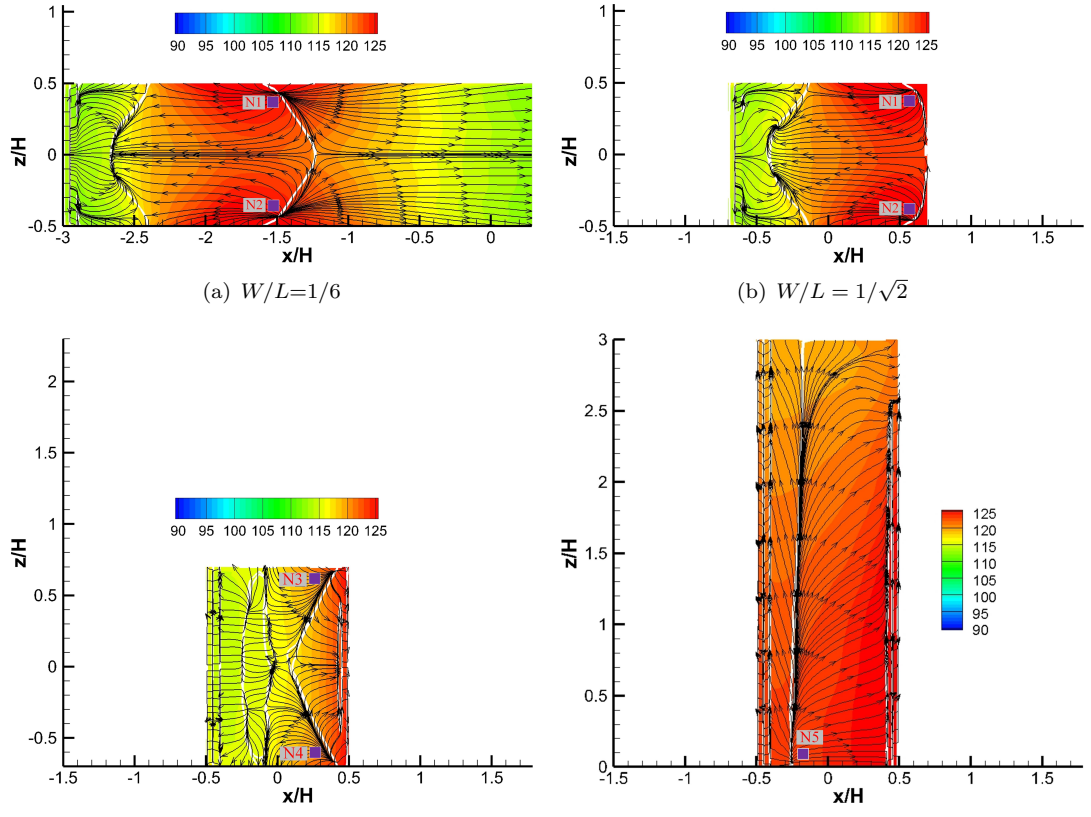

(a) W/L=1/6 (b) $W/L = 1/\sqrt{2}$

(c) $W/L = \sqrt{2}$ (d) W/L=6

Figure 6.20: Mean streamlines and contours of the pressure fluctuation (L_p) on the top surface of cuboids with different aspect ratios at $Re = 100,000$

6.3 The effect of the aspect ratio on the radiated noise

Based on the fluctuating pressure on the surfaces of the cuboid obtained from CFD, the far-field noise at receivers 10 m ($133H$) away from the cuboid centre in the streamwise, cross-flow and spanwise directions is predicted using the FW-H method. The overall

sound pressure level (OASPL) at each receiver is calculated by integrating the Power Spectral Density (PSD) of the emitted noise up to a Strouhal number ($St = fH/U_\infty$) of 4. Moreover, the predicted noise for each case is then rescaled to correspond to a total surface area of $6H^2$ for the cube, namely taking into account a correction:

$$\begin{aligned} L_{cor} &= -10\log_{10}((2HL + 2HW + 2WL)/6H^2) \\ &= \begin{cases} -10\log_{10}(1/3 + 2L/3W) & W/L \leq 1 \\ -10\log_{10}(1/3 + 2W/3L) & W/L > 1 \end{cases} \end{aligned} \tag{6.1}$$

as illustrated in Figure 6.21(a). The predicted OASPL for all the studied cases at the Reynolds number of 100,000 is plotted in Figure 6.21(b). As expected, when the aspect ratio is less than 1, the sound along the cross-flow direction at (0, 10, 0) is very similar to that observed at (0, 0, 10) in the spanwise direction. However, for $W/L > 1$, the noise at (0, 0, 10) drops quickly with the increase of the aspect ratio and the reduction rate is faster than that due to the surface area correction shown in Figure 6.21(a). For $W/L = 12$, the OASPL in the spanwise direction is up to about 27 dB less than that in the cross-flow direction. In addition, the sound pressure level in the cross-flow direction at the receiver (0, 10, 0) is always greater than that observed in the streamwise direction at (10, 0, 0); the greatest difference is about 9 dB, observed for the cuboid with an aspect ratio of 6.

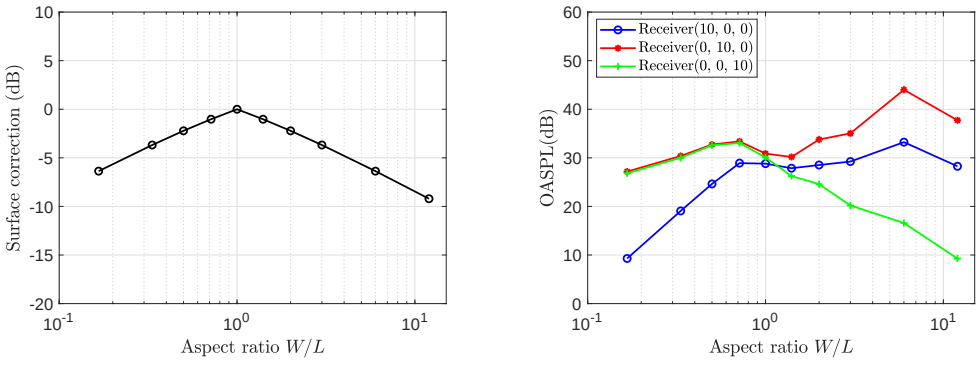

(a) (b)

Figure 6.21: (a) Surface correction of the OASPL (b) Predicted OASPL at the Reynolds number of 100,000 for cuboids with different aspect ratios ranging from 1/6 to 12

Noise spectra for representative cases at $Re = 100,000$ predicted at the three receivers are shown in Figure 6.22. The surface area correction (Equation (6.1)) is not implemented for these noise spectra. Since the noise spectra for cases with $W/L < 1$ are similar, only the spectra for the bounding cases of $W/L = 1/6$ and $1/\sqrt{2}$ are plotted in Figure 6.22. In addition, the main features of the noise spectra for cases with $W/L = 2$ and 3 are similar to that observed in the case $W/L = 6$ and so are not shown. As shown

in Figure 6.22(a), no evident tonal peaks are found in spectra for the receiver in the streamwise direction for all investigated cases and, with the increase of the aspect ratio, the noise at Strouhal numbers smaller than 1 gradually increases.

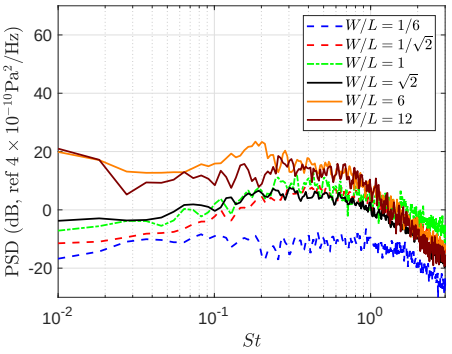

(a) Receiver (10, 0, 0)

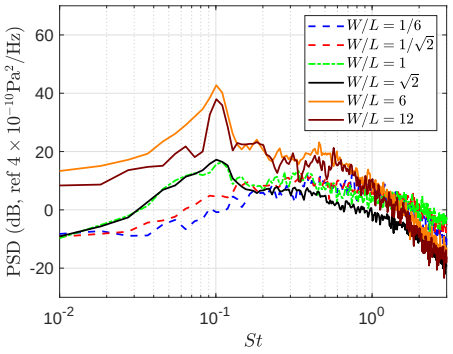

(b) Receiver (0, 10, 0)

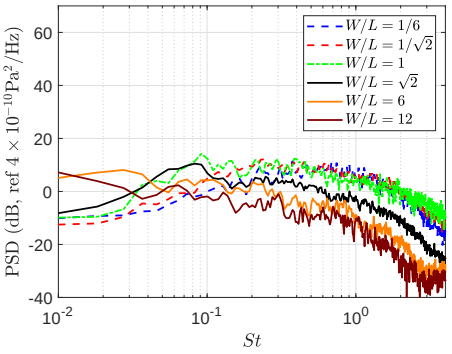

(c) Receiver (0, 0, 10)

Figure 6.22: Noise spectra along the streamwise, cross-flow and spanwise directions respectively for cuboids with different aspect ratios at $Re = 100,000$

In Figure 6.22(b) for the receiver along the cross-flow direction, although no tonal frequency is recognisable for $W/L < 1$, a dominant peak centred at about $St = 0.1$ can be clearly seen in the spectra for $W/L = 1$ to 12. For comparison, the peak St for an infinite square cylinder is about 0.13 (Lyn et al., 1995; Norberg, 1993). The Strouhal number of 0.1 found in this work is consistent with that reported by Porteous et al. (2017) for square wall-mounted cylinders in the regime $2 < W/L < 10$. This tonal peak is formed due to the periodic Karman vortices in the wake of the cuboid similar to that observed in the wake of an infinite cylinder (see Figure 6.9). With the increase of the aspect ratio, the magnitude of this Aeolian tone keeps increasing while the peak becomes more and more narrow-band. Whereas the frequencies of the dominant peak changed with respect to the aspect ratio for finite wall-mounted cylinders studied by Porteous et al. (2017), the position of the tonal peak for the cuboids with different aspect ratios studied in this work is quite constant. In addition, a bifurcation at frequencies lower than the main tonal peak near $St = 0.1$ emerges for a wall-mounted cylinder with $W/L = 12.9$

(Porteous et al., 2017), which is not observed from the spectrum of $W/L = 12$ in Figure 6.22(b). This implies that the dual cellular shedding modes for a finite wall-mounted cylinder with the aspect ratio close to 12 do not happen for cuboids in free space, where only one shedding mode happens for the finite length square cylinder in cross flow studied in the current work. From Figure 6.22(c), for the receiver in the spanwise direction, a broadband peak centered at about $St = 0.1$ can be seen in the case with $W/L = 1$. However, when the aspect ratio exceeds 1, this broadband peak disappears.

The predicted noise in the streamwise, cross-flow and spanwise directions at different Reynolds numbers for all the studied values of aspect ratio is summarized in Figure 6.23. The OASPL is corrected of the surface area according to Equation (6.1) and is rescaled by U_∞^6 to correspond to 40 m/s ($Re = 200,000$). This means that for the incoming flow of 10 m/s ($Re = 50,000$) 36 dB is added, while that for $U_\infty = 20$ m/s ($Re = 100,000$) 18 dB is added.

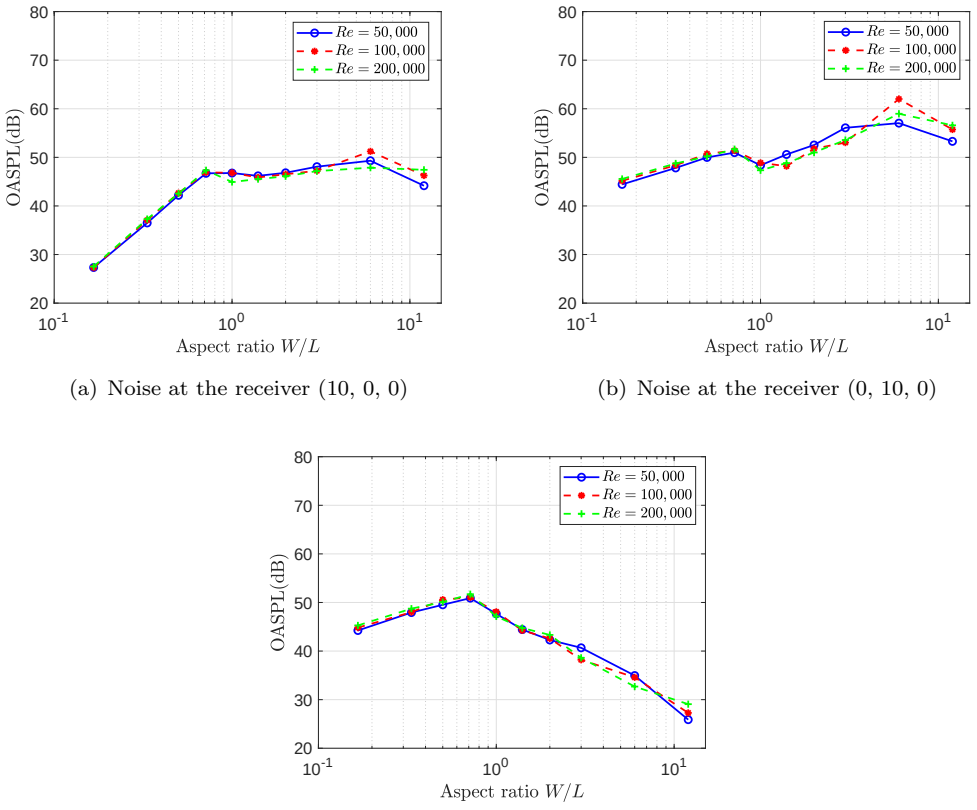

(a) Noise at the receiver (10, 0, 0)

(b) Noise at the receiver (0, 10, 0)

(c) Noise at the receiver (0, 0, 10)

Figure 6.23: A summary of the predicted OASPL along the streamwise, cross-flow and spanwise directions respectively

As shown in Figure 6.23, the trends of the OASPL with respect to the aspect ratio are similar at different Reynolds numbers for all three directions, especially for cases with small values of W/L. This confirms that the emitted noise follows a sixth power law with respect to the flow speed. For all three directions shown in Figure 6.23, the

maximum OASPL for $W/L \leq 1$ is always observed for the case with $W/L = 1/\sqrt{2}$. In this case, the separated flow from the leading edge reattaches to the location close to the trailing edge. For $W/L > 1$, in general, the noise along the streamwise direction shown in Figure 6.23(a) changes only slightly with increase of the aspect ratio, while the noise in the cross-flow direction displayed in Figure 6.23(b) keeps growing and the sound along the spanwise direction in Figure 6.23(c) decreases rapidly.

Figure 6.24 shows the sound directivities in the $z = 0$ plane for cuboids with representative aspect ratios. These are obtained based on the OASPLs from 72 evenly distributed receivers in a circle 10 m away from the cuboid centre. The OASPLs at different flow speeds are scaled to 40 m/s using the sixth power law of the flow speed on the far-field noise. The surface area of cuboids is also rescaled (see Equation (6.1)) to obtain the OASPL. Similarly, the sound directivities in the $y = 0$ plane for $W/L = \sqrt{2}$, 6 and 12 are presented in Figure 6.25.

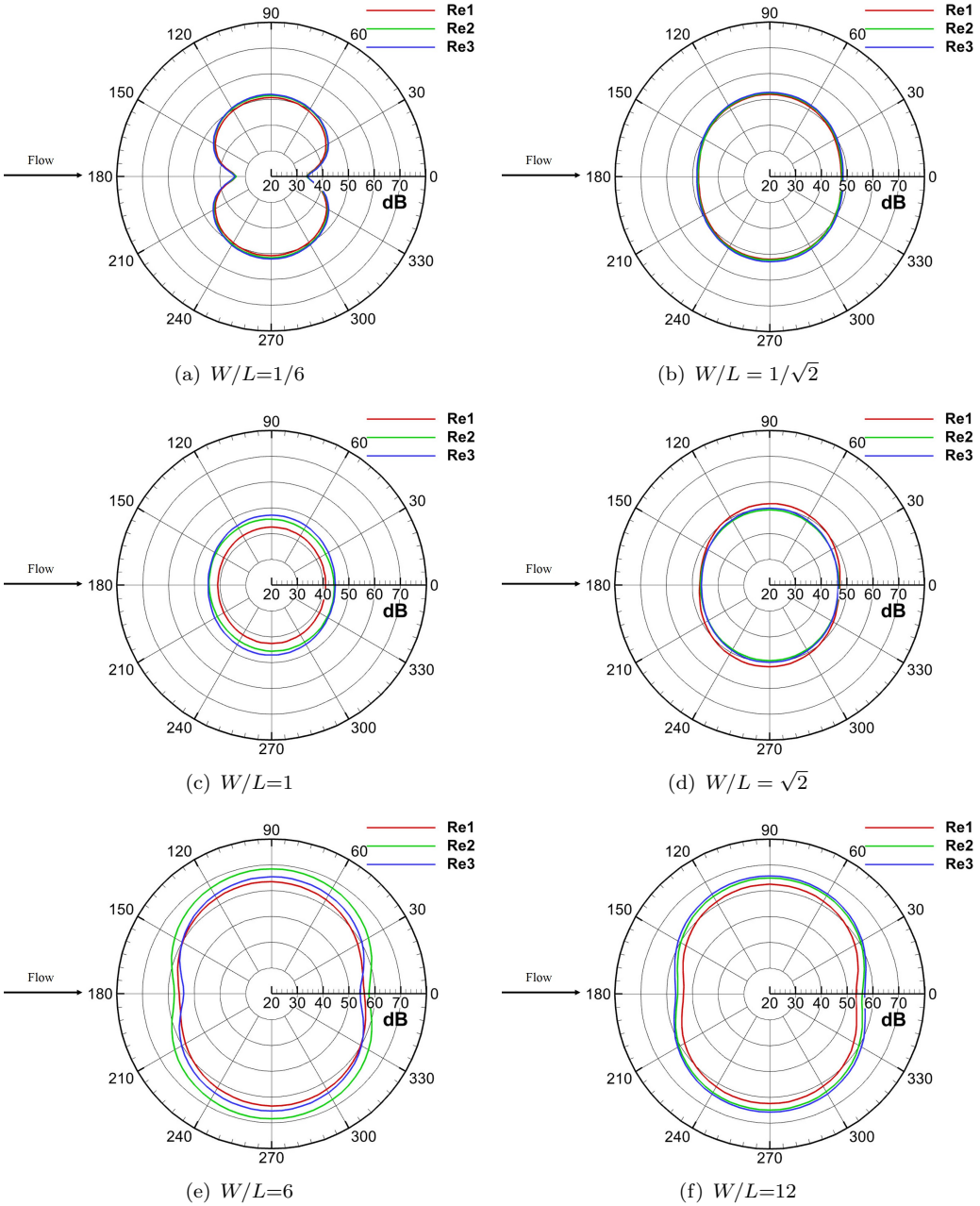

(a) W/L=1/6 (b) $W/L = 1/\sqrt{2}$

(c) W/L=1 (d) $W/L = \sqrt{2}$

(e) W/L=6 (f) W/L=12

Figure 6.24: The sound directivity in the $z = 0$ plane normalised to $Re = 100,000$ (Re1: $Re = 50,000$; Re2: $Re = 100,000$; Re3: $Re = 200,000$)

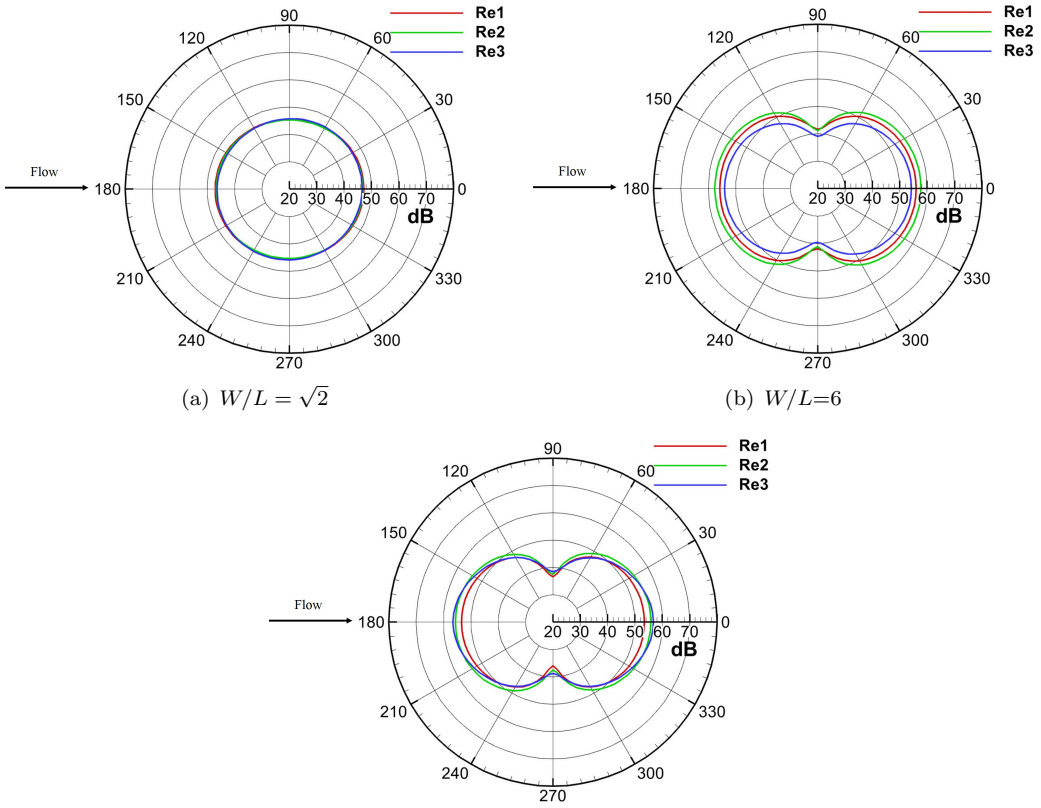

(a) $W/L = \sqrt{2}$ (b) W/L=6

(c) W/L=12

Figure 6.25: The sound directivity in the $y = 0$ plane normalised to $Re = 100,000$ (Re1: $Re = 50,000$; Re2: $Re = 100,000$; Re3: $Re = 200,000$)

As shown in Figure 6.24, with the increase of the aspect ratio from $W/L = 1/6$ to 1, the sound directivity changes from a typical dipole pattern to be more and more omni-directional. However, for further increases in aspect ratio, the sound along the cross-flow direction grows faster than that in the streamwise direction and the directivity becomes more like a dipole pattern again. Typical dipole patterns can also be observed in the $y = 0$ plane for cuboids with $W/L > 0$ as shown in Figure 6.25, since the noise in the spanwise direction reduces quickly as the aspect ratio is increased.

6.4 Summary

In this chapter, the effect of aspect ratio on the flow past cuboids and the emitted noise is investigated numerically. Ten aspect ratios from 1/6 to 12 are taken into account at $Re = 50,000$, 100,000 and 200,000 respectively.

The flow always separates from the leading edges of the cuboids at the studied Reynolds numbers and main features of the mean flow change only slightly with variations of the Reynolds number. The separated flow reattaches to the top and lateral surfaces of cuboids with aspect ratios smaller than 1. In particular, it reattaches at the trailing

edge for $W/L = 1/\sqrt{2}$. However, for further increases of aspect ratio, the separated flow convects downstream to the wake instead of reattaching to the top surface and a secondary vortex is formed near the trailing edge in the $z = 0$ plane. The lowest mean drag coefficient is observed for the cuboid with $W/L = 1/\sqrt{2}$ and the trend of the mean drag coefficient with respect to the aspect ratio is the opposite to that of the base pressure coefficient. The highest pressure fluctuations occur in the region of the flow reattachment for $W/L < 1$ while they occur close to the trailing edge for $W/L \geq 1$ due to the formation of the secondary vortex.

No evident tonal peaks can be observed in the noise spectra for cuboids with $W/L \leq 1$ at receivers in the streamwise, cross-flow or spanwise directions. For the cuboids with aspect ratios greater than 1, a dominant tonal peak centred at about $St = 0.1$ is found in the noise spectra along the cross-flow direction. With the increase of the aspect ratio, the magnitude of this dominant peak increases gradually but the position of the central frequency remains constant, which is different from the noise spectra of finite wall-mounted cylinders with similar aspect ratios presented in the literature. In addition, the far-field noise from cuboids with different aspect ratios grows at a rate close to $60\log U_\infty$ with respect to the incoming flow speed.

Chapter 7

Conclusions and Future Work

7.1 Conclusions

Motivated by the need to understand and control railway aerodynamic noise, compact bluff bodies resembling cuboids are the main research objects in this thesis. These are common components in train pantographs and bogies. The underlying physics concerning the flow field and also the noise emitted from cubes with different wall proximities and corner radii as well as cuboids with different aspect ratios are studied. To obtain details of the flow at Reynolds numbers in the range of engineering applications, the Delayed Detached Eddy Simulation method is adopted using the open source software OpenFOAM. Subsequently, based on the noise sources obtained from the CFD simulations, the noise emitted to the far field is predicted using the Ffowcs Williams-Hawkings acoustic analogy in the commercial software FLUENT.

Comparisons with measurements conducted by Castro and Robins (1977) for a wall-mounted cube in uniform flow show the feasibility of the adopted methodology for describing the flow field. Thorough grid dependence studies are conducted to explore the most suitable spatial resolution of the grids, which are used as the guideline for the mesh generation of subsequent simulations. Commendable agreement has been achieved between the simulation and the measurements, including distributions of the surface pressure, velocity profiles in the wake and near-wall flow patterns. Since no measurements of pressure fluctuations on cuboids are available in the literature for validation purposes, a separate simulation for flow over a square cylinder has been conducted using the same approach to gain confidence in the adopted methodology for predicting root mean square values of the pressure fluctuations. A reasonable agreement in terms of the fluctuating pressure along the square cylinder has been achieved between the numerical work and the experimental data from the literature (Pocha, 1971; Vickery, 1966). To evaluate the noise prediction using the FW-H analogy in FLUENT, the noise emitted from a square cylinder to the far field was predicted and compared with measurements

from (Liu et al., 2018). It was found that the discrepancies between the predicted Overall Sound Pressure Level and the measurements at different receivers were mostly less than 1 dB.

The wall-mounted cube is then elevated to different heights above the ground, from 1/12 to one times the side length and also a limiting case in free space, to investigate the effect of wall proximity on the flow over the cube and the far-field noise. It is found that the horseshoe vortex formed upstream of the wall-mounted cube is weakened as the cube is lifted slightly from the ground to 1/12 of the side length above it. The flow separation along the ground moves downstream of the cube for the elevation heights from 1/6 to 1/4 of the side length, and disappears for further increased elevation heights. The separated flow from the top leading edge of the cube reattaches to the ground for the wall-mounted cube and the case with an elevation height of 1/12 of the side length. Flow reattachments on the bottom surface of the cube can only be observed in cases with elevation heights from 1/12 to 1/5 of the side length. In particular, the separated flow from the lower leading edge reattaches to the trailing edge of the cube at 1/5 of the side length above the ground. The mean lift coefficient drops significantly once the wall-mounted cube is lifted to 1/12 of the side length above the ground, while the mean drag and side-force coefficients do not change much with the elevation height. In addition, high pressure fluctuations are observed near the trailing edge of the cube. The emitted noise along the lateral direction of the cube is higher than that in the streamwise and the vertical directions for cases with elevation heights smaller than 1/6 of the side length. However, the sound along the vertical direction grows quickly and reaches a maximum at an elevated height of 1/4 of the side length, which is about 10 dB higher than that of the wall-mounted cube.

Since the position of the flow separation may change once the edges of the cube are rounded, another benchmark case on the flow over a sphere is conducted to validate the feasibility of the adopted methodology in predicting the flow separation locations. Results from the simulation are carefully compared with the available literature and good agreement is achieved. The effects of the corner radii on the flow over a cube and the emitted noise are then investigated. A series of corner radii ranging 0 to 40% of the cube side length is considered at Reynolds numbers from 50,000 to 200,000. It turns out that the location of the flow separation moves downstream with the increase of the corner radius and periodic vortex shedding is more evident in the wake of the cube with a corner radius 40% of the side length. In general, the separated region moves towards the lateral surfaces and the recirculation length in the wake reduces for increased corner radius or higher Reynolds number. The mean drag coefficient does not change monotonically with the increase of the corner radius, but drops first with the minimum value observed for a radius of one third of the side length. The variation of the minimum pressure coefficient seems more responsible for the change of the mean drag coefficient than the base pressure coefficient does. The distribution of the pressure fluctuations

is strongly related with the near-wall flow patterns. Large pressure fluctuations occur when the flow reattachment occurs on the lateral surface and the recirculation region in the wake is reduced. It is found that corner rounding with a carefully determined radius can be an effective way to reduce the emitted noise. The minimum noise is found for a radius of 1/3 of the edge length, for which an average reduction of 8 dB is found relative to the cube.

The effect of the aspect ratio on the flow over cuboids and the generated noise is also studied. Aspect ratios between 1/6 and 12 and three Reynolds numbers are considered. The flow always separates from leading edges of the cuboid and the Reynolds number has negligible effect on the mean flow features. The separated flow reattaches to the lateral surfaces of the cuboids and in particular reaches the trailing edges for an aspect ratio of $1/\sqrt{2}$. However, for further increased aspect ratios, the separated flow convects downstream to the wake without flow reattachment and secondary vortices are observed close to the trailing edges. The trend of the mean drag coefficient with respect to changes of the aspect ratio is the opposite to that of the base pressure coefficient and the lowest mean drag coefficient is found for the aspect ratio of $1/\sqrt{2}$. For cuboids with aspect ratios smaller than 1, large pressure fluctuations are observed close to locations of flow reattachment on the lateral surfaces while for cases with aspect ratios greater than 1, the formation of the secondary vortex near the trailing edge causes large pressure fluctuations. The noise from the case with an aspect ratio of $1/\sqrt{2}$ is always the highest among cuboids with aspect ratios smaller than 1. However, for cuboids with aspect ratios exceeding unity, the sound along the cross-flow direction keeps growing while that in spanwise direction reduces rapidly with the increase of the aspect ratio.

7.2 Recommendations for future work

To develop further the component-based model for the noise prediction of train pantographs and bogies, the flow interaction between different components should be taken into account. For example, the flow over a cuboid connected to a cylinder in yaw should be studied to evaluate the flow interaction near the knee joint part of the pantograph.

In addition, the effect of sound scattering from the object surface, especially at high frequencies, also needs to be assessed. Combining CFD with the Boundary Element Method (BEM) (Wu, 2000) is a promising way to study the sound scattering at low Mach numbers. A permeable integral surface offset from the object can be used in the FW-H acoustic analogy. Equivalent noise sources on the permeable FW-H surface are calculated based on the results of CFD. The surface of the object is discretized using BEM and rigid wall boundary conditions are assigned to the object surface. The Helmholtz integral equation is then solved to obtain the acoustic pressure in the far

field. However, in this way, special attention is required to deal with the spurious noise caused by vorticity incident on the permeable FW-H surface.

Experimental validations are also important for the flow and noise fields obtained numerically in this thesis. However, as the cubes or cuboids studied are either elevated or in free space, the effect of the supporting system on the flow over the object is difficult to eliminate. In addition, since flow features of the cuboid are sensitive to the angle of attack, unexpected vibrations from the supporting struts may cause considerable effect on the measurements. As discussed in this thesis, the noise spectrum for cubes and cuboids tends to be broadband, which is more difficult to separate from the background noise in the anechoic wind tunnel than for objects with tonal noise.

References

Achenbach, E. (1968). Distribution of local pressure and skin friction around a circular cylinder in cross-flow up to Re= 5×10^6. *Journal of Fluid Mechanics*, 34(4):625–639.

Achenbach, E. (1972). Experiments on the flow past spheres at very high Reynolds numbers. *Journal of Fluid Mechanics*, 54(3):565–575.

Achenbach, E. (1974). Vortex shedding from spheres. *Journal of Fluid Mechanics*, 62(2):209–221.

Anderson, H. (1977). Investigation of the forces on bluff bodies near the ground. Master's thesis, Department of Aeronautics, Imperial College.

ANSYS (2011). Ansys FLUENT users guide. *Canonsburg, PA*.

Awasthi, M. (2015). *Sound radiated from turbulent flow over two and three-dimensional surface discontinuities*. PhD thesis, Virginia Tech.

Awasthi, M., Devenport, W. J., Alexander, W. N., and Glegg, S. A. (2018). Aeroacoustics of rounded forward-facing steps: Near-field behavior. *AIAA Journal*, 57(3):1237–1249.

Awasthi, M., Devenport, W. J., Alexander, W. N., and Glegg, S. A. (2019). Aeroacoustics of rounded forward-facing steps: Far-field behavior. *AIAA Journal*, 57(5):1899–1913.

Bakić, V., Schmid, M., and Stanković, B. (2006). Experimental investigation of turbulent structures of flow around a sphere. *Thermal Science*, 10(2):97–112.

Bearman, P. (1965). Investigation of the flow behind a two-dimensional model with a blunt trailing edge and fitted with splitter plates. *Journal of Fluid Mechanics*, 21(2):241–255.

Bearman, P., Graham, J., Obasaju, E., and Drossopoulos, G. (1984). The influence of corner radius on the forces experienced by cylindrical bluff bodies in oscillatory flow. *Applied Ocean Research*, 6(2):83–89.

Becker, S., Escobar, M., Hahn, C., Ali, I., Kaltenbacher, M., Basel, B., and Grunewald, M. (2005). Experimental and numerical investigation of the flow induced noise from a forward facing step. In *11th AIAA/CEAS Aeroacoustics Conference*, page 3006.

Behera, S. and Saha, A. (2019). Characteristics of the flow past a wall-mounted finite-length square cylinder at low Reynolds number with varying boundary layer thickness. *Journal of Fluids Engineering*, 141:061204.

Beitel, A., Heng, H., and Sumner, D. (2019). The effect of aspect ratio on the aerodynamic forces and bending moment for a surface-mounted finite-height cylinder. *Journal of Wind Engineering and Industrial Aerodynamics*, 186:204–213.

Brick, H., Kohrs, T., Sarradj, E., and Geyer, T. (2011). Noise from high-speed trains: Experimental determination of the noise radiation of the pantograph. In *Proceedings of the Forum Acusticum, Aalborg, Denmark*.

Cao, Y., Tamura, T., and Kawai, H. (2019). Investigation of wall pressures and surface flow patterns on a wall-mounted square cylinder using very high-resolution cartesian mesh. *Journal of Wind Engineering and Industrial Aerodynamics*, 188:1–18.

Carassale, L., Freda, A., and Marrè-Brunenghi, M. (2014). Experimental investigation on the aerodynamic behavior of square cylinders with rounded corners. *Journal of Fluids and Structures*, 44:195–204.

Castro, I. and Robins, A. (1977). The flow around a surface-mounted cube in uniform and turbulent streams. *Journal of Fluid Mechanics*, 79(02):307–335.

Churchfield, M. J., Lee, S., and Moriarty, P. J. (2014). Adding complex terrain and stable atmospheric condition capability to the openfoam-based flow solver of the simulator for on/offshore wind farm applications (sowfa). In *ITM Web Conferences*, volume 2. EDP Sciences.

Colonius, T. and Lele, S. K. (2004). Computational aeroacoustics: progress on nonlinear problems of sound generation. *Progress in Aerospace Sciences*, 40(6):345–416.

Constantinescu, G. and Squires, K. (2004). Numerical investigations of flow over a sphere in the subcritical and supercritical regimes. *Physics of Fluids*, 16(5):1449–1466.

Curle, N. (1955). The influence of solid boundaries upon aerodynamic sound. *Proceedings of the Royal Society of London A: Mathematical, Physical and Engineering Sciences*, 231(1187):505–514.

Délery, J. M. (2001). Robert Legendre and Henri Werlé: toward the elucidation of three-dimensional separation. *Annual Review of Fluid Mechanics*, 33(1):129–154.

Depardon, S., Lasserre, J., Boueilh, J., Brizzi, L., and Borée, J. (2005). Skin friction pattern analysis using near-wall PIV. *Experiments in Fluids*, 39(5):805–818.

Fahy, F. and Thompson, D. (2016). *Fundamentals of sound and vibration 2nd edition*. CRC Press: Boca Raton FL.

Ferziger, J. H. and Perić, M. (2002). *Computational methods for fluid dynamics*, volume 3. Springer.

Ffowcs Williams, J. F. and Hawkings, D. L. (1969). Sound generation by turbulence and surfaces in arbitrary motion. *Philosophical Transactions of the Royal Society of London A: Mathematical, Physical and Engineering Sciences*, 264(1151):321–342.

Fox, T. and West, G. (1993). Fluid-induced loading of cantilevered circular cylinders in a low-turbulence uniform flow. part 1: mean loading with aspect ratios in the range 4 to 30. *Journal of Fluids and Structures*, 7(1):1–14.

Franke, J., Hirsch, C., Jensen, A., Krüs, H., Schatzmann, M., Westbury, P., Miles, S., Wisse, J., and Wright, N. (2004). Recommendations on the use of CFD in wind engineering. In *Cost Action C*, volume 14, page C1.

Fröhlich, J. and von Terzi, D. (2008). Hybrid LES/RANS methods for the simulation of turbulent flows. *Progress in Aerospace Sciences*, 44(5):349–377.

Ganta, N., Mahato, B., and Bhumkar, Y. G. (2019). Analysis of sound generation by flow past a circular cylinder performing rotary oscillations using direct simulation approach. *Physics of Fluids*, 31(2):026104.

Gautier, P., Dine, C., and Hemsworth, B. (2000). Railway noise sources. An overview of recent approaches in identification, modelling and reduction potentials. In *Internoise 2000. Proceedings of the 29th international congress on noise control engineering, 27-31 August 2000, Nice, France, Volume 2*.

Germano, M., Piomelli, U., Moin, P., and Cabot, W. H. (1991). A dynamic subgrid-scale eddy viscosity model. *Physics of Fluids A: Fluid Dynamics (1989-1993)*, 3(7):1760–1765.

Glegg, S., Bryan, B., Devenport, W., and Awasthi, M. (2012). Sound radiation from forward facing steps. In *18th AIAA/CEAS Aeroacoustics Conference (33rd AIAA Aeroacoustics Conference)*, page 2050.

Goldstein, M. E. (1976). Aeroacoustics. *New York, McGraw-Hill International Book Co.*

Gramlich, M. (2012). Numerical investigations of the unsteady flow in the Stuttgart swirl generator with OpenFOAM. Master's thesis, Chalmers University of Technology.

Grosche, F. R. and Meier, G. (2001). Research at dlr göttingen on bluff body aerodynamics, drag reduction by wake ventilation and active flow control. *Journal of Wind Engineering and Industrial Aerodynamics*, 89(14):1201–1218.

Guo, Y. (2005). Empirical prediction of aircraft landing gear noise. *NASA Contractor Report*, 213780.

Haider, A. and Levenspiel, O. (1989). Drag coefficient and terminal velocity of spherical and nonspherical particles. *Powder technology*, 58(1):63–70.

Hao, J., Eltaweel, A., and Wang, M. (2013). Sound generated by boundary-layer flow over small steps: effect of step noncompactness. *AIAA Journal*, 51(10):1770–1775.

Howe, M. S. (2003). *Theory of vortex sound*. Cambridge University Press.

Hu, J., Zhou, Y., and Dalton, C. (2006). Effects of the corner radius on the near wake of a square prism. *Experiments in Fluids*, 40(1):106.

Hunt, J., Abell, C., Peterka, J., and Woo, H. (1978). Kinematical studies of the flows around free or surface-mounted obstacles; applying topology to flow visualization. *Journal of Fluid Mechanics*, 86(1):179–200.

Ikeda, M. and Mitsumoji, T. (2008). Evaluation method of low-frequency aeroacoustic noise source structure generated by Shinkansen pantograph. *Quarterly Report of RTRI*, 49(3):184–190.

Issa, R. I. (1986). Solution of the implicitly discretised fluid flow equations by operator-splitting. *Journal of computational physics*, 62(1):40–65.

Ji, M. and Wang, M. (2010). Sound generation by turbulent boundary-layer flow over small steps. *Journal of Fluid Mechanics*, 654(10):161–193.

Kaushik, D. K., Keyes, D. E., and Smith, B. F. (1999). Newton-Krylov-Schwarz methods for aerodynamics problems: compressible and incompressible flows on unstructured grids. Technical report, Argonne National Lab., IL (US).

Khan, M. H., Sooraj, P., Sharma, A., and Agrawal, A. (2018). Flow around a cube for Reynolds numbers between 500 and 55,000. *Experimental Thermal and Fluid Science*, 93:257–271.

Kitagawa, T. and Nagakura, K. (2000). Aerodynamic noise generated by shinkansen cars. *Journal of Sound and Vibration*, 231(3):913–924.

Kleissl, J., Kumar, V., Meneveau, C., and Parlange, M. B. (2006). Numerical study of dynamic smagorinsky models in large-eddy simulation of the atmospheric boundary layer: Validation in stable and unstable conditions. *Water Resources Research*, 42(6).

Klotz, L., Goujon-Durand, S., Rokicki, J., and Wesfreid, J. (2014). Experimental investigation of flow behind a cube for moderate Reynolds numbers. *Journal of Fluid Mechanics*, 750:73–98.

Kolmogorov, A. N. (1941). The local structure of turbulence in incompressible viscous fluid for very large Reynolds numbers. *Dokl. Akad. Nauk SSSR*, 30(4):301–305.

Kumar, R. A., Sohn, C. H., and Gowda, B. L. (2015). A PIV study of the near wake flow features of a square cylinder: influence of corner radius. *Journal of Mechanical Science and Technology*, 29(2):527–541.

Latorre Iglesias, E. (2015). *Component-based model to predict aerodynamic noise from high-speed trains*. PhD thesis, University of Southampton.

Latorre Iglesias, E., Thompson, D., and Smith, M. (2015). Component-based model for aerodynamic noise of high-speed trains. In *Noise and Vibration Mitigation for Rail Transportation Systems, Notes on Numerical Fluid Mechanics and Multidisciplinary Design 126*, pages 481–488. Springer.

Latorre Iglesias, E., Thompson, D., and Smith, M. (2016). Experimental study of the aerodynamic noise radiated by cylinders with different cross-sections and yaw angles. *Journal of Sound and Vibration*, 361(10):108–129.

Latorre Iglesias, E., Thompson, D., and Smith, M. (2017a). Component-based model to predict aerodynamic noise from high-speed train pantographs. *Journal of Sound and Vibration*, 394:280–305.

Latorre Iglesias, E., Thompson, D. J., Smith, M., Kitagawa, T., and Yamazaki, N. (2017b). Anechoic wind tunnel tests on high-speed train bogie aerodynamic noise. *International Journal of Rail Transportation*, 5(2):87–109.

Lauterbach, A., Ehrenfried, K., Loose, S., and Wagner, C. (2012). Microphone array wind tunnel measurements of Reynolds number effects in high-speed train aeroacoustics. *Noise Notes*, 11(4):35–62.

Lee, B. (1975). The effect of turbulence on the surface pressure field of a square prism. *Journal of Fluid Mechanics*, 69(2):263–282.

Lee, J. and Cho, W. (2008). Prediction of low-speed aerodynamic load and aeroacoustic noise around simplified panhead section model. *Proceedings of the Institution of Mechanical Engineers, Part F: Journal of Rail and Rapid Transit*, 222(4):423–431.

Liakos, A. and Malamataris, N. A. (2014). Direct numerical simulation of steady state, three dimensional, laminar flow around a wall mounted cube. *Physics of Fluids*, 26(5):053603.

Lighthill, M. J. (1952). On sound generated aerodynamically. i. general theory. *Proceedings of the Royal Society of London A: Mathematical, Physical and Engineering Sciences*, 211(1107):564–587.

Lighthill, M. J. (1954). On sound generated aerodynamically. ii. turbulence as a source of sound. *Proceedings of the Royal Society of London A: Mathematical, Physical and Engineering Sciences*, 222(1148):1–32.

Lilly, D. K. (1966). *On the application of the eddy viscosity concept in the inertial sub-range of turbulence*. National Center for Atmospheric Research.

Lim, H. C., Castro, I. P., and Hoxey, R. P. (2007). Bluff bodies in deep turbulent boundary layers: Reynolds-number issues. *Journal of Fluid Mechanics*, 571:97–118.

Lim, H. C., Thomas, T., and Castro, I. P. (2009). Flow around a cube in a turbulent boundary layer: LES and experiment. *Journal of Wind Engineering and Industrial Aerodynamics*, 97(2):96–109.

Liu, X. (2017). *Aerodynamic noise from components of a train pantograph and its reduction*. PhD thesis, University of Southampton.

Liu, X., Hu, Z., Thompson, D., and Jurdic, V. (2018). Reduction of aerodynamic noise from square bars by introducing spanwise waviness. *Journal of Sound and Vibration*, 435(10):323–349.

Liu, X., Thompson, D. J., Hu, Z., and Jurdic, V. (2014). Aerodynamic noise from a train pantograph. *Proc. ICSV21, Beijing*.

Lölgen, T. (1999). Wind tunnel noise measurements on full-scale pantograph models. *The Journal of the Acoustical Society of America*, 105(2):1136–1136.

Lyn, D., Einav, S., Rodi, W., and Park, J.-H. (1995). A laser-doppler velocimetry study of ensemble-averaged characteristics of the turbulent near wake of a square cylinder. *Journal of Fluid Mechanics*, 304:285–319.

Martinuzzi, R. and Tropea, C. (1993). The flow around surface-mounted, prismatic obstacles placed in a fully developed channel flow (data bank contribution). *Journal of Fluids Engineering*, 115(1):85–92.

Mellet, C., Létourneaux, F., Poisson, F., and Talotte, C. (2006). High speed train noise emission: Latest investigation of the aerodynamic/rolling noise contribution. *Journal of Sound and Vibration*, 293(3):535–546.

Menter, F. and Kuntz, M. (2004). Adaptation of eddy-viscosity turbulence models to unsteady separated flow behind vehicles. In *The aerodynamics of heavy vehicles: trucks, buses, and trains*, pages 339–352. Springer.

Miran, S. and Sohn, C. H. (2015). Numerical study of the rounded corners effect on flow past a square cylinder. *International Journal of Numerical Methods for Heat & Fluid Flow*, 25(4):686–702.

Mockett, C., Perrin, R., Reimann, T., Braza, M., and Thiele, F. (2009). Analysis of detached-eddy simulation for the flow around a circular cylinder with reference to PIV data. In *IUTAM Symposium on Unsteady Separated Flows and their Control*, pages 417–427. Springer.

Nakaguchi, H. (1978). Recent japanese research on three-dimensional bluff-body flows relevant to road-vehicle aerodynamics. In *Aerodynamic Drag Mechanisms of Bluff Bodies and Road Vehicles*, pages 227–252. Springer.

Nakamura, H., Igarashi, T., and Tsutsui, T. (2001). Local heat transfer around a wall-mounted cube in the turbulent boundary layer. *International Journal of Heat and Mass Transfer*, 44(18):3385–3395.

Nguyen, N. C., Persson, P.-O., and Peraire, J. (2007). RANS solutions using high order discontinuous Galerkin methods. *AIAA Paper*, 914:2007.

Norberg, C. (1993). Flow around rectangular cylinders: pressure forces and wake frequencies. *Journal of Wind Engineering and Industrial Aerodynamics*, 49(1-3):187–196.

Okajima, A. (1982). Strouhal numbers of rectangular cylinders. *Journal of Fluid Mechanics*, 123:379–398.

Okamoto, S. and Uemura, N. (1991). Effect of rounding side-corners on aerodynamic forces and turbulent wake of a cube placed on a ground plane. *Experiments in Fluids*, 11(1):58–64.

Patankar, S. (2018). *Numerical heat transfer and fluid flow*. CRC press.

Patankar, S. V. and Spalding, D. B. (1983). A calculation procedure for heat, mass and momentum transfer in three-dimensional parabolic flows. In *Numerical Prediction of Flow, Heat Transfer, Turbulence and Combustion*, pages 54–73. Elsevier.

Pocha, J. J. (1971). *On unsteady flow past cylinders of square cross-section*. PhD thesis, Queen Mary College, London.

Poincaré, H. (1882). LES points singuliers des équations différentielles. *CR Acad. Sci. Paris*, 94:416–418.

Pope, S. B. (2001). *Turbulent flows*. Cambridge Univ. Press.

Porteous, R., Moreau, D. J., and Doolan, C. J. (2014). A review of flow-induced noise from finite wall-mounted cylinders. *Journal of Fluids and Structures*, 51:240–254.

Porteous, R., Moreau, D. J., and Doolan, C. J. (2017). The aeroacoustics of finite wall-mounted square cylinders. *Journal of Fluid Mechanics*, 832(10):287–328.

Raul, R. and Bernard, P. (1991). A numerical investigation of the turbulent flow field generated by a stationary cube. *Journal of Fluids Engineering*, 113(2):216–222.

Revell, J. D., Prydz, R. A., and Hays, A. P. (1978). Experimental study of aerodynamic noise vs drag relationships for circular cylinders. *AIAA journal*, 16(6):889–897.

Robertson, E., Choudhury, V., Bhushan, S., and Walters, D. (2015). Validation of OpenFOAM numerical methods and turbulence models for incompressible bluff body flows. *Computers & Fluids*, 123:122–145.

Rodi, W., Ferziger, J., Breuer, M., and Pourquie, M. (1997). Status of large eddy simulation: results of a workshop. *Trans. ASME Journal of Fluids Engineering*, 119:248–262.

Rodríguez, I., Lehmkuhl, O., Borrell, R., and Oliva, A. (2013). Flow dynamics in the turbulent wake of a sphere at sub-critical Reynolds numbers. *Computers & Fluids*, 80:233–243.

Saha, A. (2004). Three-dimensional numerical simulations of the transition of flow past a cube. *Physics of Fluids*, 16(5):1630–1646.

Sakamoto, H. and Haniu, H. (1990). A study on vortex shedding from spheres in a uniform flow. *Journal of Fluids Engineering*, 112(4):386–392.

Schlichting, H. and Gersten, K. (2016). *Boundary-layer theory*. Springer.

Schmidt, M. (2002). *Grobstruktursimulation turbulenter Strömungen auf unstrukturierten Gittern mit einer parallelen Finite-Volumen-Methode*. PhD thesis, Arbeitsbereiche Schiffbau der Techn. Univ.

Shur, M., Spalart, P., Strelets, M., and Travin, A. (1999). Detached-eddy simulation of an airfoil at high angle of attack. *Engineering Turbulence Modelling and Experiments*, 4:669–678.

Smagorinsky, J. (1963). General circulation experiments with the primitive equations: I. the basic experiment. *Monthly Weather Review*, 91(3):99–164.

Smith, J. O. (2007). *Mathematics of the discrete Fourier transform (DFT): with audio applications*. W3K Publishing.

Smith, M. and Chow, L. (1998). Prediction method for aerodynamic noise from aircraft landing gear. *AIAA Paper*, 2228:1998.

Smith, M. G. and Chow, L. (2002). Validation of a prediction model for aerodynamic noise from aircraft landing gear. *AIAA Paper*, 2581(8).

Sohankar, A., Davidson, L., and Norberg, C. (2000). Large eddy simulation of flow past a square cylinder: comparison of different subgrid scale models. *Journal of Fluids Engineering*, 122(1):39–47.

Spalart, P., Jou, W., Strelets, M., Allmaras, S., et al. (1997). Comments on the feasibility of LES for wings, and on a hybrid RANS/LES approach. *Advances in DNS/LES*, 1:4–8.

Spalart, P. R. and Allmaras, S. R. (1992). A one equation turbulence model for aerodinamic flows. *AIAA Journal*, 94.

Spalart, P. R., Deck, S., Shur, M., Squires, K., Strelets, M. K., and Travin, A. (2006). A new version of detached-eddy simulation, resistant to ambiguous grid densities. *Theoretical and Computational Fluid Dynamics*, 20(3):181–195.

Stolz, S., Adams, N., and Kleiser, L. (2001). An approximate deconvolution model for large-eddy simulation with application to incompressible wall-bounded flows. *Physics of Fluids*, 13(4):997–1015.

Sweby, P. K. (1984). High resolution schemes using flux limiters for hyperbolic conservation laws. *SIAM Journal on Numerical Analysis*, 21(5):995–1011.

Takaishi, T., Ikeda, M., and Kato, C. (2004). Method of evaluating dipole sound source in a finite computational domain. *The Journal of the Acoustical Society of America*, 116(3):1427–1435.

Takaishi, T., Sagawa, A., and Kato, C. (2010). Numerical analysis of aerodynamic noise emitted from a pantograph based on non-compact Green's function. *Journal of Environment and Engineering*, 5(1):84–96.

Talotte, C. (2000). Aerodynamic noise: a critical survey. *Journal of Sound and Vibration*, 231(3):549–562.

Talotte, C., Gautier, P.-E., Thompson, D., and Hanson, C. (2003). Identification, modelling and reduction potential of railway noise sources: a critical survey. *Journal of Sound and Vibration*, 267(3):447–468.

Tamura, T. and Miyagi, T. (1999). The effect of turbulence on aerodynamic forces on a square cylinder with various corner shapes. *Journal of Wind Engineering and Industrial Aerodynamics*, 83(1-3):135–145.

Tamura, T., Miyagi, T., and Kitagishi, T. (1998). Numerical prediction of unsteady pressures on a square cylinder with various corner shapes. *Journal of Wind Engineering and Industrial Aerodynamics*, 74:531–542.

Taneda, S. (1978). Visual observations of the flow past a sphere at Reynolds numbers between 10^4 and 10^6. *Journal of Fluid Mechanics*, 85(1):187–192.

Thomas, F. O., Kozlov, A., and Corke, T. C. (2008). Plasma actuators for cylinder flow control and noise reduction. *AIAA journal*, 46(8):1921–1931.

Thompson, D. (2008). *Railway noise and vibration: mechanisms, modelling and means of control*. Elsevier: Oxford.

Thompson, D., Hemsworth, B., and Vincent, N. (1996). Experimental validation of the twins prediction program for rolling noise, part 1: description of the model and method. *Journal of Sound and Vibration*, 193(1):123–135.

Thompson, D., Smith, M., and Coudret, F. (2012). Application of a component-based approach to modelling the aerodynamic noise from high-speed trains. In *Noise and Vibration Mitigation for Rail Transportation Systems, Notes on Numerical Fluid Mechanics and Multidisciplinary Design 118*, pages 427–435. Springer.

Thompson, D. J., Latorre Iglesias, E., Liu, X., Zhu, J., and Hu, Z. (2015). Recent developments in the prediction and control of aerodynamic noise from high-speed trains. *International Journal of Rail Transportation*, 3(3):119–150.

Tomboulides, A. G. (1993). *Direct and large eddy simulation of wake flows: flow past a sphere*. PhD thesis, Princeton University.

Turkel, E., Fiterman, A., and Van Leer, B. (1993). Preconditioning and the limit to the incompressible flow equations. Technical report, DTIC Document.

Uda, T., Yamazaki, N., Kitagawa, T., Nagakura, K., and Wakabayashi, Y. (2018). Estimation of aerodynamic bogie noise through field and wind tunnel tests. In *Noise and Vibration Mitigation for Rail Transportation Systems*, pages 377–387. Springer.

Versteeg, H. K. and Malalasekera, W. (2007). *An introduction to computational fluid dynamics: the finite volume method*. Pearson Education.

Vickery, B. J. (1966). Fluctuating lift and drag on a long cylinder of square cross-section in a smooth and in a turbulent stream. *Journal of Fluid Mechanics*, 25(3):481–494.

Wang, H. and Zhou, Y. (2009). The finite-length square cylinder near wake. *Journal of Fluid Mechanics*, 638:453–490.

Wang, H., Zhou, Y., Chan, C., and Lam, K. (2006a). Effect of initial conditions on interaction between a boundary layer and a wall-mounted finite-length-cylinder wake. *Physics of Fluids*, 18(6):065106.

Wang, M., Freund, J. B., and Lele, S. K. (2006b). Computational prediction of flow-generated sound. *Annu. Rev. Fluid Mech.*, 38:483–512.

Wieselsberger, C. (1921). Neuere feststellungen uber die gesetze des flussigkeits und luftwiderstands. *Physikalische Zeitschrift*, 22:321.

Wilcox, D. C. (2008). Formulation of the kw turbulence model revisited. *AIAA journal*, 46(11):2823–2838.

Wilcox, D. C. et al. (1998). *Turbulence modeling for CFD*, volume 2. DCW industries La Canada, CA.

Wu, T. (2000). *Boundary element acoustics: fundamentals and computer codes*, volume 7. WIT Press/Computational Mechanics.

Yakhot, A., Anor, T., Liu, H., and Nikitin, N. (2006a). Direct numerical simulation of turbulent flow around a wall-mounted cube: spatio-temporal evolution of large-scale vortices. *Journal of Fluid Mechanics*, 566(1):1–9.

Yakhot, A., Liu, H., and Nikitin, N. (2006b). Turbulent flow around a wall-mounted cube: A direct numerical simulation. *International Journal of Heat and Fluid Flow*, 27(6):994–1009.

Yauwenas, Y., Porteous, R., Moreau, D. J., and Doolan, C. J. (2019). The effect of aspect ratio on the wake structure of finite wall-mounted square cylinders. *Journal of Fluid Mechanics*, 875:929–960.

Zhang, D., Cheng, L., An, H., and Zhao, M. (2017). Direct numerical simulation of flow around a surface-mounted finite square cylinder at low Reynolds numbers. *Physics of Fluids*, 29(4):045101.

Zhang, W. and Samtaney, R. (2016). Low-Re flow past an isolated cylinder with rounded corners. *Computers and Fluids*, 136:384–401.

Zhu, J. (2015). *Aerodynamic noise of high-speed train bogies*. PhD thesis, University of Southampton.

Zhu, J., Hu, Z., and Thompson, D. (2017). The effect of a moving ground on the flow and aerodynamic noise behaviour of a simplified high-speed train bogie. *International Journal of Rail Transportation*, 5(2):110–125.

Zhu, J., Hu, Z., and Thompson, D. (2018). The flow and flow-induced noise behaviour of a simplified high-speed train bogie in the cavity with and without a fairing. *Proceedings of the Institution of Mechanical Engineers, Part F: Journal of Rail and Rapid Transit*, 232(3):759–773.

Zhu, J., Hu, Z., and Thompson, D. J. (2016). Flow behaviour and aeroacoustic characteristics of a simplified high-speed train bogie. *Proceedings of the Institution of Mechanical Engineers, Part F: Journal of Rail and Rapid Transit*, 230(7):1642–1658.